U.PORTO

FEUP FACULDADE DE ENGENHARIA
UNIVERSIDADE DO PORTO

COMPOSITE MODELLING OF RUBBLE-MOUND BREAKWATERS USING ADVANCED PHYSICAL MODELLING TECHNIQUES AND A SMOOTHED PARTICLE HYDRODYNAMICS MODEL

BEATRIZ MARGARIDA DE OLIVEIRA QUEIRÓS

Doctoral Program in Civil Engineering

Hydraulics, Water Resources and Environment

Supervisors:

Prof. Dr. Francisco de Almeida Taveira Pinto

Prof. Dr Paulo Jorge Rosa Santos

Prof. Dr Alejandro Jacobo Cabrera Crespo

JUNE 2025

PROGRAMA DOUTORAL EM ENGENHARIA CIVIL 2024/2025

DEPARTAMENTO DE ENGENHARIA CIVIL

Tel. +351-22-508 1901

Fax +351-22-508 1446

✉ miec@fe.up.pt

Editado por

FACULDADE DE ENGENHARIA DA UNIVERSIDADE DO PORTO

Rua Dr. Roberto Frias

4200-465 PORTO

Portugal

Tel. +351-22-508 1400

Fax +351-22-508 1440

✉ feup@fe.up.pt

🌍 http://www.fe.up.pt

ABSTRACT

Coastal communities increasingly rely on rubble-mound breakwaters to shield critical infrastructure from the growing threats posed by climate change. With rising sea levels and the intensification of storm events, these structures are increasingly subjected to unprecedented challenges, particularly within their armour layers, where wave-induced forces can provoke displacement, rotation, and structural damage to individual units. Understanding these intricate interactions is vital for ensuring the resilience of breakwaters against future environmental pressures. This thesis combines innovative numerical modelling and experimental techniques to address these challenges, paving the way for more robust and adaptive coastal defence systems.

The research refines the Smoothed Particle Hydrodynamics (SPH) method using the DualSPHysics framework, a powerful tool for simulating complex wave-structure interactions. Laboratory experiments with Antifer blocks under controlled wave conditions provided detailed datasets for model validation, while the development and deployment of SmartAntifer blocks – a novel instrumented armour unit – enabled precise tracking of displacements and forces within the armour layer. These innovative approaches bridge critical gaps in understanding the hydraulic instability of rubble-mound breakwaters.

Results demonstrate that DualSPHysics effectively captures wave overtopping, run-up, and block displacements, offering valuable insights into the interplay between hydrodynamic forces and breakwater stability. Laboratory tests confirmed the potential of SmartAntifer blocks to deliver detailed and reliable movement data, though technical challenges and calibration errors highlighted areas for further refinement. While numerical simulations aligned well with experimental observations, discrepancies in block displacements underscored the need for improved boundary conditions and refined experimental setups.

This research advances the state of coastal engineering by improving numerical tools, experimental methods, and design frameworks for rubble-mound breakwaters. The integration of SmartAntifer blocks with SPH modelling provides a comprehensive approach to studying breakwater stability, offering scalable and cost-effective alternatives to traditional methods. These findings contribute to designing more robust and climate-resilient coastal defences, aligning with global sustainability goals. Future recommendations include refining SmartAntifer technology, improving and standardized experimental protocols, and addressing the challenges posed by climate change in breakwater design, simulating more realistic scenarios.

RESUMO

As comunidades costeiras dependem cada vez mais dos quebra-mares de taludes para proteger infraestruturas críticas face aos desafios crescentes impostos pelas alterações climáticas. Com o aumento do nível do mar e a intensificação das tempestades, estas estruturas enfrentam pressões sem precedentes, particularmente nas suas camadas de proteção, onde as forças geradas pelas ondas podem causar deslocamentos, rotações e danos estruturais nas unidades individuais do manto resistente. A compreensão destas interações complexas é fundamental para garantir a resiliência dos quebra-mares perante futuras condições ambientais adversas.

Esta tese combina técnicas inovadoras de modelação numérica e ensaios laboratoriais para enfrentar estes desafios, contribuindo para o desenvolvimento de sistemas de defesa costeira mais robustos e adaptáveis.

A investigação realizada valida e aperfeiçoa o modelo "*Smoothed Particles Hydrodynamics*" (SPH) através do solver DualSPHysics, uma ferramenta avançada para simular interações complexas entre ondas e estruturas. Ensaios laboratoriais com blocos Antifer, realizados sob condições controladas, forneceram dados essenciais para a validação do modelo. Paralelamente, o desenvolvimento e a aplicação de uma nova unidade de proteção instrumentada – os blocos SmartAntifer – permitiram registar com precisão os deslocamentos e as forças no manto resistente. Estas abordagens inovadoras preencheram lacunas críticas no conhecimento sobre a instabilidade hidráulica dos quebra-mares de talude.

Os resultados demonstram que o DualSPHysics é capaz de simular com precisão fenómenos físicos como o galgamento, o "*run-up*" e o deslocamento dos blocos, oferecendo uma visão detalhada da interação entre as forças hidrodinâmicas e a estabilidade dos quebra-mares. Os ensaios laboratoriais confirmaram o potencial dos blocos SmartAntifer para recolher dados detalhados e fiáveis sobre o movimento das unidades do manto resistente, embora se tenham identificado desafios técnicos e erros de calibração que apontam para oportunidades de melhoria. Apesar da boa correspondência entre os resultados numéricos e os experimentais, foram detetadas discrepâncias nos deslocamentos dos blocos, que evidenciam a necessidade de otimizar as condições de fronteira e de refinar os procedimentos experimentais.

Este trabalho representa um avanço significativo na engenharia costeira, ao contribuir para o aperfeiçoamento das ferramentas numéricas, dos métodos experimentais e das abordagens de projeto aplicadas aos quebra-mares de talude. A integração dos blocos SmartAntifer com a modelação numérica proporciona uma abordagem abrangente ao estudo da estabilidade dos quebra-mares, oferecendo alternativas escaláveis e economicamente viáveis aos métodos tradicionais. Os resultados obtidos contribuem para o desenvolvimento de defesas costeiras mais robustas e resilientes a impactos das alterações climáticas, em alinhamento com os objetivos globais de sustentabilidade. Recomendações futuras incluem o aperfeiçoamento da tecnologia SmartAntifer, a normalização de protocolos experimentais e a inclusão de cenários climáticos realistas no dimensionamento de quebra-mares, de forma a garantir uma infraestrutura costeira eficaz e sustentável.

ACKNOWLEDGMENTS

I would like to express my deepest gratitude and appreciation to those who have contributed to the realization of this Ph.D. thesis.

I would like to thank my supervisor, Doctor Professor Francisco Taveira Pinto, for suggesting such a compelling research topic and for providing invaluable guidance throughout this journey. His understanding during setbacks and insightful advice have greatly influenced the direction of this work.

I also extend my heartfelt thanks to my co-supervisors: Doctor Professor Paulo Rosa Santos, for his essential practical and intellectual guidance, and Doctor Professor Alejandro Crespo, who offered me the opportunity to spend time at the EPhysLab in Ourense, Spain. His unwavering support, insightful comments, and encouragement had a profound impact on my progress. A special thanks also goes to the EPhysLab team, including Doctor Ramón Gómez Gesteira, Doctor José Domínguez, and Doctor Iván Martínez Estévez, for their collaboration and support during my time in Ourense.

Appreciation is extended to all the faculty members and staff in the Hydraulics, Water Resources, and Environment Division for their collaboration and support. A special thanks to my friend Tomás, who shared this journey with me and whose companionship, thought-provoking challenges, and collaborative thinking inspired and pushed me forward. I also wish to thank Professor Francisco Piqueiro, Sr. Miguel for his willingness to assist, even with unconventional requests, and D. Esmeralda for her friendship and encouragement during this demanding process. I would also like to thank João Galante and the LSTS group for their assistance and support.

To my family—my parents and Delfim—your unwavering love and belief in me have been a source of strength and motivation. Finally, I gratefully acknowledge the financial support provided by the Fundação Portuguesa para a Ciência e a Tecnologia through the grant reference SFRH/BD/129888/2017. This work was also supported by the Faculdade de Engenharia da Universidade do Porto through the ATLANTIDA project (NORTE-01-0145-FEDER-000040) and by Universidade de Vigo under the Project SURVIWEC PID2020-113245RB-I00 financed by MCIN/AEI/10.13039/501100011033.

CONTENTS

FIGURE CONTENTS

TABLE CONTENTS

SYMBOLS, ACRONYMS AND ABBREVIATURES

a	[m/s^2]	Resulting acceleration
A	[m^2]	Surface area of the armour layer parallel to the local slope
a'	[m/s^2]	Acceleration magnitude
$a_{corrected}$	[m/s^2]	Corrected acceleration
A_e	[m^2]	Eroded area
A_{FSC}	[-]	Free surface correction coefficient
A_{FSM}	[m]	Maximum value of the particle divergence
A_{FST}	[m]	Free-surface threshold
a_{local}	[m/s^2]	Acceleration measured in the blocks local coordinate system
$a_{measured}$	[m/s^2]	Measured acceleration
$a_{resultant}$	[g]	Resultant acceleration
$a_{transformed}$	[m/s^2]	Transformed acceleration
a_x, a_y	[m/s^2]	Corrected acceleration according to x, y
a'_x, a'_y, a'_z	[m/s^2]	Acceleration readings along each block's axes x, y, z
a^p_x, a^p_y, a^p_z	[m/s^2]	Acceleration probe readings according to x, y, z
A_{pe}	[m^2]	Planar exposed area
C	[-]	Dimensionless cover depth
CFL	[-]	Courant number
C_R	[-]	Restitution coefficient
d	[m]	Water depth
D	[m]	Characteristic armour unit length
d_c	[m]	Remaining thickness of the armour layer
d_e	[m]	Eroded depth
D_e	[-]	Equivalent dimensionless damage accounting for porosity variation
D_i	[-]	Individual dimensionless damage
D_n	[m]	Nominal armour unit diameter
D_{n50}	[m]	Nominal diameter of the armour rock for which 50% of the rock mass is smaller
dp	[m]	Initial interparticle distance
d_s	[-]	Number of nominal diameters contained within a strip width
D_s	[-]	Diffusion coefficient
d_t	[m]	Total planar displacement
e	[m]	Local erosion depth during a test (always positive)
E	[-]	Dimensionless eroded depth
E_c	[GPa]	Young modulus
f	[N]	Frictional force
F	[N]	Force
$F_{Coriolis}$	[N]	Coriolis force
FH_s	[-]	Uncertainty of the wave height at a certain return period
F_{net}	[N]	Net force acting on the block

F_W	[N]	Gravitational force
g	[m/s^2]	Gravitational acceleration
g_{plane}	[m/s^2]	Gravitational acceleration componente according to the inclined plane
h	[m]	Smoothing length
H	[m]	Wave height
H_{m0}	[m]	Spectral significant wave height
H_s	[m]	Significant wave height
I	[kg·m^2]	Moment of inertia
k	[m^2/s^2]	SPS turbulence kinetic energy
k_c	[-]	Modified layer coefficient
K_D	[-]	Stability coefficient in Hudson formula
k_s	[-]	Shape coefficient
k_t	[-]	Layer coefficient
L	[m]	Wavelength
l_e	[m]	Eroded length
L_e	[-]	Dimensionless eroded length
m	[kg]	Mass
M	[kg]	Mass of concrete armour unit
n	[-]	Porosity
N	[l/m^2]	Packing density
N_a	[-]	Number of armour units in the area concerned
N_{col}	[-]	Number of collisions in the test
N_d	[%]	Percentage of displaced rocks/blocks relative to the total number of Rock/blocks in the armour layer active zone
n_l	[-]	Number of layers of armour units
N_{od}	[-]	Number of displaced units within a strip of width D_n
N_s	[-]	Stability number
n_v	[-]	Layer porosity of the concrete
N_z	[-]	Number of incoming waves during the design storm
N_{ze}	[-]	Equivalent number of waves
p or P	[kg/(m·s^2)]	Pressure
P_f	[-]	Probability of failure
p_i	[-]	Actual porosity in the strip
P_n	[-]	Notional permeability factor
p_0	[-]	Initial porosity in the strip
r	[m]	Position
R_c	[m]	Crest height of the structure above still water level
R_0	[m]	Centre of mass
r_w	[-]	Waist ratio
S	[-]	Dimensionless eroded area
S_d	[-]	Relative eroded area

s_m	[-]	Wave steepness
S_N	[-]	Dimensionless eroded area accounting for number of displaced units
s_{om}	[-]	Wave steepness based on the spectral wave period
S_0	[m]	Piston paddle stroke
S_t	[-]	Dimensionless eroded area based on planar exposed area
s_x, s_y	[m]	Displacement component according to x, y
t	[s]	Time
T	[s]	Wave period
t_a	[m]	Armour layer thickness
T_m	[s]	Mean wave period
T_P	[s]	Peak wave period
U_C	[m/s]	Corrected velocity
v	[m/s]	Velocity
V	[m^3]	Armour unit volume
V_{air}	[m^3]	Volume of air
v_i	[m/s]	Impact velocity
V_{total}	[m^3]	Total layer volume
v_x, v_y	[m/s]	Velocity according to x, y
W	[-]	Smoothing kernel
W_a	[N]	Armour unit weight
W_{core}	[N]	Core material weight
$W_{underlayer}$	[N]	Underlayer material weight
$W_\perp$	[N]	Normal force
$W_\parallel$	[N]	Downhill force

α	[°]	Angle of seaward slope of the structure
Γ		Dissipative term
Δ	[-]	Relative mass density
Δl	[m]	Initial particle spacing
Δt	[s]	Time step
η	[m]	Free-surface elevation
$\eta_{\mathrm{AWAS},i}$	[m]	Target incident free-surface elevation
$\eta_{\mathrm{WG,SPH}}$	[m]	Free-surface elevation measured in front of the wavemaker
θ	[rad]	Rotation angle
θ_0	[rad]	Initial orientation
ξ	[-]	Surf similarity parameter
Π_{ab}		Viscosity term
ρ	[kg/m^3]	Mass density
ρ_{app}	[kg/m^3]	Apparent mass density
ρ_c	[kg/m^3]	Mass density of concrete armour unit
ρ_0	[kg/m^3]	Reference mass density of the fluid

$\vec{\tau}$	[N/m^2]	SPS stress tensor
μ	[-]	Coefficient of friction
υ	[-]	Poisson ratio
υ_0	[m^2/s]	Kinematic viscosity of the fluid
ϕ	[-]	Packing density coefficient
Ψ_{ab}		Term based on the Neumann-Richtmeyer artificial dissipation
ω	[rad/s]	Angular velocity
ω_f	[rad/s]	Angular frequency
ω_j	[rad/s]	Angular velocity component with the largest standard deviation
$\omega_x, \omega_y, \omega_z$	[rad/s]	Angular velocity components according to x,y,z
Ω		Computational domain
$\Omega_x, \Omega_y, \Omega_z$	[rad]	Orientation angles according to x, y, z

AWAS	Active Wave Absorption System
BC	Boundary Conditions
BEM	Boundary Element Method
CDF	Cumulative Distribution Function
CFD	Computational Fluid Dynamics
CPU	Central Processing Unit
DBC	Dynamic Boundary Condition
DCDEM	Distributed Contact Discrete Element Method
DEM	Diffuse Element Method
DMP	Digital Motion Processor
DSP	Digital Stereo Photogrammetric
DVI	Differential Variational Inequality
EDM	Electrical Discharge Machining
FDM	Finite Differences Method
FEM	Finite Element Method
FVM	Finite Volume Method
GCI	Grid Convergence Indicator
GPU	Graphic Processing Unit
HPC	High-Performance Computing
IMU	Inertial Measurement Unit
ISPH	Incompressible Smoothed Particle Hydrodynamics
LED	Light Emitting Diode
LES	Large Eddy Simulations
LiDAR	Light Detection and Ranging
MCU	Microcontroller Unit
mDBC	Modified Dynamic Boundary Condition
MPS	Moving Particle Semi-Implicit
NN	Neural Network

ODE	Ordinary Differential Equation
OWC	Oscillating Water Column
PCB	Printed Circuit Board
PFEM	Particle Finite Element Method
PLA	Polylactic acid
RANS	Reynolds-Averaged Navier-Stokes
RF	Radiofrequency
RTC	Real-Time Clock
RZ	Relaxation Zone
SPH	Smoothed Particle Hydrodynamics
SPS	Sub-Particle Scale
TRL	Technology Readiness Level
TWS	Trainable Weka Segmentation
VoF	Volume of Fluid
WCSPH	Weakly Compressible Smoothed Particle Hydrodynamics
WEC	Wave Energy converter

1
INTRODUCTION

1.1 BACKGROUND AND MOTIVATION

Rubble-mound breakwaters are a cornerstone of coastal defence, protecting harbours and ports by dissipating wave energy and providing sheltered areas for maritime activities. However, these structures are increasingly threatened by the impacts of climate change, such as rising sea levels, intensifying storms, and shifting wave patterns. Many existing breakwaters, particularly older designs, were not conceived to withstand such dynamic, harsh and unpredictable conditions. Simultaneously, the growing emphasis on sustainability have prompted interest in transforming breakwaters into multi-functional infrastructures, capable of both dissipating wave energy and supporting renewable energy systems. Achieving such versatility demands innovative approaches to design and performance evaluation, as traditional methods fall short of addressing these complexities.

Historically, rubble-mound breakwaters have evolved to address progressively more complex marine environments. These structures typically feature a trapezoidal cross-section with a rubble stone core, porous layers, and an external armour layer composed of natural stones or specially designed concrete units. The armour layer is pivotal to the structure's stability, promoting wave dissipation and interlocking forces between the units that resist the dynamic forces of the ocean. Yet, despite their robust design, traditional methodologies often focus on overall hydraulic stability, overlooking the intricate interactions within the armour layer. Displacements, rotations, and collisions of individual units under wave action can significantly affect structural integrity and longevity, but these processes remain poorly understood.

This limited understanding of the forces and dynamics at the level of individual armour units poses a significant barrier to innovation. Empirical approaches, while providing broad insights into hydraulic performance, fail to capture the intricate phenomena influencing unit displacement, rotation, and breakage. At the same time, physical modelling, although invaluable, is constrained by challenges in instrumentation, data collection, and the ability to observe fine-scale dynamics. Numerical models, such as Smoothed Particle Hydrodynamics (SPH), offer a promising alternative for simulating wave-structure interactions with greater precision. Among these, the DualSPHysics model stands out for its efficiency in handling highly non-linear problems and complex boundaries, thanks to parallel processing and GPU computing. Despite these advancements, the model still requires rigorous validation and further development to ensure its reliability in real-world scenarios.

Addressing these challenges is essential to enhancing the resilience and multifunctionality of rubble-mound breakwaters in response to evolving environmental pressures. By advancing our understanding of the intricate dynamics between wave action and individual armour units, this research seeks to close

critical knowledge gaps. Through the integration of high-resolution experimental data and cutting-edge numerical modelling, this study paves the way for designing coastal defences that are not only more robust and adaptable but also capable of contributing to sustainable and innovative applications in modern coastal engineering.

1.2 RESEARCH OBJECTIVES AND NOVELTY

This thesis aims to address these challenges by adopting a comprehensive approach that integrates high-resolution physical modelling and advanced numerical modelling to improve the understanding of the complex interactions between wave action and individual armour units in rubble-mound breakwaters. The specific objectives of this research are as follows:

(i) **Investigate the dynamic behaviour of armour units:** examine displacements, rotations, and collisions under wave action, which are critical to the stability of rubble-mound breakwaters. This includes identifying the forces driving these movements and their effects on structural integrity, pinpointing specific locations within breakwaters, such as the toe berm and trunk, that are most vulnerable to damage;
(ii) **Enhance the Smoothed Particle Hydrodynamics (SPH) method**: refine the application of DualSPHysics for coastal engineering, focusing on improving simulation accuracy for non-linear wave-structure interactions;
(iii) **Validate numerical models with high-resolution experimental data**: compare DualSPHysics simulation results against high-resolution experimental data to ensure the reliability of the model for real-world applications and enhance its predictive capabilities in coastal defence design;
(iv) **Developing innovative instrumentation:** design and test novel instrumented concrete armour units, known as SmartAntifer blocks, equipped with wireless sensors to capture unit-level dynamics, offering valuable insights into their behaviour;
(v) **Revising design frameworks**: evaluate existing empirical formulas used for breakwater design and propose improvements based on experimental and numerical findings.

The novelty of this research lies in its combined use of state-of-the-art experimental techniques and numerical tools, alongside the development of the SmartAntifer blocks. These innovations address longstanding challenges in monitoring and understanding individual armour unit dynamics, enabling more accurate predictions of damage and failure.

1.3 RELEVANCE OF THE STUDY

This research contributes to coastal engineering by advancing knowledge, improving design practices, and addressing climate adaptation needs:

(i) **Advancing knowledge**:
- Provides insights into armour unit dynamics, addressing gaps in wave-structure interaction understanding;
- Establishes a framework for future studies combining physical and numerical modelling.

(ii) **Improving design practices**:

- Refines numerical tools like DualSPHysics, offering engineers reliable alternatives to traditional design methods, reducing the need for costly physical tests;
- Introduces SmartAntifer blocks offering detailed data for more accurate predictions and improved design reliability.

(iii) **Adapting to climate change**:

- Supports the design of breakwaters capable of withstanding harsher weather conditions;
- Aligns with global sustainability goals by facilitating the integration of breakwaters into renewable energy systems.

The expected outcome of this research is not just a more robust DualSPHysics model but also the creation of a new dataset that could reshape how wave-induced damage in rubble-mound breakwaters is understood and predicted, ultimately leading to more sustainable, cost-effective breakwater designs.

1.4 THESIS OUTLINE

This thesis is organized into five chapters, each building upon the previous to provide a comprehensive exploration of the challenges, methodologies, and outcomes of applying SPH and advanced physical modelling instrumentation to rubble-mound breakwater studies. The research was conducted at the Hydraulics, Water Resources and Environment Division (SHRHA) of the Department of Civil and Georesources Engineering (DECG) of the Faculty of Engineering of the University of Porto (FEUP).

Chapter 1 corresponds to the present chapter, which contains an introduction to the study, providing background information on the topic under investigation, research objectives, novelty of the research, showing its relevance to the state-of-the art knowledge, and structure of the contents.

Chapter 2 presents a thorough literature review, examining the historical and contemporary approaches to rubble-mound breakwater design. It delves into the evolution of hydraulic stability assessments, damage progression models, and the limitations of traditional empirical formulas. The chapter also explores recent advancements in physical modelling techniques to test rubble-mound structures and high-resolution and high-accuracy measuring equipment for assessment of the damage, including instrumented concrete armour units.

Chapter 3 delves into the theoretical foundations and applications of Smoothed Particle Hydrodynamics (SPH) in coastal engineering, with a focus on its implementation through the DualSPHysics framework. It explores the advantages and limitations of SPH as a Lagrangian meshless method, emphasizing its suitability for simulating complex wave-structure interactions. The chapter also provides an overview of the DualSPHysics code, including its architecture and recent advancements, and critically evaluates prior verification and validation studies, highlighting the framework's strengths and areas for further development.

Following this, chapter 4 describes the methodologies employed in this research, encompassing both physical and numerical modelling. It introduces the development and testing of the SmartAntifer blocks, detailing their instrumentation, calibration, and deployment in experimental setups. This chapter also outlines the implementation of the DualSPHysics model, emphasising its integration with experimental data for validation purposes. The complementary roles of these approaches are underscored, showcasing how they provide insights into both macro- and micro-scale dynamics.

Chapter 5 presents the results and integrates the findings from experimental and numerical components, providing a critical analysis of their implications for wave-induced forces and breakwater performance. Special attention is given to the validation of the DualSPHysics model and the novel insights gained from the SmartAntifer data, which inform design improvements and identify structural vulnerabilities. The chapter concludes by summarizing the key contributions of the study and reflecting on its impact on the field of coastal engineering. It also addresses the limitations encountered during the research and suggests directions for future work, aimed at enhancing the resilience and functionality of rubble-mound breakwaters in the face of evolving challenges.

2

DESIGN AND MONITORING OF RUBBLE-MOUND BREAKWATERS

2.1 INTRODUCTION

Breakwaters are built to create protected zones from ocean waves, such as harbours and ports, where maritime shipping plays a crucial role in the world economy. They work as obstacles to the natural propagation of waves that may cause run-up and overtopping, leading to potential damage and flooding of the area behind the structures. These structures create sheltered spaces for the berthing and mooring of ships, where the loading and unloading of goods and people can safely take place. Rubble-mound breakwaters are a commonly employed solution worldwide due to their effectiveness in dissipating wave energy and their advantages in terms of ease of maintenance and construction (Akarsh and Chaudhary, 2022).

In the next 20-100 years, these structures will experience increased stress due to sea-level rise and global climate change, which will modify the magnitude and frequency of storms to an uncertain degree (Rogers *et al.*, 2015). Simultaneously, continuous technological and commercial evolution will occur in the maritime ports, ocean resources exploitation will continue to increase, and coastal population will keep growing. The port authorities and social communities, increasingly conscious of the problems related to the protection of the seaside, are requiring reliable solutions. So, coastal structures, like breakwaters, need to be adapted to these new scenarios of coastal vulnerability (Rogers *et al.*, 2015). This adaptation requires the development of existing and new coastal infrastructures, paying attention to the constructive solutions adopted and the design's methodologies chosen.

At the same time, it is required a fully comprehensive and more complete hydrodynamic analysis of the ocean environment and its interaction with ocean structures and facilities (Luo *et al.*, 2021). For instance, the wave–structure interaction is a complex phenomenon, and the laws of physics and fluid dynamics only help to understand a limited number of these coastal engineering phenomena. Since breakwaters are subject to high magnitude actions with a stochastic nature, the design process is rather complex, making unfeasible to achieve analytical expressions for the calculation of actions and reactions. Hence, stability formulae and the initial design of breakwaters have traditionally relied on empirical and semi-empirical methods. These approaches rely on simplified theoretical principles derived from physical models and the designer's expertise. It is crucial to recognize that these formulas are applicable only under specific conditions, which limit both the availability of input data and their accuracy, thereby introducing another source of uncertainty. In practice, a sound engineering approach is required, based on practical experience, and supported by powerful tools such as physical and numerical models, to increase the comprehension of many phenomena and to come up with sustainable solutions.

Sometimes, the physical modelling of coastal phenomena proves to be a challenging task, not affordable for researchers and engineers. Thus, many recent efforts to provide expeditious reliable results have been focused on a proper numerical modelling of the interaction between sea waves and maritime structures (Altomare *et al.*, 2014; Luo *et al.*, 2021). With the rapid development of computational techniques and hardware, novel sophisticated tools are being actively under development to replace or/and improve the existent numerical models. One of the most flexible numerical techniques is the *Smoothed Particle Hydrodynamics* (SPH).

2.2 RUBBLE-MOUND BREAKWATERS WITH CONCRETE ARMOUR UNITS' DESIGN

Breakwaters have been used throughout history for harbour protection by changing the natural and physical system. These structures are built to reduce wave action in an area on their lee side, which may be a harbour (CEM, 2006; Eden, 2019). Its design is a complex process involving several design cycles limited by technical, economic, environmental, and other constraint categories. The outcome of a successful integrated design will have to achieve an adequate balance between all the requirements. For example, according to CEM (2006), the breakwater's layout used to protect a harbour is determined by the size and shape of the protected area. The prevailing directions of storm waves and currents, littoral drift, and the manoeuvrability of the vessels using the harbour also contribute to the breakwater's layout.

Rubble-mound breakwaters have a simple trapezoidal cross-section and are commonly used (Akarsh and Chaudhary, 2022). They are built mainly of rock and generally have an outer layer of armour stone or artificial concrete armour units called armour layer, which protects the structure against wave attack (see Fig.1). The water percolation between the armour units produces highly turbulent flow patterns that dissipate part of the incident wave energy. Armour stones and concrete armour units in this outer layer are usually placed strategically to obtain effective interlocking and, consequently, better stability (Eden, 2019).

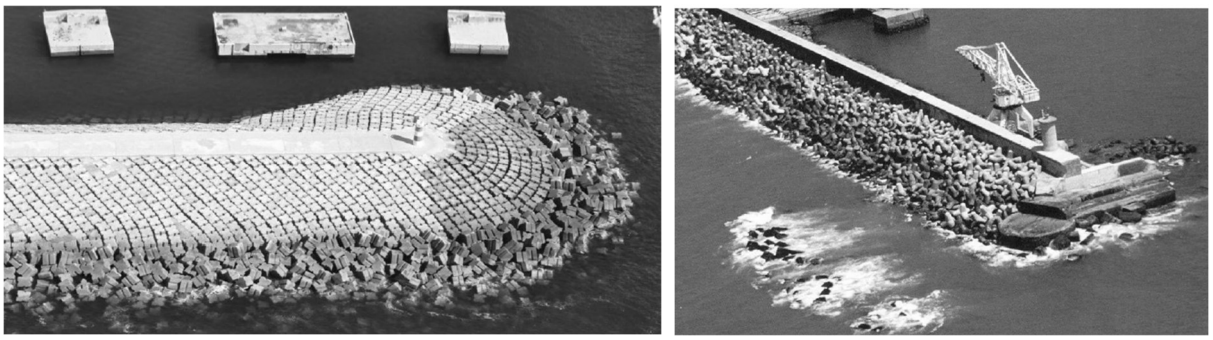

Fig.1 – Examples of rubble-mound breakwaters: the west breakwater of the port of Sines (left) and the north breakwater of the port of Leixões (right) (Freitas, 2013; Gomes *et al.*, 2013).

The partial or total loss of breakwaters functionality, compromised due to several occurrences, is defined as damage. Regarding rubble-mound breakwaters, the concept of damage usually relates to the hydraulic instability of the armour layer. Breakwaters initially function as static systems, but once wave energy exceeds the threshold required for movement initiation of the armour layer units, wave forces can induce various movements within the armour layer, including rocking, displacements, settlements, and other mechanisms, leading to the evolution of the breakwater shape and a subsequent geometric

reconfiguration. The damage progression can reach the underlayer, and then result in core material exposure, leading to the complete failure of the structure.

So, the term damage commonly refers to the geometrical evolution of a breakwater section, occasionally leading to the breakage of armour units. However, one should address the damage concept from a much more multidimensional perspective, since not every rubble-mound breakwater design follows similar functional requirements and not every structure presents the same fragility. There is a relatively wide variety of breakwater typologies, and each type of armour unit demonstrates a singular behaviour against wave actions. So, damage has a qualitative character associated with the level of functionality and a quantitative character related to armour units' movement measurement. Usually, empirical design methods based on numerous scaled experimental tests and analyses of past breakwater failures are used for movement initiation and damage progression quantification. But, given the stochastic nature of the variables involved in the process of hydraulic instability of the armour layer, it is convenient to use probabilistic and risk-based approaches. Moreover, the current design processes lack the quantification of unit forces, movements and collisions of units, concrete fatigue and hydrodynamic pressures (Campos *et al.*, 2020a; Campos *et al.*, 2020b; Eden, 2019).

Therefore, the present subsection will focus on a brief description of the design process of rubble-mound breakwaters with concrete armour units (2.2.1) and in the definition, parameterization, measurement, and modelling of artificial armour units damage (2.2.2).

2.2.1 FUNCTIONAL AND STRUCTURAL DESIGN

The breakwaters' design is a complex process involving several design cycles with an increasing level of detail. Fig.2 (CIRIA *et al.*, 2007) illustrates a logic diagram for the design process, from the project definition stage to the abandoning/removal stage.

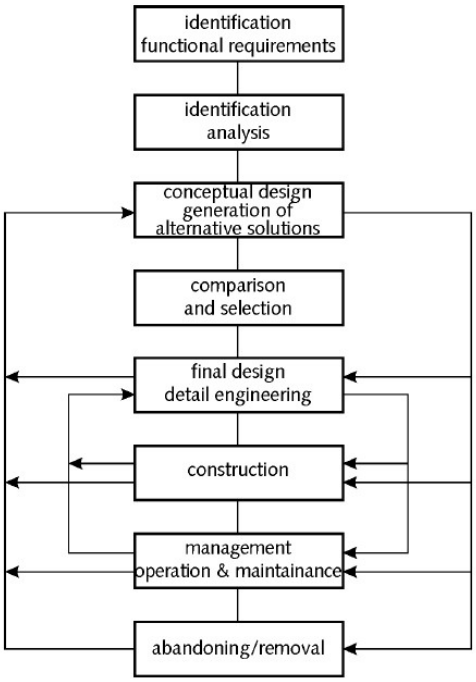

Fig.2 – Breakwaters design process and integrated approach (CIRIA *et al.*, 2007).

In coastal engineering, there is no one-size-fits-all solution for breakwater structural design. Instead, numerous alternatives exist to address the specific constraints of each project. The selection of the appropriate design choice, leading to a sustainable long-term solution, relies on a comprehensive understanding of the project's constraints. These constraints are typically provided by the client/operator and planning or regulatory authorities. The coastal engineer, as part of an interdisciplinary team, carries the responsibility of analysing this information, comparing the available solutions, and making a final decision based on the knowledge accumulated throughout the process. The design engineer faces five key constraints, which encompass the following considerations (CIRIA *et al.*, 2007; Dhanak and Xiros, 2016):

I. Technical;
II. Economic (the initial, maintenance, operation, and eventual removal or replacement costs);
III. Environmental;
IV. Social, political, and institutional;
V. Aesthetics.

The technical considerations are related to both design and construction. In the stage of geometrical design, this includes a selection of an appropriate design approach and tools. It is the key to understand the structure's behaviour and the function of its various components. The development of the general layout and purpose of the structure aims at optimum geometry. This optimization lays on:

- functional requirements (the structure' purpose; the use of the facility and the extent of protection required; layout of the facility; acceptable downtime; design life of the facility; acceptable risk during the structure lifetime; level of maintenance and ease of operations or availability of material; changes in acceptable probability of failure over time; adaptability; in-service health and safety requirements);
- technical data (material properties; accuracy design information, parameters, and analytical methods; structure specific design methods and approaches; nature of failure and failure modes);
- physical conditions (geotechnical, topographic, bathymetric, morphologic, geomorphological, and hydraulic boundary conditions);
- materials and construction aspects;
- maintenance, inspection, repair, and upgrading aspects.

The functional design of a breakwater consists of combining technical factors with economic, environmental, and other constraints, to determine the plan form layout (length and implementation) and the crest elevation. In effect, the geometric design requirements are often imposed by functional requirements, being then translated to geometric boundary conditions. This process involves calculations of (CIRIA *et al.*, 2007; Dhanak and Xiros, 2016):

- wave run-up and wave overtopping to define the structure profile and crest elevation;
- wave transmission to confirm the crest elevation, and
- wave reflection to help determine the scour potential (and, occasionally, the effect on navigation or reflection performance).

The structural design corresponds to the designing of various structure components (such as armour layer, toe berm, crest, etc.) to provide a detailed technical specification that will enable the construction with a specific strength/loading ratio. According to Zeidler *et al.* (1992), "this ratio is the ultimate criterion that follows from the functional requirements of maintaining a prescribed state of the structure under the expected loading conditions". In other words, structural design focus on the overall stability of the structure (sliding of the armour layer, overturning, etc.) and its components (toe failure, mass

displacement of blocks from the armour layer through rolling movements) and on the strength of structural constituents. This stability bases on a concept of tolerable damage or movement of the main armour layer's blocks (BSI, 1991). According to The Rock Manual (CIRIA *et al.*, 2007), the typical structural design of a rubble-mound breakwater, exposed to waves, currents, and tidal water levels, should include the following:

- The definition of the geometry of the structure's profile (slope, shape, etc.);
- Armour layer stability, which includes the definition of the type, weight, thickness, and number of blocks per unit area, to establish required material sizes and placement method for slope, toe, and crest;
- Filter criteria calculations to design underlayers and core (dimensions and thickness). Usually, these elements are empirically related to the main armour layer;
- Slope stability and foundation stability, which includes the definition of elevation and width of the toe berm;
- Rear slope integrity, which includes the definition of elevation and width of crest/superstructure.

2.2.1.1 Armour layer with artificial armour units

The armour layer is a crucial component in a rubble-mound breakwater's ability to resist wave attacks. Its importance lies in preventing damage that could impact other components of the breakwater, including the collapse of the crest structure, erosion of underlayers, and core material. Additionally, the armour layer has a significant impact on wave reflection, run-up, and overtopping, which directly impact the integrity of the toe, underlayers, and crest details (BSI, 1991). The relevant parameters for ensuring the structural stability of the armour layer using concrete armour units can be categorized into four groups, outlined below:

(i) **Wave attack** (stability number, wave height, etc.);

(ii) **Characterisation of armour units** (size, weight, density, and shape).

The armour units can either consist of natural rock units, or artificial units, such as concrete armour units (De Smet, 2016; Prashanth, 2013). The choice of unit type depends mainly on the site availability of sufficient quality, size, and quantity of armour stone to fit specified geometric characteristics and density. Using natural rocks is often the most cost-effective and visually appealing design option for lower weights (lower than 120-150 kN). Furthermore, the advantage of using natural rocks is that it eliminates the requirement for skilled and meticulous placement, resulting in time savings during construction (CEM, 2006; De Smet, 2016; Prashanth, 2013). However, the most decisive stability factor when considering rocks is their self-weight. Some more severe hydraulic boundary conditions, such as more energetic design wave conditions, increase the necessity of larger dimensions and heavier stones. Depending on the quarries nearby, the required size and weight may not be available (De Smet, 2016; Prashanth, 2013). In that case, concrete armour units with various shapes and sizes can substitute rock units.

The artificial armour units proved to be more advantageous than natural armour units in several applications. They can be manufactured in-situ as per the requirement, namely with the desired shape, size, and weight. When compared to natural armour units, artificial units present improved hydraulic and structural stability, achieved by their self-weight or/and by their interlocking capability (Prashanth, 2013).

Rocks will be the first choice for armouring in most cases because of economic and aesthetical reasons. However, more severe design conditions or when armour stone is unavailable in insufficient size, quantity, and quality, require artificial units.

The most important parameters which relate to the artificial armour units are the nominal diameter (D_n), the armour unit mass (M), the apparent mass density (ρ_{app}), and the shape characterized by the shape coefficient (k_s). The shapes and geometry of concrete armour units vary widely; thus, different hydraulic and structural behaviours can be expected for each type. They can be divided into four categories according to their structural strength, which is controlled mainly by the shape of the element:

- Massive or blocky (*e.g.*, cubes, parallelepiped block, Antifer cube): like the natural rocks, these units acquire stability mostly due to their weight. When made of good quality concrete and designed for marginal displacements, these units will not present breakage problems or damages during handling. No structural integrity design diagrams exist for massive concrete armour units.
- Slender (*e.g.*, Tetrapod, Dolos): the stability of these units is also acquired by the interlocking effects between adjacent units. They are the most vulnerable units to cracking and breaking because of the limited cross-sectional areas. Using design diagrams for concrete armour units' structural integrity can help avoid damage.
- Bulky (*e.g.*, Accropode, Core-loc, Haro, Seabee): the design of these units combines the advantages of both massive and slender elements.
- Multi-hole cubes (*e.g.*, Shed, Cob): these units present slender structural members with tiny cross-sections. They will experience little solid impact loads when correctly placed in patterns that exclude significant relative movements of the blocks. The limiting factors for their long-term durability are material deterioration and fatigue due to wave loads (CEM, 2006).

A descriptive classification for concrete armour units can also be based on CIRIA *et al.* (2007), Table 1:

- Placement pattern (orientation):
  - Random: there is neither control on the unit position nor its orientation. Truly random placing is hard to achieve. Although it is usually specified a predetermined layout for units' placement, this is also difficult to achieve except under favourable conditions of good underwater visibility and calm seas. The result is usually a semi-random pattern.
  - Uniform: the units placed at a given position with control on the orientation. Examples of this type are the Cob, the Shed, and the Seabee. These units' stability depends upon the placing pattern, the support provided by the toe and crest, and the preparation of the underlayer. The units are placed in a single layer to form a continuous revetment. In the literature published, it is possible to find information about the specific use of each unit (BSI, 1991).
- Layer characteristics, such as the number of layers:
  - Double layer or,
  - Single layer
- Shape:
  - Simple (*e.g.*, cubes, Antifer cubes, etc.) or,
  - Complex (*e.g.*, Tetrapods, Stabits, Dolos, etc.).
- Stability factor:
  - Own weight,
  - Interlocking, and
  - Friction.

Table 1 – Classification of some armour units by placement, layer characteristics, shape and stability factor (CIRIA *et al.*, 2007).

Placement pattern	# layers	Shape	Stability factor	Armour units
Random	Double	Simple	Own weight	Cube; Antifer Cube (France, 1973); Modified cube (USA,1959)
			Own weight and interlocking	Tetrapod (France, 1950); Akmon (NL, 1962); Tripod (NL, 1962)
		Complex	Interlocking	Stabit (UK, 1961); Dolos (South Africa, 1963)
	Single			Accropode (France, 1980); Core-loc (USA, 1996); Xbloc (NL, 2003)
Uniform		Simple	Own weight and friction	Cube; Antifer Cube; Haro (Belgium, 1984)
			Friction	Seabee (Australia, 1978)
		Complex		Cob (UK, 1969); Shed (UK, 1982); Tribar (USA, 1958)

(iii) **Characterization of armour layer cross-section** (thickness, slope angle, porosity, permeability, and packing density)

The parameters associated to the cross-section of the breakwater can be divided into two categories related to:

- The geometry of the cross-section

Thickness of the armour layer, t_a [m]: typically, to provide adequate protection for the inner layers, both concrete and stone armour units are randomly placed with a minimum thickness of two stones or two armour units, respectively. For **artificial armour units**, the armour layer thickness is given by the following formula:

$$t_a = nk_t D_n = nk_c D = nk_t k_s^{1/3} D \quad (1)$$

where D is the characteristic armour unit length [m], D_n is the nominal armour unit diameter [m], k_t is the layer coefficient [-], which value for artificial units is given by the developer, k_c corresponds to the modified layer coefficient [-], and k_s is the shape coefficient [-].

Slope angle, α [°]: on the seaside, the design slope angle adopted should ideally be as steep as possible to minimize the breakwater volume. However, it also depends on hydraulic and geotechnical stability considerations. For artificial armour units, the slope angle can be as steep as 1:1.33. Massive and bulky double-layer units are placed at slopes of 1:2.5 to 1:1.5. High interlocking single–layer units are placed at slopes of 1:1.5 to 1:1.33. In this case, milder slopes are also acceptable. However, in high interlocking units, using smaller steep slopes, there is no reduction in the unit mass required for stability. Tolerances can vary depending on the unit but should remain in the range of $D/5$, where D represents the characteristic armour unit length. The lee–side slope is generally as steep as possible but rarely steeper than 1:1.33.

- The construction induced condition of the cross-section:

Porosity of the armour layer: Layer porosity corresponds to the ratio between the void volume and the layer volume. It has drastic effects on energy dissipation, hydraulic and structural performance (CIRIA *et al.*, 2007). In general, the more complex or hollow the geometry, the higher the armour layer porosity. Increased porosity leads to more inter-unit pore-space available for turbulent energy dissipation and usually to rougher breakwater surfaces. However, this effect has an upper limit when the armour layer porosity reaches a point where units are not within sufficient proximity of each other. It leads to the formation of gaps, exposing and possibly compromising the underlayer or/and core. The armour layer porosity tends to decrease with the packing density increase (Eden, 2019). In the concrete armour layer case, the layer porosity of the concrete, n_v (%), can be estimated with the following equation:

$$n_v = \frac{V_{air}}{V_{total}} \cdot 100 = \left[1 - \left(\frac{N}{n_l k_t} D_n^2\right)\right] \cdot 100 = \left[1 - \left(\frac{N}{n_l k_t}\left(\frac{M}{\rho_c}\right)^{2/3}\right)\right] \cdot 100 \quad (2)$$

where V_{air} corresponds to the volume of air [m^3], V_{total} is the total layer volume [m^3], N is the packing density [l/m^2], D_n is the nominal diameter of the armour unit [m], n_l corresponds to the number of layers of armour units [-], k_t is the armour layer coefficient [-], M is the mass of concrete armour unit [kg], and ρ_c corresponds to the mass density of concrete armour unit [kg/m^3].

Permeability of the armour layer, filter layer and core: Breakwater permeability governs the ability to transmit energy to the structure (Eden, 2019). Permeable breakwaters tend to absorb more wave energy, reducing wave reflection and leading to lower forces acting on the units. So, an armour layer resting on a permeable underlayer tends to be more stable, while blocks resting on an impermeable base are less stable. The breakwater permeability depends on the gradation of the underlayer and core material. Its value can be given, for example, by a notional permeability factor, P_n, which represents the global permeability of the structure. Another simple approach to account for the influence of the permeability on the stability of rock-armoured slopes under a wave or current attack uses the ratio of diameters of the core material and armour material (CIRIA *et al.*, 2007). Equations (3) and (4) are two good general references of sizing guidelines, which promote permeability whereas blocking the escape of underlayer and core material (Eden, 2019).

$$\frac{1}{10} W_a \leq W_{underlayer} \leq \frac{1}{15} W_a \quad (3)$$

and

$$\frac{1}{30}W_a \leq W_{core} \leq \frac{1}{50}W_a \quad (4)$$

where W_a corresponds to the armour unit weight [N], $W_{underlayer}$ to the underlayer material weight [N], and W_{core} to the core material weight [N].

Packing density of armour layer: It is a parameter directly related to the placement pattern of the armour layer's blocks. For many units, published literature gives guidance on the total number required per unit area of the slope (BSI, 1991). When there is no information available, the packing density, N [1/m^2], can be estimated by the following equation:

$$N = \frac{N_a}{A} = \frac{t_a(1-n_v)}{V} = \frac{\phi}{D_n^2} = \frac{nk_t(1-n_v)}{D_n^2} \quad (5)$$

where N_a represents the number of armour units in the area concerned [-], A the surface area of the armour layer parallel to the local slope [m^2], t_a the armour layer thickness [m], V the armour unit volume [m^3], and ϕ the packing density coefficient, which is defined as the number of placed units per square nominal diameter. It is necessary to compare this with the maximum packing density that can be achieved geometrically, as well as the minimum density required to ensure hydraulic stability.

(iv) **To the response of the structure** (damage and damage evolution)

Due to varying functional requirements, breakwaters exhibit varying levels of fragility, with single-layered breakwaters sustaining different damage than multi-layered structures. Additionally, the response of each type of armour unit to wave action is distinct. The complex, non-linear flow over the slope, combined with the random placement and variable shape of armour units, necessitates a probabilistic framework for the initiation and progression of damage (Campos *et al.*, 2020a).The subsequent section outlines the diverse approaches to armour layer design and damage description.

2.2.2 Hydraulic stability and Damage of concrete armour units

Rubble-mound breakwaters are subject to external effects of the environmental in the shape of forces and pressures, labelled shortly as loading. The response of the system to this loading denominates as strength, stability, or deformation. It is presented in the form of linear and angular displacements (Zeidler *et al.*, 1992). Elementary functional relationships linking the strength to loading used to describe the acceptable (limit state) deformations and displacements are often known as the stability criteria. Therefore, loading and strength functions can be derived from the stability function. The strength (R) and load (S) effects are often functions of several stochastic variables:

$$R = R(X_1, X_2, \dots, X_m) \quad (6)$$

$$S = S(X_{m+1}, X_{m+2}, \dots, n) \quad (7)$$

The strength variables depend on material properties and the geometry of the structure. The loading variables of breakwaters are mainly originated from the environmental boundary conditions (wind, waves, currents) (Zeidler *et al.*, 1992). To verify that the structure meets the design requirements, one must assess the reliability of all the different components of the breakwater. The reliability of an element depends on the margin between the resistance and the action (Everts, 2016). The reliability function (Z) expresses that margin, and its value describes the state of the component:

$$Z = R - S = Z(X_1, X_2, \dots, X_m) \tag{8}$$

Therefore, if $Z < 0$, it indicates failure, if $Z = 0$, it represents the limit state, and if $Z > 0$, it means no failure.

Once the different states are known, the reliability can be quantified and expressed as the probability of proper function, *i.e.*, the probability $P(Z > 0)$:

$$P(Z \geq 0) = 1 - P_f \tag{9}$$

where the probability of failure, P_f, is defined as follows:

$$P_f = P(Z < 0) = P(S > R) \tag{10}$$

So, rubble-mound breakwaters behave as a static granular system until wave energy is higher than the one needed for the initiation of movement.

The functionality of the breakwaters can be compromised due to several occurrences, resulting in partial or total loss of its functionality, which is referred to as damage. The definition and parameterization of damage will be discussed in the following subsections.

Breakwaters can experience different types of damage that ultimately lead to their failure. Among these failures, hydraulic instability of the armour units is typically the most critical. When subjected to wave action, the armour units begin to move, exhibiting various movements such as rocking, displacement by plunging waves, sliding of the entire armour layer, lift outs caused by up rushes and down rushes, or settlement due to compaction. Damage to the armour layer can also have secondary effects on other parts of the breakwater, such as the collapse of the crest structure, erosion of underlayers, and exposure of core materials. Furthermore, the condition of the armour layer influences wave reflection, run-up, and overtopping, which directly impact the stability of the toe, underlayers, and crest details of the breakwater (Campos *et al.*, 2020a; Disco, 2012; Eden, 2019). Therefore, it is crucial to quantify the damage for both qualitative and quantitative analyses of rubble-mound breakwater stability.

There are two main approaches to limit the probability of failure due to instability of the armour layer:

- deterministic - single characteristic values are used for all the variables and input values, giving a single value as the output;
- probabilistic - input values are described by a probability distribution, resulting in a probability distribution.

The choice between probabilistic or deterministic approach affects the design data required. The main difference is that probabilistic methods need additional statistical information on the input data. The following levels are also defined depending on the approach to reliability:

- Level 0 – Deterministic;
- Level I – Semi-probabilistic;
- Level II – Probabilistic with approximations;
- Level III – Fully probabilistic;
- Level IV – Risk-based.

Hydraulic instability of armour layers has been studied, over the years, using these different approaches. Given the process complexity of the hydraulic instability of the armour layer, derived from the stochastic nature of both wave loading, initiation of movement, and damage progression, it is not suitable to go for a deterministic approach to the problem. In other words, the highly non-linear flow action over the slope involving wave breaking in single stones or blocks with variable shapes and random placement, and the blocks' reaction, is not reachable by analytical expressions. So, regarding the stability formulae used to characterize the initiation of movement of the armour layer, it is generally semi- or empirical, associated with experimental results that establish the relationships between wave characteristics and the structural response, usually described by armour movements, and ideally improved and validated with prototype observations (Disco, 2012; Eden, 2019). Regarding damage progression models designed to predict the evolution of rubble-mound geometry, probabilistic models based on physical/numerical studies and risk-based design are essential. However, it has been noticed a lack of standards for damage progression experiments since these models started to be explored much more recently. Besides, there are not many experimental results focused on the stochastic nature of damage progression.

Both stability and damage progression of rubble-mound breakwaters due to armour layer instability will be addressed in the following subsections, including the concept of damage itself and how it is measured.

2.2.2.1 Damage definition

The term damage in rubble-mound breakwaters is quite used to refer to the reshaping degree of the armour layer, being, consequently, linked to the failure mode known as hydraulic instability of the armour layer. This concept demands monitoring the spatial and temporal evolution of the geometrical variations of the slope. The port authority usually associates the damage definition with the economic repercussions caused by the loss of functionality of the breakwaters. It includes the structure reparation costs and the effects on the activities and goods depending on the sheltering performance of the structure. From the designer's point of view, damage depends on aspects such as typology, design, armour type, or functional requirements. At an early stage of the process, the designer needs to characterize the interaction with other failure modes, *i.e.*, develop failure diagrams considering settlements, overtopping rates, and variation of armour layer porosity, among others. Then, it is good practice to create a set of functional requirements for the structure, such as acceptable damage levels/probability of failure. Different damage levels distinctively affect the structure functionality - operational thresholds - and the evolution of the deterioration rate - structural thresholds (Campos *et al.*, 2020b; Pilarczyk, 2003). Considering double-layer armours, Losada *et al.* (1986) and Vidal *et al.* (1991) proposed four levels of damage:

- Initiation of damage: displacement of a certain number of armour units from their original position at a distance of/or larger than a unit length, or/and holes larger than average porous size are appreciable;

- Iribarren's damage: the holes are big enough to expose the units from the lower armour layer, becoming the units susceptible to being extracted;
- Initiation of destruction: a small number of units (two or three) in the lower layer are pulled out, and the filter starts to be exposed to wave action;
- Destruction: the filter is exposed to wave action, causing its units to be easily extracted. The mound is likely to eventually cease to give the designed level of service.

2.2.2.2 Damage parameterization

The damage quantification is essential for the qualitative and quantitative analysis of the structure stability. There is no single formula for calculating the extent of damage, in part due to the wide variety of typologies and designs. So, to quantify the hydraulic instability of the armour layer, it is necessary to parameterize the reshaping of the rubble-mound section using damage descriptors. The definition of these descriptors involves a concise description of the methodology for measuring and selecting its representative parameters (Campos *et al.*, 2020b; Disco, 2012). A consistent damage descriptor should: be directly proportional to breakwater damage; dimensionless to show no dependence on the scale; present a known range of variation, independently of the rubble-mound's characteristics, water level, or type of wave actions; and be easily interpretable to provide explicit information about the qualitative damage level (Abanades *et al.*, 2011). It is noteworthy that it is only possible to link the descriptor to the qualitative response or damage level if one has previously specified the structure response up to the destruction level (Campos *et al.*, 2020b).

Advancements in measurement techniques have enabled a shift from a simplified approach based on qualitative damage levels to a detailed characterization of the entire deterioration process of a structure, up to the point of failure. By modelling this progression as a random variable and monitoring prototypes, breakwater design can be made more reliable. The conceptualization and selection of a damage descriptor is affected by the available measuring techniques.

Damage initiation and progression is a 3D process, even for breakwaters tested in a wave flume (Campos *et al.*, 2020b). Besides, the spatial component and shape of damage are crucial to the comprehension of the hydraulic instability of armour units. Nevertheless, the available descriptors focused mainly on measuring an averaged magnitude on a 2D profile. Even damage descriptors based on a front view of the slope are averaged over a longitudinal width, losing information such as the planar shape of the eroded area or the number of eroded pockets (Campos *et al.*, 2020b). Up to date, the most used damage descriptors are:

Parameters that are based on the number of displaced blocks:

- **Percentage of displaced rocks/blocks relative to the total number of rock/blocks in the armour layer active zone, N_d**

It is based on counting the number of individual units that have been displaced:

$$N_d = \frac{\#\ blocks_{\ displaced\ out\ of\ armour\ layer}}{\#\ blocks_{active\ zone}} \times 100 \quad (11)$$

The extent of damage in terms of displaced units is typically expressed as the relative displacement. This is defined as the proportion of displaced units relative to either the total number of units or the

number of units within a specific zone around the still water level (SWL). Limiting the assessment of damage to a particular zone is necessary to facilitate the comparison of different structures. This is because evaluating damage without this restriction would result in different totals for each structure, making comparisons challenging. Since most of armour unit movements occur within the levels around still water level (SWL), the number of units within this zone is sometimes used as the reference number. So, the active zone is usually defined as the area between two levels, *e.g.*, SWL $\pm H_s$, where H_s corresponds to the significant wave height, or SWL $\pm nD_n$, where $\pm nD_n$ indicates the boundaries of armour displacements (CEM, 2006).

- **Number of displaced units within a strip of width D_n, N_{od}**

It is also based on unit counting and is expressed such as:

$$N_{od} = \frac{\#\ blocks\ _{displaced\ out\ of\ armour\ layer}}{width\ of\ tested\ section/D_n} \tag{12}$$

The disadvantage of N_{od} is the dependence of the slope length. It also depends on how the descriptor is considered: individually for each strip, averaged, or considering just the maximum value.

Parameters that are based on the erosion hole dimensions:

The parameters presented below are based on the dimensions of the erosion hole as depicted in Fig. 3.

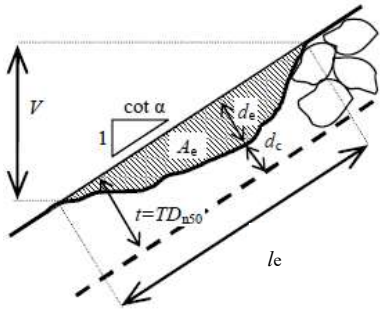

d_e – eroded depth [m]

d_c – remaining thickness of the armour layer [m]

A_e – eroded area [m^2]

l_e – eroded length [m]

Fig. 3 – Erosion hole dimensions.

- **Dimensionless eroded area (Broderick and Ahrens, 1982), S**

It is based on determining the volumetric change in areas where armour units have been displaced (CEM, 2006; CIRIA *et al.*, 2007). The descriptor is expressed as the average cross-sectional erosion area divided by the square of the nominal diameter, D_{n50}:

$$S = \frac{A_e}{D_{n50}^2} \tag{13}$$

The real number of eroded units depends on the porosity, armour grading, and stone shape. It also depends on the width considered and how to average the eroded area. There are two primary issues that hinder the interpretability of S results: first, this descriptor is not capable of characterizing the spatial shape of the damage because it represents a mean eroded area on a whole profile. Second, there is no standard methodology for measuring and calculating S.

- **Dimensionless eroded area accounting for number of displaced units (Davies *et al.*, 1994), S_N**

Davies *et al.* (1994) proposed a re-formulation of the descriptor S, using visual methods. Combining the equation (13) with the volume eroded from a section of width X, which can be expressed both in terms of the average eroded area or in terms of the number of displaced armour stones, S_N is obtained as follows, with n being the porosity:

$$S_N = \frac{V_e}{X \cdot D_{n50}^2} = \frac{N_d D_{n50}^3}{X \cdot D_{n50}^2 (1-n)} = \frac{N_d D_{n50}}{X(1-n)} \tag{14}$$

This descriptor depends on the porosity, which is not easy to measure, nor even homogeneous. Besides the diameter of the stones is also a variable. Moreover, it is assumed that the layer thickness is equal to the nominal diameter, which is not always the case, as it depends on the shape of the units and the placement method. The S descriptor shortcomings are extensible to this descriptor.

- **Dimensionless eroded area based on planar exposed area (Vidal *et al.*, 2004), S_t**

Vidal *et al.* (2004) suggested a damage descriptor based on counting the number of pixels of the planar exposed area, A_{pe}, between two consecutive layers, which is calculated according to the following equation:

$$S_t = \frac{\delta \cdot A_{pe}}{X \cdot D_{n50}} \tag{15}$$

where δ is the correcting factor that depends on the armour characteristics and the angle of the camera regarding the slope's structure (in case it is not orthogonal). This descriptor is only suitable when damage is limited to the outer layer and when there is enough colour contrast between the layers.

- **Dimensionless eroded depth (Melby and Kobayashi, 1998b), E**

This descriptor, which provides information about the biggest eroded depth, is calculated from the maximum eroded depth:

$$E = \frac{d_e}{D_{n50}} \tag{16}$$

It indicates that the progress towards failure is usually assumed to occur when the underlying layer becomes exposed. One of the main shortcomings of this descriptor is its magnitude which can differ accordingly to the way it is calculated, *e.g.*, as a maximum value of a whole section, as a maximum value from an averaged profile or as a mean value from the maximum depths on each profile.

Hofland *et al.* (2014) proposed the local damage depth, which is different from the erosion depth of Melby and Kobayashi (1998). E is calculated from a moving average applied to the cross-shore direction in 2D cases and over a circular area in 3D cases:

$$E_{2D,m} = \frac{max_x(\langle e \rangle_{w=mD_{n50}})}{D_{n50}} \tag{17}$$

$$E_{3D,m,n} = \frac{max_{x,y}(\langle e \rangle_{R=nD_{n50}})_{w=mD_{n50}}}{D_{n50}} \tag{18}$$

where e is the (always positive) local erosion depth during a test (series), obtained from survey techniques by regarding the difference of the structure elevation before (z_{before}) and after (z_{after}) a test run or test series, via $e = (z_{before} - z_{after})\cos\alpha$, where α is the structure slope angle; $\langle\,\rangle_R$ indicates an (moving) average over a circular area with radius R; m and n are integers; $\max x$ is a maximum over the (cross-shore) x-direction; $\max y$ is a maximum over an area spanning the alongshore and cross-shore horizontal area and D_{n50} is the nominal diameter of the armour rock for which 50% of the rock mass is smaller (Hofland *et al.*, 2017).

- **Dimensionless eroded length (Melby and Kobayashi, 1998b), L_e**

This descriptor, which provides information about the worst eroded length, is related to the extension of the damage area:

$$L_e = \frac{l_e}{D_{n50}} \tag{19}$$

When combined with E and S, it is a valuable descriptor, offering information about the shape of the holes.

- **Dimensionless cover depth (Davies *et al.*, 1994), C**

This parameter considers the remaining thickness of the armour layer:

$$C = \frac{d_c}{D_{n50}} \tag{20}$$

It is not considered, by many authors, a reasonable damage parameter for practical design applications. Even for $C = 0$, the breakwater preserves significant resistance.

- **Equivalent dimensionless damage accounting for porosity variation (Gómez-Martín and Medina, 2007), D_e**

In most damage descriptors, porosity is assumed to be constant instead of being considered an evolutionary parameter. It is important to acknowledge that fluctuations in armour units' packing density may result in the compromise of the structure's intended functionality. So, Gómez-Martín and Medina (2007) suggested a virtual net method for visual damage assessment, combined with a damage descriptor which considers both heterogeneous packing failure mode and the extraction of armour units. This methodology proved to be adequate for regular armour units. First, a virtual array is created over the armour layer and the porosity is evaluated on each strip with dimensions $a = nD_{n50}$ and $b = 0.75$ m:

$$p_i = 1 - \frac{N_d D_{n50}^2}{a \cdot b} \tag{21}$$

Then, individual dimensionless damage, D_i, is calculated for each strip considering the initial porosity in the strip, p_0, the actual porosity in the strip, p_i, and an integer, d, which represents the number of nominal diameters contained within a strip width:

$$D_i = d\left(1 - \frac{1 - p_i}{1 - p_0}\right) \tag{22}$$

At last, these values are integrated over the slope and the dimensionless damage, D_e, is obtained as follows:

$$D_e = \sum D_i \tag{23}$$

2.2.2.3 Damage models: stability formulae and progression models

The hydraulic instability of armour layers is a complex process affected by many aspects, from the stochastic nature of both wave loading, initiation of movement, and damage progression to the wide variety of typologies and designs. As such, it is unfeasible to achieve a unique analytical formula. So, most of the hydraulic stability formulae, initially aimed at characterizing the initiation of movement, are empirical or semi-empirical and have their range of validity and specific field of application since they are associated with experimental results (Campos *et al.*, 2020a; De Smet, 2016). The designer should ensure that the formulae are valid for the desired application (CIRIA *et al.*, 2007).

Looking historically, the design methods available for rock and concrete armour units focused on statically stable rubble-mound breakwater trunks. Considering specifically breakwaters armoured with concrete units, the design of the armour layer usually follows the general approach for armour stone, but design formulae or/and coefficients are different (CIRIA *et al.*, 2007). Private companies and research centres, which develop and patent new artificial armour units, provide specific hydraulic stability formulas and deterioration rates of these armouring. There are also publications and academic studies proposing empirical equations for the artificial unit's selection.

The Hudson's equation (24) with specific values of K_D derived from previous or generic model tests is still the simplest approach, as it is possible to observe in Table 2.

$$\frac{H}{\Delta D_{n50}} = (K_D \cot \alpha)^{1/3} \tag{24}$$

Table 2 – K_D and $H/\Delta D_n$ values for Hudson formula (Campos *et al.*, 2020a; CEM, 2006).

Units type	Slope	Placement	Layers	Trunk			
				Breaking waves		*Non – breaking waves*	
				K_D	$H/\Delta D_n$	K_D	$H/\Delta D_n$
Cubes	1:1.5	Random	2	6.5	2.1	7.5	2.2
	1:2.0				2.35		2.45
	1:3.0				2.7		2.8
Tetrapods	1:1.5	Random	2	7.0	2.2	8.0	2.3
	1:2.0				2.4		2.5
	1:3.0				2.75		2.9
Tribar	1:1.5	Random	2	9.0	2.4	10.0	2.5
	1:2.0				2.6		2.7
	1:3.0				3.0		3.1
	-	Uniform	1	12.0	-	15.0	-
Stabit	-	Random	2	10.0	2.7	12.0	2.9
Akmon	-	Random	2	8.0	2.5	9.0	2.6
Antifer Cube	-	Random	2	7.0	2.4	8.0	2.5
Dolos	1:2.0	Random	2	16.0	2.5	32.0	3.2
Haro	-	Uniform	1	8.0	-	9.0	-
Core – loc (Melby and Turk, 1997) N_{od}=0	1:1.33	Random	1	16.0	2.8	16.0	2.8
Accropodes (Sogreah, 2000) N_{od}=0	1:1.33	Random	1	12.0	2.5	15.0	2.7
Xbloc (DMC, 2003) N_{od}=0	1:1.33	Random	1	16.0	2.8	16.0	2.8

As seen previously, concrete armour units are applied in one or two-layer systems depending on the armour unit type. The most used and conventional method is the two-layer system. Depending on the shape, the units may present a greater or lesser degree of interlocking. Consequently, the overall stability

of a layer mainly hangs on the stability of individual units. When damage starts, it will increase with the increase of the wave height. For a double-layer system, critical failure only occurs after both layers displacement and underlayers erosion (CIRIA *et al.*, 2007). Table 3 presents some formulas for the design of randomly placed armour units in a double layer system.

Table 3 – Review of randomly placed armour units' stability formulae – double layer armouring.

Authors	Range of Validity and Parameters
	$$\frac{\boldsymbol{H}}{\boldsymbol{\Delta D_n}} = \boldsymbol{C_1} + \left(\boldsymbol{C_2} + \boldsymbol{C_3}\frac{\boldsymbol{N_{od}^{C_4}}}{\boldsymbol{N_z^{C_5}}}\right)\boldsymbol{s_{om}^{C_6}}$$ where: ▪ $H = H_s$ – significant wave height [m], ▪ D_n – nominal diameter of the unit [m]. ▪ $\Delta = \frac{\rho_s}{\rho_w} - 1$ [-], ▪ N_{od} – damage number [-], ▪ $N_z = \Delta t / T_m$ – number of incoming waves during the design storm [-], ▪ $s_{om} = 2\pi H_s/(g/T_m^2)$ – offshore wave steepness [-].
Van der Meer (1988c)	**CUBES** $C_1 = 0$, $C_2 = 1.0$, $C_3 = 6.7$, $C_4 = 0.4$, $C_5 = 0.3$ and $C_6 = -0.1$. **TETRAPODS** $C_1 = 0$, $C_2 = 0.85$, $C_3 = 3.75$, $C_4 = 0.5$, $C_5 = 0.25$ and $C_6 = -0.2$. **Applicable to:** ▪ Non-overtopped slopes, ▪ Non-depth-limited wave conditions, ▪ Surging waves, ▪ $1000 \leq N_z \leq 3000$. ▪ $\cot(\alpha) = 1.5$, ▪ For cubes: $3 < \xi_m < 6$, ▪ For Tetrapods: $3.5 < \xi_m < 6$. **Note:** In this case, N_{od} corresponds to the number of units displaced out of the armour layer within a strip of one equivalent cube length. This equivalent cube length was assumed to be equal to D_{n50} for cubes, $0.65h$ for tetrapods and $0.7h$ for accropodes (Campos *et al.*, 2020a).
De Jong (1996)	**TETRAPODS** $C_1 = 0$, $C_2 = 3.94$, $C_3 = 8.6$, $C_4 = 0.5$, $C_5 = 0.25$ and $C_6 = 0.2$. **Applicable to:** ▪ Non-overtopped slopes, ▪ Plunging waves, ▪ $1000 \leq N_z \leq 3000$. ▪ $\cot(\alpha) = 1.5$, ▪ $3.5 < \xi_m < 6$.
Chegini and Aghtouman (2006) Note: This formula is a derivation of the Van der Meer formula. The Van der Meer (1988c) formula for cubes is considered acceptable and conservative when applied to Antifer cubes.	**ANTIFER CUBES** $C_1 = 0$, $C_2 = 1.082$, $C_3 = 6.951$, $C_4 = 0.443$, $C_5 = 0.291$ and $C_6 = -0.082$. **Applicable to:** ▪ Non-overtopped slope, ▪ Irregular waves, ▪ $\cot(\alpha) = 1.5$, ▪ $1000 \leq N_z \leq 3000$.

Table 3 (cont.) - Review of randomly placed armour units' stability formulae – double layer armouring.

Authors	Range of Validity & Parameters
	$\frac{H}{\Delta D_n} = C_1 + \left(C_2 + C_3 \frac{N_{od}^{C_4}}{N_z^{C_5}}\right) s_{om}^{C_6}$
Burcharth and Liu (1992)	**DOLOS** $C_1 = 0$, $C_2 = 0$, $C_3 = (17 - 26r_w)\phi^{\frac{2}{3}}$, $C_4 = 1/3$, $C_5 = 0.1$ and $C_6 = 0$. where: ▪ r_w – waist ratio [-], ▪ ϕ – packing density [-]. **Applicable to:** ▪ Non-overtopped slopes, ▪ $\cot(\alpha) = 1.5$, ▪ $0.32 < r < 0.42$, ▪ $0.61 < \phi < 1$, ▪ $1000 \leq N_z \leq 3000$. For $N_z \geq 3000$ use $N_z = 3000$.
Holtzhausen and Guerrero (2017)	**DOLOS** $C_1 = 0$, $C_2 = 0$, $C_3 = 1.06{r_w}^{-0.85}\Delta^{-0.26}\phi_f^{-0.18}$, $C_4 = 0.18$, $C_5 = 0.063$ and $C_6 = -0.2$. where: ▪ r_w – waist ratio [-], ▪ $\phi_f = \exp(9.41\phi^2 - 16.49\phi + 7.08)$ – packing density factor [-]. **Applicable to:** ▪ Regular and irregular waves, ▪ Deep water conditions (h_t=25D_n), ▪ Non-overtopped slopes, ▪ Double-layered slopes, ▪ $\cot(\alpha) = 1.5$, ▪ $0.33 < r < 0.40$, ▪ $0.010 < s_{op} < 0.060$, ▪ $0.01 < N_{od} < 7$ ▪ $0.65 < \phi < 1.15$, ▪ $0.8 < \Delta < 2.0$, ▪ $2000 \leq N_z \leq 27000$.

The unit's placement in one-layer systems follows a given placement grid or density, and the orientation of the rows can be specified or random. Under wave attack, these units behave differently from a two-layer system. After construction, the initial wave attack will help settle the layer, increasing the interlocking between blocks. However, later storms can overcome the interlocking. Since a single layer generally possesses less reserve than units in a double layer system, it will be more susceptible to sudden failure progression, and underlayers will be more exposed to wave loadings. Typically, single layer armour layers are designed for no damage. However, besides being damage-free, under design conditions, single-layer systems should be further able to withstand an overload of about 20 percent without significant damage. Thus, the design of the armour layer has a relatively large safety margin for the design stability factor (CIRIA *et al.*, 2007). Besides the value presented in Table 2 for Core-loc, Accropodes, and Xbloc, Table 4 present other formulas for Accropodes and cubes one single layer design.

Table 4 – Review of randomly placed armour units' stability formulae – single layer armouring.

Authors	Equation	Range of Validity & Parameters
ACCROPODES		
Burchart *et al* (1988)	$\frac{H}{\Delta D_n} = A \cdot (D^{0.2} + 7.7)$ where: ▪ $H = H_s -$ significant wave height [m], ▪ $D_n -$ nominal diameter of the unit [m]. ▪ $\Delta = \frac{\rho_s}{\rho_w} - 1$ [-], ▪ $A = 0.46 -$ coefficient [-], ▪ $D -$ relative number of units displaced more than a distance D_{n5} [-].	**Applicable to:** ▪ Breaking and non-breaking waves, ▪ Irregular waves, ▪ Perpendicular waves ▪ Single-layered slope, ▪ $\cot(\alpha) = 1.33$, ▪ $3.5 < \xi_m < 4.5$.
Van der Meer (1988)	For start of damage, $N_{od} = 0$: $\frac{H_s}{\Delta D_n} = 3.7$ For failure, $N_{od} > 0.5$: $\frac{H_s}{\Delta D_n} = 4.1$	**Applicable to:** ▪ Non-breaking waves, ▪ Single-layered slope, ▪ $\cot(\alpha) = 1.33$. Note 1: Storm duration and wave period have no influence on the hydraulic stability. Note 2: It is recommended to apply a safety factor for design of about 1.5.
CUBES		
Van Gent *et al.* (1999) Van Gent *et al.* (2001) Van Gent and Luis (2013)	For start of damage, $N_{od} = 0$: $\frac{H_s}{\Delta D_n} = 2.5 - 3.0$ For failure, $N_{od} = 0.2$: $\frac{H_s}{\Delta D_n} = 3.0 - 3.5$	**Applicable to:** ▪ Breaking and non-breaking waves, ▪ Single-layered slope, ▪ $\cot(\alpha) = 1.5$, ▪ $n_v = 0.25 - 0.3$, ▪ $M_{Cubes}/M_{50-Filter} = 10$. Note 1: Place one side of the cube flat on the underlayer. Note 2: It is recommended to apply a safety factor for design of about 1.5.
CIRIA *et al.* (2007)	For start of damage, $N_{od} = 0$: $\frac{H_s}{\Delta D_n} = 2.9 - 3.0$ For failure, $N_{od} = 0.2$: $\frac{H_s}{\Delta D_n} = 3.5 - 3.75$	

In the 90s, besides the attempt to compile the available armour layer stability formulae and provide some design recommendations, the efforts to consolidate the probabilistic approaches were multiplied. When these approaches were firstly implemented, in earlier years, they faced a controversial acceptance by engineers. The lack of probabilistic information from the structural response and the factors affecting it, and the missing confidence due to uncertainty in the calculations, were the reasons for the scepticism of experts, whose breakwaters design knowledge was based on the experience. Despite all the difficulties, the probabilistic approach is nowadays widely used (Campos *et al.*, 2020a). Also, the reliability methodologies appear in some design codes, such as the European PROVERBS (Oumeraci *et al.*, 2001), the Spanish ROM 0.0-01 (Puertos del Estado, 2001), or the North American Coastal Engineering Manual (CEM, 2006).

With the probabilistic approaches' evolution, the first damage progression models appeared. Traditional stability formulae focus on the characterization of the start of the movement, which is convenient for estimating the design weight of armour units. However, these equations fail to give information about the evolutionary behaviour of rubble-mound breakwaters. In circumstances where the evolution of the structure is essential regarding maintenance strategies and useful-life total costs, it is convenient to move on toward damage progression models (Campos *et al.*, 2020a). These models are designed to predict the evolution of rubble-mound's geometry by means of a quantitative damage descriptor. One of the first damage progression models was presented by Van der Meer (1988b), where author's equations, (25) and (26), were rewritten to the so-called reliability functions and all the parameters were assumed to be stochastic with an assumed distribution.

$$\text{For plunging waves } (\xi \leq \xi_{cr}): \frac{H}{\Delta D_{n50}} = c_{pl} \cdot {S_d}^{0.2} \cdot P^{0.18} \cdot N_z^{-0.1} \cdot \xi^{-0.5} \tag{25}$$

$$\text{For surging waves } (\xi > \xi_{cr}): \frac{H}{\Delta D_{n50}} = c_s \cdot {S_d}^{0.2} \cdot P^{-0.13} \cdot N_z^{-0.1} \cdot \cot(\alpha)^{0.5} \cdot \xi^{P} \tag{26}$$

where S_d[-] is the relative eroded area, whose limits depend mainly on the slope of the structure, P is the notional permeability, $N_z = \Delta t / T_m$ is the number of incoming waves during the design storm and ξ corresponds to the surf similarity parameter. A more detailed description can be found in Van der Meer (1988a) and Everts (2016). The structure parameters with the mean value, distribution type and standard deviation are given in Table 5. These values are used in a level II probabilistic approach, which can be used to estimate the probability that a certain damage level would be exceeded in a certain lifetime of the structure (Van der Meer, 1998).

Table 5 – Parameters used in the level II probabilistic computations (Van der Meer, 1998).

Parameter	Distribution	Mean value	Standard deviation
D_n	normal	1.0	0.03
Δ	normal	1.6	0.05
$\cot \alpha$	normal	3.0	0.15
P	normal	0.5	0.05
N_z	normal	3000	1500
H_s	Weibull	B = 0.3	C =2.5
FH_s (*)	normal	0	0.25
s_{om}	normal	0.04	0.01
c_{pl}	normal	6.2	0.4
c_s	normal	1.0	0.08

(*) The parameter FH_s represents the uncertainty of the wave height at a certain return period. The wave height itself is described by a two-parameter Weibull distribution.

The adaptation of the equations to comply a probabilistic design presents some shortcomings, Campos *et al.* (2020a), namely:

- The scatter only focused on one parameter instead of designing a fully probabilistic formulation with an analytic cumulative distribution function;
- Van der Meer formulae are not valid for the long term, as they tend to overestimate damage for more than 7000 waves;
- Despite providing reasonable estimates of the stability number for two specified Hudson's damage levels, they failed to yield predicted damage levels with accuracy. The damage level did not approach an equilibrium value with the duration of the wave action increase, disagreeing with the evolution of the breakwater profile shape, which was initially dynamic but may eventually reach a stage of static stability.

In the '90s, some authors, considering the Van der Meer work as a starting point, began to delve deeper into the damage progression models issue.

Kaku *et al.* (1991) found that Van der Meer's predicted damage levels were not accurate enough for forecasting models. Consequently, they proposed an exponential model which included similarities between the stability number and the Shields parameters used in sediment transport.

Smith *et al.* (1992) conducted some experimental works to test the abilities and limitations of existing and new empirical predictive methods for breakwater profile changes under random waves. The authors concluded that Van der Meer (1988b) and Kaku *et al.* (1991) empirical models underestimated damage and indicated the difficulties of both empirical formulae in accounting for the wave complexity and predicting breakwater profile response with any consistent accuracy.

Medina (1996) affirmed that existing armour damage progression models, which are applicable for stationary sea states with a given storm duration, were not adequate to be applied for nonstationary stochastic models. The author identified five conditions for any rational armour damage model to properly consider the storm duration since damage must increase with the storm duration under random wave attacks in deep water. So, Medina proposed a wave-to-wave exponential model for damage evolution for the armour layer under regular wave attack, which depends on wave height, Iribarren's number, and the number of waves. Gómez-Martín and Medina (2005) slightly modified the exponential model and found that the mean damage was dependent on Iribarren's number. The authors also designed a neural network (NN) applicable to random waves in non-stationary conditions. They found that the estimation of accumulated armour damage using both wave-to-wave exponential method and NN model showed a good agreement to damage observations.

Considering the damage progression models proposed in the '90s, the formulation proposed by Melby and Kobayashi was probably the main contribution. In 1998 they published the first model (Melby and Kobayashi, 1998a; b), which was re-formulated in 1999 to allow non-zero initial damage levels (Melby and Kobayashi, 1999):

$$[\bar{S}(t)]^{1/b} = [\bar{S}(t_n)]^{1/b} + (a_s N_s^5)^{1/b} \frac{t - t_n}{T_m} \qquad t_n \le t \le t_{n+1} \tag{27}$$

where $\bar{S}(t_n)$ is the known damage at the time t_n, N_s is the stability number based on the mean of the highest one-third wave heights from a zero-up crossing analysis, T_m is the mean period, b is an empirical coefficient introduced for long duration tests, and a_s is related to the breakwater slope angle,

permeability and an empirical coefficient derived from the tests. It is an iterative damage progression model that allows the calculation of the damage at the instant t_{n+1} based on the damage level at the instant t_n and the incident wave conditions between t_n and t_{n+1} represented by constant values of H_s and T_m.

The technical report presented by Melby (1999) details the experiments, with a limited validity range, conducted by Melby and Kobayashi, including a complete description of them, analysis of the armour units stability, damage measurements and damage definition. The trends, variability and ranges of damaged profile descriptors are characterized using mean and standard deviation of different damage descriptors. The authors observed during the series that damage never truly stabilized or reached an equilibrium. Instead, it kept on increasing at a lower rate. Looking at equation (27), it does not have an asymptotical trend. Consequently, many small waves between two storms can theoretically provoke a damage increase. Thus, it is advisable to employ a critical stability number to reduce the number of storms required in a life-cycle analysis so that the damage would not increase beyond this lower limit.

Melby and Kobayashi highlighted that their damage progression model can be used to predict damage for a single design event or/and in a simulation to predict the life-cycle costs. So, by allowing engineers to balance initial costs with expected rehabilitation or maintenance costs, this model is suitable to determine the expected life of both new and damaged breakwaters and for developing life-cycle analysis. However, the authors also pointed out a few shortcomings, such as:

- Equation (27) assumes lack of memory, *i.e.*, the damage produced by waves depend only on the previous damage and the wave intensity history, but not on how the previous damage has been reached;
- The results are conservative for most applications because they are based on severely breaking waves, a relatively steep beach and a relatively impermeable core. One should take care when applying outside of the tested conditions;
- Damage initiation is unpredicted in all series studied and fails to yield accurate predictions for low damage levels;
- The model is aimed just at the mean damage evolution, not providing information about the probability density function, which is needed for a more precise analysis of damage progression in breakwaters.

Melby and Hughes (2003) used the same data set as Van der Meer (1988b) to fit a stone stability equation specifically for both deep and shallow water applications. They derived momentum-flux based stability number for incipient motion cases normal to the structure face, rolling, and sliding. The equations explicitly include the effect of water depth at the toe of the structure, assuming that the maximum wave momentum flux at the structure's toe is proportional to the maximum wave forces on armour units.

In Melby and Kobayashi (2011), the relations of Melby and Kobayashi (1999, 1998a, 1998b) and Melby and Hughes (2003) were modified to predict stability and life-cycle damage progression for seaside on rubble-mound breakwaters and revetments exposed to waves. The equations were calibrated and verified using extensive data sets. So, considering Melby and Hughes (2003) work, the recommended equation for sizing stable armour stone on a rubble-mound structure exposed to normally incident waves is:

$$N_m = \text{function}\left(\theta, P, S, N_z, s_m, \frac{R_c}{H_{m0}}\right) = \left(\frac{(M_F)_{max}}{\rho_\omega g h^2 \Delta}\right)^{1/2} \frac{h}{D_{n50}} = \frac{1}{a_m}\left(\frac{S}{K_s\sqrt{N_z}}\right)^{1/5} \quad (28)$$

where $(M_F)_{max}$ corresponds to the maximum wave momentum flux, P to the structure notional permeability, S to the damage, N_z to the number of waves at mean period during event of duration t, s_m to the wave steepness, R_c to the crest height of the structure above still water level and H_{m0} to the spectral significant wave height. The parameter a_m was estimated as:

$$\begin{aligned} a_m &= \frac{1}{5P^{0.18}\sqrt{\cot\theta}} \qquad s_m \geq s_{mc} \quad \text{(plunging waves)} \\ a_m &= \frac{s_m^{P/3}}{5P^{0.18}(\cot\theta)^{0.5-P}} \quad s_m < s_{mc} \quad \text{(surging waves)} \end{aligned} \tag{29}$$

with

$$s_{mc} = -0.0035\cot\theta + 0.028 \tag{30}$$

The recommended equations for determining damage progression in a life-cycle risk assessment analysis are given by:

$$\begin{aligned} S(t_1) &= 0.5 + 1.3\sqrt{N_{ze} + (N_z)_n}(a_m N_m)_n^5 \quad \text{for } n = 1 \text{ and } S(t_1) > 0.2 \\ S(t_n) &= 1.0\sqrt{N_{ze} + (N_z)_n}(a_m N_m)_n^5 \quad \text{for } n > 1 \end{aligned} \tag{31}$$

The coefficient of 0.5 for $n = 1$ assures that roughly one stone is dislodged before damage accumulates. The coefficient K_s is calibrated to be 1.3 for $n = 1$ and 1.0 for $n > 1$. The calibrated K_s is related to the fact that damage initiation is different from damage progression partly because of the initial adjustment of stones placed in unstable manners. The equivalent number N_{ze} of waves corresponding to the damage S_{n-1} at the start of the nth segment is given by:

$$N_{ze} = \left(\frac{S_{n-1}}{K_s(a_m N_m)_n^5}\right)^2 \tag{32}$$

The recommended equations assumed that the damage armour layer could be characterized solely by the eroded area normalized by the nominal stone diameter.

Castillo *et al.* (2012) proposed a new approach to tackle the lack of a stochastic damage progression model fully designed from a probabilistic approach and with the existing damage accumulation modelling difficulties. They presented a general methodology to build consistent stochastic models for damage progression in breakwaters resulting from random wave actions based on dimensional analysis (using II Buckingam's theorem), compatibility conditions, and functional equations. In addition, they provided a formula for the time evolution of the cumulative distribution function (CDF) of damage written in terms of the normal distribution:

$$F_{D^*(t^*)}(D) = \Phi\left(\frac{(D-\gamma)^{1/b} - \mu_0 - kt^*}{\sqrt{\sigma_0^2 + rt^*}}\right) \quad (33)$$

where γ and b are dependent on breakwater typology and characteristics, k and r include future wave action, and μ_0 and σ_0 are the mean and standard deviation of the initial damage, depending on the initial conditions. Beyond the damage accumulation reproduction, this dimensionless stochastic damage progression model also reproduces its statistical distribution. It is of general applicability because it bases on the central limit theorem. This theorem states that under very general conditions, if one sum (integrates) many random variables, the sum is approximately normal, no matter what distribution the summands have (Castillo *et al.*, 2012).

Campos (2014) carried out a set of physical experiments with limited validity to characterize the stochastic nature of damage progression in a model. Then, he used these results to accomplish an initial calibration of Castillo *et al.*'s damage progression probability model, which was fully derived under probabilistic assumptions and following premises of general validity. The experimental results not only confirmed the random nature of damage, but also pointed out the need of reproducibility of the relatively common damage accumulation experiments. The experimental results not only confirmed the random nature of the damage but also pointed out the need for reproducibility of the relatively common damage accumulation experiments. Campos (2014) also highlights the lack of a concise methodology agreed by the scientific community and shared worldwide to measure damage. The necessity of standards in damage initiation and progression is crucial for reproducibility and a consistent comparison between the results from different laboratories. The author also states that in the future, the designer's main challenge will consist of decision-making tools development and calibration, capable of accurately characterizing the structural response and its uncertainties. The damage progression probabilistic models, enhanced by the increase in computing capacity, are helping to progress (Campos, 2014; Campos *et al.*, 2020a).

2.2.2.4 Damage measurement: new techniques and new equipment

Several authors use different laboratory techniques and descriptors to quantify damage, which can be divided into two main strategies: a visual approach or a measuring approach.

The quantification of damage using visual methods corresponds mostly to counting the number of displaced units. For this purpose, a visual assessment, considering reference points, of the breakwater conditions before and after the modelled storm. In the laboratory, it is usually employed a fixed photographic camera, preferably under controlled lighting conditions. The most used technique employed for the counting process include digital overlay techniques. From overlapping photographs (taken before and after the test) and using video, it is possible, in a rudimentary way, to count the number of blocks and to access the structural/toe stability of the breakwater. It becomes a problem when the number of moving blocks is too high. To not compromise accuracy, it is essential to assure the image resolution. Besides, colour coding for the different layers or/and for strips in the same layer is commonly used to assist the identification of movements of armour units.

Additionally, one can use automated tools to detect the position of armour units in different images. For example, Vieira *et al.* (2021) used Trainable Weka Segmentation (TWS) plugin in Fiji to damage quantification.

Visual methods are easy to implement, economical and non-intrusive. Nevertheless, they also present some disadvantages, namely (Campos *et al.*, 2020b):

- These methods are only suitable for low damage levels, being highly time-consuming, inaccurate or/and directly unfeasible when dealing with a high number of displaced armour units;
- Most techniques only focus on the surface, neglecting the degree of damage penetration;
- There is a certain degree of subjectivity and expertise associated with displacement identification. Thus, ensuring reproducibility implies solving some issues, such as the standardization of the inspection process, the use of assisting software, and the concise definitions of thresholds for distinguishing between rocking and displacements.

The other strategy corresponds to a measuring approach based on 2D and 3D reconstruction of a profile or section, followed by its damage quantification using eroded area/volume regarding a non-damage part. This approach can be economically more demanding than visual methods but presents some advantages, such as (Campos *et al.*, 2020b):

- It provides more accurate information;
- It is able for any damage level, up to destruction; and
- It is independent of the subjectivity in the identification of displacement. However, the quantification of the eroded volume can be affected by the chosen measuring technique, the data acquisition procedures, and the post-processing strategies.

In Laboratory, one of the most extended methods for damage measurements was profiling several breakwater cross-sections. Profilers were recurrently used in large model structures with extensive damage. Surface profilers have rods with a sphere or a wheel at the tip. The size of the sphere/wheel depends on the rock size, typically half or one time the median nominal diameter. When moving the rods down the slope, the heights are measured, followed by the profile generation. These rods give for a straight (2D) test section a limited number of profiles, typically ten. In case of negligible damage, this method can be particularly inaccurate when single stones erode between the rods/profiles. In order to improve the accuracy, one can use a profiler with smaller distances between the rods, a wider test section or multiple tests can be set up (Disco, 2012). Mechanical profilers are usually the most robust technique to measure damage in scale model tests of rubble-mound breakwaters, because they work in a simple and robust way. However, they are intrusive, contact with the surface of the armour layer, composed by rock or artificial armour units, and difficult to use in several different wave channels or tanks (CEM, 2006). Moreover, mechanical profilers cannot be applied for certain types of armour layers, and during a test series are, somehow, a time-consuming procedure (Disco, 2012; Lemos and Santos, 2013).

Lately, aiming to speed up this procedure, acoustic, Laser and Stereo Photogrammetric techniques have been applied successfully. Instead of the rods or overlay photos, some more sophisticated methods are used to increase the data density of the structure to obtain a virtual 3D model and cross-sectional profiles to assess damage with more precise millimetre resolution and sub – millimetre accuracy (Disco, 2012).

In order to characterize the submerged part of the breakwater, water is usually drained out. The measurement of structure damage must preferably be obtained without emptying and refilling the flume or basin, which can take a considerable amount of time. Therefore, measurements should be able to be performed through the water surface (Moulin, 2018).

The Digital Stereo Photogrammetric technique (DSP) is relatively new and has a lot of potential that could be applied to two-dimensional and three-dimensional scale model tests of rubble-mound breakwaters. It involves estimating the three-dimensional coordinates of points on an object employing depth measurements made in two photographic images of the same scene taken from different positions – the same principle used by the human eyes –, where common points are identified on each image (Disco, 2012; Lemos *et al.*, 2017). This technique allows, starting from stereo-photogrammetric pairs,

to extract the shape, size and position of the objects contained in it (Fortes *et al.*, 2017) and the output of the package consists of a (x, y, z) file describing the cloud of reconstructed points. This is a standard file format which can be imported by various modelling tools (Lemos and Silva, 2013).

The typical setup of the digital stereo photogrammetric technique consists of:

- two digital cameras, which can be mounted side by side in a support structure. There are also systems where the cameras can be moved. It is usual to take the pair of photos before and after each test;
- a laptop to attach the cameras during photographing, and
- a set of markers, which consists of one base plate marker that defines the origin of the coordinate system, and several regular markers. The required number of markers depends on the size of the model area (Hofland *et al.*, 2013).

For example, Hofland *et al.* (2014) used the DSP technique to describe and quantify the average damage pattern to eight identical rubble-mound breakwater roundheads with rock armour. In Fig.4 a typical test setup for a DSP measurement of a breakwater head is described: the photographer walks around the scale model and typically takes about 20-30 double pictures. In each picture both (a part of) the scale model and several markers should be visible (Hofland *et al.*, 2013). The damage to 8 roundheads was measured simultaneously (Hofland *et al.*, 2014).

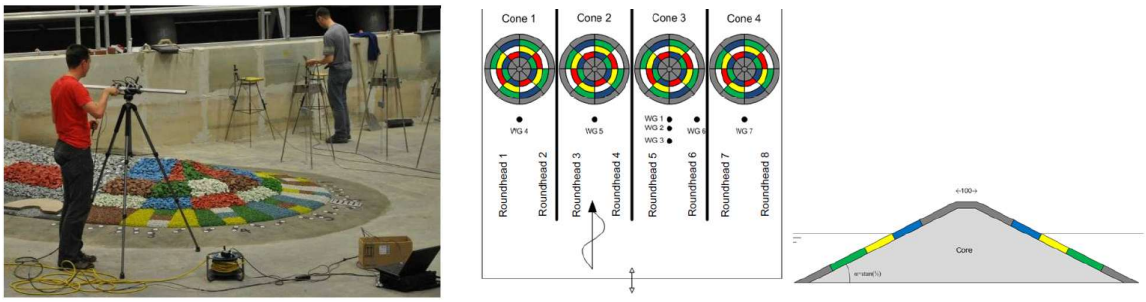

Fig.4 – Execution of a DSP-measurement (Left side) (Hofland *et al.*, 2013). Top view of the test lay out and cross section of roundhead (Right side) (Hofland *et al.*, 2014).

In order to obtain a larger dataset of high – resolution damage scans, Hofland *et al.* (2017) performed 3D tests at the Faculty of Engineering of the University of Porto (FEUP), Portugal. In those tests, the influence of wider test sections, a roundhead, and short-crested wave attack was investigated, for a constant wave steepness. The damage in the structure was measured using a stereo photography technique. The structure was photographed with a set of handheld double-cameras in a drained wave basin (Fig.5). Using a typical number of 50 photo pairs, point clouds of measurements were created before and after each test run. These point clouds were filtered and interpolated on a 1x1 mm^2 grid. The post-processing steps were the ones described in Hofland *et al.* (2013).

Fig.5 – Damage measurement using the DSP technique (Hofland *et al.*, 2017).

Lemos and Santos (2013) also used the DSP technique in the measurement of the eroded volume of a rubble-mound breakwater roundhead model, in which, refraction due to the air-water interface was corrected (Ferreira, 2006). This means that is not necessary to empty the flume or wave tank to get a good coverage of the whole armour layer. Tests were carried out in one of the LNEC's (Laboratório Nacional de Engenharia Civil) irregular wave basin, approximately 40 m long and 23 m wide. The armour layer consisted of a double rock layer and surveys of the breakwaters's head section were performed with and without water in the wave basin. The two cameras were mounted side by side in a 3 m high support structure and plugged into laptops. This enables to photograph simultaneously the photogrammetric pairs by remote triggering from the computers.

The same authors had already tested intensively this survey technique in long -term scale models for two – dimensional scale models with rock units (Fig.6). Several tests were also carried out, aiming to measure the breakwater armour layer erosion, using both natural and artificial units (Lemos and Santos, 2013).

Fig.6 – Setup for two - dimensional scale model tests and targets used in DSP technique (Lemos *et al.*, 2018).

van Gent *et al.* (2019) and de Almeida *et al.* (2019) also applied the DSP technique in test campaigns carried out at Deltares wave flume with rock armoured slopes. In the van Gent *et al.* (2019) work, two test series were performed five times, allowing for a statistical analysis of the damage to rock armoured slopes, which is uncommon due to the absence of statistical information based on a systematic repetition of the test series.

In more recent years, the 3D laser scanning technique and LiDAR technology has been used in coastal engineering domain by some authors as Infante *et al.* (2012), Streicher *et al.* (2013), Puente *et al.* (2014b), Hofland *et al.* (2015), Tulsi (2016) and Shen *et al.* (2017). The laser scanning technique is a method to scanning objects and land features based on LiDAR (Light Detection and Ranging) technology, which is an active remote sensing technology measuring distances by electromagnetic waves (Infante *et al.*, 2012). In global terms, the 3D laser scanning is based on the principle of reflection less measurement (with no special reflecting devices) of distances by means of a laser operating in pulses (Infante *et al.*, 2012). The scanner is composed of an impulse EDM (Electrical Discharge Machining) and various optical–mechanical apparatuses (rotating mirrors, servomechanisms, etc.) (McLelland *et al.*, 2016). The laser impulse, directed towards an object by small rotating mirrors (up to 10 – 100 rotations per second) regulated by servomotors is reflected by the solid surface, returning to the point of emission and then the travel time is recorded by the receiver (EDM) (Balzani *et al.*, 2002, Infante *et al.*, 2012). The receiver converts the optical returns into electronic signals which are digitized for waveform processing (Tulsi, 2016). Next the distance to the measuring point is calculated from the known laser beam travel velocity and time values (Infante *et al.*, 2012). The waveform analysis calculates the optical echo signals by multiplying it with the known speed of light (299 792 458 m/s) leading to a point at a distance away from the scanner (Tulsi, 2016).

Puente *et al.* (2014a) used a Terrestrial Laser Scanner to extract geometry and monitor changes in rubble-mound breakwaters. They used a Faro Focus 3D to extract the geometry from an area of 14 x 5.5 m of the Baiona breakwater in north-western Spain, which is an old rubble-mound breakwater with conventional concrete cubes armour units. This novel approach allowed to automatically monitor the concrete armour units' displacements and rotations, using point clouds of different times. This method proved to be useful to detect local flaws at early stages, avoiding them to affect the structural stability of the breakwaters. Besides this is a phase-based system, whose measurements are taken continuously. That fact makes it suitable for precise surveys (Puente *et al.*, 2014a).

Another study from Puente *et al.* (2014b) was performed to evaluate short-term changes in Cubipod armoured breakwater roundheads. The authors also employed the Faro Focus 3D to extract data. Only the damage that occurred above the water level was studied, since the damage of the entire slope from toe to crest cannot be monitored, due to the attenuation of the infrared LiDAR in water (Puente *et al.*, 2014b). A total of seven scans of the breakwater roundhead were gathered from the same scanner. Since sampling efficiency was crucial, scanner parameters were chosen such as not to exceed a scan time of 20 min. Then, the sampled surfaces were analysed for vertical deformations using an algorithm. Puente *et al.* (2014b) developed a damage-growth monitoring procedure using some Matlab image processing techniques. The automated image analysis allowed to minimize the manual interactions from the maintenance personnel. The results achieved from Puente *et al.* (2014b) study were useful for structural monitoring applications and maintenance strategies.

Hofland *et al.* (2015) used a standard laser scanner to measure the hydraulic responses of a dike slope in the (old) Delta Flume. The signal intensity of the laser reflection produced by a SICK LMS511 Pro HR sensor was used in the determination of the wave runup height. The scanning plane was inclined

from the vertical (slant angle, φ=26°) to avoid a direct reflection of laser light from the water level which yields erroneous measurements (Fig.7).

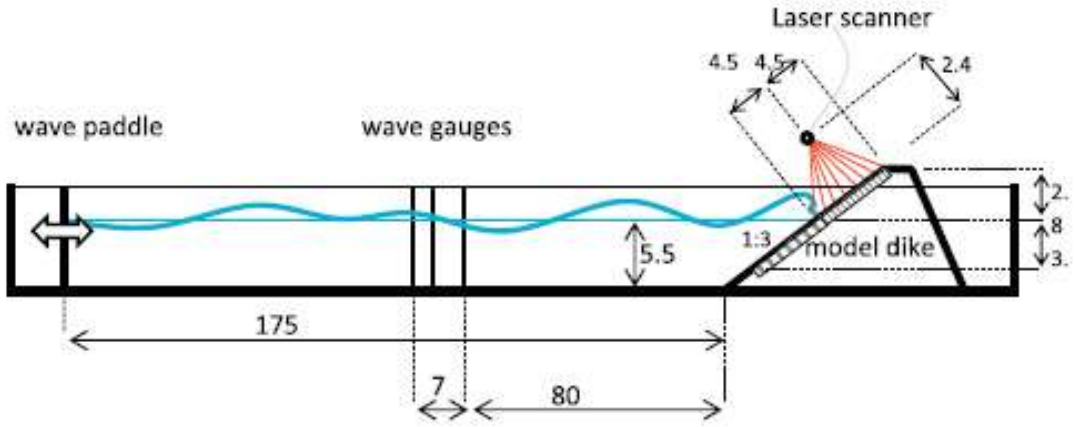

Fig.7 – Schematic setup of the tests. Longitudinal section of flume (Hofland *et al.*, 2015).

The extreme wave runup heights measured by laser scanner using a reflection intensity threshold were still typically 10 cm smaller than the optical measurements. Part of this deviation resulted from the fact that the visual runup measurements were three-dimensional - a wave passing a shore-parallel line of 2 m width at any transversal location is considered - while the laser scanner measurement was taken at one transversal position. Consequently, the maximum runup could occur outside the laser line and be slightly higher. Additionally, virtual wave overtopping volumes and mean overtopping discharge are determined by considering the maximum water volume above a certain virtual crest level on the dike slope, for each runup event. The study describes the technological applicability of the technique, including postprocessing methods and made some estimations of the accuracy that can be reached (Hofland *et al.*, 2015).

Tulsi (2016) study focused on the quantitative 3D assessment of different degrees of damage to breakwaters with dolos armour units above and below water. Three-dimensional data analysis using high - resolution laser and acoustic technologies, like LiDAR and multibeam echo sounders respectively, was aimed at providing a more realistic method to quantify damage than two - dimensional photographs. The investigation started with an idealized undamaged model breakwater slope in a laboratory experiment comparing the repeatability of the 3D method with sequential scans and the 2D method to compare the deviation in repeatability of data captured and to determine the 3D method accuracy. The repeatability test was carried out by comparing 10 consecutive scans with the first scan. The standard deviation was 0.001 cm^3. The Riegl VZ-400 3D laser scanner was used for the experiment. The manufacturer's specification indicates that the scan data acquisition produces 5 mm accuracy with 3 mm precision and repeatability within a range of 600 m. Then the 3D method was applied to a 3D physical model study of the spur breakwater at the root of Table Bay's main breakwater, South Africa (Fig.8). The physical model was built at a geometric scale of 1:54. The comparison of the cumulative damage progression monitored by the visual 2D photographic method with that calculated by the 3D method showed that there is a good correlation between the two damage quantification methods. The results of the 2D and 3D methods differ in cases of small settlements and larger displacements (Tulsi, 2016).

Fig.8 – Laser scanner and fixed camera positioned over the test section (Left side). The model with scanner and calibration box (Right side).

The aim of the research presented by Shen *et al.* (2017) was to quantify changes in different rock slopes after wave attacks and address the application of a 3D laser scanner in coastal engineering at laboratory conditions. A Leica C10 Scan Station scanner (Fig.9) was used to obtain 3D coordinates of the rock surfaces at a laboratory scale, before and after each experiment. This scanner, with an effective operating range of ± 1 - 200 m (up to 300 m with 90% reflectivity), presented a reported accuracy of 6 mm in a single position and 4 mm in depth at ranges up to 50 m. After each test, the water was drained from the flume and different scans were made. One was obtained just after the flume water got drained, therefore the stones on the bed were still wet; the second one was obtained after the stones had dried up. According to the authors, "*Laser scanners not only provide information about the 3D location of object surfaces but also store the amount of reflected energy as an intensity value. The wetness of the rocks has a serious negative effect on the intensity. A lower intensity also implies a lower Signal to Noise ratio, which will in turn affect the precision of individual points*." Therefore, to avoid the influence of moisture on the quality of the point clouds, Shen *et al.* (2017) used scans that were obtained after the rocks turned dry. Next, through a series of processing steps, the point clouds were converted to a suitable 2D raster for change analysis. This allowed to estimate detailed and quantitative change information (Shen *et al.*, 2017).

Fig.9 – A Leica C10 Scan Station (Russhakim *et al.*, 2019).

Each of the aforementioned methods solve unique problems to provide the best solution within different contexts. In Table 6 two 3D survey techniques are compared: laser scanning and digital stereo photogrammetry, by presenting their advantages and disadvantages.

Table 6 – Comparison between two 3D survey techniques: laser scanner and DSP.

Laser Scanning	Digital Stereo Photogrammetry (DSP)
Advantages	Advantages
▪ High level of accuracy over large spaces ▪ Error rate is fixed based on the capabilities of the equipment ▪ Automated process after targets are placed and scanner is started – less chance for user error ▪ Less time spent on site ▪ Availability of auto-extraction / meshing software for point clouds	▪ Significantly cheaper equipment ▪ Better tool if one wants to study and reconstruct smaller spaces ▪ Most improvements are on software side so no need to buy new equipment to keep up with progress ▪ More visual photo realism ▪ Better visual representation of textures ▪ Using an extra software/code, it is possible to reconstruct both merged and submerged scenes
Disadvantages	Disadvantages
▪ Equipment can be prohibitively expensive to own ▪ Generally, need to upgrade physical equipment to keep up with progress ▪ Fuzzy point cloud on highly textures / reflective surfaces ▪ Expensive equipment	▪ Accuracy is lower than the one obtained with laser scanners over large space ▪ Lower quality method of 3D capture ▪ Scale limitations based on camera lenses maintaining clarity over long distances ▪ Less automated process allows for more user error – results depend greatly on experience of operator ▪ More time spent on site ▪ Auto extraction / meshing software not as advanced ▪ Errors when dealing with reflective/transparent surfaces, because DSP needs some contrast points to calculate depth

Regardless of the measurement method adopted, Campos *et al.* (2020b) pointed out that all factors involved in the data acquisition process should be specified, including the characteristics and settings of the measuring instruments. Acquired data would consist of images, videos, profiles, point clouds, or meshes, depending on the damage characterization technique. Regardless of the data type, it should be temporally and spatially correctly identified. The authors also highlighted that comparisons between several repetitions of the same measured section are relevant to estimate the error derived from the measuring process and surface reconstruction. Regarding post-processing strategies, the authors noted that they should include:

- Criteria for distinguishing between rocking movements and displacements,
- Filtering methods for erroneous values, settlements, or rocking,
- Smoothing strategies, when applied,
- Surface reconstruction methods, and
- Methods for integrating the eroded volume.

2.2.3 INSTRUMENTED CONCRETE AMOUR UNITS

The current design process, commonplace in the industry, is based on the hydraulic instability of the structure, measuring the damage through the number of displaced units. However, the used formulas do not consider some secondary effects derived from the lack of understanding of the complex interaction between the armour layer and the wave hydrodynamics. More specifically, design methods lack the quantification of unit forces, concrete stresses, hydrodynamic pressures, and non-linear effects.

For a greater understanding of the complex hydrodynamic interactions and structural behaviour, it is relevant to evaluate the behaviour of the individual armour units since they are exposed constantly to loads throughout the design lifetime, which includes the following load conditions, according to BSI (1991):

(i) Construction loads. These occur during manufacture, transport and placing. The cracks resulting from stresses arising during manufacture or other conditions can significantly reduce the unit's capacity to withstand later applied loads;
(ii) Static loads. These are due to self-weight and interlocking forces, support of overlying units and units jam caused by the settlement of the core and underlayer;
(iii) Hydraulic loads. These are due to wave breaking, uprush and downrush and can be transferred by bearing contact to another unit. Hydraulic loads cause other secondary effects, including motion of units, unit-to-unit interactions, porous underlayer interaction, and a host of other ones difficult to quantify;
(iv) Dynamic loads. These are due to the rocking and unit displacement resulting in an impact on other units. Although they are not necessarily the highest loads imposed on blocks, they are probably the most significant ones. Repeated loading due to rocking can result in breakage due to fatigue. In the 1970s and 1980s, several large breakwaters failed due to the breakage of concrete armour units. After these events, extensive research was carried out on the wave-induced unit motion, the resulting stresses, and the subsequent breakage of these units. Since stresses are difficult to measure directly in a scale model, the rocking motion of units is, nowadays, used for design. A relevant parameter of rocking behaviour is the magnitude of the impact velocity and its stochastic and spatial distribution (Hofland *et al.*, 2018).

More fundamental research is required to enable accurate quantification of the loads. During the last years, although not a usual procedure in laboratory tests, the introduction of instrumented armour units in the hydraulic model tests to measure various parameters was game-changing, presenting enormous potential. Different studies use them with distinct purposes, including the assessment of hydraulic pressures and forces on the individual blocks, the damage assessment of a rubble-mound breakwater through the new spatial distribution of the blocks, and to provide quantitative measurements of translation, rotation, peak accelerations, impact velocities, and others. The resulting data set collection, which includes unit locations and movements, allows an insightful comprehension of unit-to-fluid, unit-to-structure and unit-to-unit interactions. All this accurate information also helps to support the calibration and validation of numerical models.

Some works and publications that use this innovative technique are exposed below in chronological order.

As part of an extensive research project on the strength of concrete armour units, coordinated by the Centre for Civil Engineering Research and Codes work-group C70 (CUR, 1989; 1990), Van der Meer and Heydra (1991) conducted model tests on breakwater sections armoured with Cubes and Tetrapods. These tests were integral to the broader study, which aimed to better understand the dynamics of these

units under wave impact. To advance this understanding, Van der Meer and Heydra (1991) embedded accelerometers in the centre of these units to measure peak impact accelerations and velocities. This work also included the quantification of unit rocking and unit collisions. Due to the randomness of the wave field and the placement of units, each rocking impact is unique. The results proved to be a step towards a better understanding of armour unit dynamics within the armour layer, showing that the random nature of breakwater-wave interaction is highly variable, both in space and time. The authors concluded that wave conditions with a lower Iribarren number, given by $\xi = \tan\alpha / \sqrt{H_S/L}$ where α is the slope of the structure, H_S is the significant wave height, and L is the wavelength, tend to produce higher peak forces and accelerations.

Burcharth and Liu (1995) inserted load cells on slender armour units, like Dolos and Tetrapods, to study the impact loads and internal concrete stresses. The authors identified some complications involved in the load-cell technique, namely the installation process that makes the material properties of the unit different from those of the homogeneous prototype. Consequently, this affects the impact responses, which depend on the elastic behaviours of the bodies. The authors also included the Dolos designs diagrams for breakage and hydraulic stability prediction.

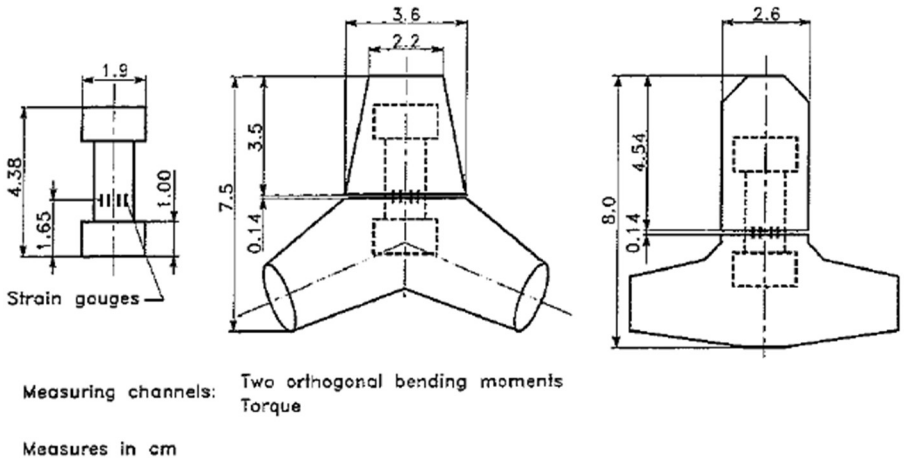

Fig.10 – Dolos and tetrapod schemes with the load-cells (Burcharth and Liu, 1995).

Le (2016) conducted a comprehensive study aimed at enhancing the understanding of the behaviour and rocking motion of single-layer armour units. The experimental setup featured two configurations: a single cube on a slope and a cube embedded within a slope of multiple cubes. A high-frequency accelerometer was attached to the primary cube, securely connected to the slope via a hinge, and linked to a computer for data acquisition. Distinct from earlier research by CUR, which measured acceleration during the impact, Le's methodology focused on measuring acceleration leading up to the impact to calculate the related velocity. This approach, requiring a lower sampling frequency, successfully identified the highest impact velocities just below the still water level. Despite its findings, the study identified limitations in the experimental setup, such as the absence of breakwater porosity representation and the slope's roughness not matching that of a prototype breakwater. Le's research suggested the development of a wireless device that integrates both an accelerometer and a gyroscope to improve the accuracy of capturing and analysing armour unit movements.

In a different context, Gronz *et al.* (2016) introduced the Smartstone probe, a compact device designed for monitoring the movement of small stones, particularly in fields such as geomorphology and hydraulic engineering. The probe is encased in a metal cylinder and contains a Bosch BMX055 sensor, which integrates a triaxial accelerometer, magnetometer, and gyroscope. It also features memory for data storage, active radio-frequency identification (RFID) for data transmission and is powered by two button cells. The Smartstone probe was evaluated in laboratory flume experiments, where its performance in tracking stone movement was compared to high-speed camera footage. The results showed a deviation exceeding 30% between the probe's measurements and the visual data. This discrepancy was attributed to several factors, including noise, integration error, and orientation error. Noise levels varied with power consumption and sampling intervals, with higher noise observed at lower power settings. Integration errors, due to the double integration process used for position estimation, resulted in increasing positional drift over time and distance. Additionally, orientation errors impacted the accuracy of velocity and position calculations, as the derived orientation used to align the accelerometer readings was imprecise. Despite these challenges, the Smartstone probe represents a significant advancement in monitoring small-scale stone movement. However, the author recommended further improvements to reduce noise and enhance orientation accuracy to improve the device's precision.

Arefin (2017) focused on the spatial and stochastic distribution of the rocking behaviour and strength of breakwater armour units. This research aimed to estimate the magnitude and distribution of impact velocities, and to compare, validate, and build upon findings not addressed in the CUR (1989) study. Since no subsequent research had been conducted to validate the CUR C70 findings, this study employed a state-of-the-art measurement technique developed at Deltares and TU Delft. The author performed experimental tests considering cubes disposed in a double and a single layer. Since the rocking process depends on numerous parameters, such as wave height, wave period, armour unit position, acceleration and impact velocity, the author placed eight instrumented aluminium cubes in his experiments. The main goal was to determine the impact velocity distribution for different locations of the cubes on the slope. Arefin placed a new type of sensor, Tinyduino, in the centre of the 4 cm cubes and connected them to the computer through a very flexible wire, increasing test efficiency. The sensor's placement inside a hollow cavity of the cubes made the effective density of the cubes close to that of the other model cubes. The real-time collection using accurate multiple sensors provided the statistics for spatial variability of rocking behaviour. Although the cable used for connecting the instrumented cubes was good and flexible, it made the cubes vulnerable to water. So, the author recommended the use of watertight wireless connection in future works. An important conclusion of the author was that a sensible estimate of the spatial statistics of the variation in rocking behaviour between cubes is only possible when using the order of ten instrumented cubes. Moreover, the number of collisions is assumed to be equal to the number of peaks in the time signal of the absolute angular velocity.

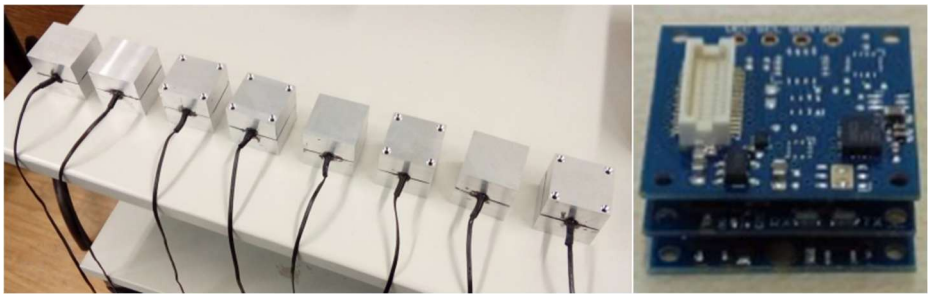

Fig.11 – Instrumented cubes (left) and Tinyduino Sensors (right) (Arefin, 2017).

Fig.12 – Model preparation: empty mold for slope preparation (left), prepared slope for testing (middle), and cubes placed randomly in a double layer arrangement (right) (Arefin, 2017).

Hofland *et al.* (2018) focused on a robust and efficient way to determine the characteristic impact velocity of rocking armour units at a laboratory scale using modern embedded 9-axis IMU (inertial measurement unit) sensors. These sensors, data storage, and batteries were all embedded in the model units, enabling them to work without wires. These miniature sensors work with the Arduino software platform. The placement of a magnetic sensor inside the model units allowed to switch on/off the sensor without the need to remove the block from the armour layer or to open it. Tests were performed, applying the technique to a double-layer, comparing the results with existing knowledge for this type of breakwaters armour layers. In contrast to previous research, this study used the gyroscope reading instead of the accelerometer record to determine the (rocking) impact velocities. This logical decision resulted from the realization that the typical mode of movement is rotation rather than rocking. A gyroscope measures the angular velocity, so when using this signal no integration was needed, but rather a single velocity measurement just before the impact. This new technique implies, first, obtaining the absolute value for the angular velocity using the three measured angular velocity components $(\omega_x, \omega_y, \omega_z)$ as follows:

$$|\omega| = \sqrt{\omega_x^2 + \omega_y^2 + \omega_z^2} \tag{34}$$

Next, the impact velocity is based on peak angular velocities by assuming a pure rotational motion of the cube:

$$v_i \approx D_n|\omega| \tag{35}$$

In the end, the exceedance curve is made by ordering the impact velocities according to magnitude, in descending order with $v_{i,1}$ being the largest, and the exceedance probability estimate as:

$$p(v_i > v_{i,1}) = \frac{n}{N_{col}} \tag{36}$$

where N_{col} is the number of collisions in the test and n is the rank of the velocity in the ordered list. An additional advantage of using the gyroscope over the acceleration signal is the absence of gravitational acceleration influence.

The authors performed the first series of tests with a stand-alone Tetrapod unit made of two solid pieces of aluminium, as presented in Fig.13. The recordings clearly showed that the impact peaks due to rocking could be easily distinguished.

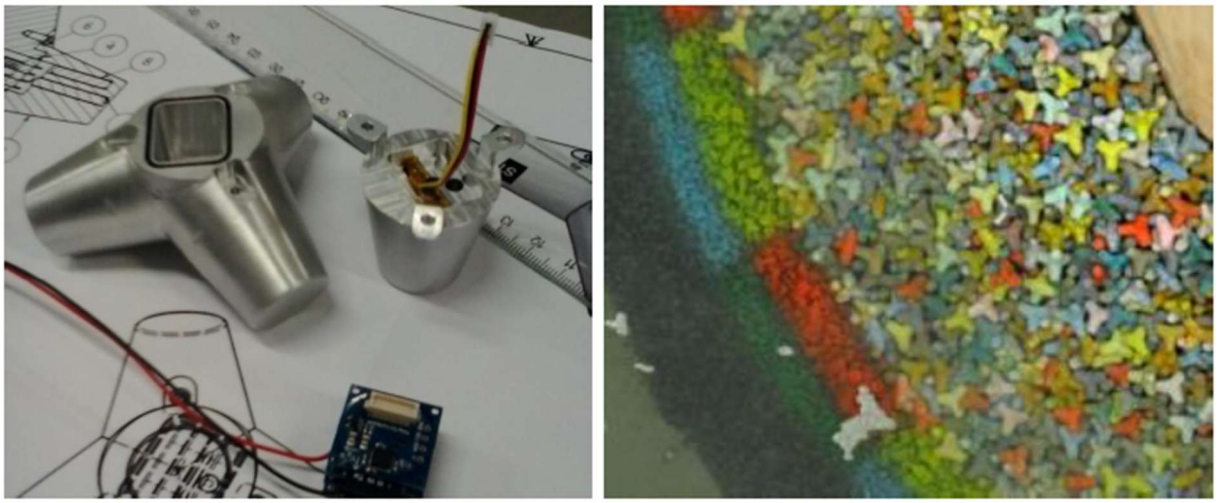

Fig.13 – Tetrapod model unit with sensor (left) and tetrapod model unit in slope (right) (Hofland *et al.*, 2018).

As part of the Hydralab-plus project, Santos *et al.* (2019) describes a set of executed tests to assess the performance of rubble-mound breakwaters in climate change scenarios, including the data collection process. The proposed experiment intended not only to extend and improve the validity range of the available empirical formulas for armour layer stability but also to calibrate and validate run-up and overtopping empirical formulas. In the instrumentation chapter, the research team included three 3-D printed Antifer cubes with identical dimensions and weight as the other cubes in the breakwater armour. Inside were small Arduino computers, which comprised processing boards, 9-axis IMUs, batteries, SD cards, waterproof Micro-USB connections and a reed switch to switch the sensor off. These blocks allowed the measurement of three components of acceleration (including gravitational acceleration) and angular velocity. The blocks were initially always placed on the slope with the same orientation. Fig.14 presents the instrumented blocks.

Fig.14 – Model instrumented Antifer unit (left) and instrumented units in the breakwater (right).

Eden (2019) contributed to a better understanding of armour unit hydrodynamics. The author developed innovative measurement techniques that enabled the acquisition of unique datasets describing the loading on a single isolated armour unit placed on an impermeable slope. These techniques provided quantitative measurements of wave pressures and forces that were previously unavailable and information useful for improving breakwater design methods. Additionally, they provided data to support the calibration and validation of numerical models. So, part of his study consisted of an experimental program investigating the impact of waves on concrete armour units used on rubble-mound breakwaters. Experimental tests were performed in a wave flume at the National Research Council of Canada - Ocean, Coastal and River Engineering Research Centre (NREC_OCRE). A Core-Loc armour unit was 3D printed using PLA plastic at the University of Ottawa Maker Space, instrumented with six pressure sensors (Honeywell TBF-LPNS001BGUCV) placed at six different locations on the unit's surface, as presented in Fig.15. In addition, the Core-Loc was mounted on a six-degree-freedom force transducer (model ATI Mini45 IP68) to record forces and moments acting on the unit during testing. Following testing and calibration, the instrumented unit was placed on a rigid impermeable slope, Fig.16, and exposed to a wide range of wave conditions to investigate: (i) the hydrodynamic loading due to waves and (ii) the sensitivity to various wave conditions and unit placement locations. The test results proved that the instrumented "Smart-Units" used for experimental testing of breakwater armour units provide reliable measurements and valuable insights into the hydrodynamic interaction between waves and armour units. Moreover, they showed that: (i) decreasing surf similarity parameter, also known as Iribarren number, and increasing wave steepness, defined as the ration of wave height to wavelength, were correlated with increased forces and pressures on the unit and (ii) the units located just below the still water level experienced the highest loads during wave impact. In conclusion, the author considered that this embedded system would be implemented in future versions of either specially crafted concrete or machined metal units that are free to move, interact and transmit data wirelessly in real-time or after testing. Some of the author's recommendations for future work included the consideration of additional breakwater design parameters and the replacement of the coupling nuts used to mount the unit on the force transducer with low-cost accelerometers and gyroscopes, as in Hofland *et al.* (2018).

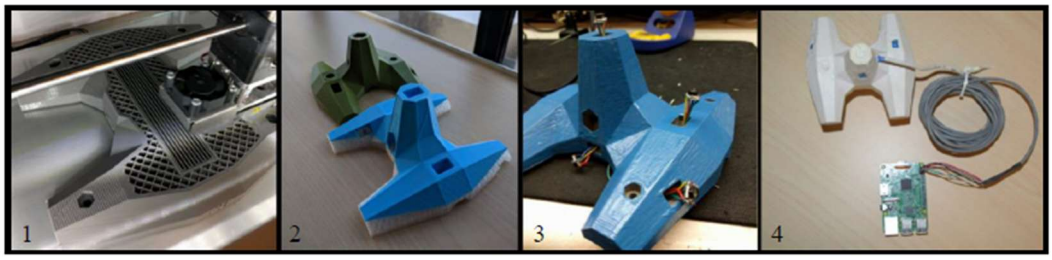

Fig.15 – Printing the unit (1), printed unit (2), circuit assembly (3), and final instrumented unit (4) (Eden, 2019).

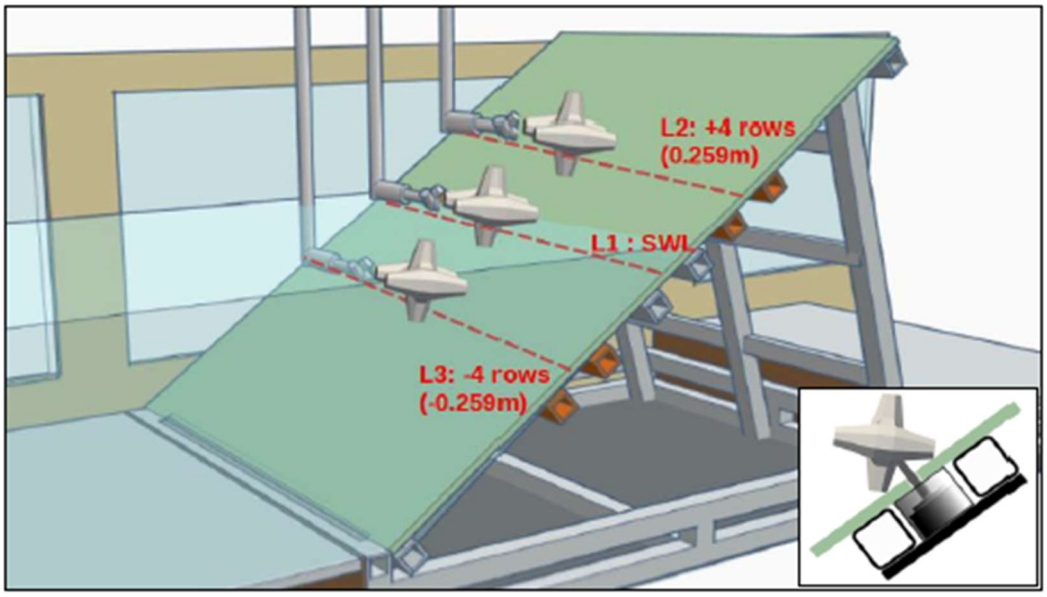

Fig.16 – Schematic of breakwater slope and unit testing locations (L1 = SWL, L2 = upper, L3 = lower) with inset figure showing force transducer mounting system (Eden, 2019).

Caldera (2019) advanced the study of rocking armour units by applying the technique to measure the impact velocities of Xblocs under wave action, specifically focusing on their magnitude, spatial distribution, and stochastic characteristics. A wireless, standalone sensor was embedded within a 3D-printed Xbloc unit, with two test units created and tested in a physical model. This Arduino-based sensor system, which measured accelerations and angular velocity at a sampling frequency of 100 Hz, included a battery, data storage, and a waterproof USB connector for charging and data retrieval. The initial physical model tests confirmed the feasibility of this method for capturing the complete rocking motion of single-layer armour units. Data analysis showed that the technique effectively interprets both upward and downward movements, which are often challenging to observe visually during model testing. The study also established that a 100 Hz sampling frequency is sufficient to capture the critical motion just before impact. Notably, the angular velocity data from the gyroscope exhibited less noise compared to the accelerometer data. Although peaks in acceleration often corresponded with gyroscope readings, calculating impact velocity from accelerometer data requires integration, which can lead to error accumulation. Therefore, it is recommended to rely on the impact velocity provided by the gyroscope for a more accurate representation. While the study validated the technique, it also highlighted the need for further testing with more sensors to fully evaluate and refine its accuracy.

Dost *et al.* (2020) introduced the Smartstone probe v2.0, highlighting its advancements over the initial version presented by Gronz *et al.* (2016). The research focused on technical improvements, explaining how the new probe provides additional motion data and facilitates 2D and 3D visualization of clast trajectories, enabling better recognition of complex motion patterns. Unlike high-speed video and wired sensors, which restrict motion analysis to surface views and 2D profiles, this autonomous and wireless device captured detailed 3D spatiotemporal dynamics of landslides in both dry and wet conditions, providing continuous internal measurements without motion constraints. Equipped with an inertial measurement unit (IMU) that records acceleration and rotation at 100 Hz, the probe operates with low power using small batteries. It includes a USB gateway that serves as the interface between the Smartstone probe and its controlling software, which features a graphical user interface (GUI). This setup allows users to adjust probe settings, initiate recordings, and read out data. Users can set a recording threshold to prevent minor signals, like environmental vibrations, from occupying memory before significant motion occurs. Additionally, individual sensors can be disabled, and the sampling rate can be customized.

The data from laboratory experiments with the Smartstone probe were systematically presented, encompassing three key aspects: (i) sensor recordings, (ii) derived movement characteristics, and (iii) 2D and 3D visualizations. The qualitative description and interpretation of the sensor data provided insights into the motion dynamics of the clasts, including acceleration components along the x_p, y_p, and z_p axes (the superscript indicates that the values are probe readings), and rotational rates. The data were categorized into stationary and non-stationary periods. During stationary conditions, gravitational acceleration was recorded predominantly along the z_p axis, with minimal values along x_p and y_p. This pattern confirms that the readings are consistent with gravitational effects, validated by zero rotational readings. The resultant acceleration, $a_{resultant}$, was approximately $1g$, and is defined by:

$$|a_{resultant}| = \sqrt{a_x^{p^2} + a_y^{p^2} + a_z^{p^2}} = 1g \tag{37}$$

Each axis reading reflects a fraction of the gravity vector and is given by:

$$a_x^p = \cos\alpha \cdot 1g \;,\; a_y^p = \cos\beta \cdot 1g \;,\; a_z^p = \cos\gamma \cdot 1g \tag{38}$$

where α, β and γ define the angle between x_p, y_p, and z_p and the gravity vector, respectively. Accordingly, under static conditions the probe's orientation relative to the gravity vector (vertical direction) can be calculated from the three readings of a_x^p, a_y^p and a_z^p.

To quantify the pebble's movement relative to its starting position, derived movement characteristics such as acceleration (a^{rel}), velocity (v^{rel}), and displacement (s^{rel}) were analyzed. This was achieved by rearranging sensor readings and applying physical relations to compute these characteristics. Euler angles and quaternion representations were used to calculate the initial orientation of the clasts. After rearranging the recorded accelerations and with respect to time, *t*, the movement characteristics v^{rel} and s^{rel} were obtained from the integration as:

$$v^{rel}(t) = \int a^{rel}(t)dt \tag{39}$$

and

$$s^{rel}(t) = \int v^{rel}(t)dt \tag{40}$$

Although high-speed video recordings capturing only a segment of the pebble's motion, the full trajectory was reconstructed using the Smartstone data. The trajectory, defined by position vectors x^{rel}, y^{rel} and z^{rel} over time provided comprehensive insights into the movement.

Key findings of the study include the ability to segment motion sequences into distinct phases using acceleration and rotation data, as well as the successful 3D reconstruction of clast trajectories through sensor fusion algorithms. The research demonstrated that multiple probes could be used simultaneously to gain insights into the internal dynamics and deformation of moving landslide bodies. Although exact depositional positions couldn't always be quantitatively reconstructed, the probe effectively identified qualitative features and complex movements, enhancing the analysis of landslide mechanics. The probe's broad applicability also extends to coastal and hydro-engineering studies. The study discussed the limitations of the prototype and suggested areas for further development to enhance its capabilities. For instance, a relatively low deviation was achieved by merging only accelerometer and gyroscope data, indicating that further improvement could be possible with the inclusion of magnetometer data, which would allow for displaying the trajectory in a global reference system. Additionally, accuracy in trajectory reconstructions could be enhanced by applying methods well-established in other disciplines, such as pedestrian navigation or mobile robotics, including Kalman filtering or Markov localization.

Building on the approach developed by Caldera (2019), recent studies by Hofland *et al.* (2023) and Houtzager *et al.* (2024) introduced innovative embedded Rocking Sensors to measure critical parameters such as the number of rocking impacts, accelerations, and rotational velocities in single-layer units. These studies involved conducting physical model tests on an armour layer with Xbloc units exposed to irregular wave conditions. Measurements were captured using a 9-axis IMU (ST LSM9DS1 sensor) embedded in a compact Arduino-based TinyDuino platform, which recorded acceleration and rotation rates at a sampling frequency of 100 Hz. To optimize data storage, data was recorded only when specific thresholds for rotation (0.05 rad/s) or acceleration (1.01g) were exceeded, with periodic measurements every 0.5 s to monitor the unit's position during periods of inactivity. The system also featured an Atmega328P processor, a lithium battery, and magnetic switches for starting and stopping measurements. Validation of the system's accuracy was conducted by calibrating the accelerometers against a standard 1g gravitational reference and by testing the gyroscope with controlled rotations. These validation efforts ensured reliable data collection, which was then processed to identify individual rocking impacts and quantify the motion dynamics of the Xbloc units. However, accurately determining their orientation and motion within the global coordinate system remained challenging due to the random and changing orientation of the units during testing. The acceleration sensor is used to measure translation, while the gyroscope measures rotation. Variations in gravitational acceleration due to changes in the unit's orientation further complicated the description of rocking motion, necessitating the use of simplifying assumptions. To estimate rocking impact velocities, equations (34) and (35) were applied (Hofland *et al.*, 2018). The peak instantaneous rotational speed just before impact was related to impact velocities. Specifically, the absolute rotation speed $|\omega|$ is used to estimate the impact velocity v_i, based on the rotation of the unit's leg around its base. The value of $|\omega|$ typically exhibits two peaks

per wave, corresponding to the uprush and downrush phases. A scalar value representing rotational motion, ω_s, is derived using:

$$\omega_s = |\omega| \cdot sign(\omega_j) \tag{41}$$

where ω_j is the angular velocity component with the largest standard deviation, providing a high signal-to-noise ratio. This approach allows for distinguishing between rocking motions in the uprush and downrush phases. The resultant rotation angle during a rocking event is obtained by integrating the absolute rotational velocity over the event's duration, divided by two to account for both the uprush and downrush peaks:

$$\Delta\theta = \frac{1}{2}\sum \omega_s \tag{42}$$

The processed data revealed that the new technique offers a more comprehensive understanding of rocking behaviour, including impact velocities, than visual observations alone. Houtzager *et al.* (2024) found that the number of impacts increases with stability numbers but decreases significantly after several storms, likely due to changes in packing density. Hofland *et al.* (2023) also noted that the highest impact velocities typically occur near the water line and during the uprush phase of waves. Their study suggests that downslope settlement of the units continuously alters their orientation and placement density, affecting the overall rocking behaviour. These findings underscore the effectiveness of the embedded Rocking Sensors in capturing the detailed dynamics of single-layer armour units and provide valuable insights into the rocking impact mechanisms crucial for breakwater design and analysis.

Table 7 summarizes the key authors who have applied this type of blocks in their research, highlighting the main objectives of their studies, the instrumentation, and the primary findings

.

Table 7 – Summary of key studies on instrumented blocks: Main goal, instrumentations, and data output.

Authors	Goal	Instrumentation						Measurements	Observations
		Armour Unit	Material	Power	Storage	Sensors	Sampling frequency		
Van der Meer and Heydra (1991)	Quantification of armour unit rocking and collisions	Cube & Tetrapod	Concrete	n.d.	n.d.	Accelerometer	50 000 Hz	Number of moved units and collisions Impact velocity	
Burcharth and Liu (1995)	Impact loads and internal concrete stresses on units	Dolos & Tetrapods	Concrete	n.d.	n.d.	Load cells	n.d.	Force	
Le (2016)	Quantification of single layer armour unit rocking and collisions	Cube	Concrete	Connection via thin wires	Connection via thin wires	3-axis Accelerometer (ADXL335)	1600 Hz (x and y directions) 550 Hz (z direction)	Number of collisions Impact velocity	Cube is attached to the slope with a hinge, allowing the cube to rotate in only one direction
Gronz *et al.* (2016)	Monitoring the movement of small stones	SmartStone	Stone	External battery (Two silver-oxide button cells)	External memory	9-axis sensor (Bosch BMX055)	10-84 Hz	Accelerometer and magnetometer timeseries Derived orientation Comparison with visual footage	Deviations due to noise, quantisation, integration, orientation and clipping errors

Table 7 (cont.) - Summary of key studies on instrumented blocks: Main goal, instrumentations, and data output.

Authors	Goal	Instrumentation						Measurements	Observations
		Armour Unit	Material	Power	Storage	Sensors	Sampling frequency		
Arefin (2017)	Spatial and stochastic distribution of the rocking behaviour and strength of breakwater units	Cubes	Concrete	External battery	External memory (Flash memory)	Tinyduino sensor (IMU)	Up to 62.5 Hz	Impact velocity distribution for different locations using the gyroscope (angular velocity)	Flexible wire to increase the testing efficiency; Water penetration through the cable connection
Hofland *et al.* (2018)	Quantification of unit rocking	Tetrapod	Aluminium	External battery	External memory (SD-card)	9-axis IMU	32.5 Hz	Impact velocities using gyroscope reading (angular velocity)	Need to open the units to retrieve data
Santos *et al.*, 2019)	Armour layer stability	Antifer	3D printed (PLA)	External battery	n.d.	9-axis IMU	25 Hz	Acceleration Angular velocity	Need to increase sample frequency
Eden (2019)	Experimental technique for measure the impact of waves on concrete armour units	Core-Loc	3D printed (PLA)	External battery	n.d.	Pressure sensors (6 units)	40–320 Hz	Wave pressures Force	

Table 7 (cont.) - Summary of key studies on instrumented blocks: Main goal, instrumentations, and data output.

Authors	Goal	Instrumentation						Measurements	Observations
		Armour Unit	Material	Power	Storage	Sensors	Sampling frequency		
Caldera (2019)	Quantification of single layer armour unit rocking	Xblocs	3D printed (PLA)	External battery	External memory	Arduino-based sensor system	25-100 Hz	Impact velocity from gyroscope and accelerometer Number of collisions Amount of rotation	
Dost *et al.* (2020)	Monitoring the movement of small stones	Smartstone v2.0	Stone	External battery (One small button cells)	Internal memory	9-axis sensor (Bosch BMI160)	100 Hz	Sensor recordings (acceleration and rotation) Derived movement characteristics (double integration)	2D and 3D visualizations GUI interface
Hofland *et al.* (2023) Houtzager *et al.* (2024)	Quantification of single layer armour unit rocking	Xblocs	3D printed (PLA)	External battery	External memory (SD card)	9-axis IMU (ST LSM9DS1)	100 Hz	Number of rocking impacts Accelerations Rotational velocities Rotational angle	

2.2.3.1 Key insights and recommendations

Authors as Le (2016), Gronz *et al.* (2016), Maniatis (2021) and Hofland *et al.* (2023) have extensively examined the applicability, benefits, and challenges associated with using sensors such as accelerometers and IMUs in their research. As IMU technology and its applications continue to evolve rapidly, these studies have provided critical insights into the potential and limitations of these devices in experimental settings, leading to significant recommendations that will guide future research in this field.

The key ideas discussed by the aforementioned authors are presented below, organized into the following discussion topics: IMU applicability, laboratory experiments and measurement, and data processing. These insights provide a comprehensive overview of the challenges and considerations that researchers must address in this rapidly developing field.

Applicability

IMUs have emerged as a powerful tool in the instrumentation of armour unit blocks for hydraulic experimental tests, offering distinct advantages over traditional measurement methods. Unlike wired sensors, which can inadvertently constrain the very motions they are meant to measure, wireless IMUs eliminate inaccuracies caused by physical connections, providing a more accurate representation of the internal dynamics of armour units. This capability addresses a key limitation of previous studies that relied on wired sensors to measure internal deformation and movement characteristics.

IMUs outshine in providing continuous, detailed measurements in three dimensions, enabling researchers to explore the internal behaviours of individual armour units in ways that external observation methods - such as high-speed video or laser techniques - cannot. This capability is especially valuable for capturing the random and complex motions of armour units, such as rocking and rolling induced by wave action, which are notoriously difficult to model with numerical precision. The quantitative characterization of rotational failure processes through IMUs, based on changes in vectorial components of the gravity vector, goes beyond simple data plotting. It allows for the sampling of movement characteristics critical to understanding the stability and failure mechanisms of breakwater armour units.

Moreover, IMUs facilitate the full 3D reconstruction of multiple trajectories, enabling comparisons between different parts of a moving mass. This spatiotemporal reconstruction is essential for accurately describing the motion processes of armour units, offering insights into their collective behaviour under hydraulic forces.

However, the effective deployment of IMUs requires careful consideration of the technology's limitations and a deep understanding of the physics behind inertial measurements. The use of IMUs in hydraulic experiments is still evolving and often involves a "trial and error" approach. These sensors, originally developed for consumer electronics, operate within well-defined parameter spaces that may not fully capture the complexities of natural systems encountered in these studies. Researchers must be mindful of these limitations, understanding the accuracy, precision, and potential errors associated with inertial measurements to utilize the technology effectively.

Furthermore, it is crucial to report IMU data clearly and with sufficient detail to allow for repeatability and accurate error characterization. These measurements should be explicitly linked to the underlying physics of armour unit motion to ensure that the data meaningfully contributes to the broader understanding of these phenomena.

In conclusion, as sensor technology continues to advance, with improvements in accuracy and adaptability to complex natural systems, IMUs are likely to become increasingly integral to the study of concrete armour units.

Laboratory experiments and data measurement

The instrumented units have proven to be a valuable tool for studying the behaviour of armour layers under wave action. However, to further enhance their effectiveness and the quality of data collected, several improvements and considerations are recommended during the laboratory tests, namely (Dost *et al.*, 2020; Hofland *et al.*, 2023; Houtzager *et al.*, 2024; Le, 2016):

(i) Increasing the number of embedded units: to capture the full range of variability in rocking behaviour across individual armour units, it is advisable to embed at least 10 smart units within the armour layer during physical model tests. This larger sample size is essential because the variation in rocking between individual units is significant – rocking frequency and magnitude are influenced by the random position of the units, and the wave conditions. A more extensive dataset will allow for a more accurate and comprehensive analysis of the interactions between units and the overall performance of the armour layer;

(ii) Using 3D-printed units: The use of 3D printing technology for fabricating smart units presents several advantages, particularly in creating complex shapes in a cost-effective manner. This method allows for the practical design of units that can be easily opened and closed, facilitating the replacement of electronic components and wires during testing;

(iii) Scaling considerations for sensor applications: when adapting measurement methods to different experimental scales or velocities, it is essential to adjust the recording ranges and sampling frequencies accordingly. The Nyquist frequency, which helps avoid under sampling, varies with the rate of movement and the size of the measured object. As movement rates and unit sizes change, the sensor settings must be scaled to accurately capture the dynamics of different experimental conditions. This ensures that the sensor performance is optimized for varying experimental scenarios;

(iv) Evaluating and adjusting measurement frequency: Initial studies used much higher measurement frequencies, up to 50 kHz, with externally wired sensors to capture high-frequency impact-related data. However, this approach required extensive processing time, making it less practical for regular use. According to Hofland *et al.* (2023), a lower frequency of 100 Hz is adequate for capturing key velocities in dynamic processes like the rocking of armour units. This frequency is well-suited to detecting the larger impact peaks with sufficient resolution. Thus, while earlier methods employed extremely high frequencies, the current standard of 100 Hz provides a good balance between accuracy and processing efficiency, making it a more viable option for regular testing setups.

(v) Updating data storage mechanisms: continuous data capture is generally preferred over bursts when measuring dynamic events, as it ensures that no critical information is lost. In cases like monitoring the rocking behaviour of armour units, continuous sampling allows for uninterrupted recording of both upward and downward movements, providing a more accurate representation of the event. Despite the advantages of continuous measurement, hardware limitations - such as memory constraints or slower data writing speeds - often lead to the use of burst sampling. In this method, data is collected in short intervals and written to storage between bursts, reducing the risk of overwhelming the system's memory or processing capacity. While effective, this approach risks missing key moments during pauses between bursts, especially in fast or complex events like double-rocking. Upgrading to hardware that

supports continuous sampling at 100 Hz would enhance data accuracy, but burst sampling remains a practical alternative in resource-constrained environments;

(vi) Synchronization with wave data: For a more comprehensive analysis, it is essential to synchronize the data collected from the smart units with wave data. This synchronization would allow for a deeper understanding of how specific wave conditions influence the rocking behaviour of the units and the overall performance of the armour layer. Such an integrated approach would enhance the accuracy and relevance of the findings;

(vii) Realistic modelling of armour units' movement: the difference in orientation before and after movement gives information about the angle of movement and type of movement. When modelling the rocking movement of the units, it is important to use realistic angles of rotation. While a 90-degree rotation was used in some works for simplicity, such a large degree of movement is uncommon in a conventional breakwater layer, where surrounding armour units limit the rotation. A more realistic angle of rotation that reflects the actual conditions in a breakwater layer would provide a more accurate representation of unit behaviour;

(viii) Photographic documentation of armour layer changes: to complement the sensor data, it is recommended that photographs of the armour layer be taken during physical model tests. This visual documentation would provide valuable insights into the changes in the armour layer, such as settlement patterns and variations in packing density. This information could enhance our understanding of the relationship between rocking, packing density, and the overall stability of the armour layer.

Data processing

Processing data from IMUs is a complex task that requires careful consideration of various factors to ensure accurate results. The raw data provided by these sensors is subject to numerous challenges, such as noise, drift, integration errors, and the influence of gravity. To address these challenges, researchers need to apply advanced calibration techniques, use advanced algorithms, and ensure careful compensation for the inherent errors that arise from the measurement process.

A primary issue when working with accelerometer data is the influence of gravity. Accelerometers measure changes in acceleration, but they do not distinguish between forces caused by motion and those caused by the Earth's gravitational field. When stationary and aligned with gravity, one axis reads +1g. However, if the sensor rotates, all axes detect components of the gravitational field, complicating the interpretation of actual translational movements. Gravity compensation - removing the gravitational component from raw measurements - is essential for accurate translational acceleration and displacement calculations. Continuous orientation tracking of the IMU is also needed to apply proper gravity compensation, making this a crucial step in data processing. An estimate of the orientation of the IMU is also needed for estimating the direction of the applied forces.

Accurate orientation estimation is another significant challenge. Traditional methods, like using Euler angles, can experience issues like Gimbal Lock, which occurs when two of the three rotational axes align and result in a loss of one degree of freedom. This makes Euler angles unsuitable for tracking particles that rotate freely. Quaternions, while more complex, provide a robust alternative by avoiding these singularities and offering more reliable orientation tracking. To enhance the field, it is crucial to standardize the use of open-source quaternion libraries and provide training for their effective application.

However, even with orientation compensation and tracking, integration errors remain a persistent issue when estimating position from IMU data. Displacement is traditionally calculated by integrating acceleration data twice - first to obtain velocity, and then to derive position. Unfortunately, this process

is highly sensitive to sensor noise and drift, especially with low-cost consumer-grade IMUs. As a result, small measurement errors accumulate over time, leading to significant inaccuracies in position estimates. For practical purposes, reliable displacement tracking is usually limited to very short time periods, typically less than two seconds. Beyond that, the integration errors grow too large, making long-term tracking unreliable. Therefore, when reporting displacement and position values in research, it is critical to clarify the methods used and acknowledge the inherent limitations of IMU-based estimates over extended periods.

Another key issue is sensor calibration. For IMUs to provide accurate measurements, they must be carefully calibrated. Accelerometers and gyroscopes require frequent calibration to account for their individual biases and noise characteristics. While accelerometers tend to be stable over long periods, they are susceptible to external vibrations and forces, leading to noisy data. In contrast, gyroscopes are more reliable in the short term but suffer from drift over time due to bias accumulation. Calibration methods typically involve shaking tables, pendulum experiments, or simple moving tests to calibrate each axis separately. However, these methods have inherent limitations due to the interdependence of IMU errors across axes, which means that calibrating one axis does not entirely address errors present in the other axes. Moreover, the shape of the sensor's enclosure plays a critical role in calibration accuracy. Placing an IMU in different armour units' shapes, affects the calibration. Calibration is only reliable if the IMU is positioned exactly at the centre of mass, which is technically difficult, especially with irregular shapes. If the IMU is not precisely cantered, errors such as Coriolis and centrifugal forces arise, requiring recalibration. Additionally, when calculating movements like kinetic energy, the shape of the enclosure changes the moment of inertia, further complicating calibration and measurement.

To mitigate these various errors, researchers, as Gui *et al.* (2015), have increasingly turned to sensor fusion techniques. Sensor fusion combines data from multiple sources - typically accelerometers, gyroscopes, and magnetometers - to produce more accurate orientation and position estimates. By merging the strengths of each sensor, these algorithms reduce the impact of individual sensor limitations, such as accelerometer noise or gyroscope drift. Common sensor fusion methods include Kalman filters and complementary filters, which use statistical techniques to cross-validate sensor readings and adjust estimates based on measured variance. These methods have proven effective in electronics and robotics and are gradually being adapted for other applications where motion tracking is more complex. One of the most promising applications of sensor fusion is when integrating the full motion of an armour unit, such as for a unit tumbling down a slope. By combining acceleration and rotation data, researchers can track the movement of objects within a local reference system, without the need for external reference points or visual contact. Sensor fusion algorithms can quantify motion characteristics such as relative acceleration, velocity, and displacement, making it possible to study movement dynamics even in challenging conditions. However, these algorithms depend heavily on accurate initial conditions and assumptions, and proprietary software often obscures the parameters used in the calculations. As a result, there is a growing push for the adoption of open-source tools in the research community. Open-source solutions offer transparency and allow researchers to reproduce and validate each other's results, fostering collaboration and standardization.

In summary, processing IMU data requires a detailed understanding of the limitations and potential errors associated with the sensors. Using advanced techniques such as sensor fusion, quaternions for orientation tracking, and rigorous calibration procedures, many of these errors can be mitigated, though not eliminated. As IMU technology continues to evolve, these solutions will play a key role in enhancing the accuracy of measurements and advancing the understanding of complex, dynamic systems.

2.3 CONCLUSIONS

Rubble-mound breakwaters, which constitute over half of all breakwaters globally, are essential structures in coastal protection, safeguarding harbours and ports by dissipating wave energy. They also offer potential for multifunctional applications, such as integrating ocean energy harnessing technologies, contributing to the sustainability of ports. However, their armour layers remain particularly vulnerable to hydraulic instability, driven by wave-induced movements like rocking, displacement, and settlement. If unaddressed, these processes can result in progressive damage, exposing underlayers and ultimately jeopardizing the structural integrity of the breakwater.

The increasing impacts of climate change, including sea-level rise and intensifying storm events, along with the growth of coastal population and the exploitation of ocean resources, exacerbate vulnerabilities, highlighting the urgent need for resilient, adaptive, and innovative breakwater design. Traditional deterministic design methods, which often assess damage by counting displaced units, overlook secondary effects, such as unit collisions, hydrodynamic pressures, concrete fatigue, and non-linear responses, limiting their accuracy in predicting damage progression. To bridge this gap, probabilistic and risk-based frameworks have emerged as powerful tools. These approaches address the stochastic and dynamic nature of wave-structure interactions, reshaping how damage is assessed and offering insights into maintenance strategies and lifecycle costs. However, their broader adoption is hindered by the lack of standardized experimental protocols and high-resolution datasets, necessitating further advancements in measurement and modelling techniques.

Concrete armour units are an alternative to natural rock, particularly in regions where suitable natural materials are scarce, offering solutions with improved stability and adaptability. They also play a central role in physical modelling enabling researchers to integrate innovative technologies that deepen the understanding of wave-structure dynamics. Instrumented armour units equipped with sensors have transformed hydraulic research by offering detailed measurements of forces, pressures, and block motion. Significant progress has been made in monitoring critical parameters such as rocking velocities and wave-induced forces; however, challenges remain, particularly in tracking the full range of unit movements under complex wave conditions.

Among the most promising tools addressing these gaps are Inertial Measurement Units (IMUs), which deliver three-dimensional, continuous data capture. Despite their potential, IMUs face challenges such as noise, drift, and integration errors, which can obscure meaningful results, particularly for displacement tracking over longer durations. Advances in calibration and data processing techniques, such as gravity compensation, the use of quaternions for orientation tracking, and sensor fusion, are mitigating these issues and enhancing the accuracy and reliability of IMU data. Laboratory innovations, such as 3D-printed customizable units and synchronized wave force measurements, further enhance the application of IMU technology, enabling more realistic modelling of complex hydrodynamic scenarios.

These technological advancements are reshaping the study of breakwater dynamics by providing the high-resolution data needed to refine probabilistic models and enhance the predictive capabilities of numerical simulations. Future research should prioritize the continued refinement of IMU methodologies to extract meaningful and actionable data, and the integration of numerical and physical modelling approaches. By combining the strengths of these hybrid systems, researchers can develop adaptive, resilient, and cost-effective solutions for rubble-mound breakwaters. As environmental and technological pressures on coastal structures intensify, a multidisciplinary approach that balances technical innovation with economic, environmental, and societal considerations will be critical to ensuring the long-term reliability and functionality of these essential coastal structures.

3

ADVANCED NUMERICAL MODELLING OF RUBBLE-MOUND BREAKWATERS USING SPH

3.1 INTRODUCTION

Complex systems, like nature, can be modelled by finding the analytical solutions for the equations that define the system (or mathematical model). Its behaviour can be predicted by calibrating some parameters and imposing a set of initial conditions. In numerical modelling, these equations are solved numerically rather than analytically. Through algorithms it is possible to simulate complex real-world processes and predict their evolution (Domínguez, 2014).

As mentioned in the previous chapter, when it comes to designing coastal structures - such as breakwaters - empirical and semi-empirical methods are typically used, where parameters are derived from physical models. This means that the formulas used have a limited validity range, restricted by the values that have been tested. Besides, to better respond to the maritime environmental actions, increasingly complex geometries have emerged. The empirical, semi-empirical, or analytical solutions are not valid to describe these kinds of geometries. Most of the time, it is necessary to resort to physical or numerical models to solve maritime engineering real problems (Altomare *et al.*, 2014; Didier and Neves, 2010).

In the last few decades, with computational development, numerical modelling is becoming more and more relevant. A branch of fluid mechanics called Computational Fluid Dynamics (CFD) appeared, which studies fluid behaviour using numerical modelling. The computer's capability of executing millions of mathematical operations per second allows the simulation of complex systems and realistic problems. When comparing the cost in time, resources, and money, numerical modelling presents some advantages over physical experiments. Also, this technique provides data that can be difficult, or even impossible, to measure in a physical model. Despite the accuracy of the numerical schemes, these cannot replace the construction of scale models, mainly in coastal structures cases, whose results are verified based on physical models and prototypes. However, numerical models can lead to significant savings by extensively reducing the number of physical tests, which require time, good infrastructure, financial resources, and researchers' experience (Didier and Neves, 2010; Domínguez, 2014).

In conclusion, in most cases, numerical modelling is an excellent complement to physical modelling. According to Didier and Neves (2010), one of these situations corresponds, as mentioned above, to the concrete case of the interaction between waves and coastal structures, for which, over the last decades, numerical models have been developed, with different degrees of complexity, following the evolution of numerical methods. These numerical models, which include free surface modelling, allow the accurate description of the physics involved in the process and the prediction of the essential

characteristics of the flow. Therefore, for the fluid motion description, there are two possible numerical approaches:

- Eulerian approach: solves the equations at the fixed nodes of a mesh. The velocity and pressure fields are represented as a function of position and time;
- Lagrangian approach: it is a meshless approach (does not use a fixed or dynamic grid). The positions where equations are solved move with the fluid. By following individual fluid particles through time, the trajectory, velocity, and pressure fields are obtained as a function of the initial position and time.

The mesh-based methods, which include: the Finite Volume Method (FVM), Finite Differences Method (FDM), Finite Element Method (FEM) and Boundary Element Method (BEM), have dominated the field of computational fluid dynamics. They are robust, well-developed, and their application to a wide range of ocean and coastal engineering problems produces usually a very accurate answer. For instance, FVM, FDM, FEM, and BEM accurately solved Fully Non-linear Potential Flow (FNPT) problems (Luo *et al.*, 2021). Mesh-based methods are very mature, both mathematically and algorithmically.

Despite the great successes achieved in the last decades, Eulerian methods also present limitations, especially when problems involve complex topological changes and highly non-linear deformed moving interfaces (Altomare *et al.*, 2014). Mesh-based methods proved to be adequate for confined computational domains and computations where the boundaries are not moving. In cases where the fluid surface deformation is large, the mesh generation process can be time-consuming. Besides, the Eulerian models usually need to be combined with the explicit surface capturing technology (Altomare *et al.*, 2014; Wen *et al.*, 2018).

Another category of numerical methods, *i.e.*, the Lagrangian Particle methods, has some distinct advantages compared to Eulerian methods, making it very attractive for the ocean and coastal engineering community. First, particle-based discretization, meshless, makes particle methods naturally capable of modelling large surface deformations (*e.g.*, fluid merging and splitting) because the connectivity between nodes is changing and being calculated at run-time. These methods allow dealing effortlessly with complex geometrical boundaries of the coastal structures. They are suitable for highly non-linear, multi-phase interaction problems, such as wave structure and wave-sediment interactions. They are also superior to Eulerian methods in modelling advection-dominated flows (*e.g.*, violent surface flows) due to their Lagrangian feature and the absence of the advection terms in the governing equations. These methods are convenient for situations where mesh-based methods application is not possible (Luo *et al.*, 2021; Wen *et al.*, 2018).

There are a lot of meshless methods, such as the Particle Finite Element Method (PFEM), Diffuse Element Method (DEM), Moving Particle Semi-Implicit (MPS), Free Mesh Method, or the Smoothed Particle Hydrodynamics (SPH). The last one is possibly the most popular and mature meshless method, being an important computational tool for scientific research and engineering design. It proved to be a suitable method for practical applications in coastal engineering (Gotoh and Khayyer, 2018).

3.2 SMOOTHED PARTICLE HYDRODYNAMICS (SPH) FOR COASTAL APPLICATIONS

Smooth Particle Hydrodynamics (SPH) is a meshless Lagrangian particle method, where the particles move according to the governing dynamics. Primarily developed for solving astrophysical problems during the '70s (Gingold and Monaghan, 1977), SPH has evolved, over the past two decades, into a versatile numerical tool capable of solving a wide range of problems in areas from solid mechanics to

the mechanic of fluids (Puri and Ramachandran, 2014). The significant development of this method resulted from continuous theoretical contributions (Gomez-Gesteira *et al.*, 2010a; Liu and Liu, 2003; Monaghan, 1992; 2005; Violeau, 2012), combined with computational improvements, specially affordable high-performance computing hardware. SPH is, nowadays, applicable to multiple problems in the Computational Fluid Dynamics (CFD) field (see subsection 3.2.1). According to Violeau and Rogers (2016), some SPH codes have become an inherent part of the numerical arsenal of industrial research and development laboratories and academic institution. Despite this, SPH is still a young numerical method, presenting some drawbacks compared to classical Eulerian mesh-based methods. In subsection 3.2.2 the principal advantages and problems of SPH are discussed. The SPH rEsearch and engineeRing International Community (SPHERIC), founded in 2005, join researchers and industrial users worldwide to push the development of the SPH method. They discuss new and current concepts, define benchmark test cases, and identify SPH needs and gaps of understanding. So, this organization's final purpose is to highlight and solve some of the SPH key challenges called the SPHERIC Grand Challenges (see subsection 3.2.3) by exchanging information between researchers, developers, and users (Vacondio *et al.*, 2021). The last subsection (3.2.3) presents also a vision and perspectives of the SPH development in the upcoming future.

3.2.1 APPLICATIONS OF SPH TO COASTAL DEFENCES

In the computational fluid dynamics field, SPH is particularly suitable to describe complex physical processes, such as those found in coastal and ocean engineering problems. In 1994, Monaghan made the first attempt of modelling free-surface flows using SPH. The Lagrangian nature of the SPH allows the domain to be multi-connected without needing special surface treatment. Since the particles are in motion and interacting with each other, the free - surface is determined by the particle's position. By its positions, it is possible to know where there is fluid and where there is not. Thus, the modern SPH numerical schemes are ideal for the simulation of free-surface flows and complex phenomena of free-surface deformations, which include gravity currents, wave generation and propagation (*e.g.*, long waves, short waves, regular and irregular waves, solitary waves), the arrival of waves on a beach, dam failure, fluid-structure interaction, violent hydrodynamics phenomenon of waves impacting offshore and coastal structures, such as breakwaters. This last point includes studies about the applicability of SPH to model wave breaking, wave overtopping, wave run-up, wave impact, among others.

3.2.2 ADVANTAGES AND DRAWBACKS OF SPH

The SPH method has several advantages, derived from the fact that it is a Lagrangian and meshless method. Some of its remarkable benefits worth to be underlining:

- SPH method possesses the extraordinary capability to simulate a large variety of complex flows, involving a large spectrum of physical processes, such as highly non-linear, inertia-dominated flows, multi-fluid and multi-physics flows, fluid/structure interactions, etc.,
- There is no need for special treatment to detect complex topological changes in the free surface, such as the Volume of Fluid (VoF) method, commonly applied in mesh-based models. The free-surface particles indicate the shape of the free surface easily and naturally. SPH presents several advantages for situations where VoF and other surface tracking methods struggle or fail;
- SPH can easily include complex additional physics. This arises partially from the flexibility of the continuum modelling, partially from the fact that each element of fluid or solid has a specific

identity that stays with the material over time. There is no need for particular variables to detect different phases in the space since each particle holds material properties of its phase;
- SPH allows straightforward modelling of moving complex boundaries and interfaces, eliminating the need to create complex volume meshes. It is particularly relevant for large scale transient free-surface flows, where the space volume that needs to be meshed would be significantly larger than the volume of the fluid of interest; and
- SPH codes are conceptually simpler due to their Lagrangian nature. Besides, they should be faster than Eulerian codes since no computational effort is necessary for dealing with convective terms.

Despite all the success of the SPH method in a wide variety of problems involving free surface flows, this method also possesses some drawbacks, which still hinder its use in industrial applications, such as (Altomare *et al.*, 2014; Le Touzé *et al.*, 2016; Violeau and Rogers, 2016):

- Its expensive computational cost compared with other mesh-based methods for CFD problems, especially when considering 3D simulations. This is partially alleviated by means of hardware acceleration, being the graphics processing unit cards a cheap and accessible option,
- Difficulties in prescribing wall boundary conditions and even extensive problems at open (inflow/outflow) boundaries,
- Lack of consistent theory in relation to the mathematical foundations of the method (*e.g.*, convergence, stability),
- Inaccuracy of pressures prediction, at least for the original WCSPH variant,
- Difficulties in dealing with variable space resolution for (nearly) incompressible flows.

3.2.3 Main challenges, future developments, and perspectives for SPH

Despite being considered a method with the potentiality to evolve, SPH still suffers from a lack of broad recognition from the scientific community as a serious candidate to become an indispensable numerical tool in the future. Most of the insecurity put on the method derives from his immaturity and disadvantages compared to other methods. Many questions about the theoretical ground of this method and its unknown properties remain unanswered. Convergence, numerical stability, boundary conditions, kernel properties, time marching, existence and properties of solutions make a shortlist of SPH key issues. Despite the continuous improvements and modifications of the SPH method, it remains a lot of work to do.

The SPHERIC community is carrying out systematic research to overcome SPH's drawbacks. Since 2005, it started building a working group on SPH numerical development, named the SPHERIC Grand Challenge Working Group (GCWG), which identified the SPH grand challenges to be addressed in the following years to conduct the method to a mature stage. The SPHERIC SPH Grand Challenges are grouped into five categories (Vacondio *et al.*, 2021):

(i) Convergence, consistency and stability: In the SPH method, a significant lack of understanding and formalism remains concerning the notions of these three properties remains. Lax Equivalence theorem proves that convergence, consistency, and stability are interlinked, stating that for consistent finite difference schemes considering well-posed linear problems, the method is stable if and only if it is convergent. Several different scheme's categories exist to achieve more accurate solutions to the equations in the particle method's context. An example of these numerical treatments is the particle regularization schemes applied to improve stability and convergence since these properties are critically dependent on particles distribution. One robust and well-known particle regularizing scheme is the Particle Shifting scheme, frequently used in free-

surface flows. Considering weakly compressible SPH (WCSPH), one can also achieve higher levels of accuracy and stability through the incorporation in the formulation of artificial viscosity, δ-SPH, Riemann solvers, and higher-order accurate SPH.

Regarding convergence, it is still one of the challenging aspects of the particle method. Consistency and convergence are closely linked. When looking for irregular distributions of particles as often found in Lagrangian particles, one may construct consistent formulations. This can be costly, and convergence is not necessarily ideal. So, a goal of this grand challenge remains in improving the mathematical formalism around error quantification, convergence rates, and stability.

(ii) Boundary conditions: Initial conditions (ICs) and boundary conditions (BCs) are necessary to close the fluid dynamics equations. The last ones include solid boundaries, free-surface, inlet/outlet, stress conditions in structural mechanics, those related to the coupling with other models, etc. Considering free-surface flows, BCs are probably the cause of all problems. Due to the meshless nature of the SPH method, imposing boundary conditions is not trivial. Researchers use diverse techniques to incorporate ICs and BCs in SPH. According to Vacondio *et al.* (2021), there still are some clear challenges progressing, namely: identifying and validating BCs that are robust for arbitrarily complex non-orthogonal geometries for the vast range of SPH applications; extending the behaviour of SPH BCs to possess higher-order convergence properties; maintaining the intrinsic conservation properties of SPH while retaining the consistency of operators.

(iii) Adaptivity: Efficient simulations are the key to engineering problems. The advancement of adaptive multi-resolution schemes leads to significant improvements in computational efficiency. These numerical schemes can use a domain discretisation based on different size elements (computational nodes that move with the fluid velocity, in Lagrangian meshless-based numerical methods). This feature allows increasing the number of computational particles only in the portions of the domain where the flow features require higher resolutions. Thus, it is possible to dramatically reduce the total number of computational nodes used to discretise a domain and consequently the computational cost for the simulation. Several algorithms to dynamically adjust the mesh resolution have been implemented with success in mesh-based methods. Despite the necessity to introduce a variable resolution in SPH numerical schemes for fluids to simulate all inherently multi-scale engineering problems, almost all SPH codes are based on uniform resolution. From computational aspects, development of adaptative codes that can take in different computational resolutions and thus can reliably model different physical scales would be of crucial importance. Some authors have already studied this subject, such as Vacondio *et al.* (2013) and Vacondio *et al.* (2016). However, in future, substantial developments for particle-based multi-resolution schemes are expected. It needs to improve both in terms of efficiency and performance. Application of the advanced versions of multi-scale schemes will be accompanied by rigorous considerations regarding conservation of volume, momentum, and energy.

(iv) Coupling to other models: Due to its meshless formalism, the SPH method can naturally resolve multi-mechanism problems and include different physical models. As with other Lagrangian meshless methods, SPH is very accurate and efficient when dealing with moving boundaries and complex interfaces, which, on the other hand, are usually addressed with difficulties by conventional numerical methods (*e.g.*, FVM, FEM). However, for problems where the latter ones are currently used and well established, SPH is generally less effective. For the same level of attained accuracy, results are more costly. So, in several contexts, it can be much more effective to couple an SPH solver with another numerical solver, enhancing the capabilities of both methods within their specific application fields. The hybrid models resulting from the coupling of particle methods with other computational frameworks will take advantage of eminent privileges included

in different frameworks, complementing each other shortcomings, and allowing them to address a wide range of problems. Coupling SPH models with other numerical solvers is a perspicuous effective strategy to expand the intrinsic capabilities of SPH-based models to solve complex physics and hydrodynamics while reducing the computational cost related to the meshfree nature of the method. Despite the clear advantages and all the good results achieved so far, coupling algorithms are of complex implementation and generalisation due to the different nature of the coupled models. There is no general methodology for merging the frameworks, mainly because coupling depends on the boundary conditions, which are still an open problem. The treatment of interfaces and accurate implementation of boundary conditions at the phase or/and computational interfaces are the most relevant issue for coupling particle-based methods and other computational frameworks. But the coupling algorithm and the related implementation complexity can also vary depending on the following aspects: one-way or two-way coupling; heterogeneity of the modelled physics; Lagrangian or Eulerian approach adopted in the method coupled to SPH; discrete coupling interfaces between solvers; time stepping and stability of the coupled algorithm; and preservation of conservative quantities by the coupling. Besides the variation in formulation, there is an added difficulty of integrating methodologies that are designed or have been extensively optimized for distinct hardware acceleration and coding structures. The impressive gains in efficiency and first encouraging results counterbalance the difficulties and complexities related to the coupling of very different solvers and justify the increasing use of coupling algorithms for practical applications and real engineering problems. However, one should validate the coupled methods through more challenging situations.

(v) Applicability to industry: The industrial world changed its perspective regarding the SPH method only recently, starting to accept it as a valuable's CFD method.

The scientific progress on Grand Challenges 1 and 2 has convinced engineers of the ability of the SPH method to solve some industrial applications with highly distorted complex interfaces, free surfaces, and dynamic flows.

Nevertheless, industrial engineering applications are arduous and will remain like this for a long time. Some topics of concern for industrialists still need to be solved. One of them is the reduction of the elapsed time of the simulation. The progress in High-Performance Computing (HPC) in accelerating SPH software on different architectures (CPUs or GPUs) enables SPH to be competitive with conventional mesh-based methods. SPH is inherently more expensive than classical mesh-based methods due to the enormous number of neighbours for a given computational point and the need for a minor computational step because of the weakly compressible explicit formulation. Work has been done to increase the order of convergence of SPH schemes for a given number of neighbours. However, this causes extra calculations. Besides, the gain in terms of accuracy is not demonstrated yet for industrial applications. The semi-implicit incompressible SPH (ISPH) scheme's development leads to gains in the time step. Its GPU implementation will probably reinforce its efficacy. However, one should not pursue that progress in HPC to the detriment of the accuracy of the numerical scheme. The temptation of introducing simplifications in the adopted numerical scheme to increase efficiency should not supplant the interest in accuracy's hard-won gains.

If the SPH method is unable to progress on the HPC objectives, it should only be used in portions of the domain characterised by strong dynamics and complex interfaces. The complete simulation can be obtained by effective coupling of SPH with other numerical methods.

In summary, the method must keep progressing to maximise opportunities to extend its field of application, considering complex physical phenomena, such as turbulence, surface tension, and phase change, plus staying competitive with other methods.

Beyond the five grand challenges previously introduced, there are other fields where further research in SPH is needed, for example, fields such as:

(i) Turbulence modelling: it is a challenging topic in its own, and it is yet to receive a comprehensive investigation. In the early applications of SPH to free-surface flows, turbulence was normally ignored since SPH proved particularly appropriate for representing violent flows, where inertia, pressure and gravity play a crucial role. However, turbulence started to be addressed in SPH when it was also applied to confined flows. According to Violeau and Rogers (2016), despite the efforts made over the past ten years, advanced turbulence models for SPH are still poorly developed, requiring huge computation time even with GPUs;

(ii) Multiphase flows: in diverse problems associated with coastal/ocean engineering, the flow is characterized by distinct physical phases. Applications involving multiple phases can be extraordinarily complex, and to date, only simple cases or applications have been simulated in SPH. More specifically, numerical simulation of liquid-gas multi-phase flows is among the most challenging topics for coastal engineers. The complexities involved in the multi-phase problems mainly arise from the abrupt density variation at the phase interface. It would lead to a mathematical discontinuity of density and, consequently, a discontinuous pressures gradient field. Developing robust adaptivity schemes for multi-phase flows whose properties can evolve represents a formidable challenge.

In the end, weighing the method's advantages, disadvantages and challenges, the following questions arise:

- Is the SPH formulation the most suitable method for simulations involving the complex physics present in coastal engineering problems?
- What are the following steps in the SPH future?
- What are the SPH's long-term aims?
- How can one contribute to the development and validation of the model?

According to Violeau and Rogers (2016) long-term vision, SPH should become part of the overall CFD landscape for hydraulic, water, energy, and environmental companies and governmental agencies, used appropriately and with experience-based insight. In order to achieve this goal, there are significant developments to undertake before the method use becomes widespread. One should apply the principal efforts in addressing the issues that prevent the industry from investing in and using the method. First, the community of researchers, developers, and engineers should eliminate poorly validated codes and formulations that are not generalizable. It means that the SPH community needs to:

- keep the developed numerical methods free of any numerical term with constants that require calibrations;
- focus on optimized simulations with minimized uniform error distributions;
- integrate well-validated SPH codes into the design methodologies of, for example, breakwaters; and,
- identify new applications of SPH, which help push the development of the method forward by identifying SPH's shortcomings and highlighting new opportunities for its development. These last two points imply a dialogue with industrial companies to identify their needs simultaneously, as preparing potential users of tomorrow to use the new technology properly, identifying the possibilities and limitations of the method.

To accomplish the developments listed above, it is also crucial to define standards of acceptability for future research and publications, which contribute to the future credibility of the methodology. Violeau

and Rogers (2016) proposed that, before any practical application, rigorous validation of particle-based codes must be conducted by considering appropriate benchmark tests with exact analytical solutions or semi-analytical solutions or converged reference numerical solutions from validated numerical codes. Experimental or field data with high degrees of repeatability and estimations of variability should supplement the analytical benchmarks. Where a reference solution exists, comprehensive numerical investigations on conservation and convergence properties need to be conducted to estimate error norms, preferably using a consistent error's measure, such as the grid convergence indicator (GCI). The SPH research community should also report, in its papers, plots of all relevant flow fields which highlight problematic issues. The Violeau and Rogers (2016) vision to drive the development of SPH, specifically for free-surface flows, is summarized in Fig.17.

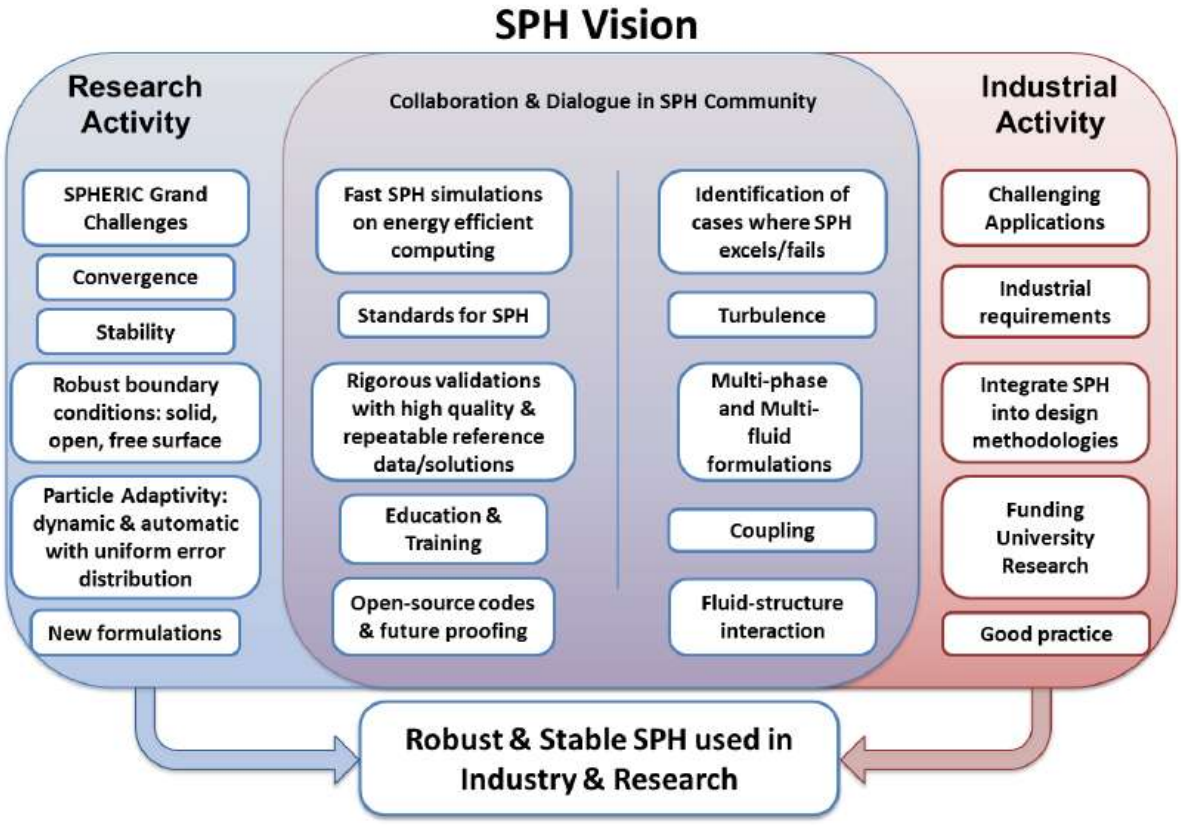

Fig.17 – SPH vision for free-surface flow (Violeau and Rogers, 2016).

3.3 SPH SOLVER DUALSPHYSICS – STATE-OF-THE-ART

3.3.1 INTRODUCTION

SPHysics is a numerical SPH model developed to study free-surface problems, such as those presented in the design of coastal structures like breakwaters. It is a code written in Fortran90 with numerous options (different kernels, several boundary conditions, etc.). Since its first release in 2007, it has demonstrated high accuracy in several validations with experimental results. However, it proved to be too slow when applied to large domains. As referred previously, SPH has traditionally been an expensive computational method, mainly because of two factors: the high number of interactions with neighbouring particles for each particle, both in 2-D and 3-D simulations, and the use of explicit time

integrators in WCSPH (Weakly Compressible Smoothed Particle Dynamics), which leads to the use of a very small time step (Violeau and Rogers, 2016). So, the high computational cost of the model showed to be a real obstacle to the extensions of the code to an industrial scale since the simulation of real engineering problems requires a high resolution which implies simulating millions of particles. Even small validation cases in 3D may take days or even weeks on sequential SPH codes.

So, to overcome these limitations, it was necessary to increase the velocity of the code by applying high-performance computing (HPC) techniques. The classic options of hardware acceleration for CFD calculations include the distribution of the workload among different Central Processing Unit (CPU) cores (OpenMP) or/and the combination of multiple machines' power connected via a network (MPI). Another option corresponds to Graphic Processing Units' (GPU) use since the graphic cards are powerful parallel processors designed for graphics rendering, providing the necessary computing power at low cost and without expensive structures.

Thus, in 2009, the first version of the DualSPHysics code was born. Like SPHysics, its precursor, it is an open-source SPH code for simulating free-surface flows and results of an optimised implementation using C++ and CUDA language, capable of using the parallel processing power of either CPUs or/and GPUs, respectively. This set of C++, CUDA and Java codes makes possible the study of real-life engineering problems without requiring expensive and massive HPC resources. Despite being necessary to implement and maintain two different architectures, it allows a fair and realistic comparison between CPU and GPU, making it easier to detect errors and understand the code. This project resulted from the collaboration of different institutions from Spain (University of Vigo), United Kingdom (University of Manchester), Portugal (Instituto Superior Técnico, University of Lisbon), Belgium (University of Ghent), Italy (University of Parma) and the United States (New Jersey Institute of Technology).

The DualSPHysics team is trying to create a state-of-art SPH software to fulfil several objectives, two of which correspond to the software's usefulness for engineers, industry and fundamental research and to turn it easy to use for applications with different physics.

The following subsections will detail the SPH formulation that supports DualSPHysics code (3.3.2), its more recent functionalities regarding coastal engineering applications (3.3.3), the code structure, implementation and performance (3.3.4), and the most recent works using this code to simulate coastal engineering problems (3.3.5).

3.3.2 SPH FORMULATION

The DualSPHysics relies on the SPH technique, a Lagrangian meshless method. In the SPH, the continuum (fluid) is discretised using a set of material points, referred to as particles, carrying concrete entities, *e.g.*, mass (m), velocity (v), and position (r). These particles evolve according to the Navier-Stokes equations, which are write in terms of fluxes between particles. In other words, at each time step, new physical quantities of any particle can be obtained by local interpolation (summation) of the relevant properties of all particles that lie within the range of the weighting function (kernel). The contribution of those neighbouring particles depends on the distance between the particles (Violeau, 2012).

The main features of the classical SPH formulation (3.3.2.1, 3.3.2.2) and some numerical aspects of SPH dynamic fluid flows, namely density smoothing techniques (3.3.2.3), boundary conditions (3.3.2.6), and numerical stability (3.3.2.7, 3.3.2.4), will be addressed in the following chapter.

3.3.2.1 SPH interpolations and kernel functions

SPH describes a fluid by replacing its continuum properties with locally (smoothed) quantities at discrete Lagrangian locations. This method formulation starts with the integral representation of a field function using a Dirac delta function $\delta(\boldsymbol{r}-\boldsymbol{r}')$. Let f be an arbitrary scalar field defined on the computational domain, Ω, the value of the scalar field $f(r)$ at position $\boldsymbol{r}$ is given by:

$$f(r) = \int_{\Omega} \delta(r - r') f(r') dr' \tag{43}$$

However, one cannot use the Dirac delta function in the computations since it is infinitesimally narrow, meaning that the interpolation region, Ω, would not overlap with other particles/nodal interpolation points. It lacks some "normal" properties of a well-behaved function, such as continuity and differentiability (Li and Liu, 2007). Hence, for practical reasons, the interpolation procedure within SPH approximates the delta function with its weighting function called the smoothing kernel, *W*,

$$\langle f(r) \rangle = \int_{\Omega} W(r - r', h) f(r') dr' \tag{44}$$

Where $\langle f(r) \rangle$ is the integral SPH averaged quantity, $(\boldsymbol{r}-\boldsymbol{r}')$ is the interpolation distance, and h is the smoothing length, which defines the area of influence of the kernel. In other words, h controls the size of the area around a given particle where neighbouring particles are considered. It is a prime parameter in the SPH method: if h is too small, there may be not enough particles in the support domain to exert forces on a given particle, which results in low accuracy; on the other hand, if h is too large, all details of the particle, or local properties, may be smoothed out, also compromising accuracy. In DualSPHysics the smoothing length is defined as function of dp, being dp the initial interparticle distance.

When using the smoothing function, *W*, instead of the Dirac delta function, the integral representation can only be an approximation rather than an exact one (Năstăsescu and Gavrilă, 2012). In the numerical method SPH, one must approximate the integral interpolation procedure. Since the entire system is not continuous but represented by a finite number of particles, one needs to convert the function in equation (44) into a discrete form based on particles. The approximation function is interpolated at particle (a), and the summation is performed over all particles within the region of compact support of the kernel (Fig.18):

$$\langle f(r_a) \rangle \approx \sum_{b=1}^{N} f(r_b)\, W(r_a - r_b, h) \frac{m_b}{\rho_b} \tag{45}$$

where $W(r_a - r_b, h)$ represents the smoothing kernel and N corresponds to the number of neighbouring particles. The volume associated with the neighbouring particle (b) is m_b/ρ_b and m and ρ are the mass and density, respectively.

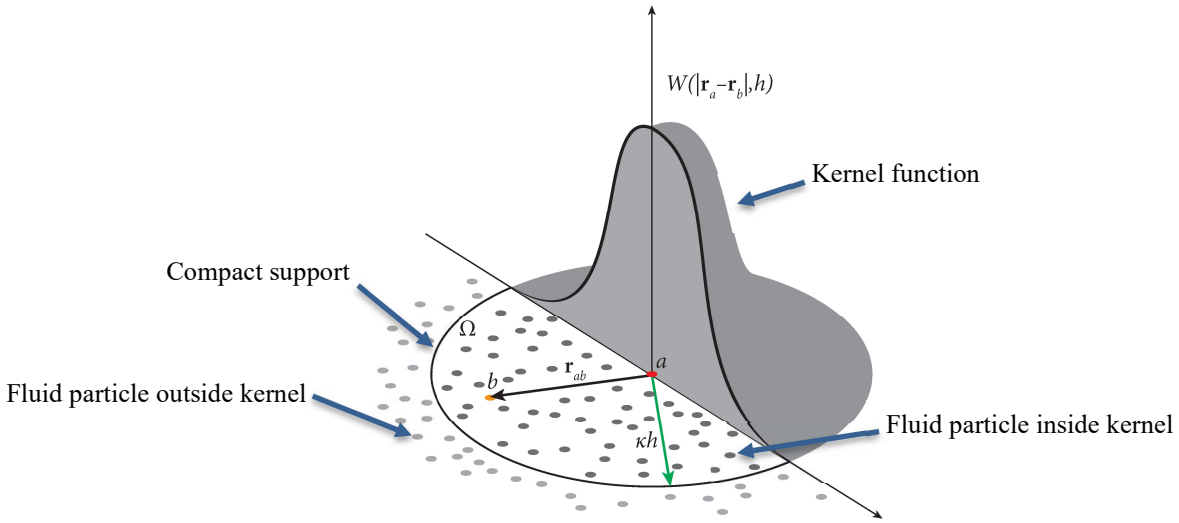

Fig.18 – Smoothing kernel function. The radius of influence of the kernel is expressed as a multiple, k, of the smoothing length, h.

The performance of a SPH model depends heavily on the choice of the kernel function. The smoothing function W must satisfy several properties such as (Liu and Liu, 2006):

- **Normalization condition**, which means the smoothing function must be normalized over its support:

$$\int_{\Omega} W(r-r',h)dr' = 1 \tag{46}$$

- **Compact support property**, which means the kernel function must be compactly supported:

$$W(r-r',h)dr = 0 \text{ when } |r-r'| > kh \tag{47}$$

where k is usually a scalar factor which determines the area of the compact support domain.

- The smoothing function has to be **positive** for any point at r' within the support domain:

$$W(r-r',h)dr \geq 0 \tag{48}$$

- The smoothing function value has to be **monotonically decreasing** with the increase of the distance away from the particle.
- **Delta function property**, which means that the kernel function value should tend to the Dirac delta function as the smoothing length tends to zero:

$$\lim_{h\to 0} W(r-r',h) = \delta(r-r') \tag{49}$$

- The smoothing function value has to be an **even** function (symmetric)

$$W_h(r - r') = W_h(r' - r) \tag{50}$$

- The smoothing function value has to be sufficiently **smooth** (smoothness).

In the literature, a range of smoothing kernels have been proposed, which are summarized in Dehnen and Aly (2012) work. Within DualSPHysics, the user can choose from Cubic Spline (Monaghan and Lattanzio, 1985) or the fifth order Wendland function or Quintic (Wendland, 1995).

3.3.2.2 Governing equations

The governing equations to model fluid dynamics are the Navier-Stokes equations, which consist of the following equation set, representing three fundamental physical laws of conservation:

(i) The momentum equation (see equation (51)),
(ii) The conservation of mass or continuity equation (see equation (52))
(iii) The energy equation.

In the classical SPH formulation, the fluid can be considered slightly compressible using an artificial equation of state, or incompressible formulations solving a pressure Poisson equation as considered by Shao and Lo (2003), Gotoh *et al.* (2004), Shao (2005) and Lee *et al.* (2008) (Gomez-Gesteira *et al.*, 2010b). The following subsections will describe the Weakly Compressible SPH (WCSPH) version, which is the most used approach for modelling water flows in SPH. It is much easier to implement and parallelize. The conservation laws of continuum fluid dynamics, in the form of differential equations, are transformed into particle forms using the kernel functions.

Being a the particle where the physical quantities are being calculated and b the neighbouring particles, the system of Navier-Stokes equations (momentum and continuity equations) can be written in the discrete SPH formalism as:

$$\frac{\mathrm{d}\boldsymbol{v}_a}{\mathrm{d}t} = -\sum_b m_b \left(\frac{p_b + p_a}{\rho_b \cdot \rho_a}\right) \nabla_a W_{ab} + \boldsymbol{g} + \boldsymbol{\Gamma} \tag{51}$$

$$\frac{\mathrm{d}\rho_a}{\mathrm{d}t} = \sum_b m_b \boldsymbol{v}_{ab} \nabla_a W_{ab} \tag{52}$$

where W_{ab} is the kernel function, v is the velocity, p is the pressure, ρ is the density, m is the mass, g is the gravitational acceleration, and Γ refers to a dissipative term and must be added explicitly in the momentum equation to smear out the unphysical oscillations or fluctuations that appear if no viscous term is included in the governing equation. Besides it helps to keep the numerical solution stable. One can find more information about viscosity and turbulence in subsection 3.3.2.5.

Throughout a WCSPH simulation, the mass of each particle remains constant, and only their associated density, computed by solving equation (52), fluctuates. The density approximation is very important in the SPH method because it determines the particles' distribution and the smoothing length evolution.

More information about the different approaches to evolving density in the SPH method are presented in subsection 3.3.2.3.

In the WCSPH approach, pressure relates to the fluid density explicitly through a stiff equation of state (Luo *et al.*, 2021). Following Monaghan and Kos (1999) and Batchelor (1974), this relationship follows the expression:

$$P = \frac{c_0^2 \rho_0}{\gamma}\left[\left(\frac{\rho}{\rho_0}\right)^{\gamma} - 1\right] \tag{53}$$

where $\gamma = 7$ is the polytropic constant, with $\rho_0 = 1000\ kg/m^3$ being the reference density of the fluid and $c_0 = c(\rho_0) = \sqrt{(\partial P/\partial \rho)}\big|_{\rho_0}$, which is the speed of sound at the reference density (Worster *et al.*, 2000). Remember that real nearly incompressible fluids such as water are characterized by very high speed of sounds of the order of $10^3\ m/s$. In practice, a numerical speed of sound, c_0, is chosen based on a typical length scale and timescale of the domain. Its value is lowered, allowing to maintain the time step size at reasonable values since the time step is calculated by a Courant condition, based on the current speed of sound for all particles. Typically, this adjustment restricts the speed of sound to be at least ten times faster than the maximum fluid particle velocity and keeps density variations less than 1%. It keeps the system weakly compressible, not introducing major deviation from an incompressible approach. However, small variations in density can lead to large pressure fluctuation. So, the results of the WCSPH can induce a noisy pressure field and spurious oscillation of pressure (Monaghan, 1994).

3.3.2.3 Density correction in WCSPH

The Weakly Compressible SPH (WCSPH) scheme was proposed to simulate incompressible flows by treating the fluid as weakly compressible and using a stiff equation of state. The greatest advantage of this method is its simplicity in terms of programming, implementation, and parallelization, making it ideal for simulating fluid flows with a free surface. However, there are also some drawbacks. One significant difficulty with the WCSPH schemes is being affected by a high-frequency spurious noise on the pressure and density fields. The non-physical pressure fluctuations result from various sources including (Moreira, 2021; Violeau and Rogers, 2016):

- A **stiff equation of state**: in equation (53) the pressure is a function of a high power of the density. So, in this case, very small density variations yield enormous pressure variations. In addition, small errors in the density may be amplified by the speed of sound, c_0, squared. Thus, the numerical speed of sound in WCSPH is artificially lowered, generally set to 10 times the maximum velocity in the flow, so that density fluctuations remain less than 1%,
- Inaccuracies in the SPH **interpolation procedure** itself, and,
- The **collocated** (in velocity and density), **centred** and **explicit** (time integration) nature of the WCSPH numerical scheme.

Several techniques have been proposed to circumvent this problem. They can be classified into three different groups:

(i) The schemes that adopt **density filters**, which correspond to re-initialise the density for each particle at every N time steps using either the zeroth-order (Shepard Filter) or a first-order moving least squares (MLS) correction.

$$\rho_a^{new} = \sum_b \rho_b \widetilde{w}_{ab} \frac{m_b}{\rho_b} \tag{54}$$

where $\widetilde{w}_{ab}$ is a corrected kernel. A simple density filter cleans up the results and proved to be sufficient for most applications (Colagrossi and Landrini, 2003; Dilts, 1999). On the other hand, this posterior numerical treatment does not address the fundamental causes of the problem. It leads to an increase in the computational costs, and, in long time simulations, the use of the filtering procedure may lead to the disruption of the hydrostatic pressure component and an inconsistency between the global volume of the fluid and the density field (Vacondio, 2021).

(ii) The models that add **density diffusive terms** (DDT) in the continuity equation. With this technique equation (52) now reads:

$$\frac{\mathrm{d}\rho_a}{\mathrm{d}t} = \sum_b m_b \boldsymbol{v}_{ab} \nabla_a W_{ab} + hc_0 D_a \tag{55}$$

where the term D_a takes the general form of (Domínguez *et al.*, 2022; Vacondio, 2020):

$$D_a = \delta \sum_b \Psi_{ab} \cdot \nabla W_{ab} \frac{m_b}{\rho_b} \tag{56}$$

where δ controls the magnitude of the diffusion term. The term Ψ_{ab} is based on the Neumann-Richtmeyer artificial dissipation and depends on the specific diffusive scheme adopted. Ferrari *et al.* (2009) proposed such an approach, with a similar technique by Molteni and Colagrossi (2009) who introduced the artificial term as:

$$\Psi_{ab} = 2(\rho_b - \rho_a) \frac{r_{ab}}{\|r_{ab}\|^2} \tag{57}$$

Equation (55) proved to be effective in improving the pressure field with almost no additional computational cost. However, demonstrated to be inconsistent close to the free-surface. Antuono *et al.* (2010) improved the work presented by Molteni and Colagrossi (2009), including a correction to the diffusive term. In this scheme, named as δ-SPH scheme, Ψ_{ab} is computed as:

$$\Psi_{ab} = \left[2(\rho_b - \rho_a) - \left(\langle \nabla_\rho \rangle_b^L + \langle \nabla_\rho \rangle_a^L\right) \cdot (r_b - r_a)\right] \frac{(r_b - r_a)}{|r_b - r_a|^2} \tag{58}$$

where $\langle \nabla_\rho \rangle^L$ is the renormalized density gradient. The δ-SPH can be easily implemented and the main benefit with respect to the standard SPH is its effectiveness in reducing the pressure spurious oscillations. It must be noted that the formulation of Antuono *et al.* (2010) is consistent close to the free surface and it can be adopted for any type of flow. However, in the absence of a gravity force, the formulation collapses to the original formulation of Molteni and Colagrossi (2009). Besides, this scheme has a remarkable additional computation cost.
Lately, Fourtakas *et al.* (2019) use the equation (57) but substitute the dynamic density with the total one. Thus, the term Ψ_{ab} takes the following form:

$$\Psi_{ab} = 2(\rho_{ba}^{T} - \rho_{ab}^{H})\frac{r_{ab}}{\|r_{ab}\|^2} \quad (59)$$

where superscripts $(\cdot)^T$ and $(\cdot)^H$ denote the total and hydrostatic component of the density of a weakly compressible and barotropic fluid by locally constructing the hydrostatic pressure as,

$$P_{ab}^{H} = \rho_0 g z_{ab} \quad (60)$$

Although both terms are not consistent near a truncated kernel support (such as free-surface or a wall boundary), thus resulting in an outwards vector net contribution, the latter term improves the behaviour of pressure near the wall boundaries by operating on the dynamic pressure (Domínguez *et al.*, 2022).

(iii) The schemes that employ **Riemann solvers** to model the particle interaction (*e.g.*, Cha and Whitworth (2003); Inutsuka (2002)). According to Domínguez *et al.* (2022), these techniques require only minor changes to the SPH formulation, replacing the classical particle interactions with individual Riemann problems between each particle pair. With higher-order upwind reconstruction techniques, this produces pressure fields that are effectively noise-free.

Another strategy to avoid spurious pressure oscillations corresponds to the use of Incompressible SPH (ISPH) schemes, which enforce incompressibility and solves pressure through a pressure Poisson equation in the form of a sparse matrix, thus no longer a dependent variable (Cummins and Rudman, 1999). They are ideal to model free-surface flows with a smooth and accurate, noise-free pressure field when used with particle regularisation or shifting. Besides, they do not involve the sound of speed and hence can use time steps that are an order of magnitude larger than the WCSPH schemes. The ISPH schemes have the disadvantage of requiring the solution of large (but sparse) linear systems. ISPH pressure-Poisson equation is the most computationally expensive part of the algorithm, in terms of both memory and time. This makes implementing them in parallel and on GPUs fairly difficult. WCSPH implementations are generally more popular as they are much easier to implement and parallelize.

3.3.2.4 Particle shifting algorithm

An important consequence of improving the pressure field, by using density diffusion techniques, Riemann solvers or ISPH, is that particles follow streamlines more accurately. This can create problems in the particle distribution, when unphysical voids are created as particles converge on stagnation points making kernel supports no longer complete. Being a numerical tool based on interpolation theory, the DualSPHysics requires that particles be distributed as uniformly as possible for the enhancement of accuracy/stability of numerical models (Ozbulut *et al.*, 2014; Violeau and Rogers, 2016). As referred by Lind *et al.* (2020), the reliability of particle methods depends on their convergence properties, which in turn are dependent on several factors, including the regularity of particle distributions. If particles in the problem domain acquire an anisotropic spatial distribution, it is no longer possible to retain the stability and the reliability of numerical results, and in extreme cases, it can lead to the simulation breakdown (Ozbulut *et al.*, 2014). This is especially true in negligible or large dynamics and violent flows (Domínguez *et al.*, 2022).

Xu *et al.* (2009) proposed a particle shifting algorithm, which is an increasingly standard technique used to prevent unaccepted particle clustering or/and disordered particle arrangements (Lind *et al.*, 2020). It

was first created in the framework of Incompressible SPH, but it was extended to the WCSPH model used in DualSPHysics (Vacondio *et al.*, 2013). With this algorithm the particles are moved towards lower particle concentration areas, allowing the domain to maintain a uniform particle distribution, and eliminating any voids that may occur due to the noise.

An improvement on the initial shifting algorithm was proposed by Lind *et al.* (2012), who used the Fick's first law of diffusion to stabilize the particle motion and homogenize their distribution in space, by controlling the shifting magnitude and direction. At the end of each time step, each particle is shifted by a small distance, δr_a, given by (Domínguez *et al.*, 2022; Sato *et al.*, 2021; Violeau and Rogers, 2016):

$$\delta r_a = -D_s \nabla C_a \tag{61}$$

where ∇C_a is the gradient of the particle concentration and D_s is the diffusion coefficient that controls the shifting magnitude and absorbs the constants of proportionality. The particle concentration gradient, ∇C_a, is computed through an SPH gradient approximation with the particle concentration computed through the sum of the smoothing kernel:

$$\nabla C_a = \sum_b \frac{m_b}{\rho_b} \nabla W_{ab} \tag{62}$$

In DualSPHysics, the coefficient D_s is computed through a form proposed by Skillen *et al.* (2013) and is given by:

$$D_s = A_s h \|v_a\| \Delta t \tag{63}$$

where A_s is a dimensionless constant in the range of [1 - 6] with 2 used as default, $\|v_a\|$ is the velocity magnitude of particle a, and Δt is the current time step.

The shifting algorithm is heavily dependent on a full kernel support. However, the free surface particles and adjacent to it cannot obtain the full kernel support, which will introduce errors in the free-surface prediction, potentially causing non-physical instabilities. To prevent unphysical movement at the free-surface, Lind *et al.* (2012) proposed a free-surface correction that limits diffusion to the surface normal but allow shifting on the tangent to the free-surface. In DualSPHysics, a free-surface correction coefficient A_{FSC} is introduced as:

$$A_{FSC} = \frac{\nabla \cdot r - A_{FST}}{A_{FSM} - A_{FST}} \tag{64}$$

where A_{FST} is the free-surface threshold, A_{FSM} is the maximum value of the particle divergence, and $\nabla \cdot r$ is the value of the particle divergence. The A_{FSM} depend on the domain dimensions and A_{FST} is selected for DualSPHysics: for two dimensions $A_{FSM} = 2$ and $A_{FST} = 1.5$; for three dimensions $A_{FSM} = 3$ and $A_{FST} = 2.75$.

Therefore, equation (61) with the free-surface correction is given as:

$$\delta r_a = \begin{cases} -A_{FSC} \cdot A_s h \| v_a \| \Delta t \cdot \nabla C_a, & if\,(\nabla \cdot r - A_{FST}) < 0 \\ -A_s h \| v_a \| \Delta t \cdot \nabla C_a, & if\ (\nabla \cdot r - A_{FST}) = 0 \end{cases} \quad (65)$$

3.3.2.5 Turbulence and viscosity in SPH

The literature contains many definitions for turbulent flows, like the one of Markatos (1986): "A fluid motion is described as turbulent if it is three-dimensional, rotational, intermittent, highly disordered, diffusive and dissipative". A turbulent flow is characterized by the appearance of eddying motion or vortices of a wide range of length scales. These vortices can have different sizes, from the largest to the smallest, being the latter dissipated by viscous processes (Moreira, 2021). According to Tennekes *et al.* (1972), "viscous shear stresses perform deformation work which increases the internal energy of the fluid at the expense of kinetic energy of the turbulence".

In the early applications of SPH to free-surface flows, turbulence usually was ignored since SPH proved particularly appropriate for representing violent flows, where inertia, pressure and gravity play a crucial role (Violeau and Rogers, 2016). Actually, SPH generally fits within the class of simulation techniques known as Large Eddy Simulations (LES) (Cleary *et al.*, 2007).

However, many CFD flow problems are turbulent (*e.g.*, coastal flows, wave breaking, etc.). So, depending on what physics one is modelling and the importance of the boundary layers, one must consider different levels of sophistication of turbulence models and the viscous effects. And even in conditions that one can ignore turbulence models, at least viscous forces are diffusive and help numerical schemes stabilization (artificial viscosity) (Souto-Iglesias, 2021).

In the momentum equation (51), Γ refers to dissipative terms. DualSPHysics offers different options for including the effects of dissipation:

(i) Artificial viscosity

The artificial viscosity method, which Monaghan (1992; 2005) firstly proposed, is an usual method within fluid simulation using SPH, mainly because of its simplicity. The artificial viscosity term based on the Neumann-Richtmeyer artificial viscosity is added to the SPH gradient operator to reduce oscillations and stabilise the SPH scheme. The viscosity term Π_{ab} is given by:

$$\Pi_{ab} = \begin{cases} \left(\frac{-\alpha \overline{c_{ab}}}{\overline{\rho_{ab}}}\right)\left(\frac{h v_{ab} \cdot r_{ab}}{r_{ab}^2 + \eta^2}\right) & v_{ab} \cdot r_{ab} < 0 \\ 0 & v_{ab} \cdot r_{ab} \geq 0 \end{cases} \quad (66)$$

where $r_{ab} = r_a - r_b$ and $v_{ab} = v_a - v_b$, with r_k and v_k being the particle position and velocity, respectively, and $\overline{(\cdot)_{ab}} = [(\cdot)_a + (\cdot)_b]/2$. Herein, c denotes the numerical speed of sound, $\eta = 0.001h^2$ and α is the artificial viscosity coefficient, which needs to be tuned to introduce the proper dissipation. The parameter α depends on the smoothing length (h) and the initial distance between particles. The value of $\alpha = 0.01$ has proven to give the best results in the validation of wave flumes to study wave propagation and wave loadings exerted into coastal structures (Altomare *et al.*, 2015b).

The final form of the momentum equation in the presence of artificial viscosity is:

$$\frac{\mathrm{d}\boldsymbol{v}_a}{\mathrm{d}t} = -\sum_b m_b \left(\frac{p_b + p_a}{\rho_b \cdot \rho_a} + \Pi_{ab}\right) \nabla_a W_{ab} + \boldsymbol{g} \tag{67}$$

At first, the viscosity term in the equation of motion was used to represent viscosity and prevent particles from interpenetrating. For flows with a free surface, it also has the effect of keeping the scheme stable numerically. However, in many cases, it is too dissipative and affects the shear in the fluid. It is especially relevant when using SPH to capture coherent turbulent structures.

(ii) Laminar viscosity

In the laminar regime, the viscous dissipation of momentum, in DualSPHysics, is approximated by Lo and Shao (2002):

$$\upsilon_0 \nabla^2 v_a = \sum_b m_b \left(\frac{4\upsilon_0 r_{ab} \nabla_a W_{ab}}{(\rho_a + \rho_b)|r_{ab}|^2}\right) v_{ab} \tag{68}$$

where υ_0 denotes the kinematic viscosity of the fluid (10^{-6} m^2s in the case of water). Note that the laminar viscous term diverges close the free-surface as discussed in Colagrossi *et al.* (2011). Equation (51) can be written using the laminar viscous stresses as:

$$\frac{dv_a}{dt} = -\sum_b m_b \left(\frac{P_b + P_a}{\rho_b \cdot \rho_a}\right) \nabla_a W_{ab} + g + \sum_b m_b \left(\frac{4\upsilon_0 r_{ab} \nabla_a W_{ab}}{(\rho_a + \rho_b)|r_{ab}|^2}\right) v_{ab} \tag{69}$$

(iii) Sub-Particle Scale (SPS) turbulence

For coastal and oceanic wave hydrodynamics, the fluid turbulence is taken into account predominantly by two strategies. These two strategies are (Luo *et al.*, 2021):

- the k-ε model, which models the Reynolds stress in the RANS (Reynolds-Averaged Navier-Stokes) equations, and
- the sub-particle scale (SPS) model, which captures the effects of unresolved small-scale fluid motions in the Large-Eddy Simulation (LES) framework.

The LES resolves the fluid motions to a prescribed scale (*i.e.*, the particle or mesh size). Then it adopts a Sub-Particle Scale (SPS) model to capture the small-scale physical processes, which occur at length scales not adequately solved on the computational particles (Luo *et al.*, 2021). For large-scale eddies, resolved by the grid or particle sizes, the averaged equations are sufficient to solve it. The smaller turbulent eddies, smaller than the particle size, need a closure scheme to model their effects on the flow field (Dalrymple and Rogers, 2006). The concept of the Sub-Particle Scale (SPS) was described for the first time by Gotoh (2001) to represent the effects of turbulence in their Moving Particle Semi-implicit (MPS) model. The momentum conservation equation is defined as:

$$\frac{dv}{dt} = -\frac{1}{\rho}\nabla P + g + \upsilon_0 \nabla^2 v_a + \frac{1}{\rho}\nabla \cdot \vec{\tau} \tag{70}$$

where the laminar term is treated as per equation (68) and $\vec{\tau}$ represents the SPS stress tensor. According to Dalrymple and Rogers (2006), Favre averaging is needed to account for WCSPH, where eddy viscosity closure is used to model the SPS stress tensor with Einstein notation for the shear stress component in coordinate directions *i* and *j* as:

$$\frac{\vec{\tau}_{ij}}{\rho} = 2\nu_t\left(S_{ij} - \frac{1}{3}k\delta_{ij}\right) - \frac{2}{3}C_I\Delta^2\delta_{ij}|S_{ij}|^2 \tag{71}$$

Here, k is the SPS turbulence kinetic energy, $\nu_t = (C_s\Delta l)^2|S|$ is the turbulent eddy viscosity, where $C_s = 0.12$ is the Smagorinsky constant, $C_I = 0.0066$, Δl is the initial particle spacing, and $|S| = \sqrt{2S_{ij}S_{ij}}$, where S_{ij} is an element of the SPS strain tensor.

Finally, equation (70) is rewritten as:

$$\begin{aligned}\frac{dv_a}{dt} = -\sum_b m_b\left(\frac{P_b + P_a}{\rho_b \cdot \rho_a}\right)\nabla_a W_{ab} + g + \sum_b m_b\left(\frac{4v_0 r_{ab}\nabla_a W_{ab}}{(\rho_a + \rho_b)|r_{ab}|^2}\right)v_{ab} \\ + \sum_b m_b\left(\frac{\vec{\tau}_{ij}^b}{\rho_b^2} + \frac{\vec{\tau}_{ij}^a}{\rho_a^2}\right)\nabla_a W_{ab}\end{aligned} \tag{72}$$

Nevertheless, turbulence in SPH is a strenuous subject, and there is not a vast quantity of knowledge about turbulent Lagrangian statistics. SPH usually struggles with these problems and is competitive only if distorted/fragmented free surfaces are involved. The description of the Lagrangian turbulence is still very under-developed.

3.3.2.6 Boundary conditions

The open and solid boundary conditions implementation in the SPH method is not as straightforward as in the mesh-based numerical methods. In this method, when a fluid particle approaches a solid boundary, only the particles inside the domain are involved in the SPH interpolants. The Lagrangian nature of SPH together with the incompleteness of the kernel interpolation can generate odd effects and, consequently, create difficulties in enforcing boundary conditions in SPH. Therefore, the treatment of boundary conditions is still an open question and has been highlighted as one of the Grand Challenges of SPH. When implementing BCs, important issues to be addressed include: (i) measures of consistency, (ii) maintaining intrinsic SPH conservation properties, and (iii) discretization of complex real geometries. Over the last few years, extensive research has been conducted to develop accurate and efficient boundary conditions (BCs) in SPH. Many different approaches have been proposed in the literature to apply solid boundary conditions. Currently, existing boundary conditions methodologies can be grouped into three main categories: (i) boundary repulsive forces, (ii) fictitious particles, and (iii) boundary integrals (Fig.19) (English et al., 2021).

(a) Repulsive forces (b) Fictitious boundary particles (c) Boundary integral

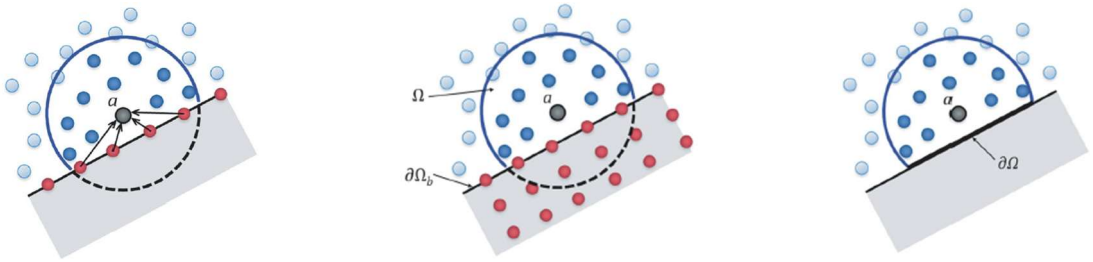

Fig.19 – Generic SPH boundary treatments for rigid walls as particle approaches the boundary $\partial\Omega_b$. The grey shaded area is the solid boundary, the blue particles are fluid particles and the red particles are boundary particles (adapted from Violeau and Rogers (2016)).

Table 8 – Description, advantages, disadvantages and examples of three different boundary conditions methodologies.

BCs methodologies	Boundary repulsive forces	Fictitious boundary particles	Boundary integral
Description	A repulsive function is added to the particles that interact with the boundary. In this method, the magnitude of the repulsive force experienced by the fluid particles is a direct function of the distance between the particle and the boundary.	The fluid is virtually extended across the boundary – *e.g.*, two or more layers of ghost particles are placed beyond the boundary –, conveniently setting the fields properties values on such fictitious fluid.	It uses an approximation to the surface integral to account for the truncated kernel. This introduces a correction factor into the SPH summations and additional terms in the conservation equations in order to mimic the presence of the boundary.
Advantages	- Easy to implement, - Enables the discretization of 2-D and 3-D irregular geometries, - Computationally cheap.	- Fictitious particles can take the form of stationary fluid particles or similar to whom conditions of impermeability.	- Rather accurate.
Disadvantages	- Not directly completing the kernel support, - Leads to spurious behaviours of the particles as the SPH equations are inaccurately solved close to the boundaries, and - Lack of literature analysing its consistency and stability.	- Extend the method to 3-D is challenging for irregular geometries, - Not prevent particles from penetrating the boundary and, - Create unphysical separations.	- Complex, and - Computationally expensive.
Examples & References	(Monaghan, 1994; Monaghan and Kajtar, 2009)	Dynamic Boundary Condition (DBC), Local Uniform Stencil (LUST) (Adami *et al.*, 2012; Colagrossi and Landrini, 2003; Crespo *et al.*, 2007; Fourtakas *et al.*, 2019; Marrone *et al.*, 2011)	Boundary integral (Integral) (Campbell, 1989; Ferrand *et al.*, 2013; Kulasegaram *et al.*, 2004; Leroy *et al.*, 2014; Mayrhofer *et al.*, 2013)

In DualSPHysics, the boundary is described by a set of particles distinct from the set of fluid particles. The software currently has implemented the following BCs functionalities for **solid impermeable**:

(i) Dynamic Boundary Condition (DBC) (Crespo *et al.*, 2007)

It is the default method provided by DualSPHysics. In this method, solid objects, such as the wave channel, floating objects, paddle wavemakers, etc., are discretized by a set of boundary particles. These particles satisfy the same equations as fluid particles, but they do not move according to the forces imposed on them. Instead, they remain fixed in position or move according to an assigned motion function. When a fluid particle approaches a boundary, and the distance between its particles and the particles of fluid becomes smaller than the interaction distance (equal to twice the interaction distance), the density of the affected boundary particles increases, resulting in a pressure increase. Consequently, this results in a repulsive force exerted on the fluid particle due to the pressure term in the momentum equation (Crespo *et al.*, 2017).

DBC proved to be a successful method when applied to some coastal engineering problems. Its success is due to: its reliability and versatility; its computational simplicity, since density and pressure can be calculated inside the same loops as fluid particles, resulting in a saving of computational time; and its ability to deal with very complex 2-D and 3-D geometries – for more details see works of Altomare *et al.* (2014) and Zhang *et al.* (2018). However, this approach also presents some drawbacks such as (English *et al.*, 2022):

- Non - physical density values on the boundaries,
- Pressure measurement is very noisy close to the boundaries,
- The high repulsive force results in a gap between fluid and boundary particles, and
- The boundary layer is not accurately solved when considering the steady state 2D channel flows unless a high resolution is used. The approximation of no-slip by setting zero velocity at each boundary particle fails to capture the condition for lower resolutions. Then, this leads to higher-than-expected velocities close to the boundary and throughout the flow.

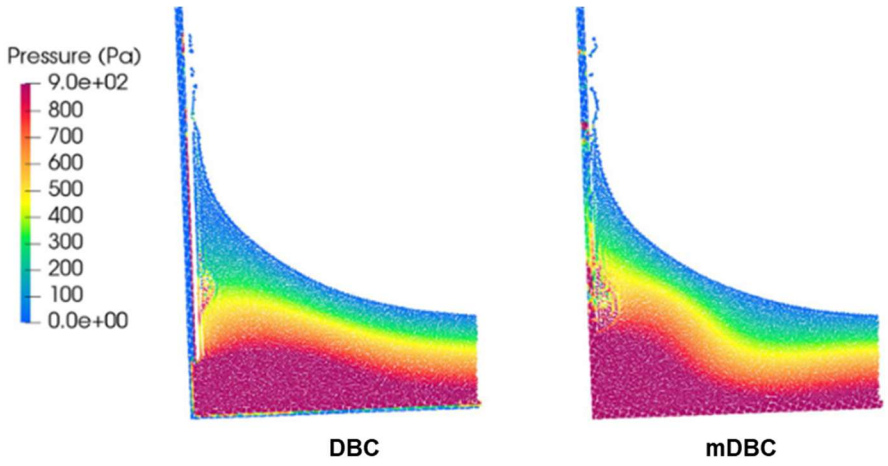

Fig.20 – Examples of some DBC problems: close up of the pressure field in the corner and the gap in the lateral wall in the sloshing tank simulation for DBC (left) and mDBC boundaries (right) (adapted from English *et al.* (2022)).

(ii) Modified Dynamic Boundary Condition (mDBC)

A modification of DBC has been proposed by English *et al.* (2022) to solve some of the limitations of the previous method while maintaining the capability of discretizing complex geometries without compromising the efficiency of the GPU implementation (English *et al.*, 2022). The boundary particles of mDBC are arranged in the same way as the boundary particles in the original DBC, but with an additional boundary interface (solid black line in Fig.21) created between the fluid and the boundary particles and located (for simple geometries) at half an inter-particle distance ($dp/2$) from the innermost layer of boundary particles. For each boundary particle, a ghost node (crosses in Fig.21) is created in the fluid domain using a mirroring procedure based on an approach similar to Marrone *et al.* (2011). This ghost node is projected according to the normal vector of the boundary pointing to the fluid part of the domain (arrows in Fig.21). For a flat surface, the ghost node is mirrored across the boundary interface along the direction of the boundary normal pointing into the fluid (see Fig.21).For boundary particles located in a corner, the normal is defined as the direction between the boundary particle and the corner, being the ghost node mirrored through the point of this corner into the fluid domain (see Fig.21). Then, fluid properties (density, velocity) are computed at the ghost nodes according to the surrounding fluid (particles inside the kernel radius in Fig.21) using a corrected SPH approximation and finally mirrored back to the boundary particles. For the density of the boundary particles, the ghost density and its gradient are computed according to the first-order consistent SPH interpolation proposed by Liu and Liu (2006).

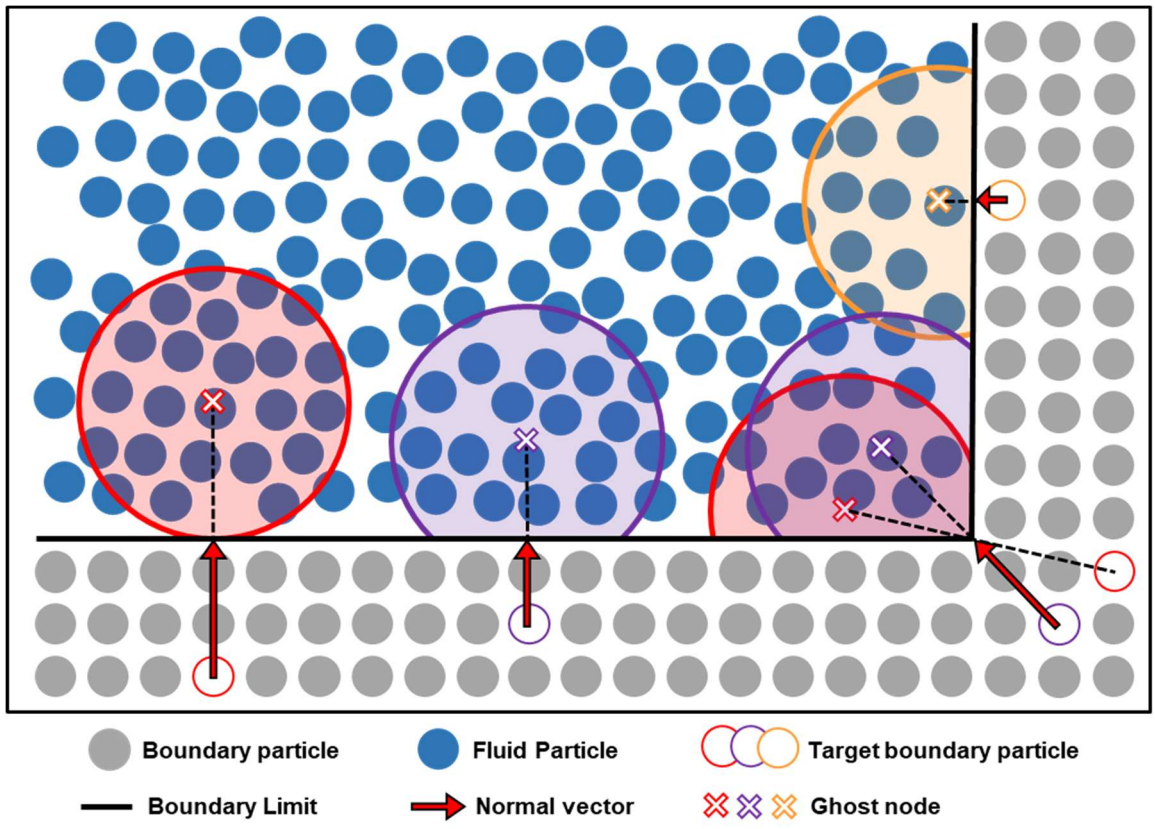

Fig.21 – Mirroring of ghost nodes (crosses), the kernel radius (shaded circles) around the ghost nodes and fluid particles included in the kernel sum around ghost nodes for boundary particles in a flat surface and a corner.

The mDBC approach presents several improvements regarding DBC: through the modified version, density and pressure fields are smoother and have more realistic physical values; the size of the gap between the fluid and the boundary has been drastically reduced, allowing for a more accurate approximation of the boundary layer; and finally, a more accurate no-slip condition is employed that can accurately describe channel flows with fewer particles than the original method (English *et al.*, 2022). The method has been implemented in the DualSPHysics code, in both CPU and GPU implementations, with a minimal increase in computational cost. Despite the modified method keeps the advantages of the original one (DBC) while tackling some of the drawbacks, the creation of the initial condition for mDBC is more complicated since (Domínguez *et al.*, 2022; English *et al.*, 2022):

- Several boundary particle layers are necessary, depending on the SPH smoothing length. The use of an adequate number of layers of boundary particles prevents inconsistencies due to kernel truncation effects for fluid particles located near the boundaries,
- Distance between boundary limit and boundary particles should be half the initial inter-particle distance ($dp/2$),
- Vectors from boundary particles to actual boundary limit are necessary.

Open boundaries are required as soon as one wants to simulate a large-scale flow. DualSPHysics provide support for these boundaries in the form of a **periodic open boundary condition**, which allow particles that are near an open lateral boundary to interact with the fluid particles near the complimentary open lateral boundary on the other side of the domain (Gomez-Gesteira *et al.*, 2012). Finally, methods for **pre-imposed boundary motion**, which allow boundary particles to be moved according to fixed forcing functions, are also present in the software.

3.3.2.7 Time integrators and time step

Since the SPH equations have been reduced to a set of ordinary differential equations (ODEs), they may be integrated using any convenient, stable method for integrating ODEs (Monaghan and Kos, 1999). There are several ways to develop the solution of the SPH equations in time. It is advisable to use at least a second-order accurate scheme in time. Consider the momentum, density, position equations in the following form:

$$\frac{dv_a}{dt} = F_a; \frac{d\rho_a}{dt} = R_a; \frac{dr_a}{dt} = v_a \tag{73}$$

These equations are integrated in time using the two numerical schemes implemented in DualSPHysics: (i) the Verlet time integration scheme (Verlet, 1967) and (ii) Symplectic position Verlet scheme (Leimkuhler *et al.*, 1996).

(i) Verlet time integration scheme

The Verlet algorithm, which is a second-order accurate space integrator, is probably the most used time integration scheme in molecular dynamics. It provides low computational cost compared to other integration techniques, primarily because this velocity Verlet version does not require multiple calculation steps within an interaction interval. The predictor step calculates the WCSPH variables according to (Verlet, 1967):

$$v_a^{n+1} = v_a^{n-1} + 2\Delta t F_a^n \tag{74}$$

$$r_a^{n+1} = r_a^n + \Delta t v_a^n + \frac{\Delta t^2}{2} F_a^n \tag{75}$$

$$\rho_a^{n+1} = \rho_a^{n-1} + 2\Delta t R_a^n \tag{76}$$

Due to the integration over a staggered time interval, the equations of density and velocity are no longer coupled. This may lead to the divergence of integrated values through time. So, an intermediate step is required every N_s steps ($N_s \approx 40$ is recommended) according to (Domínguez *et al.*, 2022):

$$v_a^{n+1} = v_a^n + \Delta t F_a^n \tag{77}$$

$$r_a^{n+1} = r_a^n + \Delta t V_a^n + \frac{\Delta t^2}{2} F_a^n \tag{78}$$

$$\rho_a^{n+1} = \rho_a^n + \Delta t R_a^n \tag{79}$$

According to Crespo *et al.* (2015), in cases where the Verlet scheme is used but it is found that numerical stability is an issue, it may be sensible to increase the frequency at which the second part of this scheme is applied. However, if it is necessary to increase this frequency beyond $N_s = 10$, the scheme may not be able to capture the dynamics of the case in hand suitably and the Symplectic scheme should be used instead.

(ii) Symplectic position Verlet scheme

The Symplectic integration algorithms are numerically more stable, but computationally more intensive. The Symplectic position Verlet time integration (Leimkuhler and Matthews, 2016) scheme implemented in DualSPHysics is second-order accurate in time. It is perfect for Lagrangian schemes since it is time reversible and symmetric in the absence of friction or viscous effects that preserve geometric features. The position Verlet scheme in the absence of dissipation forces reads (Leimkuhler and Matthews, 2016):

$$r_a^{n+1/2} = r_a^n + \frac{\Delta t}{2} v_a^n \tag{80}$$

$$v_a^{n+1} = v_a^n + \Delta t F_a^{n+1/2} \tag{81}$$

$$r_a^{n+1} = r_a^{n+1/2} + \frac{\Delta t}{2} v_a^{n+1} \tag{82}$$

Considering the viscous forces and density evolution in DualSPHysics, it is required the velocity at the $(n + 1/2)$ step. Thus, a velocity Verlet half step is used to compute the required velocity for the

acceleration and density evolution for $F(r_{n+1/2})$ and $R(r_{n+1/2})$, respectively. The scheme implemented in DualSPHysics reads:

$$r_a^{n+1/2} = r_a^n + \frac{\Delta t}{2} v_a^n \tag{83}$$

$$v_a^{n+1/2} = v_a^n + \frac{\Delta t}{2} F_a^n \tag{84}$$

$$v_a^{n+1} = v_a^n + \Delta t F_a^{n+1/2} \tag{85}$$

$$r_a^{n+1} = r_a^n + \Delta t \frac{(v_a^{n+1} + v_a^n)}{2} \tag{86}$$

where $r_a^{n+1/2}$ is substituted to r_a^{n+1} in the previous equations - (80) to (82) - to eliminate dependence from $v_a^{n+1/2}$.

Finally, the corrected value of density is calculated using the half time steps of the symplectic position Verlet scheme as follows (Parshikov *et al.*, 2000):

$$\begin{aligned} \rho_a^{n+1/2} &= \rho_a^n + \frac{\Delta t}{2} R_a^n \\ \rho_a^{n+1} &= \rho_a^n \frac{2 - \varepsilon_a^{n+1/2}}{2 + \varepsilon_a^{n+1/2}} \end{aligned} \tag{87}$$

where $\varepsilon_a^{n+1/2} = -(R_a^{n+1/2}/\rho_a^{n+1/2})\,\Delta t$.

Variable time-step

Like all numerical models, SPH suffers from numerical instabilities if the time step is not carefully controlled. Thus, restriction on the time-step size must be enforced (Violeau and Leroy, 2014). With explicit time integration schemes, the time-step control is dependent on the Courant-Friedrichs-Lewy (CFL) condition, which ensures that the time-step remains lower than the maximal convection time on the smoothing length during the simulation; the forcing terms; and the viscous diffusion term. A **variable time-step**, Δt, is calculated according to Monaghan and Kos (1999) using:

$$\Delta t = CFL \cdot \min\left(\Delta t_f, \Delta t_{cv}\right), \quad \Delta t_f = \min_a\left(\sqrt{h/|f_a|}\right) \quad and \quad \Delta t_{cv} = \min_a \frac{h}{c_s + \max_b \frac{|h v_{ab} \cdot r_{ab}|}{r_{ab}^2 + \eta^2}} \tag{88}$$

where Δt_f is based on the force per unit mass ($|f_a|$), and Δt_{cv} combine the Courant and the viscous time step controls. The variable time step is selected as the minimum of Δt_f and Δt_{cv}, being bounded by the Courant number CFL, usually in the range of 0.1 to 0.2 (Domínguez *et al.*, 2022).

3.3.3 FUNCTIONALITIES

3.3.3.1 Wave generation and absorption

Waves and currents are major driving forces in ocean and coastal environments. For numerical simulations in the coastal engineering field, the reproduction of waves in a relatively small domain that can represent the key features of realistic sea states is an important issue as the first step of design of coastal structures. Its success relies on the precise generation of waves or/and currents on the inflow boundaries, minimizing unphysical numerical wave dissipations after long-distance propagation and removing unwanted wave reflections (Luo *et al.*, 2021). In DualSPHysics different techniques to generate sea waves are implemented:

(i) The use of **moving boundary particles** to mimic the displacement of a **piston-** or a **flap-type wavemaker** as in physical facilities. It is employed as a stand-alone generation method,
(ii) **Relaxation zones** employed either as a stand-alone generation method or as coupling method with other phase-resolving models,
(iii) **Inlet open boundaries** developed initially for two-way coupling with wave propagation models but also suitable for stand-alone wave generation, and
(iv) **Multi-layered piston moving boundaries** coupled with an external method. This coupling technique is a one-way offline coupling with no reflection compensation, for which it is suitable only for low-reflective cases or very short time series used, such as the modelling of the main pulse of a single solitary wave.

Regarding points (ii), (iii) and (iv), more details are given in subsection 3.3.3.3.

Concerning the waves generated by means of moving boundaries, the motion of the wave generator is prescribed controlling its position (linear or angular) at each instant of time. Both 1st and 2nd order wave generation theories for regular (monochromatic) and random waves are implemented in the DualSPHysics code (Altomare *et al.*, 2017). Moreover, it is also possible to generate solitary waves using a piston-type wavemaker (Domínguez *et al.*, 2019).

Table 9 – Summary of the wave generation theories available in DualSPHysics.

Wave theory			Reference
1st order	Regular	Far-field solution for the free-surface elevation: $\eta(x,t) = \frac{H}{2}\cos(\omega_f - kx + \delta)$ where H is the wave height, $\omega_f = \frac{2\pi}{T}$ is the angular frequency, $k = \frac{2\pi}{L}$ is the wave number with T equal to the wave period and L the wavelength. The initial phase δ is given by a random number between 0 and 2π. Bisel transfer function for a piston-type wavemaker: $\frac{H}{S_0} = \frac{2\cdot\sinh^2(kd)}{\sinh(kd)\cdot\cosh(kd)+kd}$, where S_0 is the piston stroke and d the water depth. The displacement of a piston-type wavemaker: $e_1(t) = \frac{S_0}{2}\sin(\omega t + \delta)$	(Biesel and Suquet, 1951)

Table 9 (cont.) – Summary of the wave generation theories available in DualSPHysics.

Wave theory			Reference
	Irregular	Generation of random waves by implementing a first-order wave generation algorithm: the irregular wave train is generated by combining the discrete amplitude spectrum (JONSWAP or Pierson-Moskowitz spectrum) corresponding to the target wave energy spectrum with random phases obtained by a random number generator. More detail can be found in Domínguez *et al.* (2022). A phase seed is also used to obtain different time series of irregular waves assigning randomly a value for the original phase to each wave component. Changing the phase seed allows generating different irregular wave time series with the same significant wave height (H_{m0}) and peak period (T_P).	(Liu and Frigaard, 1999)
2nd order	Regular	Correction implemented for both piston- and flap-type wavemakers to prevent the generation of spurious secondary waves that travel at a speed slightly lower than the primary waves – Madsen's theory (1971): - It is simple, controllable and affordable computationally, - It proves to be accurate and quite efficient for waves of first and second order, and - This solution is only valid within the following range: $HL^2/d^3 < 8\pi/3$ <u>The displacement of a piston-type wavemaker:</u> $e(t) = \frac{S_0}{2}\sin(\omega t + \delta) + \left[\left(\frac{H^2}{32d}\right)\cdot\left(\frac{3\cos\ (kd)}{\sinh^3(kd)} - \frac{2}{m_1}\right)\right]\sin(2\omega t + 2\delta)$ where the second part of the right-hand term represents the second-order term, and $m_1 = H/S_0$.	(Frigaard *et al.*, 1993; Madsen, 1971)
	Irregular	The solution for random waves is extended to the second-order wave generation in order to cancel out the parasitic long waves and the spurious displacement long waves (Hansen *et al.*, 1980), the latter ones caused by finite wavemaker displacementes away from the mean position. The method implemented in DualSPHysics is based on the solution for the control signal of the wavemaker that is described in Barthel *et al.* (1983), and it is applicable to piston-type wavemakers only	(Barthel *et al.*, 1983)
Solitary waves	Single	<u>The displacement of a piston-type wavemaker:</u> $x_s(t) = \frac{2H}{Kd}\tanh\left[K\left(ct - x_s(t)\right)\right]$, where the parameter K is the outskirt coefficient, which describes the way the free-surface elevation tends towards the mean level at infinity. Three different solitary wave generation theories have been implemented in DualSPHysics: 1) Rayleigh approximation (Serre, 1953), 2) First-order shallow water model (KdV) (Clamond and Germain, 1999), 3) Boussinesq (Goring, 1978). For all cases, solitary waves are generated by the horizontal displacements of a piston-type wavemaker.	(Clamond and Germain, 1999; Goring, 1978; Serre, 1953)
	Multiple	To generate a series of multiple solitary waves, the law of motion of the wavemaker is calculated for each *i*-th solitary wave. Any of the aforementioned generation theories can be used. Then, the time lag between the (*i* + 1)th and *i*-th solitary waves has to be specified as a fraction or multiple of the generation time used for the *i*-th solitary wave. The generation of multiple solitary waves is a simple but efficient way to model a wave train of several tsunamis that might have been triggered by the same tectonic event.	

Besides wave generation, another key issue in any physical or numerical model applied to coastal engineering is the wave absorption. In DualSPHysics, the displacement of moving boundaries does not consider any compensation for the reflected waves that might reach the generation zone. Therefore, this method does not allow wave generation over longer time periods. To solve this problem, two wave absorption techniques, categorized as passive and active, are implemented in the software (Altomare *et al.*, 2017; Domínguez *et al.*, 2022; Zhang *et al.*, 2018).

The **passive wave absorption** consists of a damping system at the end of the domain to reduce the wave energy and the reflection exerted by the boundary of the model domain. This system can be either a dissipative beach or a damping area. In the case of using a dissipative beach, the wave energy is dissipated through the process of wave breaking. When used, the beach should be quite gentle and long, and exert very little reflection. The efficiency of the beach depends on the wave periods that characterise the wave trains. The alternative to the dissipative beach corresponds to the damping areas. The implemented damping system consists in gradually reducing the velocity of the particles at each time step according to their location but using a quadratic decay rather than an exponential one. The velocity is modified as following:

$$v = v_0 \cdot f(x, dt) \tag{89}$$

where v_0 is the initial velocity of the particle i, v is the final velocity and $f(x, dt)$ is the reduction function defined as:

$$f(x, dt) = 1 - dt \cdot \beta \cdot \left(\frac{x - x_0}{x_1 - x_0}\right)^2 \tag{90}$$

where dt is the duration of the last time step, x is the position of the particles, x_0 and x_1 are the initial and final position of the damping zone, respectively. According to Lind *et al.* (2012), it is recommended to use one wavelength, L, as the length of the damping zone. The coefficient β modifies the reduction function that is applied to the velocity. In DualSPHysics, it is also possible to use a combination of damping zone and dissipative beach (Altomare *et al.*, 2017).

The **active wave absorption** technique consists in the correction of the real-time displacement of the wavemaker to cancel out the reflected waves at the wavemaker and, consequently, to damp the unwanted re-reflection phenomenon (Altomare *et al.*, 2017; Domínguez *et al.*, 2022). The active wave absorption system (AWAS) implemented in the DualSPHysics is based on the time-domain filtering technique that uses the free-surface elevation at the wavemaker position as feedback to obtain a control signal to correct the wavemaker displacement (Altomare *et al.*, 2017; Zhang *et al.*, 2018). Hence, the target wavemaker position, $e(t)$, is corrected in real time to avoid reflection at the wave generation. The position in the real-time is obtained through the velocity correction of its motion. The wavemaker velocity is modified to match the velocity induced by the wave that will be absorbed. For a piston-type wavemaker, the wave absorption is performed using linear long wave theory (Schäffer and Klopman, 2000). The corrected velocity, U_C, is the difference between the theoretical wavemaker velocity, U_i (equal to the derivative in time of the piston-type wavemaker displacement $e(t)$), and the corrected velocity to absorb the reflected waves, U_R. It can be expressed as follows (Domínguez *et al.*, 2022):

$$U_C(t+\Delta t) = U_i(t) - U_R(t) = U_i(t) - \left(\eta_{\mathrm{WG,SPH}}(t) - \eta_{\mathrm{AWAS},i}(t)\right)\sqrt{g/d} \tag{91}$$

where $\eta_{\mathrm{AWAS},i}$ is the target incident free-surface elevation and $\eta_{\mathrm{WG,SPH}}$ is the free-surface elevation measured in front of the wavemaker. This is measured at $4 - 10 \cdot h_{\mathrm{SPH}}$ from the wavemaker. Finally, the wavemaker position at $t + \Delta t$ is corrected at the end of the time step using the following equation:

$$e(t+\Delta t) = e(t) + \left(U_C(t+\Delta t) + U_C(t)\right)\frac{\Delta t}{2} \tag{92}$$

A drift correction algorithm is implemented in the code. It prevents those little deviations from the mean water level from zero, which can accumulate over time, causing a wave generator deviation from its initial position to grow indefinitely. The algorithm checks when 80% of the maximum forward or backward wave board stroke is reached, and in such cases, it forces the average position of the wave plate to match its initial zero position. A smoothed transition, in form of a power function, is used to prevent abrupt changes in the wavemaker displacement (Altomare *et al.*, 2017).

3.3.3.2 Fluid-driven objects

The simulation of fluid-driven objects is other useful capability of SPH models. This functionality, implemented in DualSPHysics, derives the movement of a floating object by considering its interaction with fluid particles and using the resulting forces to drive its motion. By assuming that the body is rigid, the net force on each individual particle that form the same floating object is computed as a summation of the contributions of all surrounding fluid particles according to the designated kernel function and smoothing length. In this way, each floating particle $a \in K$ experiences an acceleration (dv/dt) given by:

$$\left.\frac{dv}{dt}\right|_{a\in K} = \sum_{b\in F} m_b \frac{dv_{ab}}{dt} \tag{93}$$

For the motion of the moving body, the basic equations of the rigid body dynamics can then be used:

$$M\frac{dv}{dt} = \sum_{k\in K} m_k \frac{dv_k}{dt} \tag{94}$$

$$I\frac{d\Omega}{dt} = \sum_{k\in K} m_k (r_k - R_0)\frac{dv_k}{dt} \tag{95}$$

where M is the total mass of the object, I the moment of inertia, v the velocity, ω the angular velocity, and R_0 the centre of mass. Both equations are integrated in time to obtain the values of v and ω at the beginning of the subsequent time step. Each particle belonging to the object will move with a velocity:

$$v_k = v + \omega \cdot (r_k - R_0) \tag{96}$$

Finally, the particles within the rigid body are moved by integrating equation (96) in time. The works of Monaghan *et al.* (2003) show that this technique conserves both linear and angular momentum (Domínguez *et al.*, 2022).

3.3.3.3 Coupling with other models

The SPH method proved to be very accurate and efficient when dealing with moving boundaries and complex interfaces, being adequate to resolve multi-mechanism problems. However, it is still less effective to solve problems where conventional numerical methods are currently used and well established. So, following the guidelines in the "SPHERIC Grand Challenge #4: Coupling to other models", it has been concluded that, depending on the problem in question, it can be more effective to restrict the use of SPH to relatively small domains and to employ a coupling strategy to inject some information into an SPH model from another model. In this way, the capabilities of both methods are enhanced within their specific application fields (Domínguez *et al.*, 2022; Violeau and Rogers, 2016). This subsection describes two of the successful coupling strategies of DualSPHysics with other models:

- **Coupling with wave propagation models**

SPH solvers are capable of simulating properly all processes involved in cases of coastal engineering applications, from wave generation to wave-structure interaction. Although, the employment of only one stand-alone model in multi-scale complex simulations, often characterized by three-dimensional domain and long durations, requires extensive computational resources. Note the case of the DualSPHysics solver. The software allows a detailed model of local phenomena, such as wave-structure interaction. Its mesh-free nature is also successful at mimicking the wave generation system of experimental facilities, employing moving boundaries. However, to properly simulate wave transformation when using these schemes and guarantee the correct wave sea state at the toe of the structure, comparably to what happens in physical model tests, waves need to be generated and propagate over relatively long domains. The computational cost of such simulation can be reduced by coupling the DualSPHysics solver with less computationally demanding wave propagation models (Domínguez *et al.*, 2022).

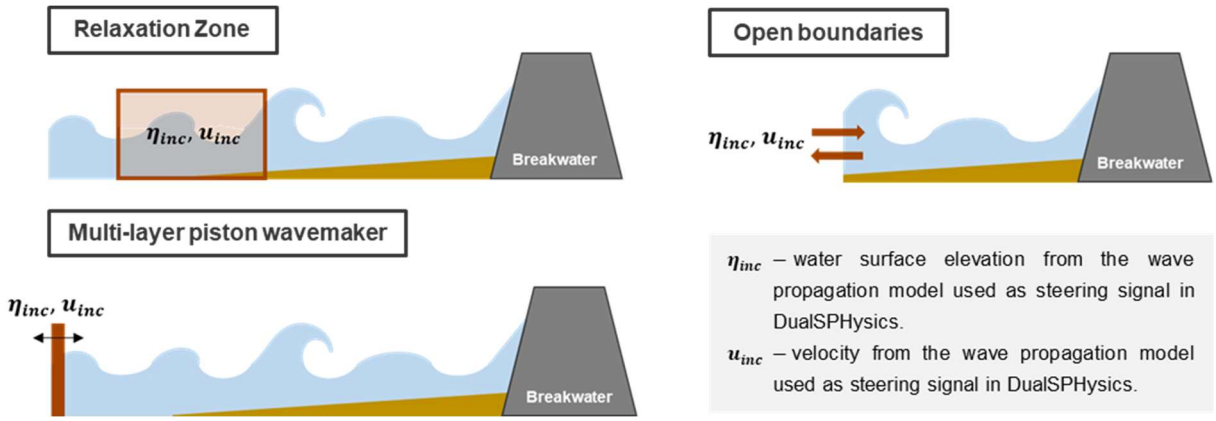

Fig.22 – Representation of the coupling techniques between DualSPHysics and wave propagation models (adapted from Domínguez *et al.*, 2021).

The three coupling schemes between the DualSPHysics and wave propagation models, presented in Fig.22, are hereby listed, and briefly described (Domínguez *et al.*, 2022):

(i) Relaxation zones (Altomare *et al.*, 2018): this technique is a general framework to generate waves and currents in DualSPHysics, which can be applied as a stand-alone wave generation and wave absorption method, as alternative to moving boundaries, or as a proper coupling scheme between DualSPHysics and a wave propagation model. The basics of the method remain the same in both cases. The coupling zone is extended from one single location to an area. In this one-way offline coupling, the orbital velocity calculated by the wave propagation model is imposed to the fluid particles in the DualSPHysics. The particle velocity distribution between the centre of the relaxation zone (RZ) and its extremes is controlled by a weighting C function (Fig.23 bottom), which prevents potential disorder due to the discontinuity of particle velocities at the interface between the RZ and the main computational region. In this way, the reflected waves are compensated inside the RZ (Crespo, 2020a; Domínguez *et al.*, 2022). The weighting function is implemented in the form of a hyperbolic function, and it depends on the set of values chosen for the ψ and β parameters, and on the distance from the centre of the RZ, being zero at both extremes. The variation of both parameters allows exploring the performance of the RZ depending on the shape of C. In Fig.23 (top), the basic scheme of the RZ is presented: the RZ is defined by the area bounded by the red dotted line; at the right side of the RZ it is located the main fluid domain. Since the generated waves will freely propagate in both directions along the *x*-axis, a damping area is placed at the left side of the RZ, bounded by a blue dotted line (Crespo, 2020a). A correction for the velocity of fluid particles is implemented to avoid unrealistic increase of the water level outside the generation zone, caused by Stokes drift velocity (Domínguez *et al.*, 2022).

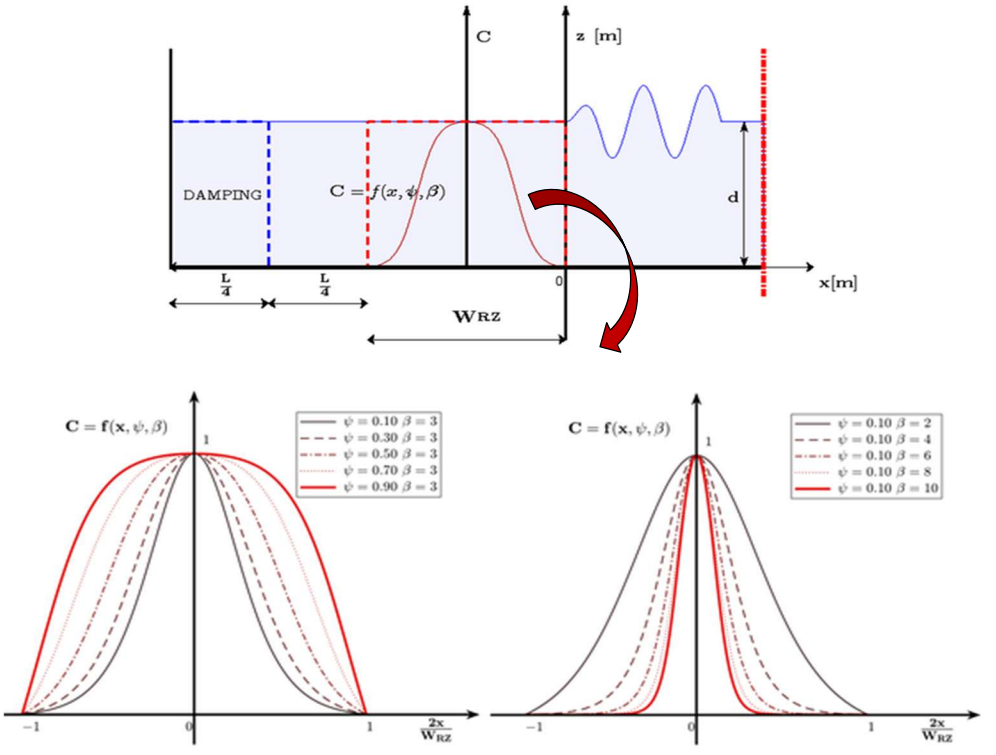

Fig.23 – Generic scheme of relaxation zone in DualSPHysics model (top) and shape of the weighting function C for different values of ψ and β (bottom) (Altomare *et al.*, 2018).

(ii) Inlet open boundaries (Verbrugghe *et al.*, 2019): The implementation of open boundaries in DualSPHysics, discussed in detail in Tafuni *et al.* (2018), is done in a versatile way, using the buffer region strategy. The logic behind using buffer zones is to attach several layers of fictitious SPH particles to a region of the computational domain where an open boundary is needed, for example an inlet or an outlet. A buffer area can work simultaneously as an inlet and outlet, enabling the application of DualSPHysics to problems with backflow and flow reversion. The implemented open boundary condition is illustrated in Fig.22, where a fluid is flowing near a buffer zone, implemented as an open boundary. The buffer zone is located in between the domain edge and the threshold boundary, the fluid-buffer interface. The buffer zone is filled with a finite number of layers of buffer particles chosen to equal or exceed the kernel radius, ensuring full kernel support for the closest fluid particles to the inlet/outlet threshold. Once the buffer particles are created, it is necessary to enforce boundary conditions appropriately. There are two possibilities to provide physical information to the buffer particles: the first correspond to the pre-assignment of the quantities to these particles (*e.g.*, velocity, pressure) by the user; the second option is to extrapolate the physical quantities from the fluid domain using so-called "ghost nodes", properly placed within the fluid particles neighbouring the open boundary. The placement of ghost nodes is calculated through mirroring the position of the buffer particle into the fluid domain, following the normal direction to the open boundary. When extrapolating fluid properties from the ghost nodes, the idea for retrieving quantities of the buffer particles is to perform an interpolation at the ghost nodes, and then transport that information back to the buffer particles. However, a standard SPH particle interpolation would not be consistent. Due to the proximity of these nodes to an open boundary, and thus not fully surrounded by fluid particles, the kernel would be truncated. Therefore, to obtain first-order kernel and particle consistency, the method proposed by Liu and Liu (2006) is applied (Domínguez *et al.*, 2022; Verbrugghe *et al.*, 2019).

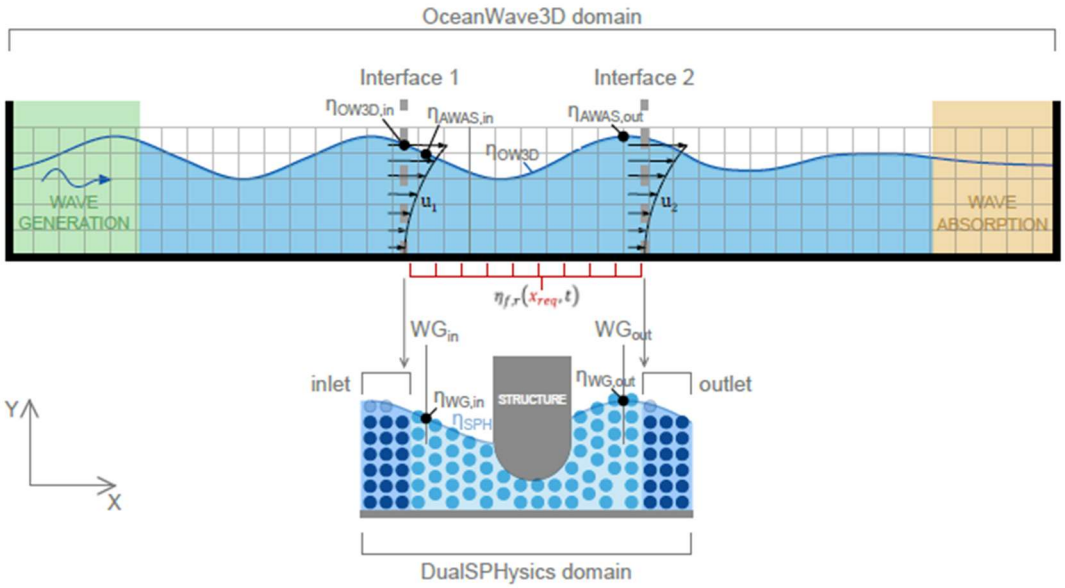

Fig.24 – General sketch of coupling methodology between the OceanWave3D (top) and the DualSPHysics domain (bottom) (Verbrugghe *et al.*, 2019).

Verbrugghe *et al.* (2019) presented an improved two-way coupling with OceanWave3D, employing the open boundary algorithm at the coupling interfaces, as illustrated in Fig.24. At the inlet, horizontal orbital velocities and surface elevations are imposed on the buffer particles. At the outlet, horizontal orbital velocities are imposed, while surface elevation is extrapolated from the DualSPHysics fluid domain. A velocity correction algorithm based on linear shallow water theory is applied for absorbing wave reflection in the SPH fluid domain. The DualSPHysics surface elevation is coupled back to OceanWave3D to replace the original signal. Inherently, open boundaries allow coupling in shallow waters, where wave non-linearity and mass transport are dominant (*e.g.,* in wave breaking zone) (Domínguez *et al.*, 2022).

(iii) Multi-layered piston wavemaker (Altomare *et al.*, 2015a) consists of a set of boundary particles that are bound together but do not move as a whole rigid body. The real time horizontal displacement of the multi-layered piston wavemaker is reconstructed based on the velocity time series calculated by one model employed for wave propagation (*e.g.*, OpenFOAM, SWASH, OceanWave3D) and interpolated along the water depth at a specific x-coordinate (here the *x*-axis corresponds to the direction of wave propagation). This coupling technique is a one-way offline coupling with no reflection compensation; therefore, its use is recommended for low-reflective cases or very short time series (Domínguez *et al.*, 2022; Mitsui *et al.*, 2021).

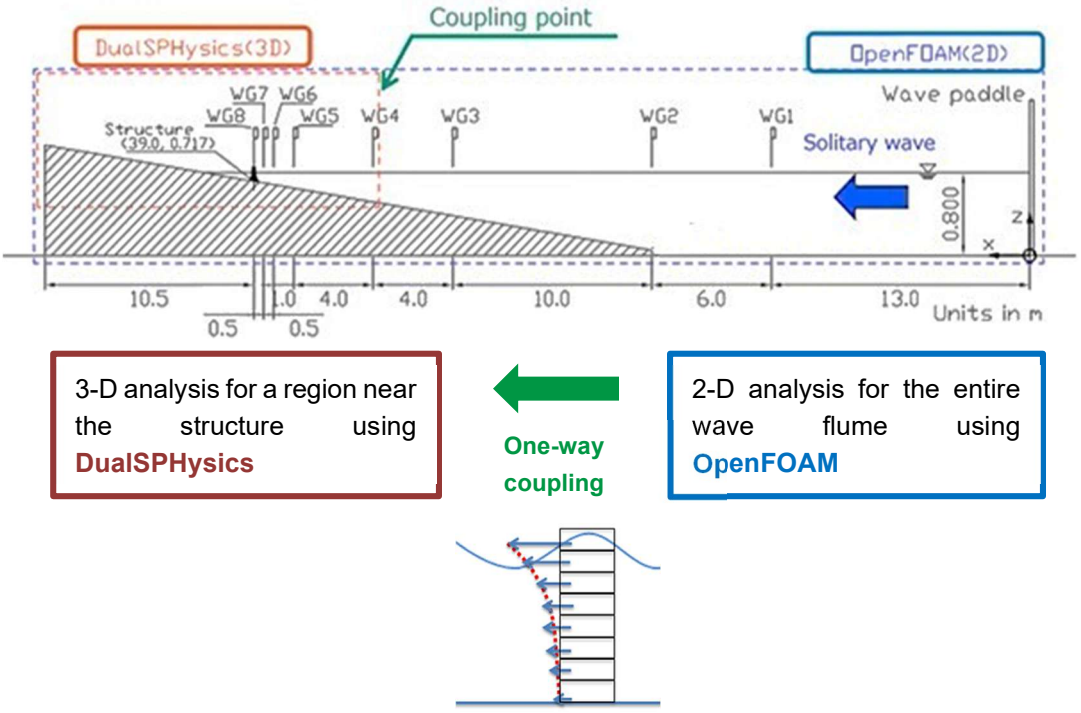

Fig.25 – Scheme of the multi-layered approach (adapted from Mitsui *et al.*, 2021)

- **Coupling with Project Chrono**

A set of problems common to coastal and maritime engineering corresponds to the simple simultaneous solid-fluid and solid-solid interactions. DualSPHysics offers a solid-solid Distributed Contact Discrete Element Method (DCDEM) model, in which the general concept is to compute the forces acting on the

fluid-solid particle pair using the SPH formulation and the solid-solid interactions via DEM, retaining the same explicit integrator and the software meshless framework. However, this model presents some drawbacks, which are common to all general DEM formulations: the explicit nature may impose very small stability regions (not unconditionally stable contact description), complex friction models are either computationally expensive or inaccurately reproduced, being difficult to model intricate mechanisms (Martínez-Estévez *et al.*, 2023).

Given the limitations of the DCDEM approach for general simulations, the use of a Differential Variational Inequality (DVI) based non-smooth multibody dynamics solver is encouraged, allowing for efficient and accurate modelling of fluid-mechanism interactions, a ubiquitous scenario in nature. So, an open-source integrated framework to model fluid-structure-structure coupled systems is presented by implementing the open-source high-performance library Project Chrono under DualSPHysics. The SPH fluid model deals with flow non-linearities, free-surface and intense topological changes, while the rigid body dynamics available in Project Chrono handle discontinuous frictional contacts and kinematic restrictions. The interactions between bodies are computed in a similar fashion to the DEM implementation, but in a more stable manner. In addition, thanks to the efficiency of the DVI formulation, the impact on the computational time is residual, allowing the simulation of large and complex Multiphysics systems (Martínez-Estévez *et al.*, 2023).

The Project Chrono library (Tasora *et al.*, 2016) is coupled with DualSPHysics to address fluid-structure interaction problems, particularly those involving mechanical constraints on rigid bodies. The initial description and validation of this coupling are detailed in Canelas *et al.* (2018), where a simply supported platform exposed to a dam break scenario demonstrated collapse and partial transport of the structure. Additionally, Martínez-Estévez *et al.* (2023) introduced a restructured version of the DualSPHysics code, coupled with the multiphysics library in a co-simulation environment, enhancing its applicability to industrial problems. Martínez-Estévez *et al.* (2023) also conducted a thorough validation of the collision detection algorithm, following the experimental setup by Hagemeier *et al.* (2021). The results showed good agreement between the numerical and experimental data for the vertical component of a fully submerged sphere falling and impacting the bottom surface of a steel tank.

The implementation strategy couples both models with a message-passing interface. The DualSPHysics implementation is mainly split into three steps: (i) creation of the neighbour list, (ii) particle interaction where force between particles is solved, and (iii) the variables of the system are updated at the new time step. During the particle interaction, the DualSPHysics code computes the force exerted on the fluid-driven object. Once the quantities from the rigid bodies are computed, the time step (Δt_{SPH}), along with the linear and angular acceleration (dV/dt, $d\Omega/dt$) to be applied in the center of mass of the object, are transferred to the Chrono library. During that time step, Project Chrono returns the linear and angular velocities, as well as the movement and the new position of the gravity center, computed by integrating the fluid contributions and considering the mechanical constraints of the system, including collisions.

The collision detection is activated when the distance between two approaching objects is less than a user-defined minimum distance. Therefore, Project Chrono uses the outer envelope surface of those objects to detect collisions in terms of surfaces (not in terms of particles). Remember that two rigid bodies should not penetrate, and, if they are in contact, there should be friction acting at the interface. To enforce the non-penetration constraint, a function, $\phi(q)$, called the gap function, is used that satisfies (Martínez-Estévez *et al.*, 2023):

$$\phi(q) = \begin{cases} > 0, & \text{Bodies are separated} \\ = 0, & \text{Bodies are in contact} \\ < 0, & \text{Bodies are interpenetrating} \end{cases} \quad (97)$$

If a position q is feasible and the contact is active ($\phi(q) \geq 0$), then at the contact point exists a normal force and a tangential force. The normal force (F_n) is solved using the expression:

$$F_n = k_n \delta_n^{3/2} \hat{n} - c_n \delta_n^{3/2} v_n \quad (98)$$

where k_n is the normal stiffness, c_n is the normal damping, v_n is the normal component of the relative velocity at the point of contact, δ_n is the normal overlap, and n is the unit vector pointing from one particle center to the other (or from one surface object to the other). The values of normal stiffness and damping depend on user-defined material properties like Young's modulus, Poisson's ratio, and coefficient of restitution. The tangential force (F_t) follows the Coulomb friction condition that defines a maximum allowable force $|F_{t,max}| = \mu_s |F_n|$, but can be written in a general way as:

$$F_t = \min \left[\mu_s |F_n| \frac{\delta_t}{|\delta_t|'} - k_t \delta_n^{1/2} \delta_t - g_t \delta_n^{1/4} v_t \right. \quad (99)$$

where μ_s is the coefficient of static friction that defines when passing from tangential sticking to tangential slipping, k_t is the tangential stiffness, v_t is the tangential component of the relative velocity at the point of contact, and δ_t is the tangential displacement vector. The normal and tangential forces computed on each body as a result of the collision are included in the basic equations of the rigid body dynamics to compute the final motion of the solids.

Finally, DualSPHysics updates the data of the rigid body particles according to the information received from Project Chrono. The coupling between these two models and the implemented constraints allows the modeling of many different and complex cases. However, one should not forget that Project Chrono is a library, not an application, and like DualSPHysics, the code is in active development. Additionally, Project Chrono uses only CPU, leading to high computation times when dealing with meshes with high triangle counts (Martínez-Estévez *et al.*, 2023).

3.3.4 CODE AND IMPLEMENTATION

SPH has traditionally been an expensive computational method. The main problem with its application to real engineering problems is the excessively long computational runtimes. Note that real problems require high resolution, large areas and long periods of time which implies simulating millions of particles and a high number of interactions with neighbouring particles for each particle (typically 40 in 2D and 250 in 3D). Besides, the computational cost increases when the number of particles grows, and small-time steps are required due to the use of explicit time integrators in WCSPH. Consequently, the time needed to simulate a few seconds is too large, and one second of physical time can take several days of calculation (Domínguez, 2014; Moreira, 2021).

Making SPH more appropriate and versatile for engineering applications requires hardware acceleration and parallel computing. Notice that the choice of hardware determines the options of parallelization technique. For example, initially, the implementation of hardware acceleration for CFD calculations was usually done by using High-Performance Computing (HPC) on parallel (supercomputers) machines consisting of thousands of Central Processing Units (CPU) cores. Despite they can be easily programmed, general purpose processors CPUs are not the best architecture to make faster scientific computations (Moreira, 2021). More recently, General Purpose Graphic Processing Units (GPUs) presented themselves as a disruptive technology and an accessible tool to accelerate SPH and all numerical methods. The main HPC techniques used to reduce computation times by including multiple techniques of parallel computing and distributed computing that allow the execution of several operations simultaneously are summarized in Table 10 (Domínguez, 2014).

DualSPHysics is developed to run on two different hardware architectures: the traditional CPU and the more recent GPU. The programing language C++ is used to code the SPH formulation for CPU execution, but also implements the main program logic and all tasks not related to SPH calculation, such as the initial configuration and input/output data. The GPU execution is performed using the Compute Unified Device Architecture (CUDA), which is a NVDIAS's parallel computing platform that allows software to use GPU capabilities, designed to work with C/C++ language. Therefore, the parallel power computing of GPUs can be also applied for SPH formulation where the same loops for each particle during the simulation, kernels or functions can be executed on GPU rather than CPU (Domínguez, 2014).

This dual capability of DualSPHysics execution provides significant advantages but also some drawbacks. Among the advantages (Domínguez, 2014):

- This code can perform extensive simulations using the computational power of the GPUs. It can also run simulations on workstations without GPUs, using the current multicore CPU version of the code;
- This solver enables fair comparisons in both CPU and GPU since the SPH formulation is implemented, in an optimized way, to best perform on both hardware architectures. The implementation of these algorithms is complex, leading to undetected errors. One can draw comparisons between these two implementations as it is easier to understand the native C++ code used for CPU implementation than the CUDA instructions for the GPU execution.

With the advent of more mature compilers and development environments, the CPU code has become more accessible than the GPU one, principally when modifying and debugging. It represents an attractive option for users approaching DualSPHysics for the first time. This is paramount since this solver was developed as an open-source framework for the SPH method, and researchers use it to create and test new formulations.

The main drawback is the higher maintenance cost of the solver and optimization of new functionalities since it is necessary to maintain two different implementations and apply different optimization strategies for each architecture (Domínguez, 2014; Domínguez *et al.*, 2013).

Table 10 – Description, advantages, disadvantages and examples of three different HPC techniques.

HPC Technique	Description	Advantages	Disadvantages
OpenMP Open Multi-Processing 	Best option to optimize the performance of the multiple cores of the Central Processing Units (CPUs).	▪ Model of parallel programming for systems of shared memory. ▪ Portable and flexible programming interface using directives. ▪ Its implementations do not involve major changes in the code.	▪ The improvement is limited by the number of cores.
MPI Message Passing Interface 	Best option to combine the resources of multiple machines connected via network.	▪ Message-passing library specification for systems of distributed memory: parallel computers and clusters. ▪ Several processes are communicated by calling routines to send and receive messages. ▪ The use of MPI is typically combined with OpenMP in clusters by using a hybrid communication model.	▪ Very expensive for a small research group. ▪ The use of MPI implies an over cost in terms of communication (time dedicated to the interchange of data between processes) and synchronization.
GPGPU General-Purpose Computing on Graphics Processing Units 	Best option to manage huge amounts of data, since their computing power has increased much faster than conventional CPUs.	▪ It involves the study and use of parallel computing ability of a GPU to perform general purpose programs. ▪ GPUs are designed for graphics rendering and provide a high calculation power with very low cost and without expensive infrastructures. ▪ New general purpose programming languages and APIs (such as Brook and CUDA) provide an easier access to the computing power of GPUs. Researchers and engineers of different fields are achieving high speedups implementing their codes with the Compute Unified Device Architecture (CUDA) platform.	▪ New implementation of the algorithms used in CPU is necessary for an efficient use in GPU. ▪ An efficient and full use of the capabilities of the GPUs is not straightforward. ▪ Optimizing a SPH code to be run on GPUs is dependent upon the GPU characteristics used (*e.g.*, compute capability, number of cores, number of registers and cache memory).

3.3.4.1 Implementation

For the implementation of SPH, the code is organized in three main steps that are repeated each time step till the end of the simulation: (i) **neighbour list** (NL); (ii) **particle interactions** (PI), and (iii) **system update** (SU). Table 11 presents the flow diagram of the CPU implementation and a description of each of the steps mentioned above (Domínguez, 2014).

Table 11 – CPU implementation flow diagram and implementation steps description.

CPU implementation

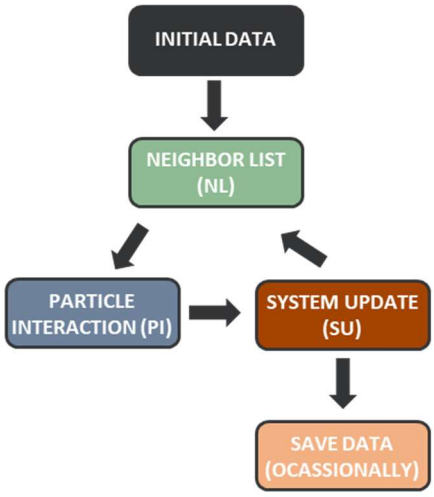

Neighbour list (NL): it prepares the data needed to find the neighbouring particles of each SPH particle efficiently in the next task. DualSPHysics implements a cell-linked list approach. First, the simulation domain is divided into cubic cells of size *2h* (using the Wendland kernel). Then, a list of particles, ordered according to the cell to which they belong, is generated; finally, all the arrays with the physical variables belonging to the particles are reordered according to the list of particles. Despite representing a small percentage of the total execution time, this task is crucial to optimize the performance of the subsequent step.

Particle interactions (PI): computation of the forces between particles, solving momentum and continuity equations by the interaction of each particle with its neighbouring particles. The neighbour search is performed efficiently since, for each particle, only the particles of the same cell and adjacent cells are candidates to be neighbours and will contribute to the particle interaction. Each particle interacts with all its neighbouring particles (at a distance < *2h*). The PI is the most time-consuming task, representing more than 95% of the total execution time.

System update (SU): starting from the values of computed forces, the physical quantities of the SPH particles (position, velocity, density) are updated for the next simulation step.

Other less important but necessary tasks are the initial configuration (**Initial Data**) and data loading (**Save Data**), which are executed once at the beginning of the calculation, and during the periodic data output, where particle information (velocity and density) is saved on local storage (the hard drive) at defined times (usually performed every hundreds or thousands of simulation steps).

The GPU implementation presents some key differences compared to the CPU version. The main difference being the parallel execution of all tasks that can be parallelised, such as all loops regarding

particles. There are two options for GPU implementation: partial GPU implementation or full GPU implementation. The first one is focused on force computation since this is the most time-consuming part regarding runtime (see Fig.26). Each GPU execution thread computes the interaction between a target particle and its neighbours. However, the most efficient technique is minimising communications between the CPU and GPU for the data transfers, performing DualSPHysics' calculations entirely on the GPU (see Fig.26). When implementing neighbour list and system update on the GPU, the CPU-GPU memory transfer is needed at (Domínguez *et al.*, 2022):

- the beginning of the simulation, where a copy of all particle data is done to the GPU memory,
- relevant data transfer to the CPU memory when saving output data in the long-term memory is required, which occasionally happens during the simulation and thus with negligible impact on performance.

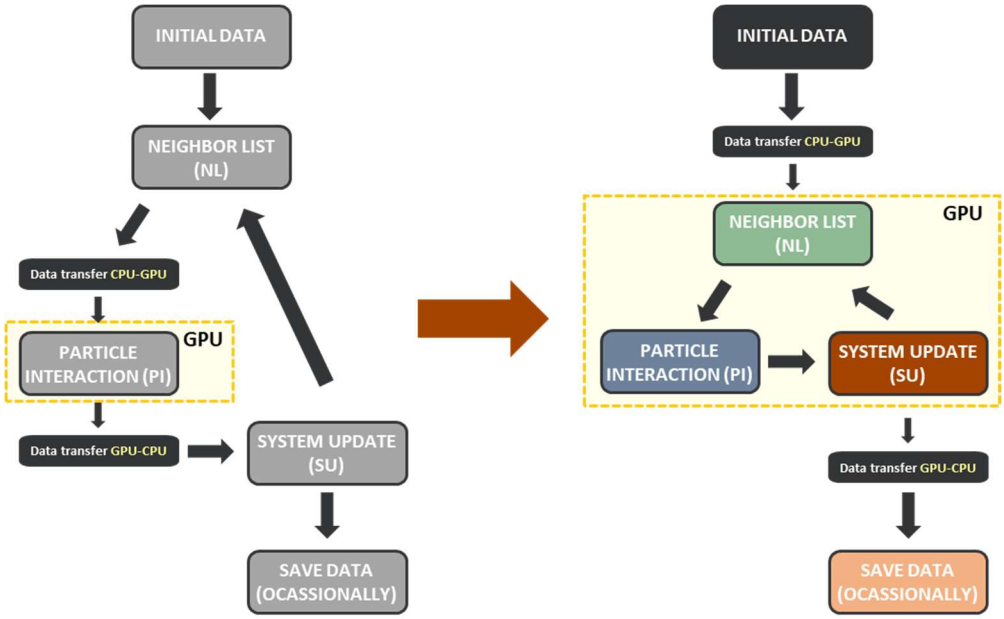

Partial GPU implementation

GPU is used only in PI, which consumes over 90% of the execution time.

Drawback: Particle data and NL information must be transferred from CPU to GPU, and the interaction results from GPU to CPU each time step.

Full GPU implementation

Using GPU in all steps (NL, PI and SU) is the most efficient approach.

All particle data is kept in GPU memory, and the transfers CPU-GPU are removed.

A speedup in this part of the code can be achieved by parallelizing NL and SU steps.

Fig.26 – Partial GPU implementation (left) and Full GPU implementation (right) flow diagrams.

3.3.4.2 Performance

The SPH is computationally demanding. It is therefore essential to apply optimization strategies for CPU and GPU implementations, such as presented by Domínguez *et al.* (2013) to maximize the performance. For example, the principal CPU optimization corresponds to the implementation of multi-core programming. Current CPUs have several cores or processing units, so it is essential to distribute

the computational load among them to maximize the CPU performance and accelerate the SPH code. As mentioned previously, improving SPH applications requires hardware acceleration and parallel computing. Depending on the hardware, which choice determines the parallelization techniques options, and the HPC techniques previously presented, five basic programming options exist:

(i) Single thread (one task after another),
(ii) Multiple cores using OpenMP (shared memory) – divide the task into different parts, but they compete using the same memory,
(iii) Multiple Processes in Multiple Nodes using MPI (distributed memory) – four different computer cores that don't have shared memory. The communication back and forwards need to be done correctly,
(iv) MPI and OpenMP,
(v) CPU and GPU.

As mentioned above, there are two main options to implement a parallel code in CPU: MPI or/and OpenMP. In DualSPHysics, the CPU implementation uses the application programming interface OpenMP to perform parallel execution of the SPH method on one or several multi-core CPUs hosted on the same workstation or computation node. Each CPU thread executes, in parallel, the interactions with the neighbours of a given set of particles. Meanwhile, a CUDA thread is created to compute the interaction of each particle on GPU (Domínguez *et al.*, 2022). Efficient and full use of the capabilities of the GPUs is not straightforward, being necessary to know and consider the details of the GPU architecture (*e.g.*, compute capability, number of cores, number of registers, and cache memory) and the CUDA programming model. The use of one GPU presents relevant limitations, namely the memory size of the GPU and the execution time. The memory size of the GPU limits the maximum number of particles. This limitation can be eliminated, in DualSPHysics, by using a multi-GPU approach. Initially, this approach used the MPI to combine the computation power of different GPUs hosted in the same or different computation nodes. This approach considers the simulation physical domain division into subdomains so that the size of the simulation scales with the number of machines. Each MPI process only needed to assign resources to manage a subset of the total amount of particles for each subdomain. However, the use of MPI implies an over cost in communication – time dedicated to the interchange of data between processes – and synchronization – all processes must wait for the slowest one (Domínguez 2017). Solutions, such as overlapping between force computation and communications and load balancing, were used to minimize the drawbacks of MPI use. However, consumers can now easily purchase desktop machines or a single compute node with 4-8 GPUs for only a few thousand euros. It allows the simulation of a limit of 200 million particles. In that way, a new multi-GPU code optimized for multi-GPU machines allows more efficient communication, including the MPI removal.

The runtime is one way of DualSPHysics performance measurement. The execution time increases rapidly with the number of particles since each particle interacts with more than 200 neighbouring particles in 3D. However, the total execution time is also influenced by other factors, such as:

- the resolution whose increase leads to the growth of the number of simulation steps per physical second,
- the rapid time-varying events, which demand a small timestep during the simulation,
- the distribution of fluid in the simulation domain, which can increase or reduce the total number of interactions between particles,
- the physical time to be simulated,
- the complexity of the chosen formulations,
- some hardware features.

Another way to measure the performance of DualSPHysics is through Particle Interactions Per Second (PIPS), by focusing on the actual number of particle interactions regardless of the number of simulation steps, the particle's amount, or their distribution during the simulation. It is relevant to bear in mind that the performance of the computing devices increases according to the size of the problem since an efficient and full use of the hardware needs a minimum number of particles. So, one can consider the device saturated when the performance does not increase as the number of particles increases. The GPIPS (10^9 PIPS) value is almost constant when the number of particles is large enough to saturate the calculation device (Domínguez *et al.*, 2022).

3.3.4.3 Pre- and Post-processing tools

The DualSPHysics package includes the binaries executables for Linux and windows, the source files of the SPH executable, some documentation, including DualSPHysics guides and help, and a lot of examples of working cases (Fig.27). It also includes advanced pre-processing tools to create more complex geometries and post-processing tools for analysis of the numerical results. The pre-processing tools exist to convert into SPH particles any complex geometry, loaded from different format files like CAD, 3ds, STL, ply, dwg, DXF, shp, IGS, vtk, csv, and to provide configuration for simulation. Post-processing tools allow the calculation of quantities of interest, such as forces exerted on different objects, maximum wave heights, or just plotting particle's different physical quantities (Fig.27) (Crespo et al., 2015).

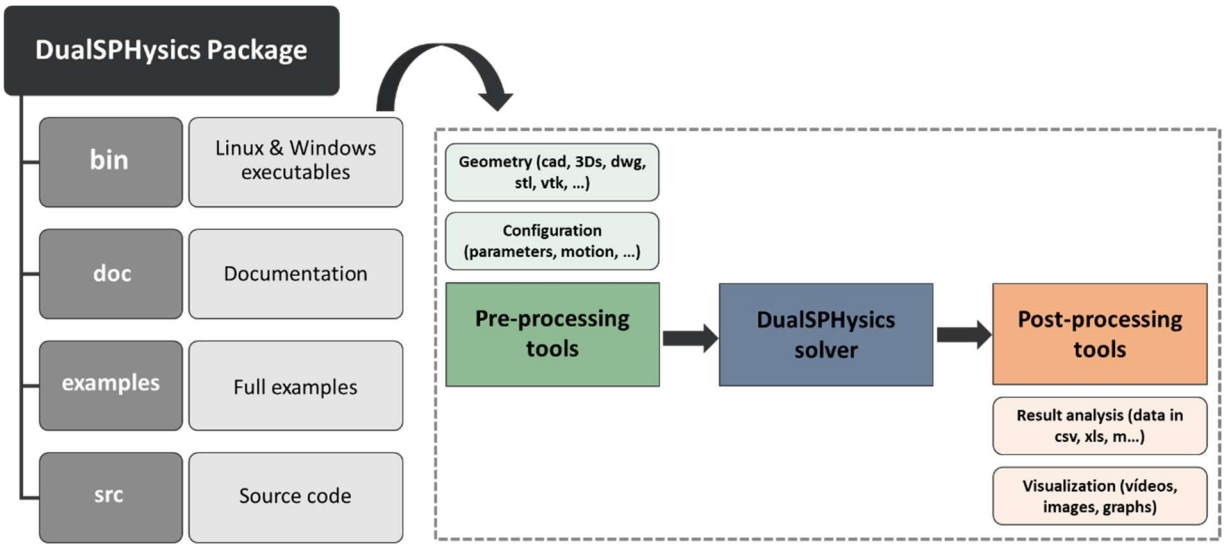

Fig.27 – DualSPHysics package's content and workflow.

Fig.28 shows the program's working scheme with representative examples of executable input and output files. Next, some of the codes and main tools of DualSPHysics will be explained in more detail (Crespo *et al.*, 2015).

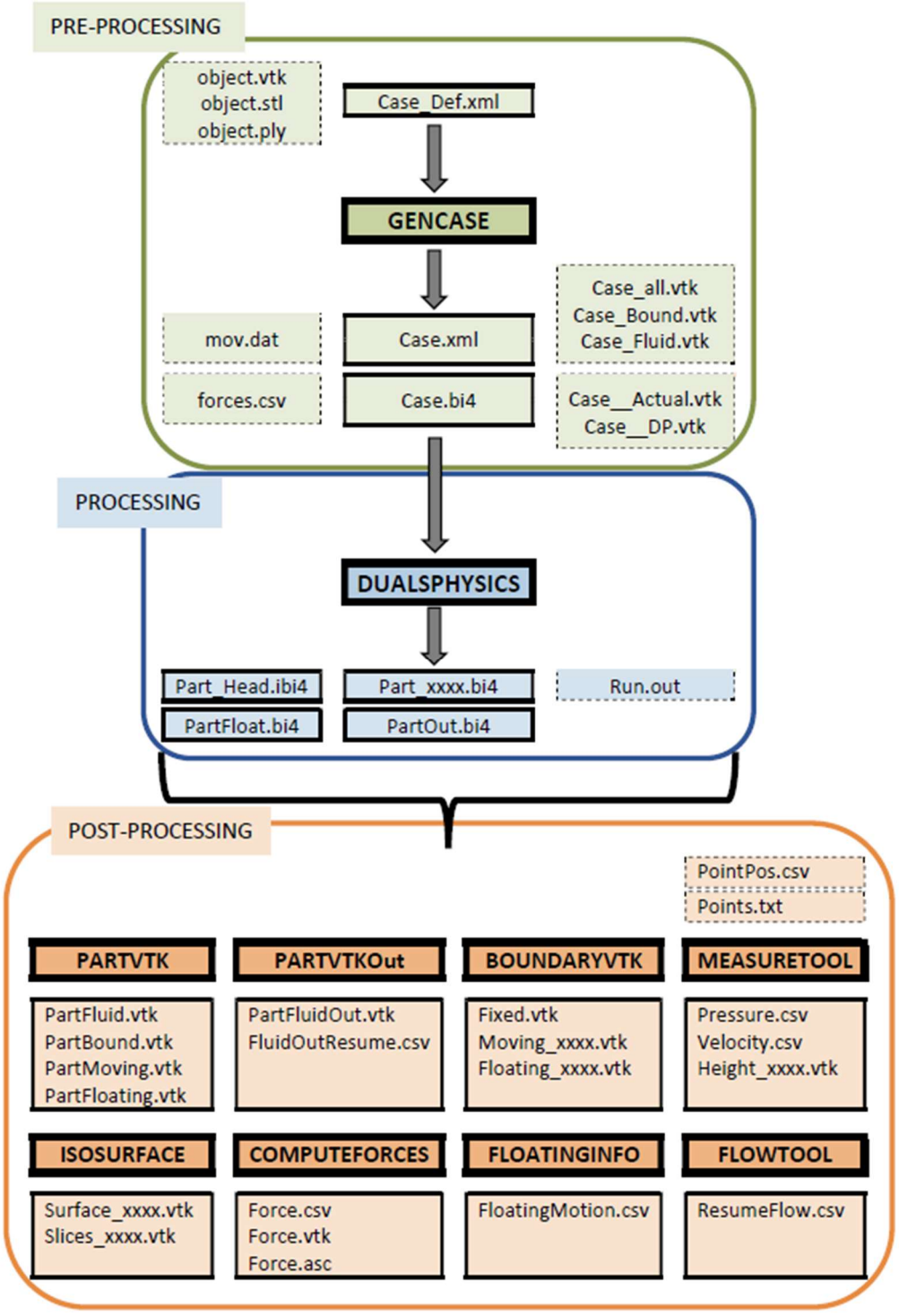

Fig.28 – DualSPHysics' workflow with representative example of input and output files of the executable files.

The pre-processing step includes a program named GenCase to define the initial configuration of the simulation, movement description of moving objects and the execution parameters in DualSPHysics. A definition input file (Case_def.xml), in XML format, contains all this information and divides into two sections:

(i) **casedef**: this section, created by the user and used by the GenCase program, allows the definition of the case with initial geometry and configuration. It includes information such as:
- the constants needed in SPH (constantsdef), among which are the speed of sound (coefsound), the coefficient to calculate the smoothing length (coefh),
- label configuration (mkconfig),
- the system geometry ("geometry"). In this subsection is defined the distance between particles (*dp*) and the minimum and maximum dimensions of the domain where particles can be created (pointmin and pointmax),
- special features for boundary and fluid particles ("initials"),
- the description of floating objects ("floatings") and
- the boundary movement description (motion), for example, a wave paddle movement imposed by an external file resultant from the experimental model.

(ii) **execution**: this section is created by the user, modified by GenCase and only used by the DualSPHysics solver. It contains the information required to execute the case, which includes:
- the configuration of different features used in DualSPHysics simulation ("special"), namely the automatic wave generation, the active wave absorption system, wave gauges, collisions using Project Chrono, and external forces,
- the execution parameters in DualSPHysics (<parameters>), among which are the kernel type, the viscosity treatment (ViscoTreatment), the maximum simulation time (TimeMax), and the timestep (TimeOut).

In the XML guides available on the software package, one can find a complete description of the code and XML files. These documents help in a new case generation, using the XML file as input, and explaining all the XML parameters by relating them to the SPH equations.

After the XML file creation, GenCase employs a 3D Cartesian mesh to locate particles. The idea is to build any object using particles. Two output files are created after running GenCase: Case.xml and Case.bi4, corresponding to the input files for DualSPHysics code. Particle geometries created with GenCase can be initially verified by visualising in ParaView software the files Case_All.vtk, Case_Bound.vtk and Case_Fluid.vtk.

The processing step corresponds to running the SPH simulation using the particles, resorting to the main code, named DualSPHysics. The input files to run DualSPHysics code include one XML file (Case.xml) and a binary file (Case.bi4). The Case.xml contains all the parameters of the system configuration and its execution. It includes relevant variables (smoothing length, reference density, gravity, coefficients to compute pressure starting from density, speed of sound, etc.), the number of particles in the system, movement definition of moving boundaries and properties of moving bodies. Case.bi4 contains the initial state of particles (number of particles, position, velocity, and density) in a BINX4 format. The output files consist of files in binary format with information about the particles for different times of the simulation (Part0000.bi4, Part0001.bi4, Part0002.bi4, etc.), files with excluded particles (PartOut.obi4) and a text file with the run log (Run.out).

Finally, the DualSPHysics package possesses a set of post-processing tools useful for the analysis of simulation results, including the calculation of magnitudes using particle data and visualization starting from SPH particles. A list of these tools and their description is presented below (Crespo, 2020b):

- PartVTK code converts the DualSPHysics output binary files into a different format that can be visualized.

- PartVTKOut code generates files with the particles excluded from the simulation for one of these three reasons: position, density, and velocity. For example, when one particle moves beyond the limits of the domain, the particle is excluded.
- BoundaryVTK code creates triangles or planes to represent the boundary shapes formed by the boundary particles.
- IsoSurface code creates surfaces using the marching cubes algorithm. This computer graphics technique extracts a polygonal mesh of an isosurface from a 3D scalar field. It helps to improve the visualization of the simulation by representing surfaces instead of particles.
- FloatingInfo code uses PartFloat.fbi4 and other binary files as input to obtain different data of the floating objects, such as linear velocity, angular velocity, displacement of the centre, motions and angles of rotation.
- MeasureTool code allows the computation of different physical quantities (velocity, pressure, free-surface elevation) at a set of given points by means of an SPH interpolation of the values of the neighbouring particles around a given position (see Table 12). It enables the comparison between experimental and numerical values.

Table 12 – Computation schemes and equations of different physical quantities.

Physical quantities	Computation Schemes	Equation
Velocity	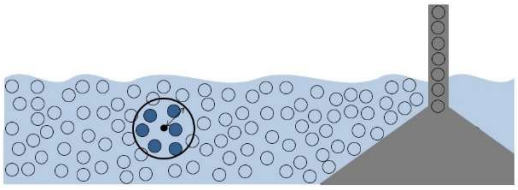	For a given location, is computed the numerical velocity using velocity values of neighbouring fluid particles: $V_a = \frac{\sum_b V_b W_{ab}}{\sum_b W_{ab}}$
Pressure	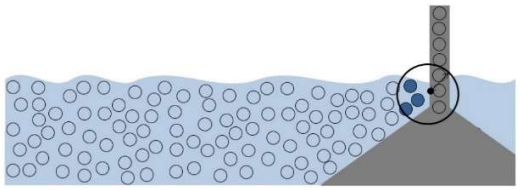	For a given location, is computed the numerical velocity using velocity values of neighbouring fluid particles: $P_a = \frac{\sum_b P_b W_{ab}}{\sum_b W_{ab}}$
Free-surface elevation	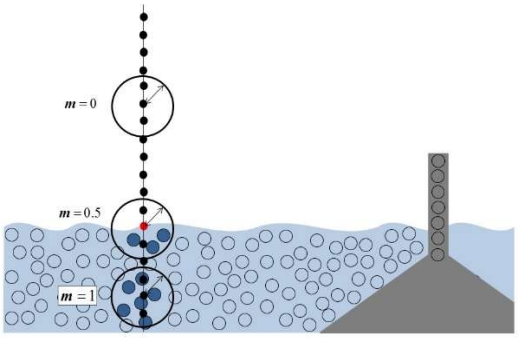	For a given (X,Y) position numerical mass is computed at different Z positions using mass values of neighbouring fluid particles: $m_a = \sum_b m_b W_{ab}$ One will choose as wave elevation the Z value for which $m = 0.5 \times m_{reference}$.

- ComputeForces code computes the force exerted by the fluid onto a boundary object. The force value is the summation of the acceleration values multiplied by the mass of each boundary particle that form that object (Fig.29).

- FlowTool code calculates the number of fluid particles that enter or leave the domain defined by the user and the average velocity of the particles that enter that domain. This tool is appropriate to compute discharges or overtopping in the case of coastal protection since it is easy to determine the inflow and outflow. First, one can calculate the volume in some defined domain by multiplying the volume of just one particle by the number of particles. Then, one obtains the inflow by dividing the fluid volume by the interval time (output time).

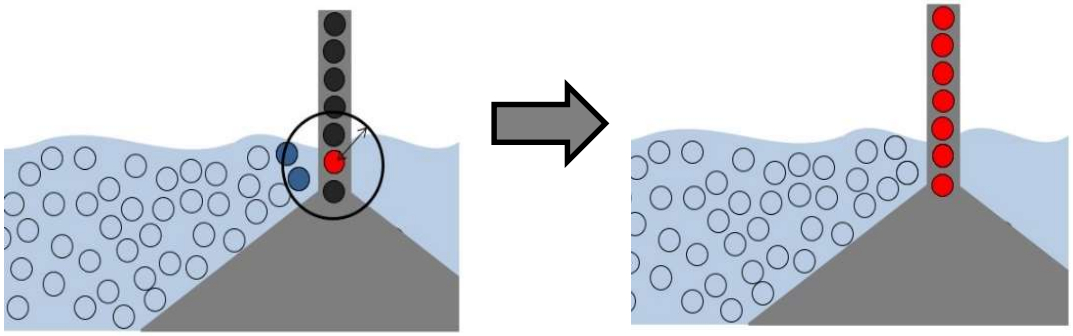

For a range of boundary particles, the numerical acceleration of those boundary particles is computed by solving the particle interactions with fluid neighbouring particles:

$$\frac{d\boldsymbol{v}_a}{dt} = -\sum_b m_b \left(\frac{P_b}{\rho_b^2} + \frac{P_a}{\rho_a^2} + \Pi_{ab} \right) \nabla_a W_{ab} + \boldsymbol{g}$$

It is done the summation of acceleration values of those boundary particles:

$$F = m \sum \frac{d\,\boldsymbol{v}_a}{dt}$$

Fig.29 – Scheme of computation of forces exerted by the fluid on the boundary.

3.3.5 APPLICATIONS

DualSPHysics evolved significantly over the last years. The validation of the features developed in its different versions with analytical solutions, numerical benchmarks and experimental results demonstrate accuracy and convergence. As mentioned previously, one of the code's key fields of application is coastal engineering, employing the model as a complementary tool to experimental measurements. The accurate modelling of wave generation and propagation is a fundamental requirement for proper capturing the wave-structure interaction phenomena. By gaining a detailed insight into the physics involved and structure responses, engineers have the potential means to optimise the structure's design and improve its survivability. Table 13 includes some relevant works focused on coastal engineering applications of DualSPHysics published over the last almost ten years, emphasising validated applications (Domínguez *et al.*, 2022).

Table 13 – Examples of coastal engineering and multiphysics simulations in the literature over the last years using DualSPHysics.

#	Reference	Main topics and achievements
Coastal structures		
1	Altomare *et al.* (2014)	▪ Regular waves colliding with a rubble-mound breakwater armoured with grooved cubic blocks ▪ Time series of wave run-up ▪ Comparison with empirical solutions and experimental data (Zeebruge breakwater)
2	Altomare *et al.* (2015a)	▪ Regular and random waves colliding with coastal structures with focus on wave impact on vertical structures and storm return walls ▪ Comparison with experimental data and analytical solutions
3	Altomare *et al.* (2015b)	▪ One-way coupling with the time-domain wave model based on a finite difference method - Simulating WAve till SHore (SWASH) ▪ Waves generated by means of a moving boundary (multi-layer piston) ▪ Comparison with experimental data
4	Pringgana *et al.* (2016)	▪ Tsunami-induced bore impact on onshore structure on a dry bed ▪ Coupling with Finite-Element (FE) using Abaqus to model the dynamic response of a representative timber structure ▪ Solitary waves with different characteristics generated by the numerical paddle wavemaker ▪ Numerical probes uniformly distributed on the structure's vertical surface providing detailed measures of the pressure distribution across the structure ▪ Comparison with semi-empirical approaches
5	Altomare *et al.* (2017)	▪ Numerical flume resembling a physical wave facility and moving boundaries mimic the action of a piston-type wavemaker ▪ Automatic wave generation (long-crested second-order waves and random waves) ▪ Passive (damping system) and active wave absorption (see Fig. 30) ▪ Comparison with experimental data and analytical solutions, in terms of water surface elevation, wave orbital velocities, wave forces and capacity for damping the re-reflection inside the fluid domain
6	Altomare *et al.* (2018)	▪ Coupling with the non-hydrostatic wave flow model SWASH (Relaxation Zone, RZ) ▪ Description of the procedure for a proper design of the RZ (*i.e.* shape of the weighting function, size of the RZ) ▪ Validation of wave generation and wave reflection for monochromatic waves employing RZ both as stand-alone wave generation technique and as coupling framework with SWASH model ▪ Test also for generation and absorption of irregular waves ▪ Comparison with experimental data concerning the wave flow impacts on vertical walls and theoretical solutions

Table 13 (cont.) – Examples of coastal engineering and multiphysics simulations in the literature over the last years using DualSPHysics.

#	Reference	▪ Main topics and achievements
7	Zhang *et al.* (2018)	▪ Regular waves interacting with porous breakwater (see Fig.31) ▪ Time series of wave run-up ▪ Comparison with experimental data (analyse of a real sea dike from the coast of Chongwu in China)
8	Roselli *et al.* (2018)	▪ Optimisation of model setup for wave propagation through genetic algorithms ▪ Comparison with theoretical solutions
9	Sarfaraz and Pak (2018)	▪ Regular waves interacting with low-crested breakwater constructed using cubic armour blocks. ▪ Coupling with Polyhedral – DEM ▪ Time series of fluid velocity and pressure near the armour units ▪ Time series of the vertical and horizontal forces (and moments) applied to various armour units ▪ Proposal of a practical non-dimensional relationship for calculating the required dimension of the cubic armour units, based on the numerical simulation results and used for preliminary design
10	Verbrugghe *et al.* (2019)	▪ Two-way coupling with OceanWave3D ▪ Open boundary conditions ▪ Validation using a 2D test case of a floating box in terms of its three degrees of freedom (heave, surge and pitch) ▪ Comparison with experimental data from Ren *et al.* (2015) ▪ 3D proof of concept considering overtopping waves acting on a heaving cylinder
11	González-Cao *et al.* (2019)	▪ Propagation of a regular wave train and its collision with a vertical sea wall with a hanging horizontal cantilever slab using SPH (DualSPHysics) and mesh based (IHFOAM) models ▪ Time series of free-surface elevation and horizontal force exerted on the wall ▪ Comparison with experimental data ▪ Comparison of the accuracy of DualSPHysics and IHFOAM considering different metrics (skill index, normalized standard deviation, correlation coefficient and root-mean square error)
12	Domínguez *et al.* (2019)	▪ Implementation of an advanced solitary waves generation system (different theories) to simulate tsunami-like solitary waves ▪ Comparison with analytical solutions and experimental data (forces exerted on harbour protections, run-up of solitary waves on a gentle beach, and the impact of double solitary waves on two cylindrical reservoirs)
13	Lowe *et al.* (2019)	▪ Spilling and plunging wave breaking within the surf zone ▪ Simulation of two distinct bathymetric profiles - a plane beach and a fringing reef ▪ Comparison with experimental data (measurements of waves flows and mean water levels)

Table 13 (cont.) – Examples of coastal engineering and multiphysics simulations in the literature over the last years using DualSPHysics.

#	Reference	▪ Main topics and achievements
14	Subramaniam *et al.* (2019)	▪ 3D modelling of wave-run on convex and concave dikes using SPH (DualSPHysics) and mesh based (OpenFOAM) models ▪ Regular waves ▪ Comparison with experimental results and mesh-based methods
15	Altomare *et al.* (2020)	▪ Large-scale structure (Pont del Petroli, around Badalona, Spain) under extreme wave conditions (storm Gloria, January 2020) (see Fig.33) ▪ Wave generation by Open boundaries to alleviate the high computational cost of a full 3D simulation ▪ Pier failure analysis – assessment and characterization of the wave loading that determined the structural failure ▪ Fist known application of SPH open boundary conditions to model a real-world engineering case
16	Mitsui *et al.* (2023)	▪ 3D modelling of the stability of Tetrapods armour units paced above a submerged mound against solitary waves (see Fig.33) ▪ Coupling with Project Chrono ▪ Time series of free-surface elevation, wave force exerted on the Tetrapods ▪ Comparison with experimental data (displacements of Tetrapods and damage ration under different solitary waves) ▪ Test of the stability for different coefficients of friction between mound and Tetrapods to simulate the effects of different materials and surface roughness
Multiphysics problems		
17	Canelas *et al.* (2015)	▪ Spatially detailed and time-resolved simulation of fluid-solid interaction ▪ Validation using a buoyancy-driven motion of an unrestricted rigid body ▪ Comparison of the model with numerical experiments and analytical solutions recovered from the literature ▪ Investigation on the influence of the stabilizing δ-SPH terms
18	Canelas *et al.* (2018)	▪ Simulation of a dam break flow impacting a supported platform to validate frictional contacts ▪ Coupling with Project Chrono (DVI solver) ▪ Comparison with experimental data (numerical times for movement initiation and the angle inversion times were consistent with the experimental ones) ▪ Test of different pendulum systems – gravity pendulum and spring pendulum ▪ Application cases to showcase the potential of the model: WaveStar, Tidal turbine, Ragdoll)
19	Ropero-Giralda *et al.* (2020)	▪ Simulation of point-absorber wave energy with power take-off system ▪ Coupling with Project Chrono ▪ Comparison with experimental data of regular waves interacting with the point-absorber (heave displacement and velocity of the device)

Table 13 (cont.) – Examples of coastal engineering and multiphysics simulations in the literature over the last years using DualSPHysics.

#	Reference	▪ Main topics and achievements
20	Hagemeier *et al.* (2021)	▪ Simulation of the settling process and wall impact of large spherical particles in a stagnant, highly viscous fluid ▪ Study of collision behaviour of spherical particles and wall effect ▪ Comparison of settling curves and settling velocities with experimental data and analytical solution for the Stokes and the Newton regimes
21	Martínez-Estévez *et al.* (2023)	▪ Two-way coupling with Project Chrono (SPH-FEA solver) to solve fluid-structure interaction ▪ Validation of the SPH-FEA coupling against four reference cases (e.g., dam break impacting a flexible obstacle) ▪ Comparison with other approaches presented in literature to prove accuracy of the novel model and performance and resource optimisation

Other relevant works involving overtopping analysis (Altomare *et al.*, 2021; Suzuki *et al.*, 2022) and wave interaction with breakwaters effects assessment (Wen *et al.*, 2018) were published in the last few years. Note that these works are merely qualitative analyses, not validating the numerical results using experimental results.

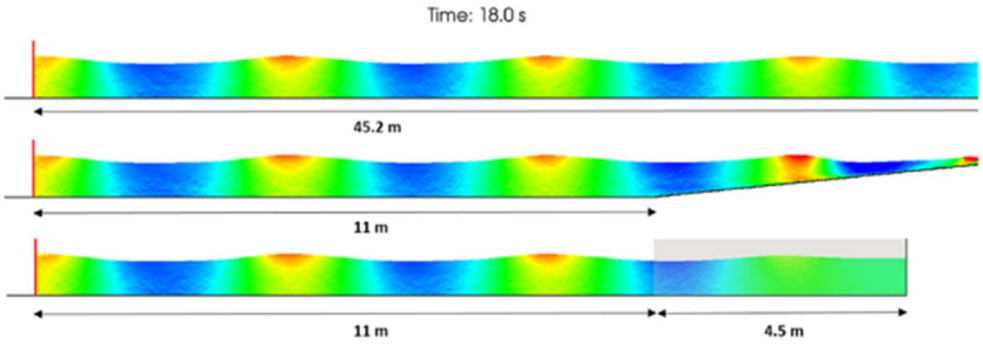

Fig. 30 – Instant of the simulation with regular waves and using a dissipative beach and damping area (grey plane) (Altomare *et al.*, 2017).

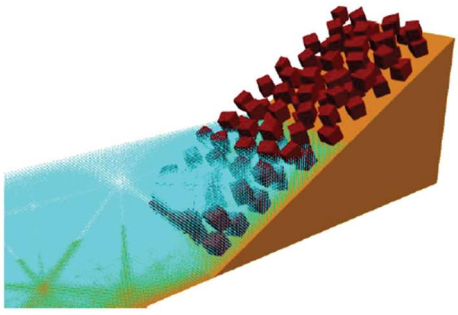

Fig.31 – Initial setup of the experiment with the armoured dike (Zhang *et al.*, 2018).

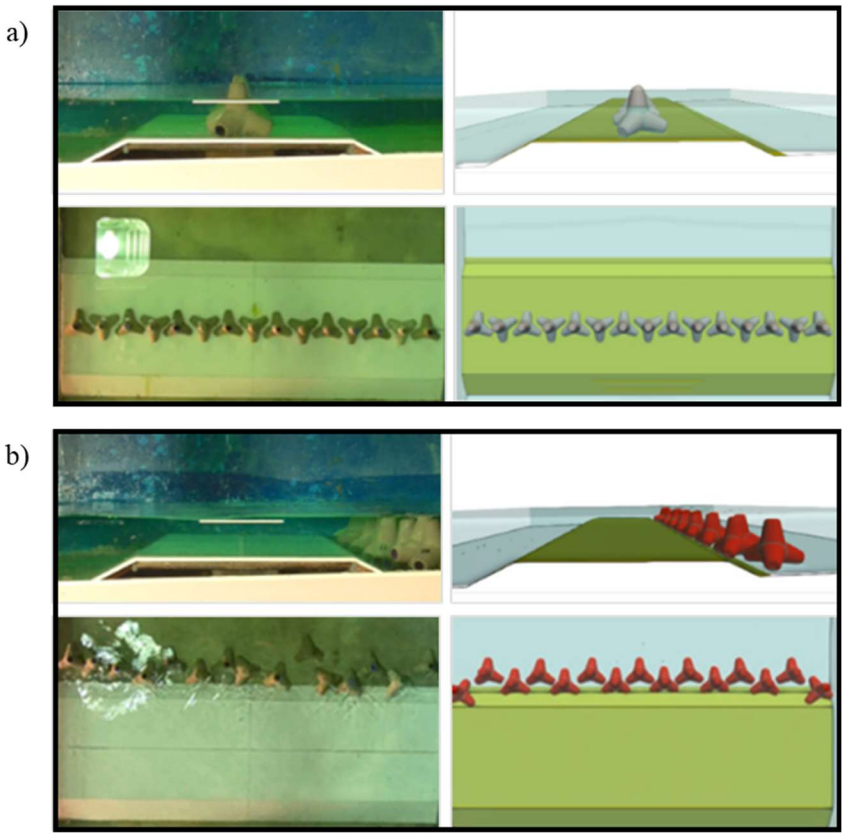

Fig.32 – Lateral and top views of the initial (a) and final situation (b) of the Tetrapods after the interaction with a solitary wave during the experiments (left) and with the numerical simulations (right) (adapted from (Mitsui *et al.*, 2023)

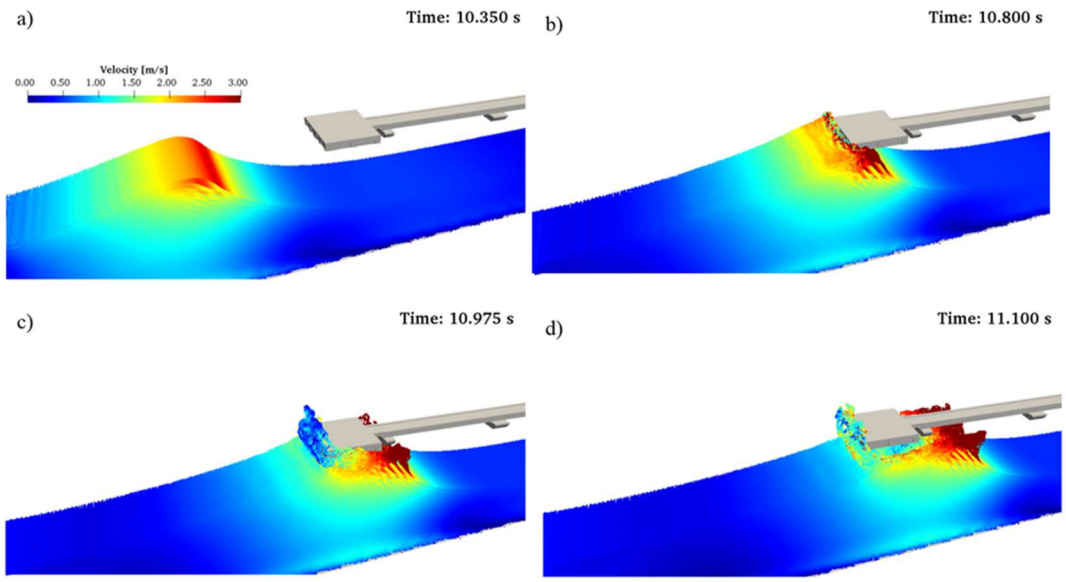

Fig.33 – Snapshots of the SPH horizontal velocity contours for a wave impacting the Pont del Petroli pier (Altomare *et al.*, 2020).

Taking into account the studies listed in Table 13, numbered from 0 to 20, Table 14 provides a summary of the SPH formulation and the functionalities employed in these works.

Table 14 – Summary of SPH formulation and functionalities employed in works from Table 13.

		1	2	3	4	5	6	7	8	9	10	11	12	13	15	16	17	18	19	20	21
SPH FORMULATION																					
Density correction	Density filters	•																			
	Density diffusive terms						•		•		•	•	•	•	•	•	•	•	•		•
	Riemann solvers																				
Particle shifting algorithm																					
Turbulence and viscosity in SPH	Artificial viscosity	•	•	•	•	•	•	•	•		•	•	•	•	•	•	•	•	•		•
	Laminar viscosity																			•	
	Sub-Particle Scale turbulence									•											
Boundary conditions	DBC	•	•		•	•	•	•	•	•	•	•	•	•	•		•	•			
	mDBC															•					•
	Periodic open boundary condition		•		•														•		
Time integrators	Verlet time integration scheme		•								•										
	Symplectic position Verlet scheme	•		•	•			•	•	•	•		•	•	•	•					•
	Variable time step						•		•				•	•	•	•					•
FUNCTIONALITIES																					
Wave generation	Moving boundary particles	•	•	•	•	•		•	•	•		•	•	•							
	Relaxation zones						•														
	Inlet open boundaries										•				•						
	Multi-layered piston moving boundaries															•					
Wave absorption	Passive wave absorption					•	•														
	Active wave absorption (AWAS)	•				•	•	•			•	•		•							
Coupling with other models	Wave propagation models			•			•				•										
	Project Chrono															•	•	•	•		•
	Others (FE models, etc.)				•				•	•											

3.4 CONCLUSIONS

Advanced computational fluid dynamics (CFD) has become a critical tool in coastal engineering, providing significant insights into the complex wave-structure interactions that are crucial for the design and analysis of rubble-mound breakwaters.

Among the available methods, Smoothed Particle Hydrodynamics (SPH) has proven particularly effective for tackling non-linear problems. Its meshless Lagrangian framework allows for the simulation of large surface deformations, dynamic free-surface flows, and intricate boundary conditions, making it a valuable complement to physical modelling. However, despite significant benefits of mesh-free methods like SPH, their applicability is not universal, facing challenges when addressing large-scale, three-dimensional problems in practical engineering contexts.

One of the primary challenges for SPH methods lies in their high computational demands and difficulty in scaling up to simulate large domains with complex geometries, porous structures, and multi-body interactions. DualSPHysics, a leading SPH solver, has made notable progress in overcoming these limitations by incorporating GPU acceleration and high-performance computing techniques. These advancements enable simulations of higher resolution and complexity, broadening its applications in coastal engineering.

Despite these improvements, replicating real ocean conditions remains a persistent challenge for both numerical and physical models. Laboratory facilities, no matter how sophisticated, are inherently limited in their ability to replicate the full complexity of natural ocean environments, even when accounting for factors such as wind, currents, and temperature gradients. This limitation extends to numerical models like DualSPHysics, which rely on simplifying assumptions and may exhibit discrepancies when compared to real-world behaviour. Key factors such as the non-repeatability of experimental tests and the need for wave re-reflection compensation must also be considered when interpreting numerical results.

Significant technical advancements in DualSPHysics have enhanced its reliability and performance. It employs the Weakly Compressible SPH (WCSPH) scheme, which is valued for its efficiency in modelling free-surface flows, though issues such as spurious noise in pressure and density fields persist. Refinements, including density diffusive terms (DDT) and artificial viscosity, have mitigated these issues, improving numerical stability and accuracy. Additional features such as modified Dynamic Boundary Conditions (mDBC) have further enhanced the solver's ability to simulate realistic wave-structure interactions, avoiding unphysical energy build-up and improving the fidelity of simulations.

The versatility of DualSPHysics has expanded further through its transition into a multiphysics framework, integrating libraries like Project Chrono to model rigid body dynamics. These developments allow for more comprehensive studies, such as wave-structure interactions and armour unit behaviour. Notable studies by Sarfaraz and Pak (2018) and Mitsui *et al.* (2023) have demonstrated the potential of coupling DualSPHysics with external models like Polyhedral DEM and Project Chrono to simulate wave forces and collision dynamics. These studies offer valuable insights into the stability of breakwaters and the performance of individual armour units under wave action, though more research is needed to explore these dynamics in detail.

Several recommendations emerge from the literature to guide future research and applications:

- For problems involving violent collisions with coastal structures, mesh-free methods such as SPH have achieved maturity in predicting macro-scale parameters like wave elevation and force.

- Hybrid approaches that combine the use of mesh-free and mesh-based methods is advisable to leverage their respective strengths and mitigate their limitations. For example, DualSPHysics has been validated for its wave generation capabilities using innovative techniques like Relaxation Zones and Input Open Boundaries. These advancements enable DualSPHysics to be efficiently coupled with external wave models such as SWASH and OceanWave3D, which are more computationally efficient for generating realistic waves.
- Active wave absorption systems are particularly effective mimicking real wave facilities and avoiding unphysical energy build-up. These systems are particularly suitable for studies involving sea wave interactions with coastal structures, while passive absorption systems are more appropriate for offshore applications such as wave energy converters and floating bodies.

In conclusion, the advancements in SPH methods, particularly DualSPHysics, underscore their growing utility in coastal engineering. While challenges persist, particularly in simulating fine-scale interactions and improving computational efficiency, ongoing refinements and robust validation against analytical solutions, numerical benchmarks and experimental data will further enhance their accuracy and applicability. Hybrid approaches that combine SPH with traditional mesh-based models hold significant potential for addressing complex engineering challenges. By dividing computational tasks effectively, these hybrid methods can focus on smaller, high-resolution domains, enabling more precise simulations of wave-structure interactions. These developments will play a critical role in designing adaptive and sustainable coastal protection systems, essential for addressing the growing vulnerabilities of coastal infrastructure in the face of climate change.

4

EXPERIMENTAL STUDY OF RUBBLE-MOUND BREAKWATERS AND SPH APPLICATIONS

4.1 INTRODUCTION

Traditionally, the assessment of the hydraulic and structural behaviour of rubble-mound breakwaters was made using physical models. Physical modelling has become a fundamental tool in maritime hydraulics for studying complex hydraulic phenomena and supporting the analysis of problems such as the design of maritime structures and the search for cost-effective and accurate solutions. This tool allows the closest representation of the set of phenomena involved in the sea-wave action in coastal structures, given the complexity associated with both wave propagation, wave-structure interaction phenomena (so diverse and complex as refraction, diffraction, wave breaking, reflection, wave run-up and overtopping) and the bathymetry.

Some authors (*e.g.*, Dalrymple, 1985; Kamphuis, 1991; Le Méhauté, 1990 and Hughes 1993) pointed out some distinct advantages of using physical models to reproduce nearshore processes:

- The physical model integrates the "proper equations" governing the processes without simplifying assumptions made for analytical or numerical models;
- The inherent limits of deterministic fluid mechanics due to turbulence makes laboratory experimental techniques one of the most useful tools in coastal engineering;
- The scale model tests allow the reproduction of complex boundary conditions beyond the accuracy of finite step differences. Convective and dissipative non-linear effects are also in near similitude;
- The size and magnitude of coastal projects lead to expensive and hard-to-achieve field measurements, whereas the small size of scale model tests allows easier data collection, and its technology remains cost-effective;
- Physical models offer the chance to monitor and measure the physics in a controlled environment, simulating varied or sometimes rare environmental conditions at the convenience of the researcher;
- Physical contact with the fluid element remains the best guide for intuitive discovery, once the physical model demonstrates visually, and with credibility, what will happen.

On the other hand, physical modelling is considered an expensive and time-consuming technique. In the last few years, numerical models have evolved significantly, proving to be a fast, cheap, and flexible

complement to physical modelling, allowing significant savings by reducing the number of experimental tests to be performed. Numerical modelling can be a useful predictive tool because it can cover multiple spatial and temporal scales. Using remarkable evolutions in the numerical models' fields, software like DualSPHysics proved to be an appropriate option to accurately simulate some highly non-linear problems using complex boundaries (see chapter 3). In the coastal engineering field, it has been demonstrated that the DualSPHysics solver is a robust computational tool to simulate free-surface flows, solid-solid interactions, modelling damage and failures, and fluid-structure interaction (see subsection 3.3.5).

Despite all the advancements and significance of numerical models, they still require adjustments and calibration based on field evidence obtained from physical modelling. As a result, neither physical nor numerical models can provide a complete set of results on their own. However, when used in a complementary manner, they enable a more comprehensive study of complex phenomena. This combination allows for the evaluation and optimization of various aspects of a project, such as the stability and overtopping performance of maritime protective structures, in a faster and more efficient manner (Reis *et al.*, 2015).

Fig.34 illustrates the complementary use of physical and numerical models, specifically DualSPHysics, to simulate phenomena associated with wave interaction with a breakwater, including wave loadings, overtopping, and damage assessment.

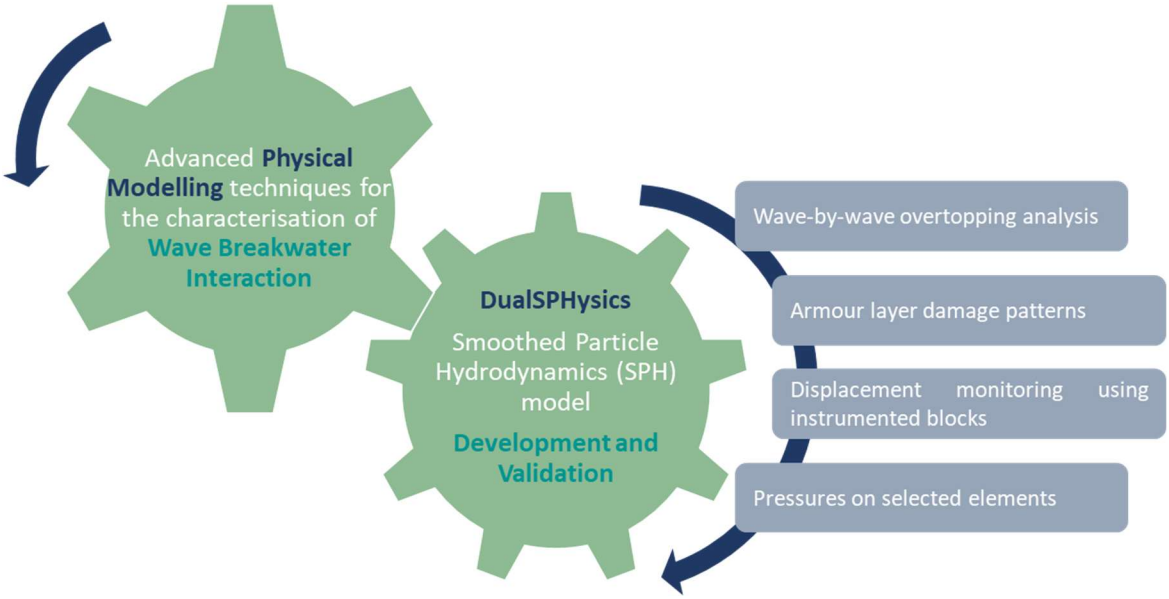

Fig.34 – Representative diagram of the complementarity between physical and numerical modelling.

Therefore, considering the undeniable interest in these tools, many physical and intellectual investments are maintained to improve concepts, techniques, equipment, and experimental procedures to collect more information from these tests as well as to automate the collection and analysis of results needed to improve numerical models' validations (Fortes *et al.*, 2017; Lopes *et al.*, 2013).

Le Méhauté (1990) said "knowledge gaps in present mathematical representations of flow processes will dictate the direction of future experimental efforts understanding of the basic laws of fluid flow".

Based on these points, the general goal of this thesis is to perform a comprehensive study of rubble-mound breakwaters in terms of wave loadings, overtopping and damage assessment, using physical and numerical modelling in a complementary way, seeking its optimized design. For that, high-resolution and accurate results from physical model tests were used to validate the application of DualSPHysics solver on the simulation of the fluid-structure interaction and the interaction among different bodies (*e.g.*, sliding Antifer units) by coupling with Project Chrono.

Therefore, the practical component of this thesis is divided into 3 phases, as presented in Fig.35, which will be described in this chapter, including all methodologies and results obtained.

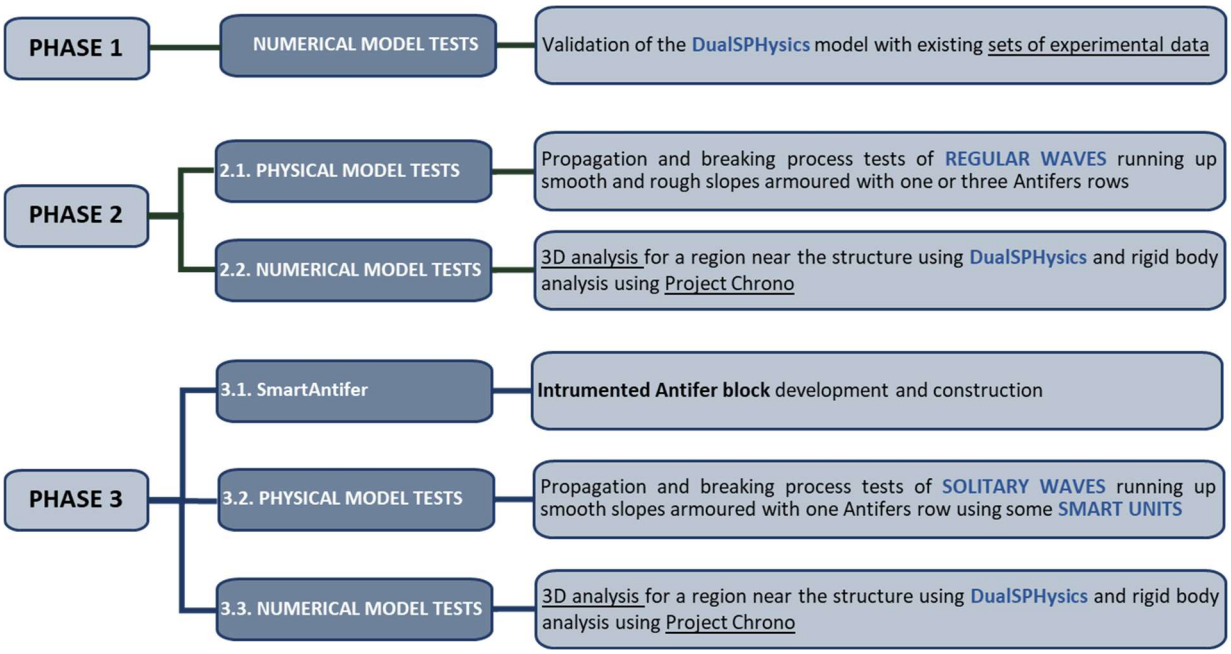

Fig.35 – Representative scheme of the practical component of the thesis and respective phases and tasks.

Phase 1 (subsection 4.2) encompasses the implementation of DualSPHysics on a breakwater consisting of a roundhead and trunk, leveraging the data obtained from experimental studies conducted at FEUP within the HydraLab+ and SE@PORTS projects. The validation of the DualSPHysics model uses data from damage scans of the structure's armour and measurements of overtopping to replicate a 3D section of the breakwater. This process has allowed for a deeper comprehension of the numerical code, including its inherent model limitations.

To keep improving reliability and confidence in the results, it is essential to persist in advancing the numerical model by validating it against reliable experimental data. To this end, the 2nd phase is divided into two different tasks: task 2.1 (subsection 4.3) refers to the physical model study in the multidirectional wave basin of FEUP representing the propagation and breaking process of regular waves running up a smooth slope armoured with one or three Antifer rows, planned to provide all the required data for the subsequent numerical simulations. In addition, the tests allow a deeper understanding of the fluid-structure interaction. Task 2.2 (subsection 4.3.2) corresponds to the numerical simulation of the experimental setup. In this way, it is possible to validate the capability of DualSPHysics to simulate fluid-structure interactions and solid-solid interactions by coupling with other

models, such as Project Chrono, and by comparing them with the experimental results. For this, it is important to know the location of the wave probes relative to the wavemaker and model.

The 3rd phase is divided into three different tasks. Task 3.1 (subsection 4.4.1) corresponds to the development and construction of an instrumented armour unit – SmartAntifer. These blocks are incorporated in the second phase of experimental tests, 3.2, in which the main goal is to improve the phase 2 results. In this case, solitary waves are used instead of regular ones, and the motion of wavemaker paddles is recorded. Then, these experimental results are compared with the numerical ones resulting from the numerical simulation of the experimental setup, in task 3.3.

4.2 VALIDATION OF THE DUALSPHYSICS MODEL WITH EXISTING EXPERIMENTAL DATA SETS

4.2.1 DESCRIPTION OF THE HYDRALAB+ AND SE@PORTS PROJECTS

Phase 1 involves applying DualSPHysics to a breakwater consisting of a roundhead and trunk, utilizing data from an experimental work conducted at FEUP as part of the HydraLab+ and SE@PORTS projects. A brief description of these projects is presented below.

Horizon 2020 – HydraLab+ R&D Project

The experimental work relative to UPORTO participation in TASK 8.2 of HydraLab+ project, entitled "Damage characterization under variable and unsteady test conditions", was carried out in 2016. The work was done in cooperation with LNEC and Deltares, having received advice and input from the other institutions involved in Task 8.2, namely from HR Wallingford, UK.

The work included 3D damage tests on a rubble-mound breakwater with a rocky armour layer to study the damage progression in the trunk (front and rear slopes) and roundhead of the structure, for two water levels, and considering the effect of sea level rise. In addition to obtaining high-resolution data on damage progression in rubble-mound structures, these experiments also included overtopping measurements.

The tests were carried out in the multidirectional wave basin (28.0 m long, 12.0 m wide and 1.2 m deep) of the Hydraulics Laboratory of the Hydraulics, Water Resources and Environment Division of the Faculty of Engineering of the University of Porto, Portugal, equipped with a 12.0 m wide multi-element wavemaker, piston-type (16 independent paddles), which also includes an active wave reflection absorption system (model HR Wallingford, UK).

A reference rubble-mound breakwater was reproduced in the wave basin on a geometric scale of 1:35, to ensure reduced scale effects, and according to the Froude similarity criteria. The geometric scale was also fixed after analysing the granular materials available for the armour layer. The 4.0 m wide trunk section was placed perpendicularly to the basin sidewall and a semi-circular roundhead was placed at its other side, Fig.36. The breakwater physical model was 5.6 m long, 3.1 m wide and 0.68 m high. Fig.36 also presents a close view of the physical model that allows identifying: (i) the front slope; (ii) the roundhead; (iii) the rear slope; (iv) and the overtopping measurement area, where the chute and the overtopping tank were placed.

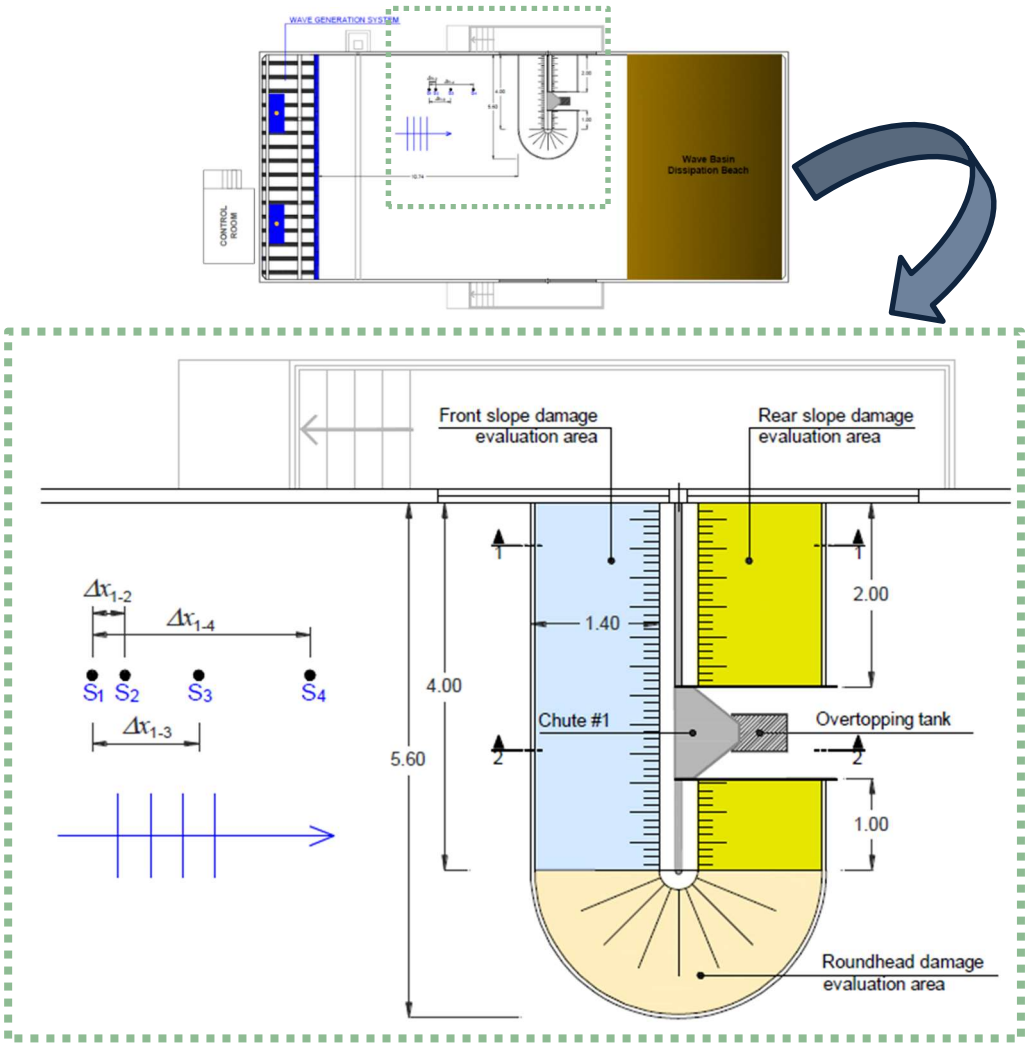

Fig.36 – Model setup in FEUP basin.

The following equipment was used: resistive-type wave probes (a set of four aligned gauges was placed in front of the model to determine the characteristics of incoming and reflected waves); digital cameras; and stereophotogrammetry system. In addition, there was also three chutes to direct the overtopping water to three auxiliary reservoirs and level gauge set-ups for application in the overtopping reservoirs. A stereophotogrammetry equipment was used to measure the 3D damage progression in the armour layer (front and rear slopes and roundhead) of the rubble-mound breakwater.

The tests were carried out with irregular waves, either long or short crested. Three water depths were considered, but only the first two were used in the core tests: 0.566 m (mean high water level); 0.592 (mean high water level plus sea level rise) and 0.480 m (mean low water level). The most extreme wave conditions were defined to avoid wave breaking before the structure, since the breaking criteria was the most limiting condition. Those conditions were relatively far away from the wavemaker performance curves. Those conditions were (model values):

- Irregular waves according to the JONSWAP spectrum (peak enhancement factor of 3.3), using the filtered white noise technique;

- Significant wave heights: 0.071, 0.094, 0.118 and 0.142 m, corresponding to 60, 80, 100 and 120% of the breakwater design wave height, respectively;
- Peak wave periods: 1.29, 1.58, 1,87 and 2.18 s, defined to maintain the local wave steepness constant and equal to 0.030;
- Standard test duration: 1000 waves.

The principal results of this study can be found in Hofland *et al.* (2017).

SE@PORTS Project

SE@PORTS project was an EU-funded project (OCEANERA-NET) whose main goal was to assess existing Wave Energy Converters (WEC) suitable for integration on harbour breakwaters and increase their Technology Readiness Level (TRL). Therefore, an innovative device was idealized from a combination of an overtopping device (OWEC) with an oscillating water column (OWC) system. The novel WEC concept needed to reach TRL 3/4 - a proven concept sustained by established feasibility tests - thus being ready to be integrated into seaport infrastructures. As such, the Leixões North Breakwater, on the north-western coast of Portugal, was considered as reference for implementing the hybrid WEC concept idealised and developed in the project. This device resulted from a combination of an overtopping device (OWEC) with an oscillating water column (OWC) system. Following the selection of the technologies to be used in the hybrid WEC for integration in the Port of Leixões, its preliminary design, and the numerical study for optimization of the device's efficiency, a series of 2D tests were carried out at the Hydraulics Laboratory of the Hydraulics, Water Resources and Environment Division of the Faculty of Engineering of the University of Porto.

The work included a 3D reproduction of the hybrid OWEC-OWC device at a geometric scale of 1:50. A representative scheme of the hybrid WEC is presented in Fig.37. The selected domain was a channel within the wave basin that extended 14.30 m in length and 0.84 m in width. A sandy slope was placed to represent a simplified bathymetry in front of the structure (seabed). It intended to mimic the relevant wave transformation process during the propagation from the wavemaker paddle to the physical model.

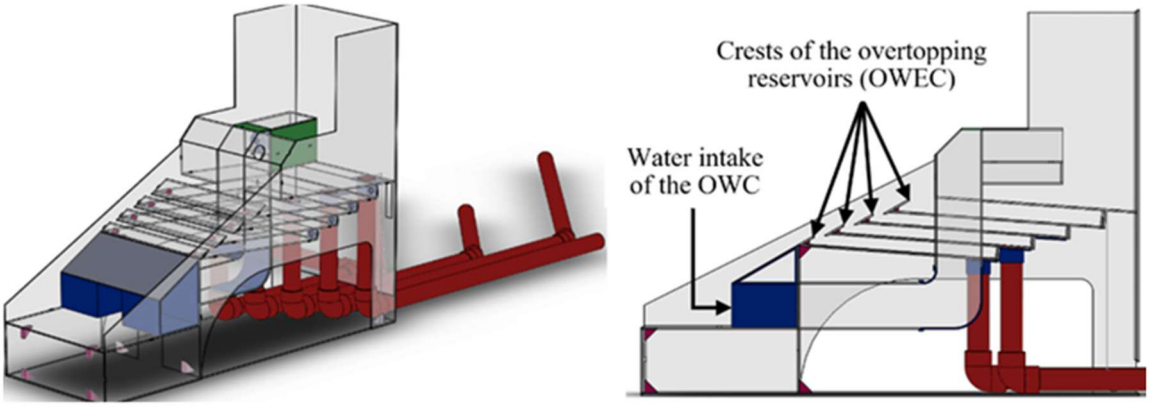

Fig.37 – Representative scheme of the Hybrid WEC model (Clemente *et al.*, 2021).

A wide variety of equipment was used, namely resistive-type wave probes (a set of gauges aligned in front of the model to determine the characteristics of the incoming waves); pressure sensors; 2D bed

profiler; digital cameras; among others. In addition, for this work, a discharge flow measurement system was developed and used to determine both the device's impact on the breakwater's effectiveness in preventing overtopping and measure the flow rate that enters each device's reservoir during the tests (to assess the harvested wave energy). So, auxiliary reservoirs were used to collect the water gathered by the hybrid WEC reservoirs, connected through ducts to each device's reservoir. Clemente *et al.* (2021) presents a more detailed description of the system. Regarding overtopping measurements, the volume of water that overtops the breakwater crest, whether considering or not the integration of the hybrid WEC, was also collected in an auxiliary reservoir (AR). This AR was positioned behind the physical model, connecting to the top of the structure through a channel. The setup with and without the WEC integrated is represented in Fig.38.

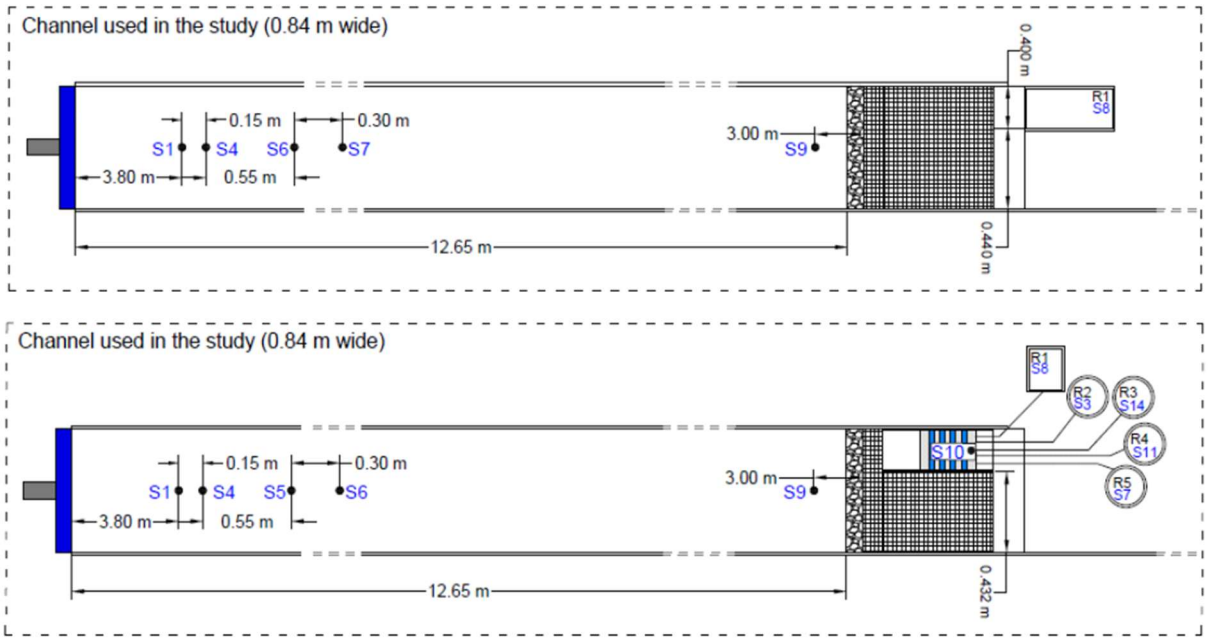

Fig.38 – Experimental setup: initial case, without WEC (top); and case with integrated WEC (bottom) (Clemente *et al.*, 2021).

The experimental study encompassed a wide range of wave conditions, including regular and irregular long-crested waves, based on data from the case study area, and to study the WEC energy conversion performance under operational conditions. The generation of irregular sea states involved the definition of a JONSWAP spectrum, with a peak enhancement factor of 3.3. The principal results of this study can be found in Clemente *et al.* (2021) and Calheiros-Cabral *et al.* (2020).

4.2.2 General considerations

4.2.2.1 Required data for numerical simulation and model limitations

The Phase 1 goal was not to test a specific device or working principle but rather to use the previously obtained experimental data to test the ability of DualSPHysics to simulate some phenomena in a large domain, including some components of complex geometry, namely the movement of the breakwater armour layer units using, at that time, the recent coupling of the software with Project Chrono.

For the initial application and validation of DualSPHysics, data on wave-by-wave overtopping and damage progression on a rubble-mound breakwater (trunk and roundhead), available from the EU H2020 Hydralab+ project, were considered for use. However, when using the SPH method and DualSPHysics to simulate complex problems, like the reproduction of 3D breakwaters sections, some issues needed to be addressed, considering the limitations of the software. These problems usually involve the simulation of large domains at a very high resolution, which can lead to precision problems in DualSPHysics. The SPH method is expensive in terms of computational time. Therefore, to achieve optimal computational performance, the best practices suggest a wise selection of the following three parameters, which influence runtime:

- The number of simulated particles, defined by the initial distance between particles, *dp*. The higher the value of *dp*, the smaller the number of particles and, consequently, the results are less accurate;
- The type of hardware used, since the maximum number of particles to simulate depends on the computer's memory capacity. The memory space of a GPU is limited, but the computation capability is much higher when compared to a CPU, and the runtime is smaller;
- The duration of the simulation. This value should not be too high to ensure a reasonable runtime value.

Considering the previous points, it was necessary to discard the use of the Hydralab+ project data since its setup had some constraints, that would be hard to model numerically with DualSPHysics model, namely:

- Large domain and a hard-to-simulate roundhead;
- The rock armour layer with units distributed unevenly. The porosity of the breakwater, the center of mass of the stones, and the dimensions are hard to define. For that reason, it is difficult to model the rocks, fixed or as moving blocks, using Project Chrono;
- The long time series of irregular waves ($\simeq$ 2000 s, $\simeq$ 1000 waves) since the damage of the breakwater resulted from the cumulative displacement of some armour layer units from their original position.

Given the difficulties presented, one focused on the numerical reproduction of the experimental set from SE@Ports project. Compared with the Hydralab+ project, the experimental work of SE@Ports project was carried out inside a wave flume of smaller dimensions and, consequently, a smaller domain needs to be modelled. Furthermore, the armour units were well defined, and the piston wavemaker movement was recorded. It should be mentioned that the final goal was to quantify the cumulative damage of the armour layer and overtopping. However, to assess the cumulative damage, it was crucial to evaluate the action with a minimum of $\simeq$ 1000 waves to reproduce the experimental tests. The software allowed the evaluation of irregular wave action during a maximum of 60 s, which was not enough to reproduce properly the irregularity of the waves. One option was to choose the 60 s of most interest of the whole time series, but by choosing just one section of the time series, it was impossible to measure the cumulative damage. Note that the decision to simulate more time with a smaller spatial resolution implies a loss of computational performance and precision.

To overcome some of the problems, it was decided to simulate 2nd order regular waves instead for a maximum of 30 s. In addition, one started to evaluate the SE@Ports' project breakwater considering a case with the armour layer blocks fixed and another assuming that the toe berm blocks move under the action of waves. After overcoming the time series length problem, the numerical 3D reproduction of the wave channel and physical model still presented some difficulties related to its dimension and a lack of appropriate data from the SE@Ports project to compare with the numerical results. A complete 3D

reproduction of the wave flume is time-consuming in terms of software computation due to the number of fluid particles involved. The correct operation of the software, in a reasonable computational time, can be ensured by placing the piston wavemaker at a distance smaller than 2 wavelengths from the structure. In the SE@Ports case, the domain was too large, and the piston wavemaker was at approximately 3 wavelengths from the structure. One way of reducing the simulation domain and the number of fluid particles was by applying a coupling technique. For the application of coupling or relaxation zone techniques, it is relevant to place wave probes at strategic points during the experimental campaign. It is also essential to record the motion of wavemaker paddles during the tests with irregular waves. However, there are instances where the lack of laboratory equipment, such as waves probes, or the incorrect assessment of software inputs, such as placing wave probes in irrelevant locations, hinders the accurate replication of the physical model through numerical means due to insufficient information availability. It also contributes to the inaccurate simulation of the physical model, making it impossible to compare the experimental results with the numerical ones. It was the case with the SE@Ports project, in which wave probes data collection was insufficient. Throughout the identification of software needs in advance, one could have reproduced larger domains with irregular waves for a longer simulation time.

4.2.2.2 Simulation results and recommendations for future work

Phase 1 only allowed a qualitative analysis of the numerical model of the SE@Ports project. During this phase, the latest features of the DualSPHysics – version 4.4. – were tested for fixed and moving blocks, namely:

- New density diffusion terms that gave more accurate density/pressure fields;
- New version of Chrono that solved collisions between moving blocks much faster due to its parallel computation module;
- New option to solve collisions, not only inelastic (only considering restitution and friction coefficient) but also elastic (considering young modulus and Poisson ratio).

The inadequate data led to an unsatisfactory reproduction and validation of the numerical model. Phase 1 primarily resulted in some recommendations and requirements that the experimental model study must fulfil to foster favourable numerical outcomes, namely:

(i) A systematic record of data, such as the water surface elevation, the piston-type wavemaker motion, the porosity considered for the breakwater armour layer, and the friction between the blocks;
(ii) Use of regular waves instead of irregular waves (2^{nd} order preferable);
(iii) Placement of wave gauges at strategic points;
(iv) The minimum distance between the piston-type wave maker and the structure should be equivalent to one wavelength to ensure proper wave development. If this distance exceeds two wavelengths, alternative wave generation techniques must be implemented in the 3D numerical simulation to reduce the simulation domain. These techniques require knowledge of both the incident and reflected (H_i and H_r) waves, which necessitates installing a row of three wave gauges in the experimental model at 1 to 2 wavelengths from the structure to gather this information;
(v) When necessary, the AWAS system should be activated;
(vi) Run-up should be measured using run-up gauges, step gauges or spiderweb instead of resistance-type wave gauges;
(vii) Assessment and recording of the porosity considered for the breakwater armour layer;

(viii) Preparation of AutoCAD files of the breakwater cross section and of the experimental facility;
(ix) Take into account the reliability, repeatability and reproducibility of the tests.

Thus, Phase 2 was initiated, with laboratory tests incorporating the recommendations from Phase 1 to ensure the acquisition of accurate and high-quality data for numerical validation.

4.3 SLOPE ARMOURED WITH ANTIFER BLOCKS UNDER THE ACTION OF REGULAR WAVES

The Phase 2 is divided into two different tasks: task 2.1 (subsection 4.3.1) refers to the physical model study representing the propagation and breaking process of regular waves running up a smooth slope armoured with one or three Antifer rows, planned to provide all the reliable experimental data for the subsequent numerical simulations. Task 2.2 (subsection 4.3.2) corresponds to the numerical simulation of the experimental setup. In this way, it is possible to validate the capability of DualSPHysics to simulate fluid-structure and solid-solid interactions by coupling with other models, such as Project Chrono, and by comparing them with the experimental results.

4.3.1 LABORATORY EXPERIMENTS

The experimental tests of phase 2.1 were performed in the multidirectional wave basin of the Hydraulics Laboratory of the Hydraulics, Water Resources and Environment Division of the Faculty of Engineering of the University of Porto, Portugal. Waves were generated by a multi-element piston-type wavemaker designed by HR Wallingford (UK), which generates both regular and long or short crested irregular waves. It also has incorporated an active wave reflection absorption system. On the opposite side of the wavemaker, there is an 8 m long dissipation beach with an 18% slope that ensure minor wave reflections.

For 2D studies, several guide walls can be used to create flumes within the tank. The side windows allow the visualization of the physical model and its interaction with the generated waves. Fig.39 shows the wave basin scheme.

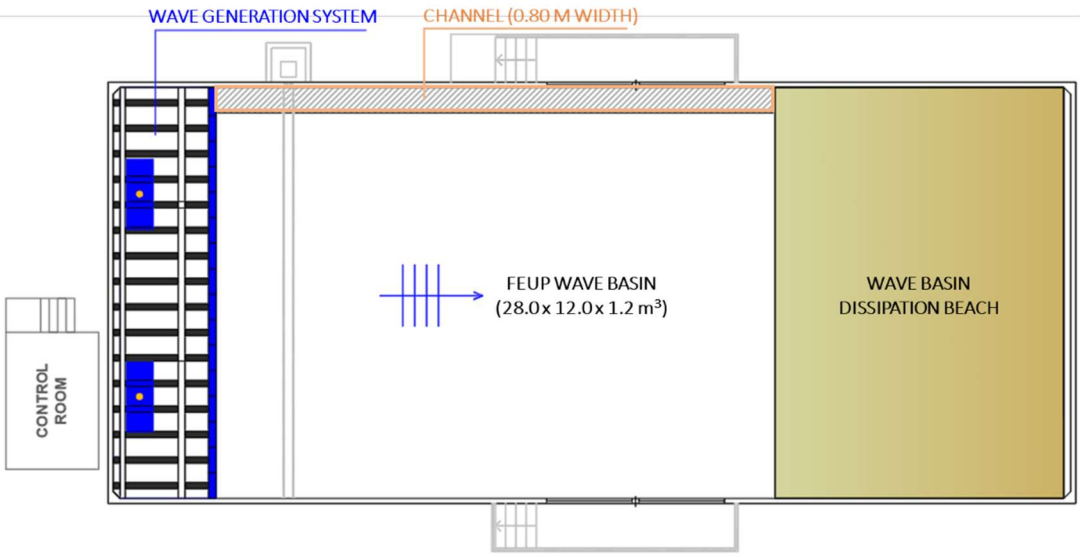

Fig.39 – FEUP wave basin scheme.

Phase 2.1 refers to tests of the propagation and breaking process of regular waves running up smooth and rough slopes armoured with one to three rows of Antifer blocks. These tests were used mainly for comparison purposes when testing the Antifer blocks' stability using numerical model tools.

4.3.1.1 Model configuration

Experimental set-up

The physical model, designed and built at FEUP, corresponds to a simple slope armoured with one to three rows of Antifer blocks, reproduced on a geometric scale of 1:40 to ensure reduced scale effects. The slope, built with acrylic, can assume two different slope values: 1V:2H and 1V:1.5H, depending on the test series, and has a diagonal extension of 1.80m. In the smooth version, where the acrylic slope was covered with two layers of paint to check the roughness, a printed 10 cm grid was used for a more effective qualitative and quantitative assessment of the Antifer block's movement. The second version corresponds to a rough slope covered by rubble. Both versions are presented in Fig.40.

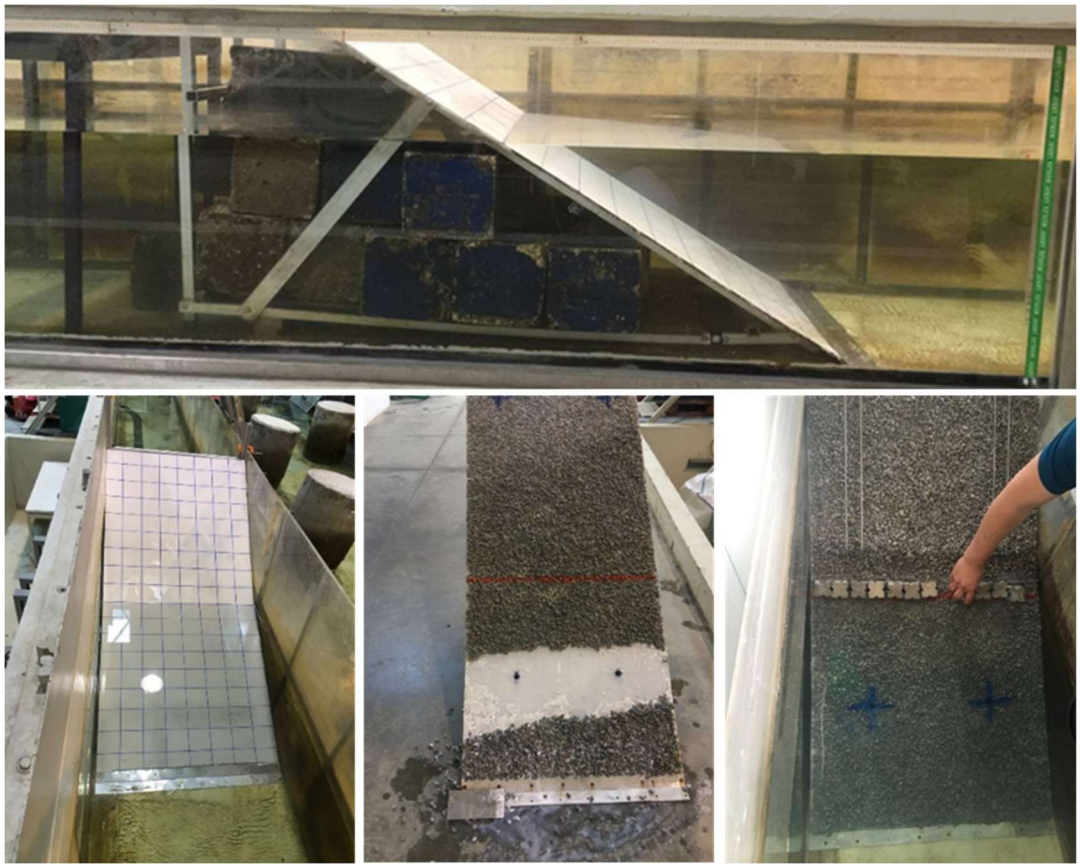

Fig.40 – Side view (top) and top views (bottom) of the model: smooth (bottom left) and rough (bottom middle and right) configurations.

The model was positioned in a channel 0.80 m wide, 12 m long and 1.20 m high. The distance from the slope toe to the wavemaker paddle (when in its middle position) was equal to, approximately, 9.95 m. The bathymetry in front of the structure was not reproduced. Thus, the water depth was kept constant

and fixed at approximately 0.50 m (20 m in the prototype). The Antifer blocks were installed in the active zone of the slope, at a 0.45 m high. Fig.41 and Fig.42 present the final experimental setup.

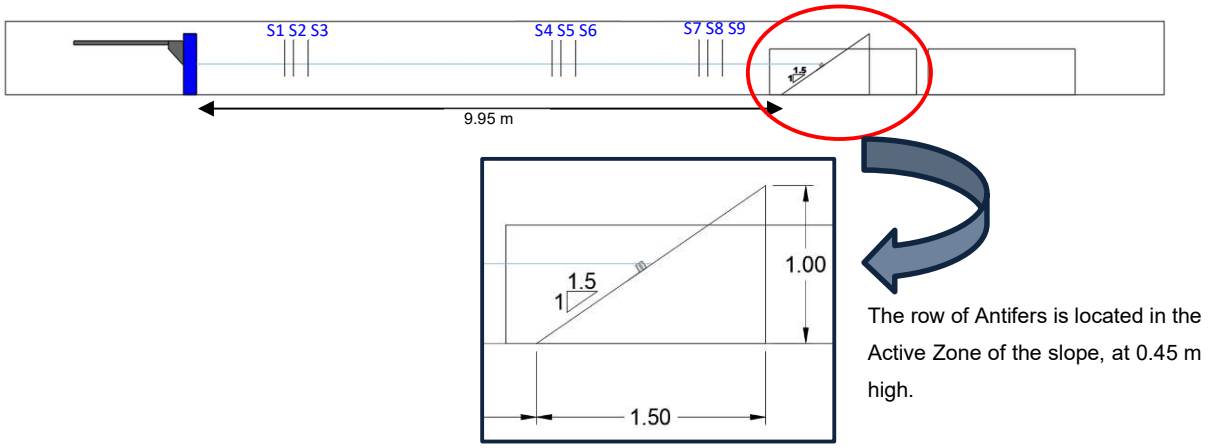

Fig.41 – Experimental setup profile in FEUP flume, considering a slope of 1V:1.5H.

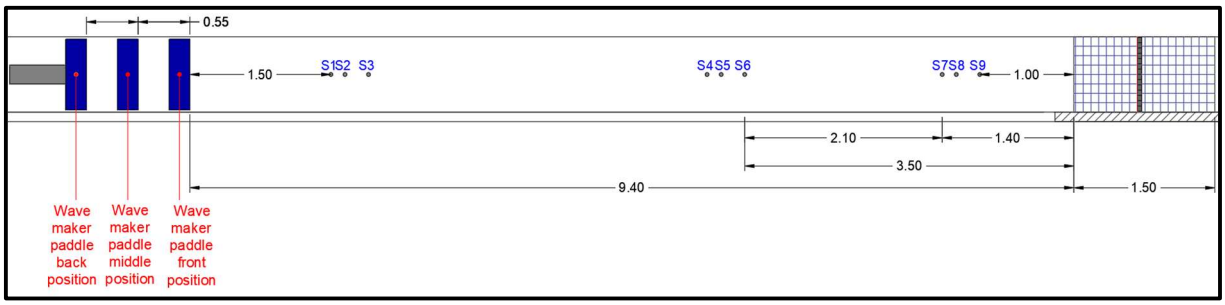

Fig.42 – Experimental setup top view in FEUP flume, considering a slope of 1V:1.5H.

Antifer blocks characteristics

The Antifer blocks used in the experimental study present the geometric parameters introduced in Table 15, which follows the geometric characteristics shown in Fig.43.

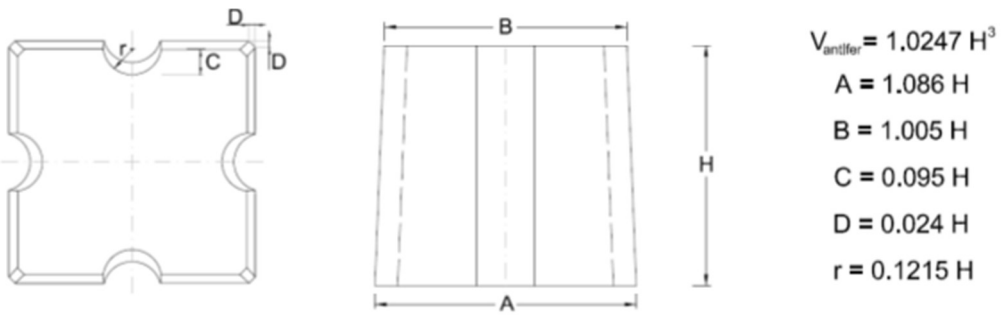

Fig.43 – Geometric characteristics of Antifer blocks.

Table 15 – Geometric parameters of Antifer blocks.

Geometric Parameters	Values
A [m]	0.056
H [m]	0.052
B [m]	0.052
V [m^3]	0.140
D_n [m]	0.052

From the available assortment of Antifer blocks in the hydraulic laboratory, two distinct groups of blocks were selected: 14 blocks of type 1 and 28 blocks of type 2. The corresponding average mass properties of blocks type 1 and 2 are meticulously outlined in Table 16. The first group, comprising type 1 blocks, was heavier and was specifically employed in a scenario where a single row of blocks was used, ensuring that blocks would not slide off the slope when at rest, yet providing enough mobility to slide when impacted by waves. On the other hand, the type 2 blocks, were reserved for scenarios involving multiple rows of blocks due to their lighter weight. In this context, the blocks exhibited a heightened level of interlocking, necessitating the use of lighter blocks to achieve the desired motion.

Table 16 – Mass properties of Antifer blocks.

Mass properties	Type 1	Type 2
$m_{Antifer}$ [g]	365.3	291.5
$\rho_{Antifer}$ [kg/m^3]	2600	2023
ρ_{Water} [kg/m^3]	1000	1000
Δ	1.600	1.023

4.3.1.2 Instrumentation

Equipment description and setup

The principal equipment used during the tests were:

- Resistive wave probes to measure the water's free-surface elevation and, consequently, determine the incident wave conditions and estimate the reflection coefficient and run-up;
- Photographic and video cameras to assess the structural damage and for test recording, respectively.

The resistive wave probes measure the electric current between the two stainless steel rods, which is then converted to a voltage that is considered proportional to the submersion depth of the rods, with an accuracy of ±0.4 mm (Rosa-Santos *et al.*, 2015a). Two probe sizes with different lengths are available: 60 cm and 30 cm.

The wave probes were numbered from S1 to S14 and separated into two modules: ID1 and ID2. Module ID1 has eight channels (five were operational), and module ID2 has six. Table 17 indicates the relation

between the probe identity and its number. This designation served to identify the comma-separated files (.cvs) containing the information from each probe in the data sets. The .csv files created by the acquisition system comprise five columns: the first column has the time in model scale, in seconds; the second column has the processed data value for each time step, meaning the voltage that passes between the two probe rods, in Volts; the third column has the calibrated data value for each time step in model scale, meaning the water's free surface elevation referred to the calibrated zero, in meters; the fourth column has the time in prototype scale, in seconds; finally, the fifth column has the calibrated data value for each time step in prototype scale, meaning the water's free surface elevation referred to the calibrated zero, in meters.

Table 17 – Probes channels and designations.

Board 1 (ID1)			Board 2 (ID2)		
Probe	Channel	Designation	Probe	Channel	Designation
S1	1	ID1_Ch1_Channel 1	S7	1	ID2_Ch1_Channel 1
-	2	-	S8	2	ID2_Ch2_Channel 2
-	3	-	S9	3	ID2_Ch3_Channel 3
S2	4	ID1_Ch4_Channel 4	S4	4	ID2_Ch4_Channel 4
S3	5	ID1_Ch5_Channel 5	S10	5	ID2_Ch5_Channel 5
-	6		S11	6	ID2_Ch6_Channel 6
S5	7	ID1_Ch7_Channel 7	-	7	-
S6	8	ID1_Ch8_Channel 8	-	8	-

Nine of the eleven wave probes were displaced in the flume in sets of three aligned probes: two at a distance equal to the wavelength, L, and $2L$ from the structure (for numerical simulation reasons) and one closer to the piston paddle. The distribution of the probes sets along the flume, for the different model slopes, are presented in Fig.44 and Fig.45. As evident from these figures, the arrangement of the probes and the spacing between them varies in the two presented setups. The spacing is dependent on the water depth (d), wave periods (T) and wave heights (H) specified in the test plan.

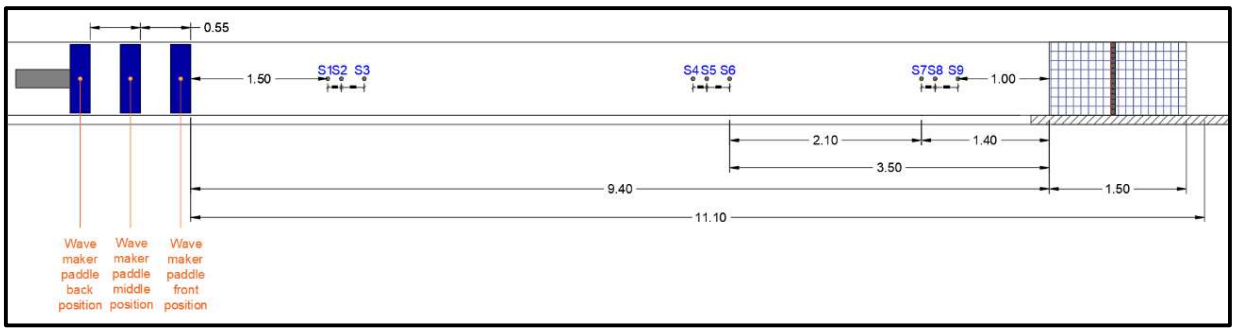

Fig.44 – Wave probes distribution considering a slope of 1V:1.5H (in meters).

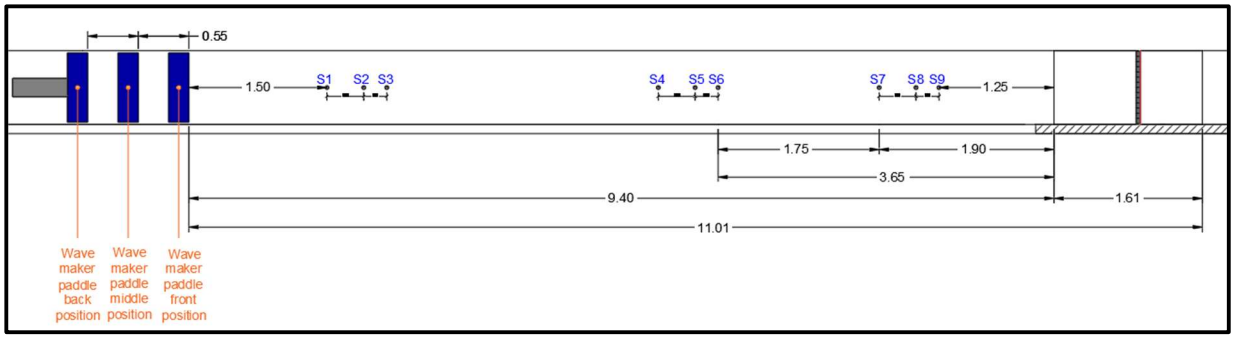

Fig.45 – Wave probes distribution considering a slope of 1V:2.0H (in meters).

The HR-DAQ software manual – Data Acquisition and Analysis Software – advises that the best spacing between the wave gauges used to make the reflection analysis should respect a rule to avoid numerical errors. This rule determines that the average of the parameter $\sin 2(kx_{ij})$ for the six possible distances (x_{12}, x_{13}, x_{14}, x_{23}, x_{24}, and x_{34}) is bigger than 0.25, defined by the following expression (Wallingford, 2013):

$$\frac{1}{6}[\sin 2(kx_{12}) + \sin 2(kx_{13}) + \sin 2(kx_{14}) + \sin 2(kx_{23}) + \sin 2(kx_{24}) + \sin 2(kx_{34})] > 0.25 \qquad (100)$$

where x_{ij} corresponds to the distance between probes i and j [m].

This routine is designed for the use of 4 wave probes, but in this case only 3 probes were utilised. The distances $x_{11} = x_{12} = 0$ (correspondent to the first probe), x_{13}, and x_{14} were introduced in the software, and values were processed by the program to verify the rule presented in equation (100). This software interface, present in Fig.46, also provided a valid frequency range for the reflection analysis.

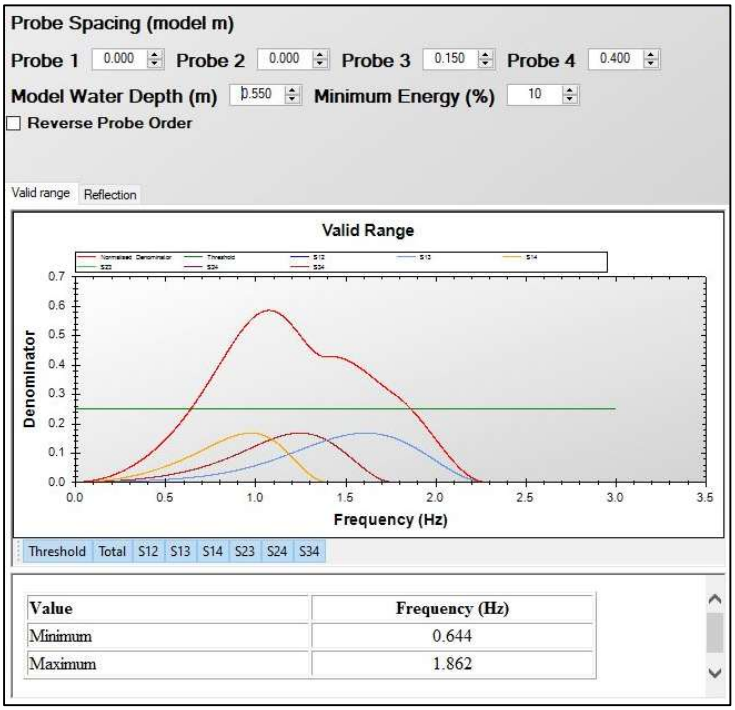

Fig.46 – HR-DAQ software interface used for reflection analysis considering the scenario of a slope of 1V:1.5H.

The spacing between the three aligned wave probes (S4, S5 and S6) chosen for each scenario (different slopes) is presented in Fig.47.

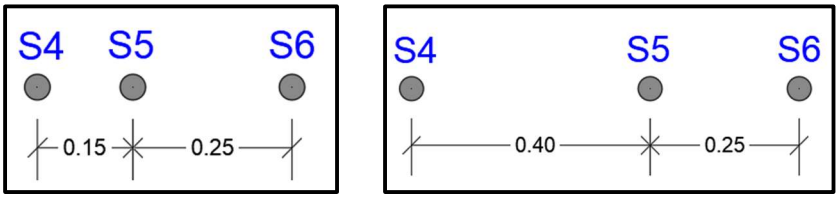

Fig.47 – Spacing between the three aligned wave probes S4, S5 and S6 (in meters) for the scenarios considering a slope of 1V:1.5H (left) and a slope of 1V:2.0H (right).

The two remaining probes were used to measure the wave run-up. These capacitive wave gauges were deployed over the slope, approximately 10 cm above the blocks, and maintaining the slope angle.

Regarding the structural damage measurement, a 24.1 megapixels Canon EOS 2000D photographic camera was used to photograph the structure orthogonally and track the Antifer blocks' movements. Prior to each test, a photograph of the model was captured to serve as a reference, and following the completion of each test, another photograph was taken. It was possible to assess the movement of the blocks by comparing the resulting photographs. Another photographic camera, a Nikon D3100, was also used to record the different tests. Both cameras were assembled above and approximately normal to the slope.

Equipment calibration

The resistive wave probes need to be calibrated every day before being used to guarantee minimum error in the measurements. The process consists of manually changing the probe's immersion depth (Fig.48) and associating the voltage between the two rods to the measured immersion depth for at least three known values (Table 18); then, a linear relation is established.

Table 18 – Wave probes type and immersion differences.

Probe	Type	Calibration	Probe	Type	Calibration
S1	60 cm	± 10 cm	S4	30 cm	± 6 cm
S2		± 16 cm (*)	S5		
S3			S6		
S10		± 18 cm	S7		
S11			S8		
(*) Series 05 and 06			S9		

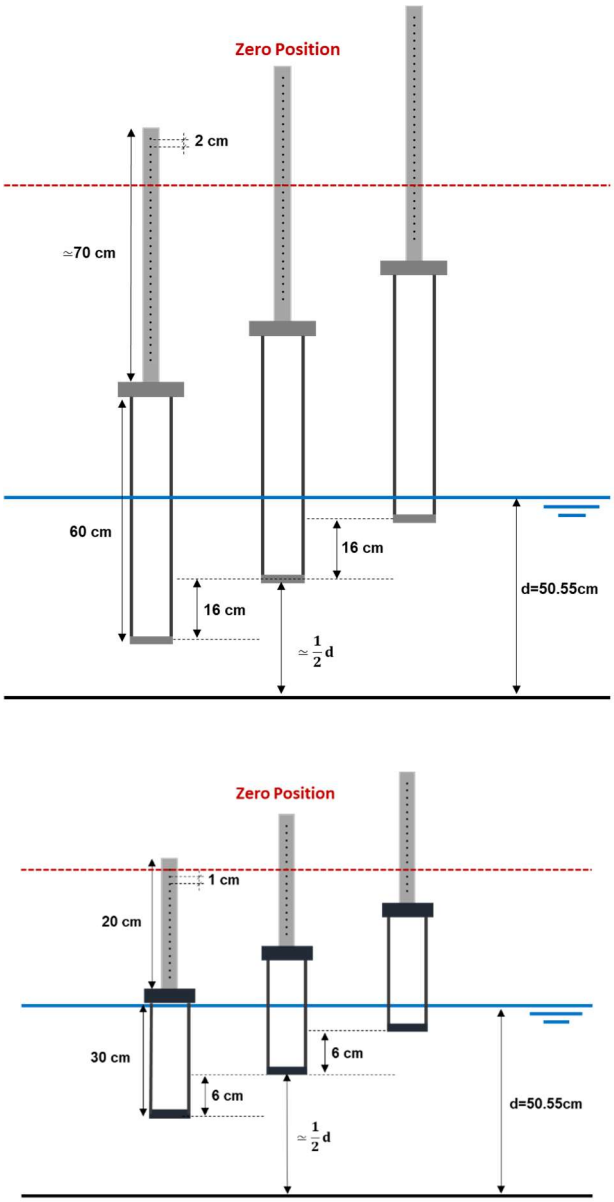

Fig.48 – Calibration procedure for 60 cm (top) and 30 cm (bottom) wave probes for series 05.

4.3.1.3 Test Procedure

The experimental tests were divided into six series:

- **Series 00** – Physical model without blocks corresponding to a smooth slope (slope made of acrylic with two layers of paint) to test the wave conditions for both slopes;
- **Series 01** – Arrangement of 1-row of 14 Antifer blocks (Type 1) and a smooth slope (slope made of acrylic with two layers of paint), considering a slope of 1V:1.5H (Fig.49);
- **Series 02** – Arrangement of 2 layers of 2 rows of Antifer blocks (Type 2) and a smooth slope (slope made of acrylic with two layers of paint), considering a slope of 1V:1.5H;
- **Series 03** – Arrangement of 1-row of 14 Antifer blocks (Type 1) and a rough slope (slope made of acrylic covered by mound), considering a slope of 1V:1.5H (Fig.49);

- **Series 04** – Arrangement of 2 layers of 3 rows of Antifer blocks (Type 2) and a rough slope (slope made of acrylic covered by mound), considering a slope of 1V:1.5H;
- **Series 05** – Arrangement of 1-row of 14 Antifer blocks (Type 2) and a smooth slope (slope made of acrylic with two layers of paint), considering a slope of 1V:2H;
- **Series 06** – Extra tests of arrangement of 1-row of 14 Antifer blocks (Type 2) and a smooth slope (slope made of acrylic with two layers of paint), considering a slope of 1V:2H and a different displacement in high of the Antifer blocks.

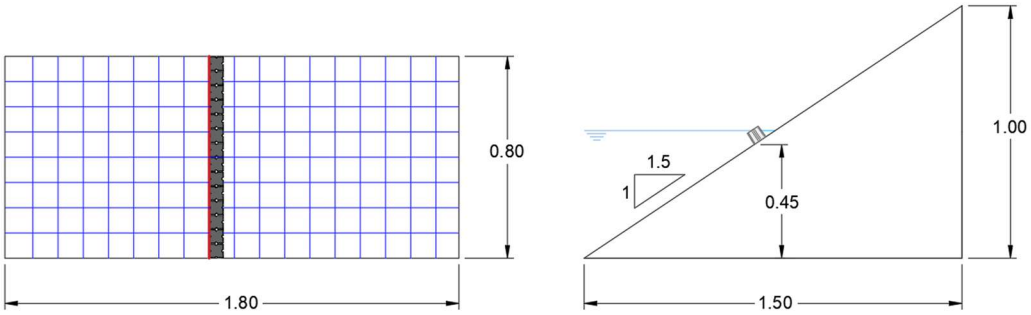

Fig.49 – Perpendicular view (left) and profile view (right) of Antifer blocks arrangement for test series 01 and 03.

In series 02 and 04, the Antifer blocks placement method was defined by the first- and second-layer pattern and the way the blocks are placed per row or layer. For each test, two different placement methods were tested, according to Table 19, where the pictures for the regular placement are top views, x oriented along the width of the slope, and distance y aligned with the direction of the slope incline.

Table 19 – General overview placement methods.

Placement method	Figure	First layer	Second layer	Placement
(A) Column	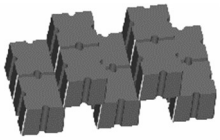	Regular 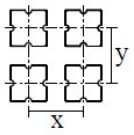	Regular	Layer by layer 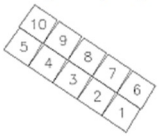
(B) Double Pyramid	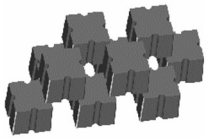	Pyramid 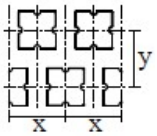	Pyramid	

In both methods it was considered that $y = A = 0.056$m (Antifer base measurement) and the distance between blocks as $x = 0.8A$. It resulted in the arrangement presented in Fig.50 to Fig.52 for geometry (A) and Fig.53 to Fig.55 for geometry (B). Note that the red line represented marks the position on the slope corresponding to 0.45 m height and served as a reference.

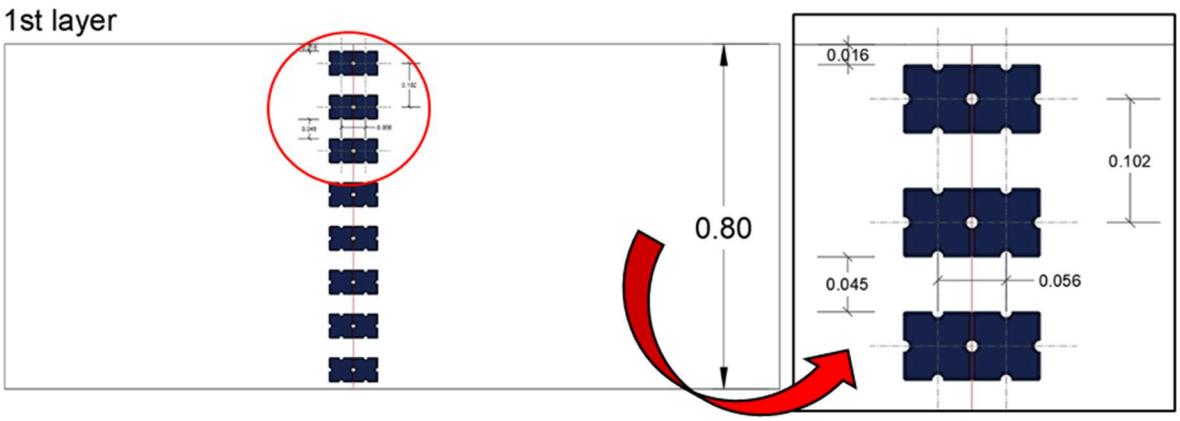

Fig.50 – First layer in column for geometry (A), with measurements in meters.

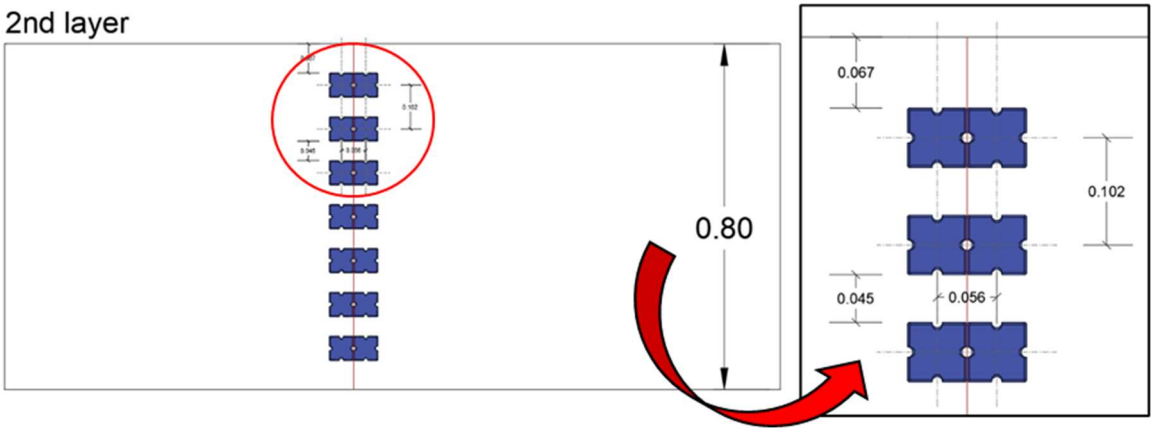

Fig.51 – Second layer in column for geometry (A), with measurements in meters.

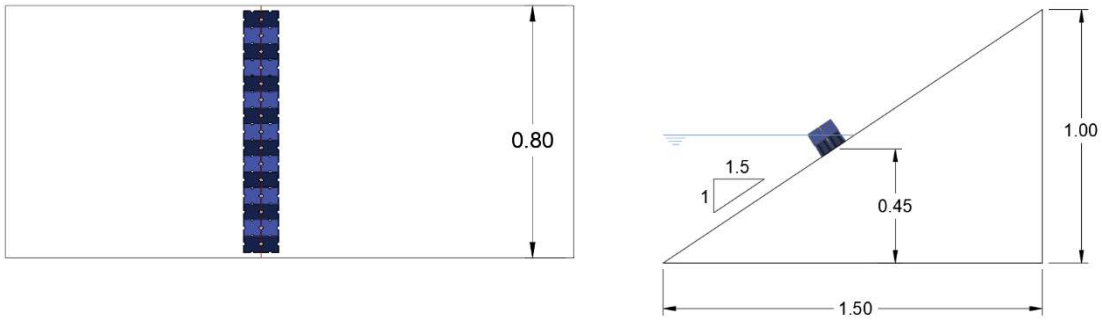

Fig.52 – Perpendicular view (left) and profile view (right) of Antifer blocks arrangement for geometry (A).

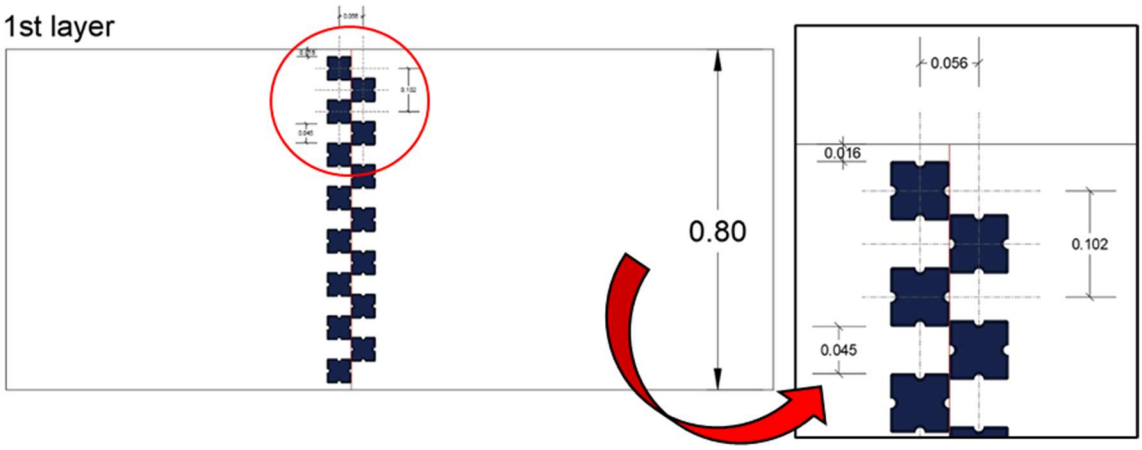

Fig.53 – First layer in pyramid for geometry (B), with measurements in meters.

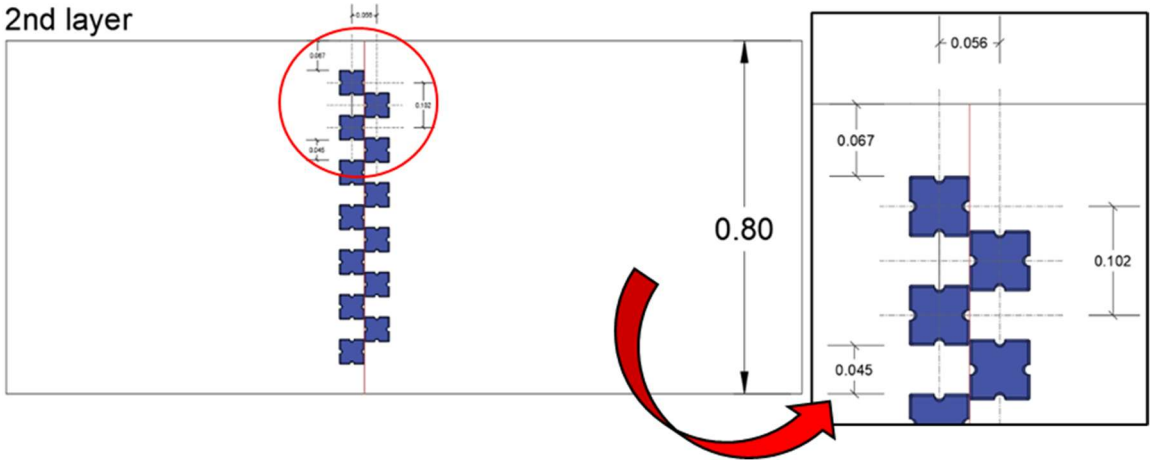

Fig.54 – Second layer in pyramid for geometry (B), with measurements in meters.

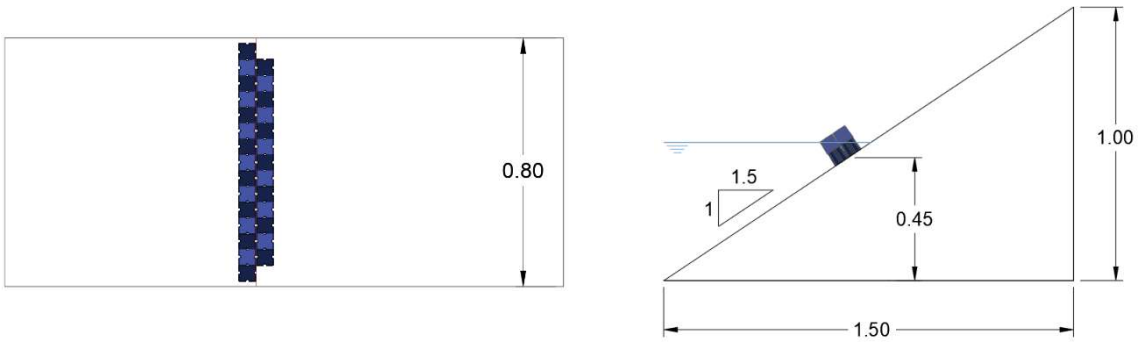

Fig.55 – Perpendicular view (left) and profile view (right) of Antifer blocks arrangement for geometry (B).

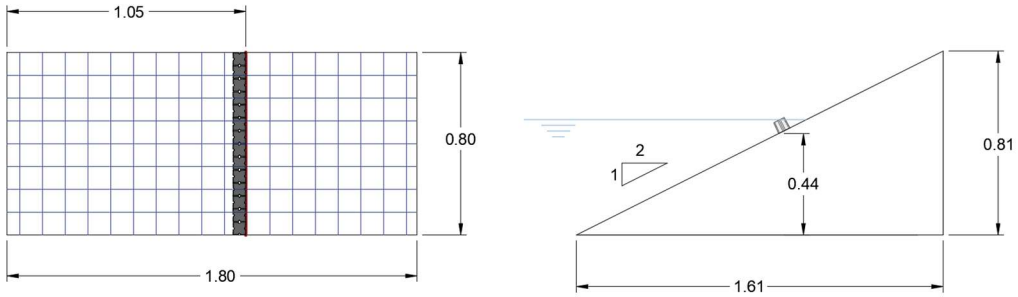

Fig.56 – Perpendicular view (left) and profile view (right) of Antifer blocks arrangement for series 05 and 06.

Testing conditions

The physical model, considering two different slopes, was tested for different wave characteristics (test conditions), as presented in Table 20. The structure was subjected to a normal wave action of regular 2nd order waves (Fig.57), with height ranging from 1.25 cm to 10 cm and periods varying from 0.603 s to 1.478 s, in a water depth of 0.5055 m. A test duration of 100 waves was considered since more than 90% of the blocks would have already moved by that time and equilibrium would have established.

Table 20 – Testing wave conditions range and characteristics (model values).

Variable	Expression	Value
Wave height	*H* [m]	0.0125, 0.01875, 0.025, 0.0375, 0.050, 0.075, 0.100
Wave period	*T* [s]	0.603, 0.739, 0.853, 0.885, 0.930, 0.988, 1.045, 1.074, 1.146, 1.207, 1.315, 1.395, 1.478, 1.518
Water depth	*d* [m]	0.5055
No. of waves	N [-]	100
Angle of wave action	[◦]	90
Wave type		Regular
Wave theory		2nd order

The tests were named based on the following nomenclature: **S**00_**H**00**RW**_**A**_**R**00

First, the test series is identified. Therefore, S00 refers to series 0, S01 to series 1, etc…Then, the H00 refers to a specific combination of the wave height (H) and the wave period (T), as presented in Table 21.

After the wave characteristics, the Wave Type and the geometry used are stated. When the wave type is "RW" it means regular waves were generated. The geometry can be geometry A or B.

Finally, the test iteration is specified. Each test (R00) was repeated at least 3 times. So, they are numbered sequentially as 01, 02, 03, etc…

Table 21 – Testing wave conditions: combinations of wave heights and wave periods.

Name	*H* [m]	*T* [s]
H01	0.0125	0.603
H02	0.0188	0.739
H03	0.0250	0.853
H04	0.0375	1.045
H05	0.0500	1.207
H06	0.0750	1.478
H07	0.0250	0.885
H08	0.0375	0.885
H09	0.0500	0.885
H10	0.0750	0.988

Name	*H* [m]	*T* [s]
H11	0.1000	1.146
H12	0.0375	0.930
H13	0.0500	1.074
H14	0.0750	1.315
H15	0.1000	1.518
H16	0.0375	1.395
H17	0.0500	1.395
H18	0.0750	1.395
H19	0.1000	1.395

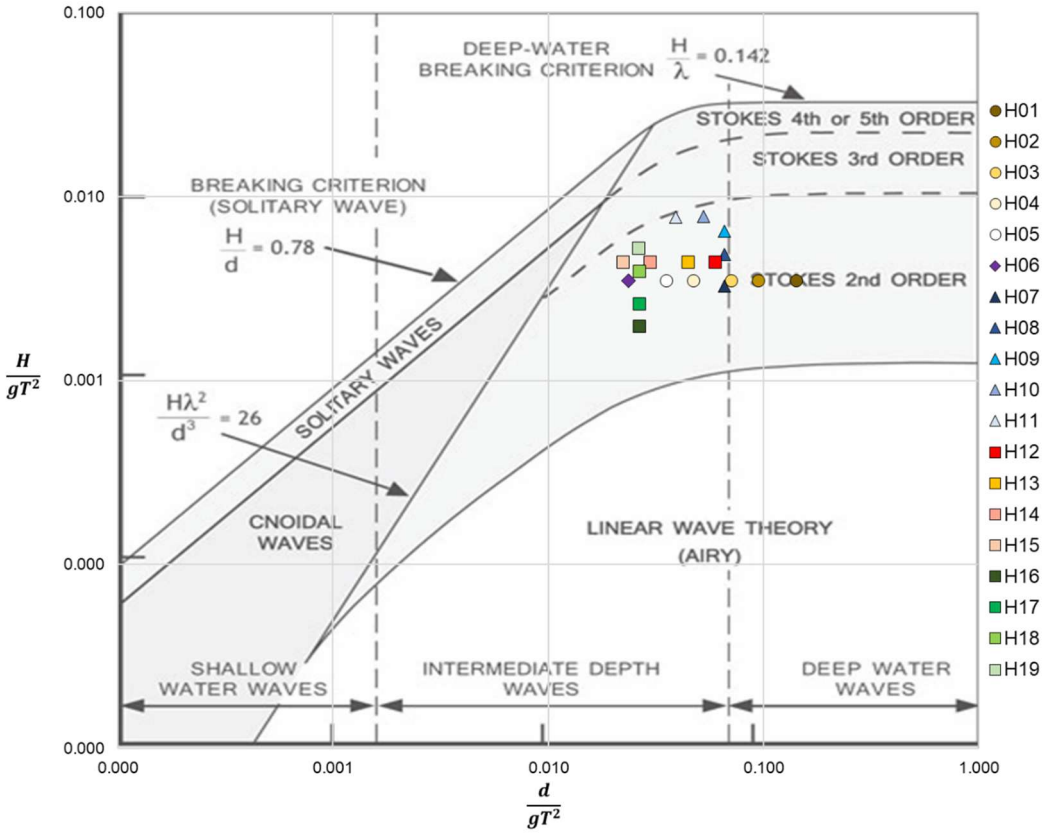

Fig.57 – Wave theories range of application (Le Méhauté, 1976) and testing wave conditions representation.

The combination of wave conditions tested in each series was:

- Series 01 and series 03: H01 to H05;
- Series 02: H01 to H05 for both geometries A and B;
- Series 04: H07 to H11 for both geometries A and B;
- Series 05: H07 to H19;
- Series 06: H12 to H15.

The wave probe acquisition frequency used was 40 Hz. After each test, the Antifer blocks were re-installed at their original position.

Image processing

A Canon EOS 2000D 18 55mm photographic camera was used to photograph the structure from above and track the Antifer blocks' movements. The camera, assembled above and approximately normal to the slope, recorded the initial and final positions of the blocks for each test, as presented from Fig.58 to Fig.64.

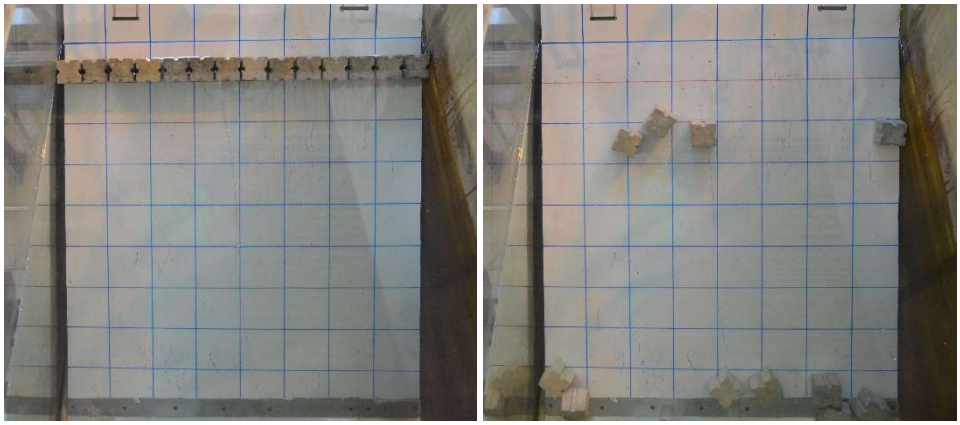

Fig.58 – Photographs for the initial and final position of the blocks for test S01_H03RW_R01.

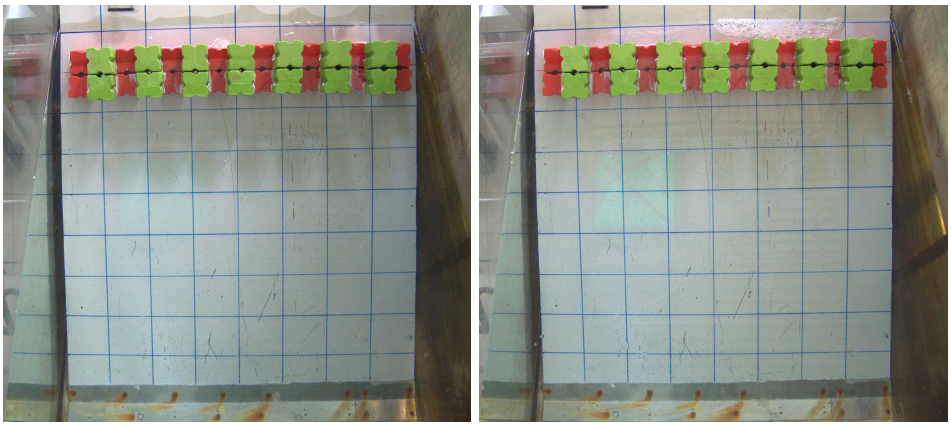

Fig.59 – Photographs for the initial and final position of the blocks for test S02_H03RW_A_R00.

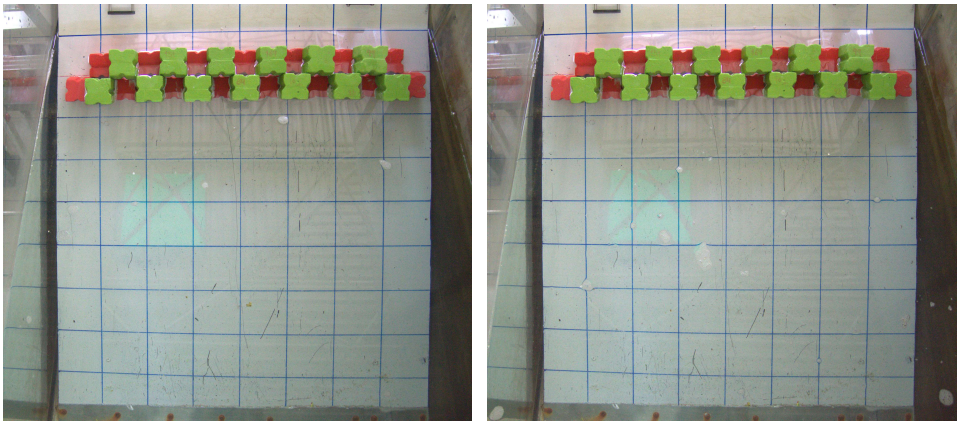

Fig.60 – Photographs for the initial and final position of the blocks for test S02_H03RW_B_R00.

Fig.61 – Photographs for the initial and final position of the blocks for test S03_H03RW_R00.

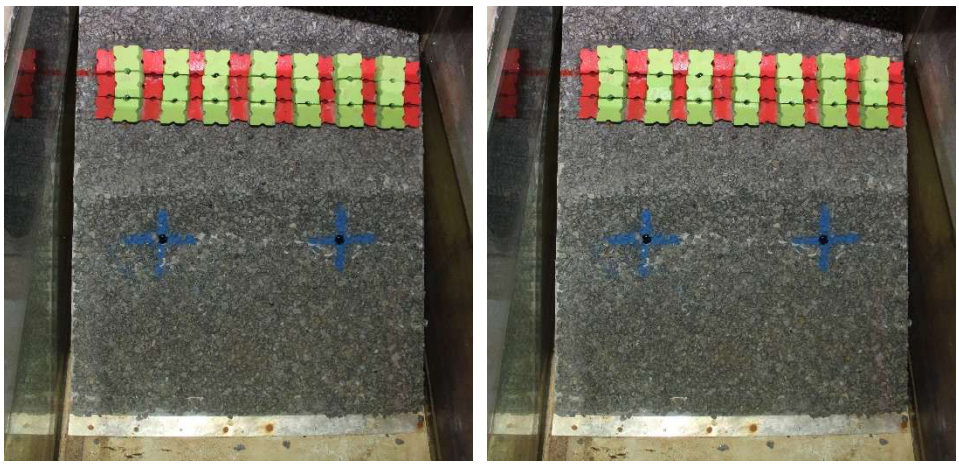

Fig.62 – Photographs for the initial and final position of the blocks for test S04_H07RW_A_R00.

Fig.63 – Photographs for the initial and final position of the blocks for test S05_H14RW_R06.

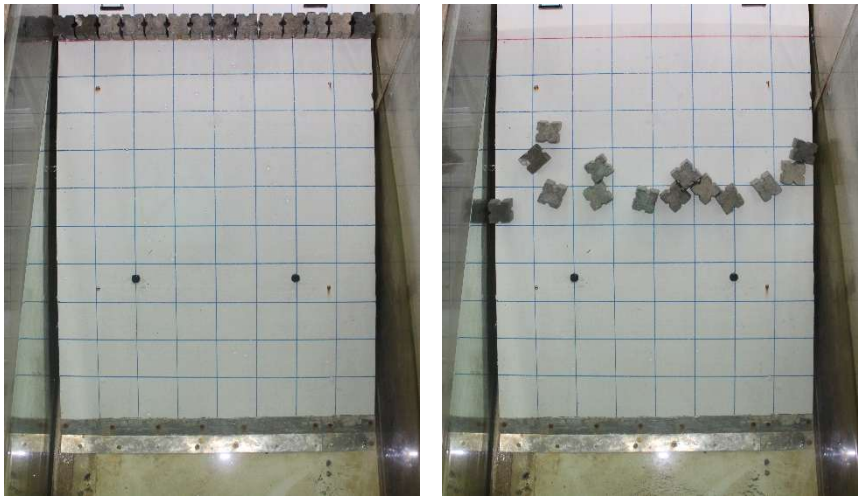

Fig.64 – Photographs for the initial and final position of the blocks for test S01_H03RW_R00, considering the blocks initially positioned above the red line.

The results of some test conditions were considered for image processing purposes. The results of series 01 and 03 were discarded because the slope was too steep, leading to the complete collapse of the row of blocks for most wave conditions. In the case of the 02 and 04 series, it was necessary to glue the first lines of blocks of both layers to the slope to prevent the blocks from completely collapsing and to create the compaction effect felt on a breakwater. However, this strongly impacted the possible movement of the blocks, with only a slight rotation of them in some of the scenarios. The most suitable results, considering their future use for numerical validation, were for waves H12 and H14 from series 05.

The distortion of the photos was corrected using Lightroom software. Finally, to carry out the quantitative analysis of the movement of the Antifer blocks, the open-source software ImageJ, distributed by Fiji, was used, with which it was possible to measure each block's initial and final displacements by considering a fixed point. The steps followed in the software, described in a simplified form, are:

1) Open the photo correspondent to the initial condition in ImageJ;
2) Use the tool *Straight* to draw a line correspondent to the channel width;
3) Define the correspondence between the image pixels and the known measure (channel width), using the tool Analyze>SetScale (see Fig.65);
4) Set a reference point, which should be the same for the initial and final conditions, and draw a straight line between that point and the centre of the blocks;
5) Use the tool Analyze>Measure to determine the angle and length of the line (see Fig.65);
6) Repeat steps 4 and 5 for the remaining blocks;
7) Export the resultant table to a spreadsheet file;
8) Repeat 1 to 7 steps considering now the photo corresponding to the final conditions' scenario;
9) Using a simple geometric relation, calculate the final displacement of the blocks.

Fig.65 – ImageJ tools: SetScale (top) and Measure (bottom).

4.3.2 VALIDATION OF THE DUALSPHYSICS MODEL WITH NEW EXPERIMENTAL DATA

The task 2.2 corresponds to the numerical validation of a model considering the experimental data previously obtained. The agreement between numerical and experimental results was accessed through the mean displacements of the units when interacting with second-order regular wave action. The research included discussion about: i) how to mimic the experimental incident wave conditions in the numerical wave tank, ii) the minimum resolution needed to obtain accurate results, iii) the use of the Modified Dynamic Boundary Conditions (English *et al.*, 2022) and of the new density diffusion terms (Fourtakas *et al.*, 2019), iv) how to define geometries of the Antifer blocks in the collision detection algorithm of Project Chrono (Martínez-Estévez *et al.*, 2023).

The DualSPHysics code was used to model the propagation and interaction of the regular waves with a smooth (PVC) slope armoured with one row of Antifer blocks. The configuration of the DualSPHysics simulation was based on the real dimensions of the laboratory wave tank but with some adaptations. The numerical tank was 16 m long, 0.80 m wide, and 2 m high. The numerical conditions were the same as the experimental test conditions.

4.3.2.1 Definition of the case geometry and initial conditions

The configuration of the DualSPHysics simulation should be based on the real dimensions of the wave tank. However, to make the simulation computationally feasible, since the software was not yet capable of simulating very large computational domains with many blocks and considering Chrono, it was decided to reduce the length of the wave tank and, consequently, the simulation domain. Therefore, a numerical tank 5.1 m long, 0.80 m wide, and 2 m high was considered, whereas the numerical domain was 9 m long, 1 m wide, and 3 m high. The incident and reflected wave heights (H_i and H_r, respectively) were obtained during the experimental tests by installing three probes at one to two wavelengths from the structure, which helped to reduce the distance between the model and the piston paddle to 2.5 m, equivalent to one wavelength. Fig.66 shows the three-dimensional representation of the numerical domain. The initial water level was 50.55 cm. The model set up of series 5 from experimental work was considered: arrangement of 1-row of 14 Antifer blocks (Type 2, see Table 15 and Fig.43) and a smooth slope (made of acrylic with two layers of paint), considering a slope of 1V:2H.

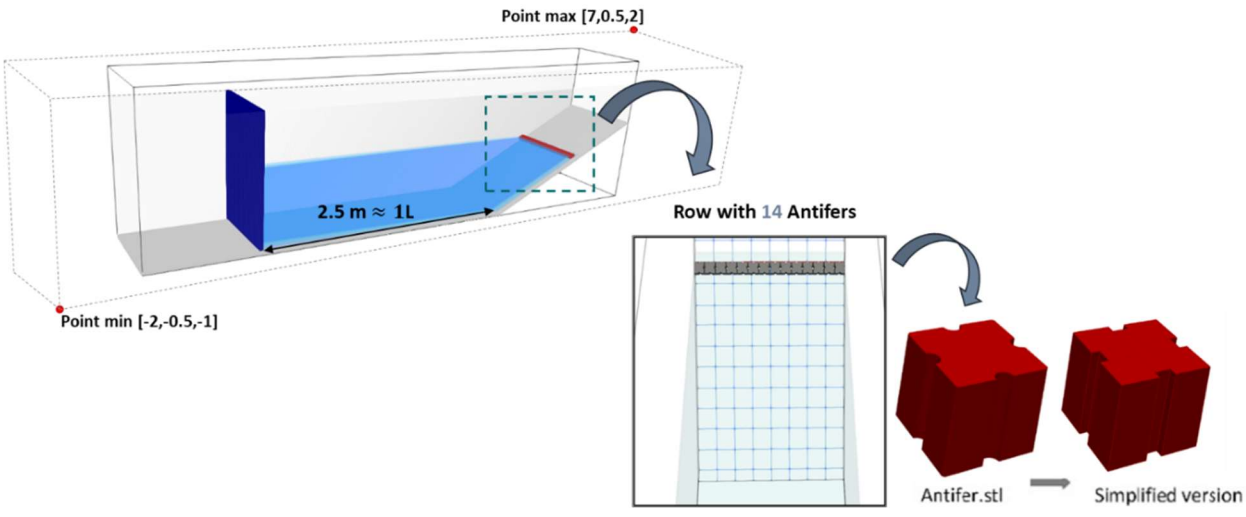

Fig.66 – Three-dimensional representation of the numerical domain (left) and top view (middle).

4.3.2.2 Boundary conditions and other numerical parameters

The following conditions were activated during the numerical implementation:

- Moving boundaries to mimic the piston wave generation;
- Active Wave Absorption System (AWAS) applied to the piston paddle wavemaker;
- Density Diffusion Term (DDT) (Fourtakas *et al.*, 2019) to get a less noisy and more accurate density and pressure field for the fluid domain;
- Consideration of STL files of the Antifer blocks to use Project Chrono and mDBC. A simplified version of the Antifer STL file, as presented in Fig.66, was used to reduce the number of faces involved in collision computations with Project Chrono, thereby decreasing the overall simulation execution time by speeding up Chrono's processing;
- Modified Dynamic Boundary Condition (mDBC) (English *et al.*, 2022) applied to a smooth slope, bottom, piston paddle and STL files of Antifers. The equations of rigid body dynamics were used to determine the movement of rigid bodies like the Antifer blocks. This involved computing the resultant force of each floating particle as the sum of the contribution of all surrounding fluid particles, as explained in Canelas *et al.* (2018). To implement the modified Direct Boundary Condition (mDBC), normal vectors were required for each particle. These vectors were created with direction towards the boundary interface, and their magnitude was equal to the distance between the position of the boundary particle and the boundary interface. The direction and magnitude of these normal vectors are crucial in obtaining the ghost node projected into the fluid across the boundary interface. To properly implement this boundary condition, four layers of ghost nodes within the fluid domain were required to obtain the density of the solid particles by linear extrapolations. Fig.67 displays the STL file of an Antifer and the bottom and slope boundaries, how they were discretized into SPH boundary particles, and the normal vectors computed for each particle. Note that the magnitude of each normal vector varied depending on the distance between the particle and the boundary interface, as illustrated in Fig.67;

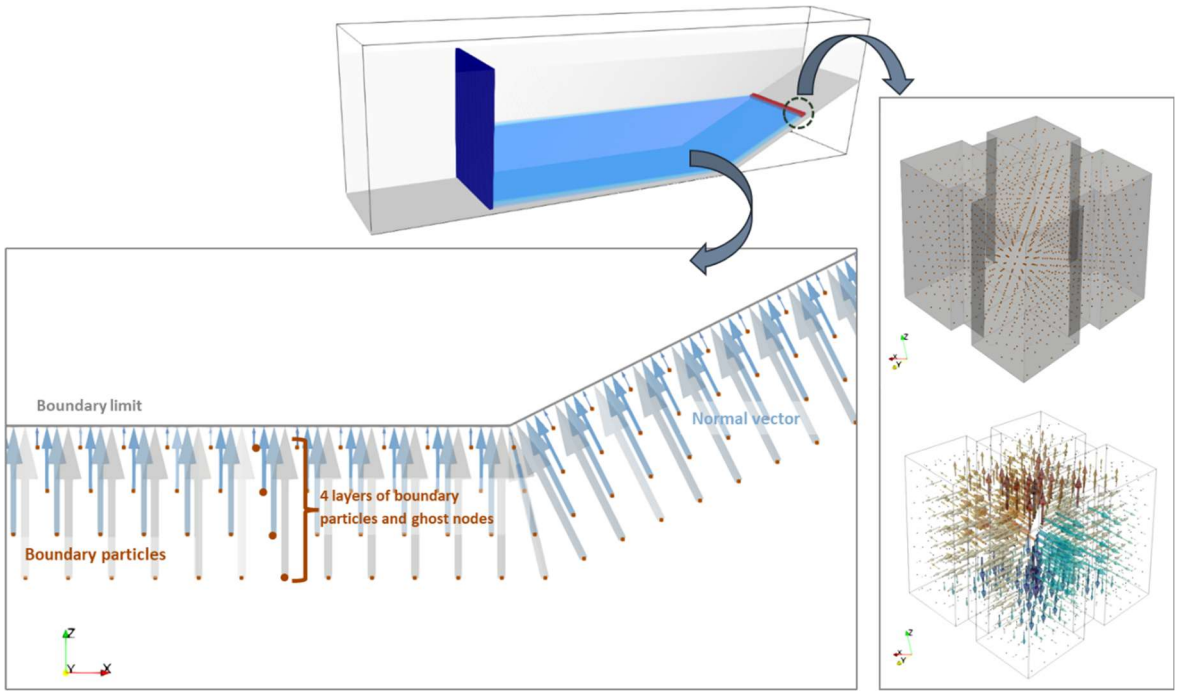

Fig.67 – mDBC application to the bottom, slope and Antifer blocks, including the normal vectors representation.

- Project Chrono for the detection of accelerated collisions between blocks. It was necessary to define the values of the friction coefficient between Antifer blocks and between Antifer blocks and the slope was necessary to solve the collisions. To obtain the static coefficient, a simple method was used: placing one block at rest on the slope in a horizontal position and gradually increasing the slope angle until the block started to slide. The tangent of the threshold angle was then used as a measure of the coefficient of friction. The properties of the materials, which values are provided in Table 22 should be given by the user.

Table 22 – Phase 2: Antifer parameters and coefficients for the numerical simulation of blocks' collisions using DualSPHysics coupling with Project Chrono.

Parameter / Coefficient	Notation [Units]	Value
Moment of inertia (*)	$I_x\ [kg \cdot m^2]$	0.00017676
	$I_y\ [kg \cdot m^2]$	0.00017676
	$I_z\ [kg \cdot m^2]$	0.00018280
Friction coefficient	$\mu_{Antifer\ (Concrete)\ VS\ Antifer\ (Concrete)}[-]$	0.65
	$\mu_{Antifer\ (Concrete)\ VS\ Mound\ (Wood+Ink)}[-]$	0.67
Young modulus	$E_c\ [GPa]$	30
Poisson ratio	$\upsilon\ [-]$	0.2
Restitution coefficient (**)	$C_R\ [-]$	0.55

(*) Results from CAD software for mass properties 1.
(**) See Sarfaraz and Pak (2018)

4.3.2.3 Validation of wave conditions

Waves selected for the study are of the regular and 2nd order type, enabling the application of automatic wave generation theories already implemented in the DualSPHysics code. However, due to the computational domain's reduction and approximation of the piston paddle's location to the model at 2.5 m, the parameters related to the piston paddle wavemaker had to be adjusted for each wave height, such as wave height (H), wave period (T), time until the wave's complete development (*ramp*) and start-period of the active wave absorption system (*startAWAS*). So, the numerical waves were validated to ensure that the first waves generated in the numerical model were equal to the experimental ones. This is very important since the first waves were the ones responsible for the movement of the blocks, despite not being completely developed.

The validation of wave conditions involved considering the blocks fixed and a two-dimensional domain. Fig.68 depicts the numerical domain. The wave validation procedure consisted of the following steps:

(i) Application of automatic second-order regular wave generation theory, which was implemented in the code, at the piston paddle wavemaker located 2.5 m away from the structure;

(ii) Adjusting the parameters related to the piston paddle wavemaker movement (H, T, *ramp* and *startAWAS*) for each simulated wave height;

(iii) Comparing the experimental and numerical free-surface elevations at wave gauge S7.

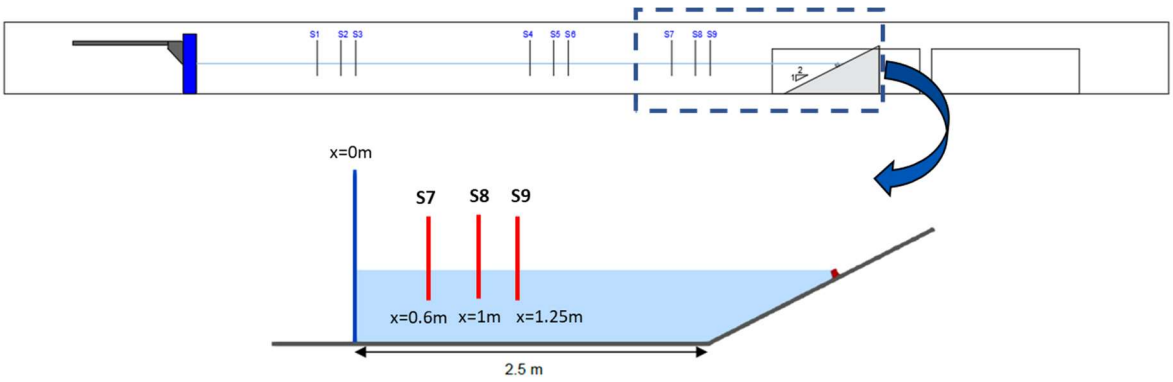

Fig.68 – Two-dimensional numerical setup for validation of wave conditions.

Applying the reflection analysis by Mansard and Funke (1980), the incident and reflected wave heights were separated from both the experimental and numerical records of the free surface elevation. As a result, Fig.69 and Fig.70 were obtained, representing the free surface elevation time series of the incident water elevation on wave gauge S7 as obtained with the two-dimensional numerical simulation and measured in the physical model test, for wave conditions H12 (H_{exp}=0.0375 m, T=0.93s) and H14 (H_{exp}=0.075m, T=1.315s).

During the initial seconds, the free-surface elevation was accurately represented, demonstrating a good agreement with the experimental data. This confirmed that the chosen numeric parameters (H_{num}, *ramp* and *startAWAS*) were well adjusted to minimize the differences that emerge as the simulation progresses in the amplitudes of the numerical and experimental waves. These discrepancies are due to the repositioning of the wavemaker paddle closer to the model, which leads to the observation of different reflections than those observed in the laboratory as they now take place in different spaces and at different times within the numerical model.

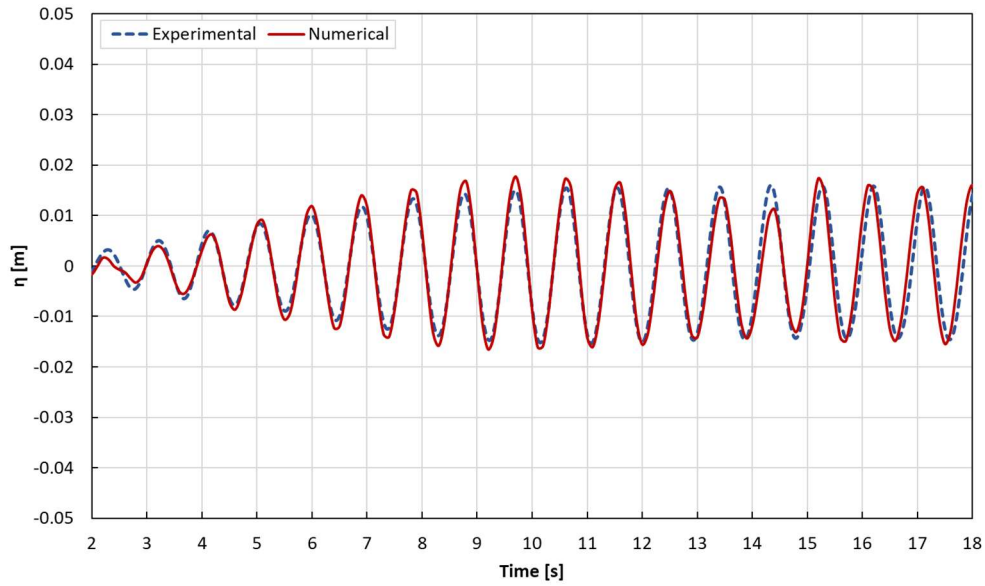

Fig.69 – Free surface elevation of the incident component at gauge S7, considering T=0.93s, H_{exp}=0.0375m, H_{num}=0.035m, d=0.5055m, *ramp*=11 and *startAWAS*=14s.

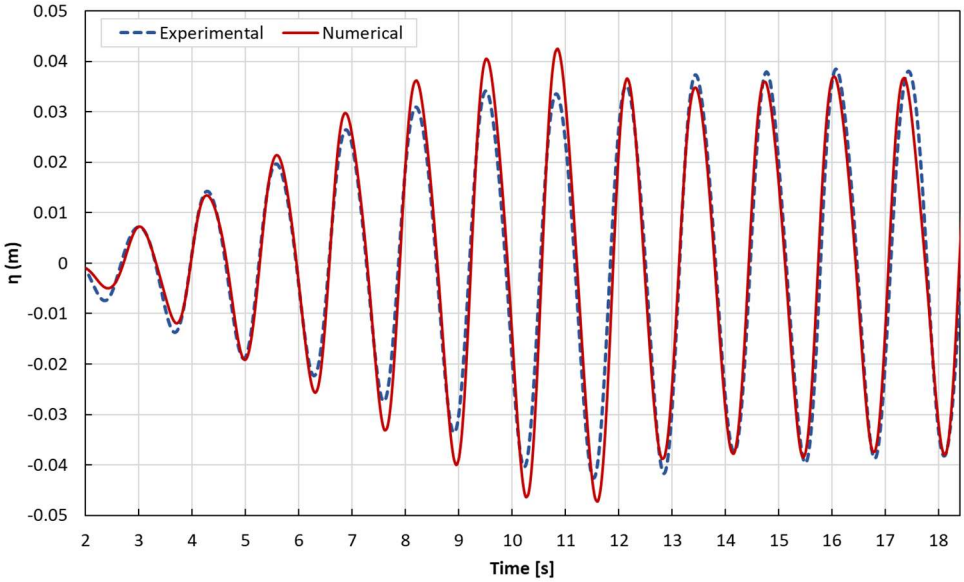

Fig.70 – Free surface elevation of the incident component at gauge S7, considering *T*=1.315s, H_{exp}=H_{num}=0.075m, *d*=0.5055m, *ramp*=9 and *startAWAS*=11.835s.

4.3.2.4 Numerical discretisation parameters and software performance assessment

An initial distance between particles, dp, should be established to discretise the numerical domain into particles. According to Altomare *et al.* (2017), a minimum of 5 particles is recommended to define the wave height (H) and, consequently, to ensure precise wave propagation ($H/dp > 5$). Based on the wave heights of tests H12 and H14, a dp of 0.005 m was selected, resulting in H/dp ratios of 7.5 and 10, respectively.

The distance of interaction (kernel radius) is defined as $2h$ = 0.02078 m (being $h = 1.2 \cdot \sqrt{3} \cdot dp$). A total of 12,346,600 particles were created with 16,086 particles discretising the 14 Antifer blocks. For H12, the simulation of 52 s of physical time took 20 days to be executed using NVIDIA GeForce RTX 2080 Ti GPU. For H14, the simulation of 38.5 s of physical time took 27 days to run using NVIDIA GeForce RTX 2080 Ti GPU. By utilising an NVIDIA GeForce RTX 3080 Ti GPU, the computational acceleration of the process could have resulted in a 50% reduction in the total simulation time. Furthermore, the entire process is delayed since Chrono uses a single-core CPU to solve the interactions between the blocks, and slope and Antifer blocks.

4.3.3 RESULTS AND DISCUSSION

In these tests, the hydraulic stability of the Antifer blocks is a function of the hydrodynamics forces, frictions forces, and block weight.

Fig.71, Fig.72 and Fig.73 illustrate the total displacements of each block for tests H12 and H14, considering the performance of three tests per wave to assess the repeatability of the measured results, and compared with the total displacement of the blocks from the numerical simulation (shown in yellow). As expected, there is some variability in the results obtained for each block, but the range of values obtained for each wave height is well-identified.

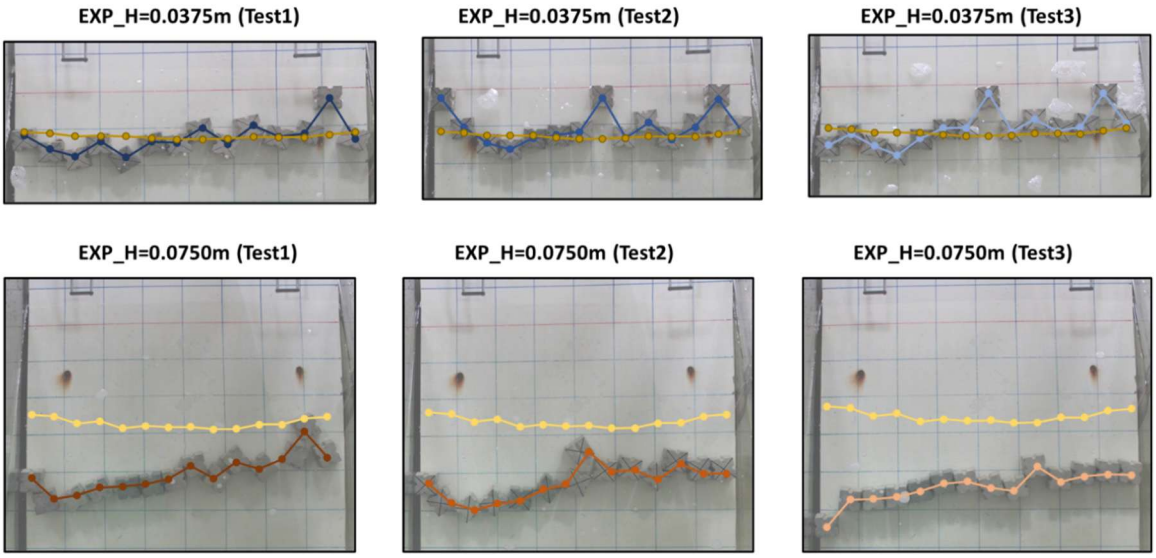

Fig.71 – Total displacements obtained for each block for H12 and H14, considering the performance of three tests, and the total displacement of the blocks from the numerical simulation.

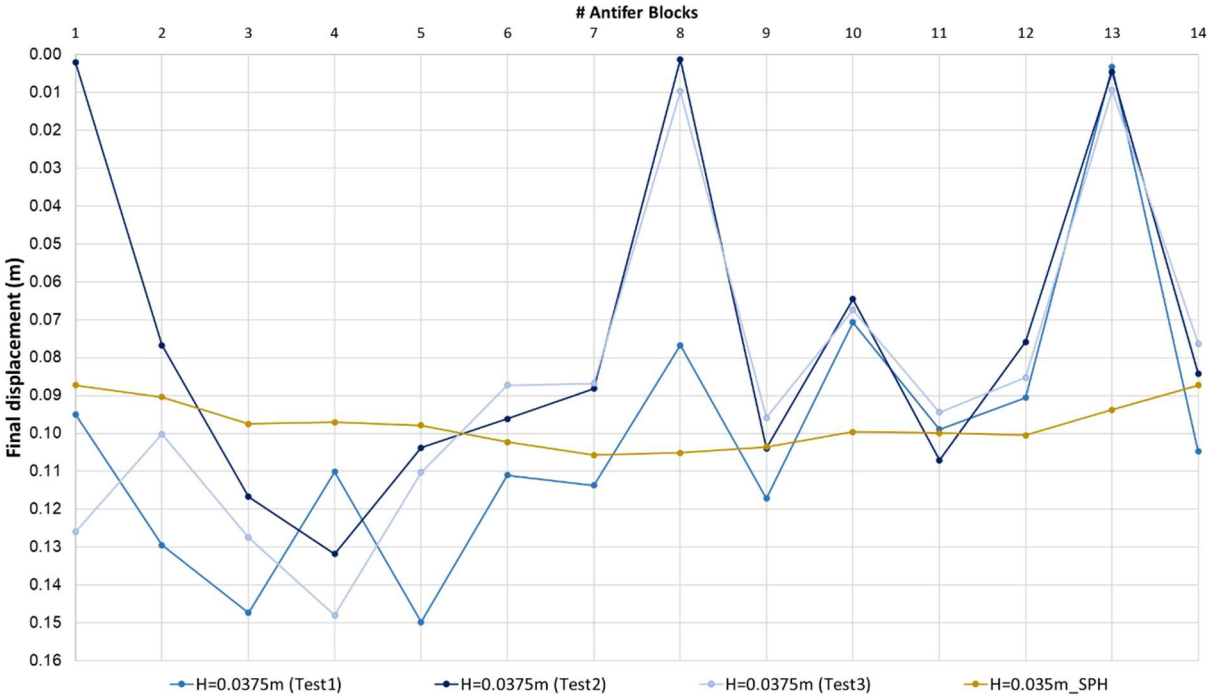

Fig.72 – Total displacements obtained for each block for H12, considering the results of three tests, and the total displacement of the blocks from the numerical simulation.

Considering the test H12 with height H = 0.0375 m, the total displacements for test 1 (R01) varies between 3 mm and 0.15 m; for test 2 (R02) between 1 mm and 0.13 m; and for test 3 (R03) between 9 mm and 0.15 m. Comparing with the numerical results, one can observe that, on average, the movement of the blocks were of the same order of magnitude. However, due to differences arising from wave tank reflections, variance in incident wave heights, and the use of an average block mass, accurate replication

of block displacement was not feasible. It is important to highlight that even the experimentally obtained results are not always consistent, as there are variations between test repetitions. Therefore, this emphasizes the notion that a certain degree of disparity between numerical and experimental results is always expected.

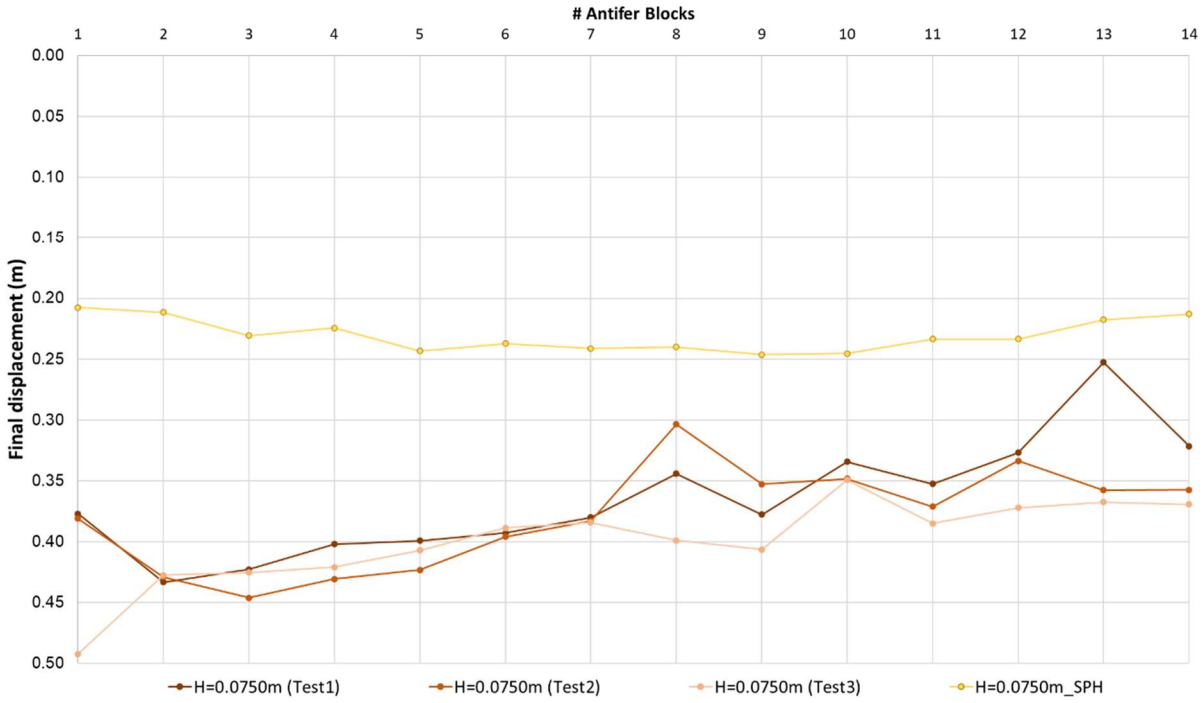

Fig.73 – Total displacements obtained for each block for H14, considering the results of three tests, and the total displacement of the blocks from the numerical simulation.

For wave H14 with height H=0.075 m, the total displacements for test 1 (R01) varies between 0.25m and 0.44m; for test 2 (R02) between 0.30m and 0.45m; and for test 3 (R03) between 0.35m and 0.50m.

Comparing with the numerical simulation, the results were poorer, casting doubt on the accuracy of the results for the previous wave height. Nevertheless, it was observed that, in the numerical simulation, more blocks rotated than in the physical model, where only one block in one of the tests rotated. If there are "jumps" in the movement graphs along the x and z axes, it indicates that the blocks have rotated (Fig.74). In this case, three blocks exhibited rotation movement. Such rotation was not observed in the experimental tests.

The graphics of Fig.75 reveal that test H12 did not produce any rotation of the blocks, either in the numerical simulations or in the experimental tests. Nonetheless, since the numerical simulation only considered 52 s, it is unclear whether the blocks would eventually rotate or move more if the simulation time was extended.

To address the challenges found in this initial phase, it is advisable that the upcoming phase of the research adheres to the following recommendations:

- Replace regular waves by solitary waves to simplify the system and eliminate effects of reflections and re-reflections;

- Integrate instrumented Antifer blocks with an Inertial Measurement Unit (IMU) to facilitate tracking of the block's movement and to maintain weight, and regularity;
- Ensure the reproducibility of results both in experiments and numerical simulations by considering various factors, such as the wave generation, experimental setup, and the location of the model, piston, and wave probes in the wave flume.

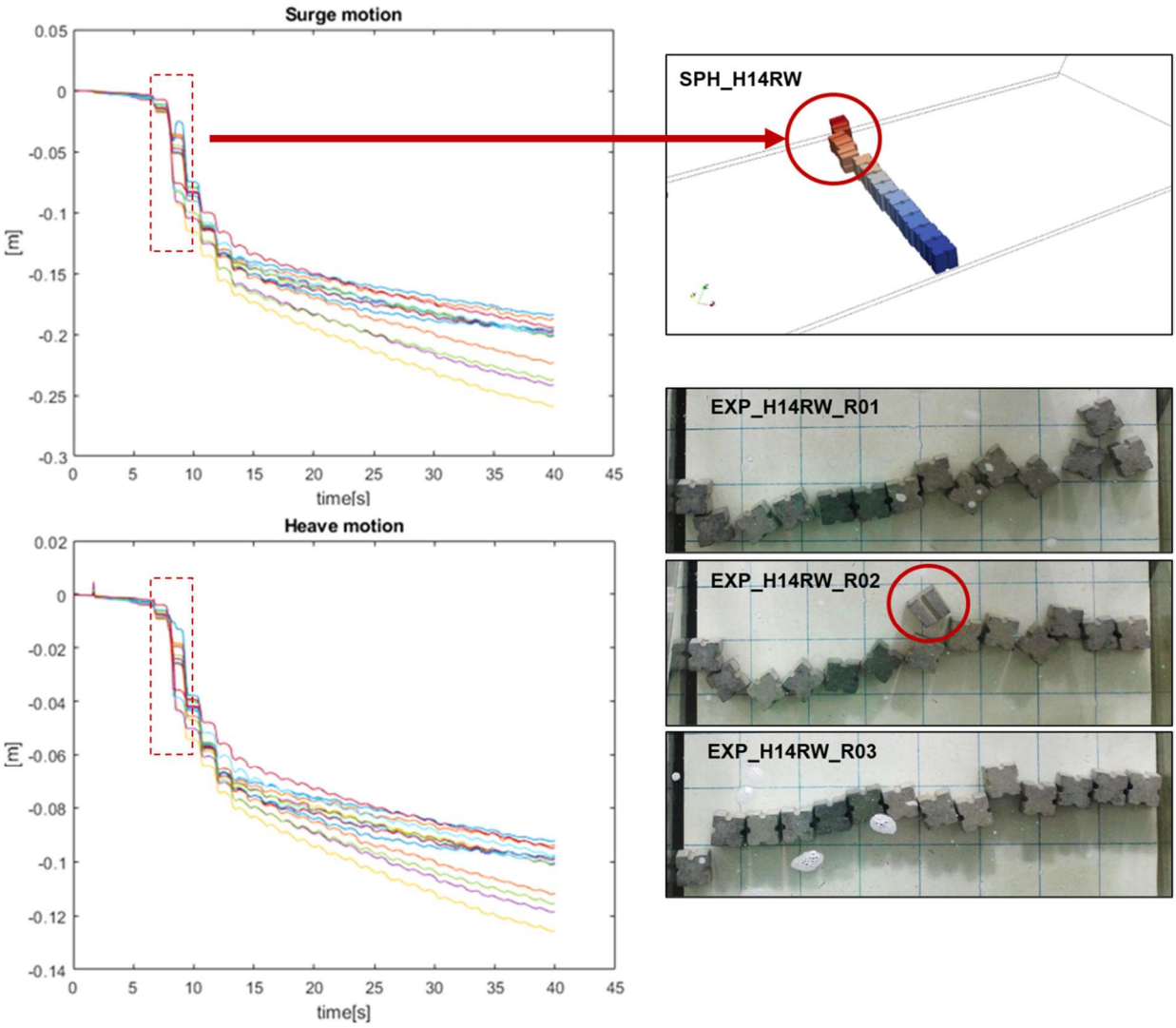

Fig.74 – Comparison between the numerical and experimental rotational movement of the blocks for wave H14.

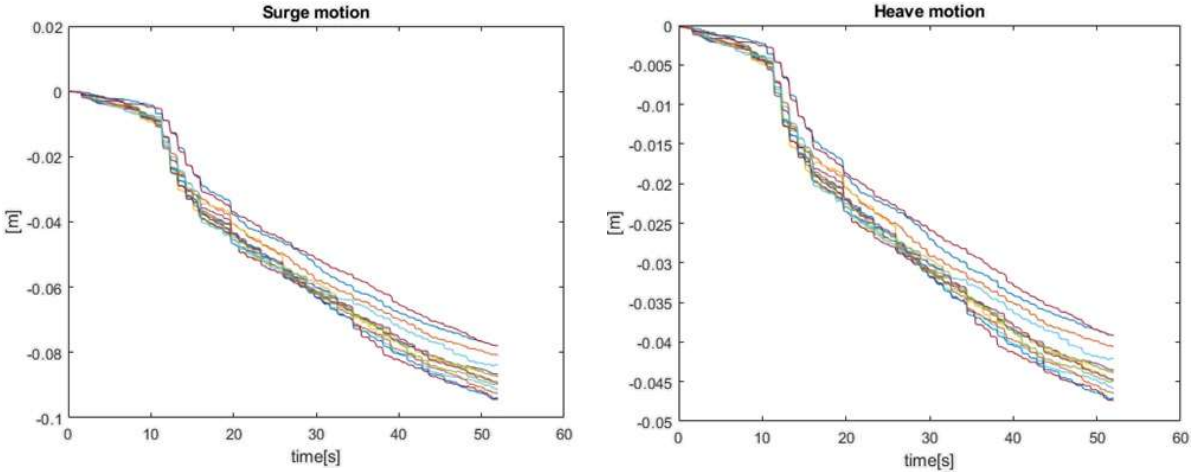

Fig.75 – Numerical rotational movement of the blocks for wave H12.

4.4 SLOPE ARMOURED WITH SMART ANTIFER BLOCKS UNDER THE ACTION OF SOLITARY WAVES

The third phase comprised three distinct tasks, being task 3.1 dedicated to designing and constructing a small-scale IoT-enabled Antifer block called the SmartAntifer. The SmartAntifer was designed to measure, record, process, and communicate the data relating to the 3D displacements and forces acting on an Antifer block in a laboratory context. The instrumented unit will be used in task 3.2 (4.3.1) of the subsequent experimental testing phase to enhance the results achieved in Phase 2. Finally, task 3.3 (4.4.3) corresponds to the validation of the numerical model considering the new experimental results.

4.4.1 SMARTANTIFER

During Phase 3.1, the primary objective was to develop the architecture for the SmartAntifer's software and hardware, whose design resulted from a collaboration between the Hydraulics Laboratory of the Department of Civil Engineering and the Laboratory of Systems and Underwater Technology (LSTS), both from the Faculty of Engineering of the University of Porto. This work was followed by an extensive testing program to evaluate the performance of the instrumented unit before proceeding to more complex testing in Phase 3.2. This testing program included a thorough analysis of the SmartAntifer's performance and calibration procedure and the creation of a proof-of-concept for future versions of the instrumented units with more advanced capabilities.

4.4.1.1 SmartAntifer development and construction

System architecture

This section provides an overview of the system architecture and its functional modules, which can be categorized into three main modules, as shown in Fig.76. The SmartAntifer block was aimed at meeting specific application requirements, including:

- 3D displacement measurement;
- wireless connectivity;
- a minimum sampling frequency of 4 Hz;
- data export in CSV format;

- compatibility with watertight systems;
- charging without physical connectors; and
- autonomy of 6-8 hours.

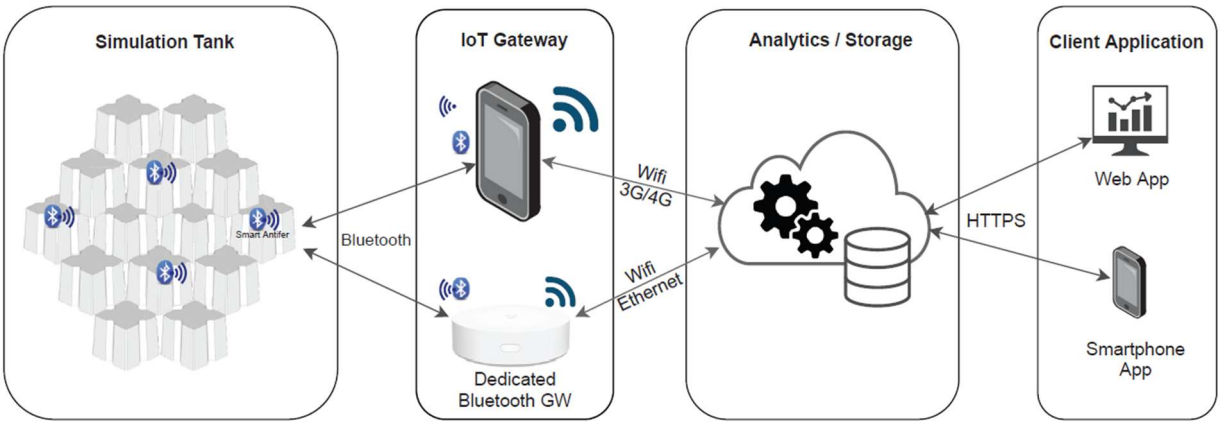

Fig.76 – Overall architecture system (Neiva *et al.*, 2021).

To collect data, Bluetooth communication technology was used to transmit data from the SmartAntifer blocks to the cloud through a computer or mobile application. Both applications offer the added functionality of changing configuration parameters for each SmartAntifer, managing stored data, and operating as a gateway for sending collected data to the cloud-based service using backhaul communications, such as Wi-Fi, 4G, or Ethernet. The IoT device was specified to operate in the laboratory, in proximity to the operator/user, the reason why other IoT communication protocols were discarded.

On the server-side, data received from the application was stored in a database and processed for visualization. Then, a block of analytics was used to identify movements and evaluate the 3D displacement of each specific SmartAntifer block that has been used in a specific experiment.

Prototypes

The SmartAntifer architecture has gone through multiple iterations to develop a basic circuit that requires the fewest components possible, while meeting the application requirements for integration into a laboratory model scale Antifer cube (type 2, 291.5 gr, A = 0.056 m, Fig.43).

An initial prototype of the SmartAntifer block was created using 3D printing. This cost-effective version was developed to examine the block's opening and closing mechanism, as well as the grooves and hollow areas for implantation, and to evaluate the size of the electrotechnical component of the instrumented block.

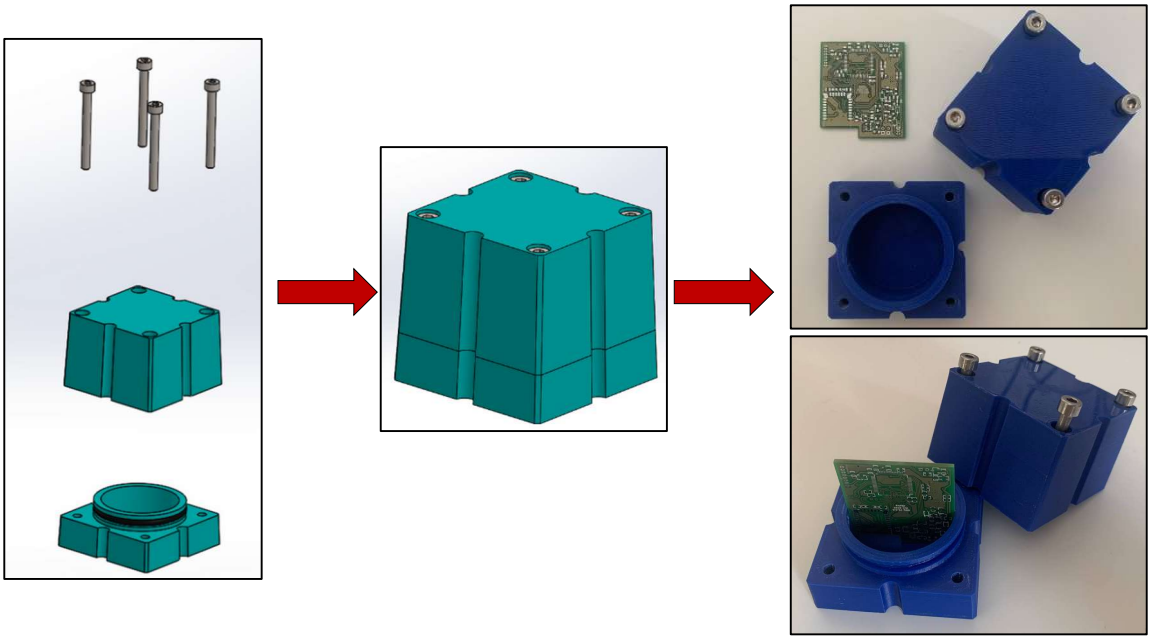

Fig.77 – CAD drawings and 1st SmartAntifer prototype (September 2020).

For the second prototype, a special aluminium alloy with a higher density than the norm was utilized to meet the required geometry and mass specifications of the block. Additionally, a steel mass was included to satisfy the necessary inertia. To further comply with the block's mass and to optimize the use of the internal space for electronic component placement, the shape of the hollow was changed from circular to ellipsoidal. An O-ring was also used to ensure the block remains waterproof when submerged in water. The CAD drawings of this prototype are presented in Fig.78.

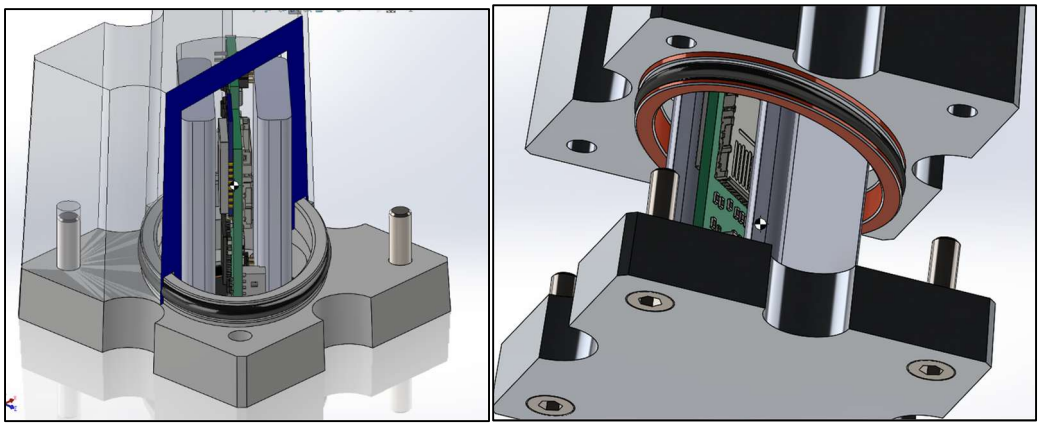

Fig.78 – CAD drawings of the 2nd SmartAntifer prototype (May 2021).

The electronic component architecture of the second SmartAntifer prototype was organized into five primary blocks, as depicted in Fig.79: microcontroller, Bluetooth module for communication, external storage (microSD and EEPROM), Inertial Measurement Unit (IMU), and power management

(comprising of control logic and wireless charger). Two Li-Polymer batteries with a capacity of 600mAh were utilized, with a recommended voltage range of 2.75V to 4.2V.

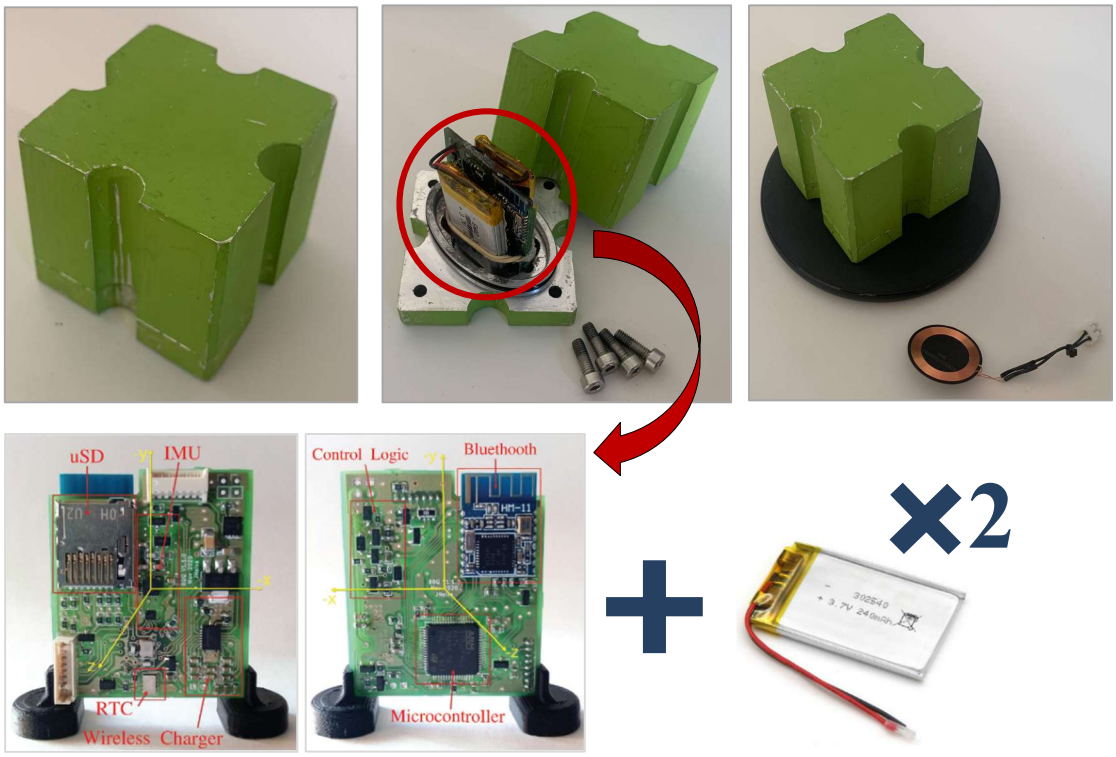

Fig.79 – Constitution of the 2nd SmartAntifer prototype.

During the assembly of the mechanical and electronic components of the block, certain incompatibilities were detected, leading to non-compliance with some of the originally imposed requirements. The thickness of the aluminium was one of such issues, inhibiting the detection of the Bluetooth signal and induction-based charging of the batteries. Consequently, it was necessary to open the block each time to charge or retrieve information stored on the memory card.

A third and final prototype was created to overcome the remaining details – Fig.80. For this final prototype, both the Bluetooth antenna and induction coil were relocated to the external base of the Antifer and covered with waterproof resin. Additionally, a LED was included to display the operational mode of the SmartAntifer, indicating whether it is in ON, Acquisition mode, Configuration mode, or OFF. Following the design of this final prototype, 10 SmartAntifers were produced, and several relevant characteristics should be noted for future integration into a slope for tests:

- Unlike the concrete blocks, the SmartAntifer is not designed to absorb water. So, the block, including electronic components, weighs a total of 316 g, equivalent to the wet weight of the concrete blocks in the laboratory;
- Geometrically, the SmartAntifers are identical to the existing laboratory concrete blocks, with A= 0.056 m;

- Both the second and final prototype of SmartAntifers were painted with the same paint used on the laboratory blocks, to ensure the same roughness when in contact with the slope and with each other (Fig.79).

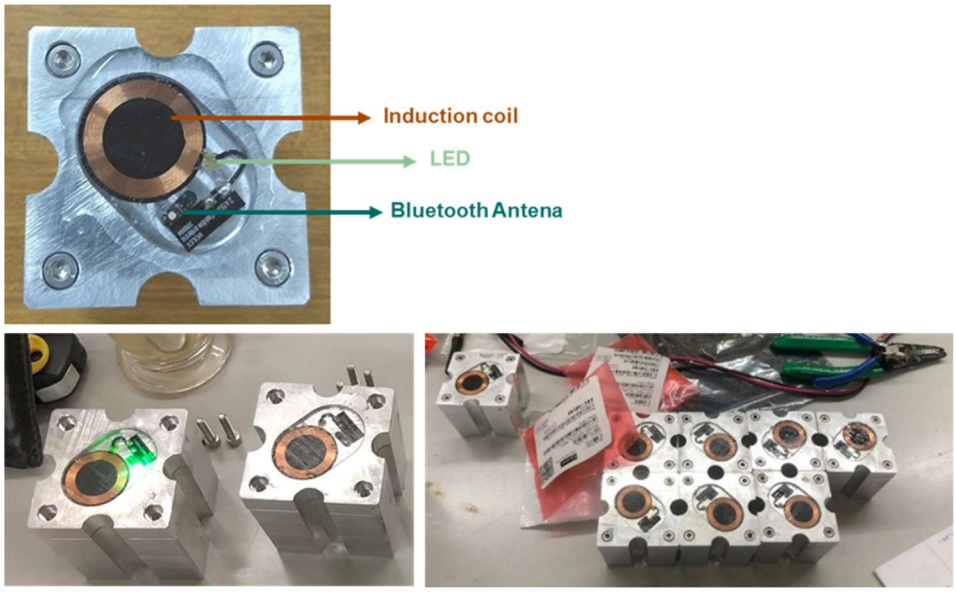

Fig.80 – SmartAntifer final product (April 2022).

The architecture of the IoT device for the SmartAntifer final prototype is described in more detail below.

Instrumentation

The final architecture version is divided into 5 main blocks: microcontroller unit (MCU), antenna for communications, external storage (microSD and EEPROM), Inertial Measurement Unit (IMU), and power management (including control logic, wireless charger). This architecture is presented in Fig.81.

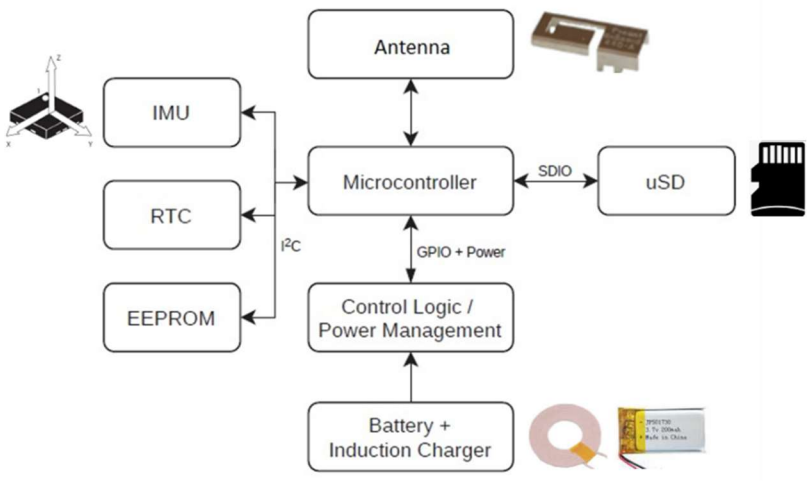

Fig.81 – SmartAntifer: IoT device architecture (adapted from Neiva *et al.*, 2021).

The SmartAntifer prototype was implemented on a four-layer printed circuit board (PCB), with key components detailed in Fig.82, including an ICM-20948 from TDK. This low-power 9-axis Inertial Measurement Unit (IMU) is designed for IoT applications and comprises a three-axis MEMS (micromachined micro-electromechanical systems) accelerometer (Acc), gyroscope (Gyr), and magnetometer (Mag). Additionally, it features an integrated Digital Motion Processor (DMP) that offloads computational demands from the host processor, optimizing power efficiency. The DMP operates at a refresh rate of 200 Hz, though the sampling frequency can be adapted to suit specific scenarios. The IMU's central placement on the PCB aligns it closer to the device's centre of mass, minimizing rotational offsets during measurements. Furthermore, integrated circuits are co-located on the same PCB side to simplify assembly, and package choice is prioritized to ensure the shortest distance with the microcontroller.

The ICM-20948's accelerometer and gyroscope function as follows:

- MEMS accelerometer operation.

The MEMS accelerometer measures linear acceleration, which is the rate of change of velocity along a specific direction. It uses a small "proof mass" inside the sensor that displaces slightly when the device undergoes acceleration. According to Newton's second law:

$$F = m \cdot a \tag{101}$$

where F is the force applied to the proof mass m and a is the resulting acceleration. In the case of a MEMS accelerometer, this force induces a slight displacement of the proof mass, altering capacitance or resistance within the device. This change in the electrical signal is read as acceleration by the IMU. The accelerometer reads both gravitational acceleration (g, approximately 9.81 m/s^2 on Earth) and any applied acceleration (a) due to movement. When the accelerometer is stationary (*e.g.*, lying flat on a table), the only force acting on it is gravity. Here, the accelerometer measures the static acceleration due to gravity, g, which allows it to detect orientation. When a force is applied to the accelerometer, *e.g.*, if it is moved or rotated, it undergoes dynamic acceleration, a, in addition to the static gravitational acceleration. The total measured acceleration $a_{measured}$ is given by:

$$a_{measured} = g + a \tag{102}$$

- MEMS gyroscope operation

The MEMS gyroscope in the ICM-20948 measures angular velocity, which is the rate at which the device turns around an axis. Internally, the gyroscope has a vibrating structure. When the device rotates, this vibrating mass experiences the Coriolis effect, which generates a small, perpendicular force relative to the direction of vibration and the axis of rotation. This force causes a measurable displacement in the vibrating mass, which is proportional to the angular rate, ω, as described by:

$$F_{Coriolis} = 2 \cdot m \cdot v \cdot \omega \tag{103}$$

where m is the mass of the vibrating structure, v is its velocity, and ω is the angular velocity of the device. The gyroscope accurately measures rotational speed and direction by detecting changes in the vibration due to this Coriolis force,

The SmartAntifer device also includes:

- a microSD card reader for data storage during the data acquisition stage;
- an EEPROM to store important operational parameters, such as the IMU calibration data;
- a low-power Real-Time Clock (RTC) to know the date and time of each acquisition;
- a wireless charging circuit compatible with the Qi protocol to charge the batteries;
- a ESP32-PICO-D4 from Espressif Systems, which is a System-in Package (SiP) comprising a 40MHz crystal oscillator, a 4 MB flash memory, an ESP32 MCU, which is a single 2.4GHz Wi-Fi and Bluetooth combo ship, and a 50 Ohm calibrated radiofrequency (RF) circuit. In the final product, the antenna, initially embedded in the PCB was cut off and extended to the exterior;
- a circuitry responsible for externally turning the system ON/OFF using a HALL sensor when the system is installed in a watertight block;
- two connectors: one for interfacing with an external PCB with an RGB led, and another to connect the HALL effect sensor.

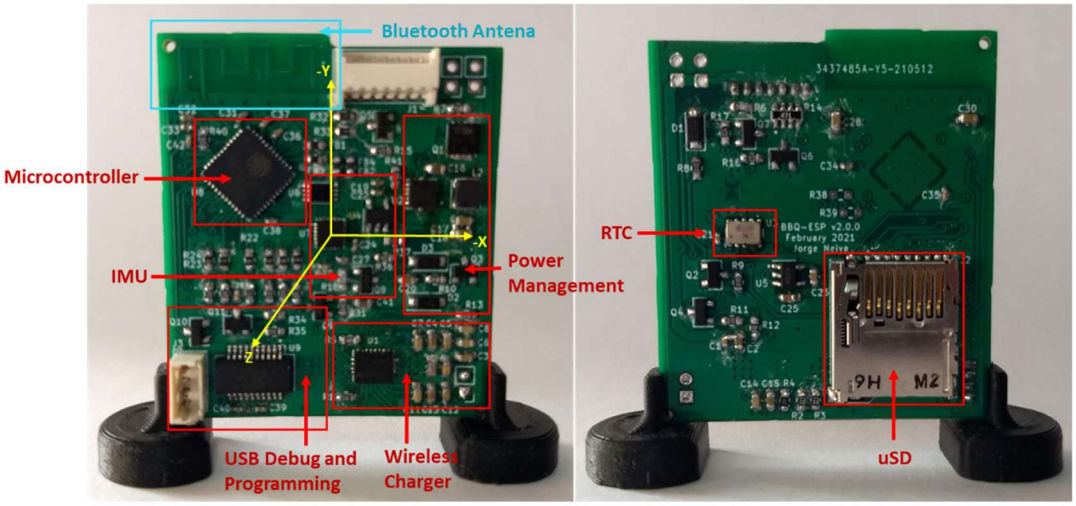

Fig.82 – Different views of the SmartAntifer IoT device prototype with all components identified in red and the 3D-axis identified in yellow (adapted from Neiva *et al*., 2021).

4.4.1.2 Signal detection

To activate a SmartAntifer, the hall sensor must be triggered by passing a magnet nearby. Once the cube is turned on, the LED will display a colour sequence and begin acquiring data from the IMU. The LED will flash briefly in white every second to indicate the acquisition process has begun.

After the startup, the SmartAntifer automatically enters data acquisition mode. When in this mode, the acquired data is stored on a micro-SD card. Upon the first daily startup of the SmartAntifer, a folder is created with the day, month, and year according to the internal clock configuration. If it is not the first startup of the day, the respective folder for that day is opened and the data is saved in a CSV file. After opening the micro-SD card on a computer, the interface will display the available folders and files. By opening a folder, all previously created CSV files can be easily accessed and listed. The following image

displays the contents of a CSV file. The initial row displays the zero values of the accelerometer, whereas the subsequent row comprises a header that denotes the nature of data in each column. Specifically, the columns represent the linear acceleration along the 3-axis (ax, ay, and az), angular velocity along the 3-axis (gx, gy, and gz), and the magnetic field strength along the 3-axis orientation (mx, my, and mz).

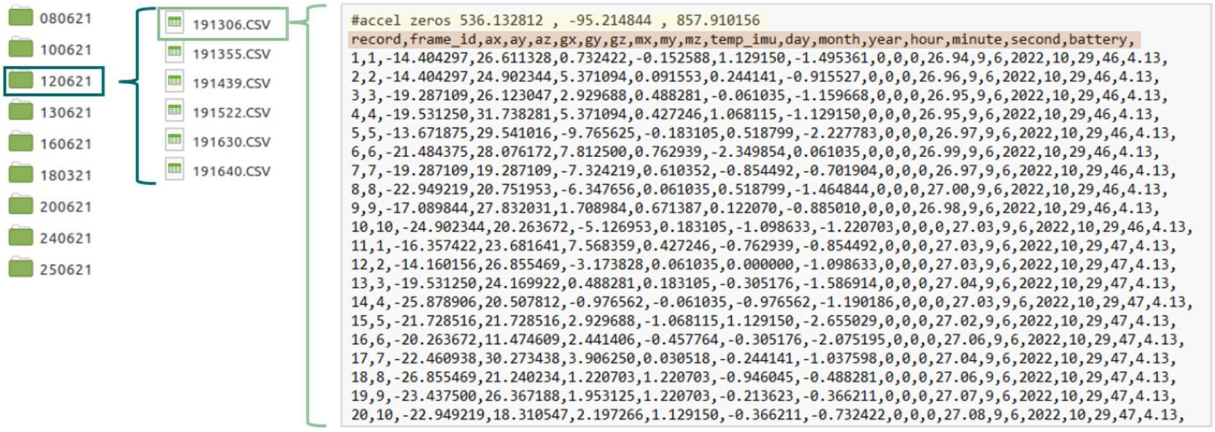

Fig.83 – Example of the available folders and CSV files inside a micro-SD card.

To switch to configuration mode, the magnet must be brought close to the hall sensor again for 2 s. If the magnet remains in the same position for more than 5 s, the SmartAntifer will enter power-off mode. When in configuration mode, the SmartAntifer can be configured using either the Android application or the Windows application, which is presented in the next subsection. Bringing the magnet close to the hall sensor again for 2 s returns the SmartAntifer to the acquisition mode, while bringing the magnet close for more than 5 s will turn off the device.

4.4.1.3 General SmartAntifer configuration: application setup and operation range

This section describes the configuration of the SmartAntifer device and the setup processes via the *BBQ Manager* application. Two dedicated applications, *BBQ Manager* for computers and a mobile app, provide a user-friendly interface for configuring the SmartAntifer's ID, data segmentation, activation scheduling, and real-time data monitoring.

Upon launching the application, a window appears, and the application automatically searches for connected SmartAntifer devices. Alternatively, new SmartAntifer devices can be manually searched for by clicking the "Scan nearby devices" button, which adds any found devices to the list on the left. If the device ID cannot be retrieved, the Bluetooth module's MAC address will be displayed instead. To establish connection with a SmartAntifer device, the user can simply select its ID from the list.

After connecting to the SmartAntifer, the window presented in Fig.84 is displayed, presenting five different sections: *Status*, *IMU*, *Settings*, *Alarms* and *Files*, providing an intuitive setup process for SmartAntifer devices:

(i) ***Status***: Displays battery status, current date/time, and time synchronization options. If the *Sync* button is red, a slight time difference exists between the SmartAntifer and the computer; clicking the button will adjust the clock. A green Sync button indicates the time is synchronized. To

ensure optimal performance and protect the device, the operational parameters and ranges must be observed. The *Battery* status should maintain a voltage between 3.3V and 4.2V to avoid potential damage to the circuit or sensors.

(ii) ***IMU***: Allows real-time data viewing of acceleration and angular velocity readings, with updates every second. The IMU section includes calibration settings to help reduce noise and drift, which can affect data accuracy. The Reset button here restores default IMU settings, helpful for reestablishing baseline measurements if needed.

(iii) ***Settings***: Configures the device ID and sets CSV file segmentation intervals, allowing better data management, especially in extended experiments. The first field allows the user to assign a new SmartAntifer *ID*, effective upon the next restart. The second option lets users set intervals for data segmentation; for instance, setting an interval of 10 minutes creates a new file every 10 minutes. The *Update* button applies new settings to the SmartAntifer, while *Refresh* retrieves previously saved parameters.

(iv) ***Alarms***: Allows scheduling of device activation with up to 12 alarms available. Users can configure the wake-up time relative to the SmartAntifer's current time and specify the duration for each activation event. Each alarm can be set by entering the desired *Time* and *Duration* fields.

(v) ***Files***: Enables file browsing and downloading files stored in the SmartAntifer. By clicking *Refresh*, the user can view an updated list of folders and files. Files can be downloaded by right clicking the file name to reveal the *Download* option. The download progress is shown in a bar below the list, and users can specify the destination folder and file name. By default, files are saved with the SmartAntifer ID, folder name, and file name in the format (*e.g.*, ID_folder_file.csv).

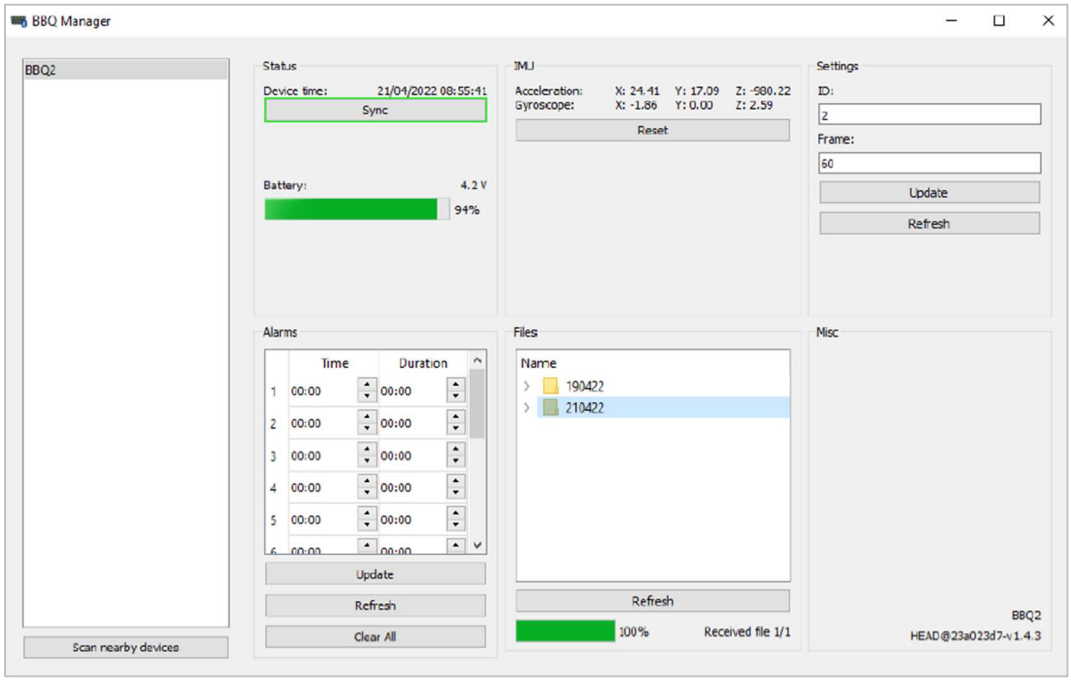

Fig.84 – "BBQ Manager" application display after connection to a SmartAntifer device.

As a final note, it is worth mentioning that the mobile application also allows powering off blocks and changing the data acquisition frequency, with a tested maximum of 100Hz.

4.4.1.4 Calibration procedure for SmartAntifer IMU

Raw sensor readings are often affected by noise and drift. Noise in IMU data can stem from electrical interference, thermal variations, and sensor limitations. Techniques such as filtering – such as low pass filtering - and averaging can help reduce the inaccuracies and random fluctuation in sensor readings. Drift, which represents a gradual deviation in sensor output from true values over time, often resulting from sensor aging, temperature changes, and cumulative biases, can significantly impact long-duration measurements. Regular calibration and the use of sensor fusion techniques - integrating data from other sensors (*e.g.*, GPS or magnetometers) - can effectively correct for drift, enhancing overall measurement reliability. This compensates for accumulated errors, improving long-term measurement stability and accuracy.

Calibration plays a central role in SmartAntifer's performance, ensuring precise IMU measurements by correcting sensor biases and alignment during data acquisition, followed by adjustments for noise and drift during data processing. This two-stage calibration approach is explored in greater depth in the following sections:

Calibration for data acquisition

(i) **Accelerometer calibration**: this includes both static calibration, where the IMU is placed in known orientations to identify and correct biases, and dynamic calibration, using controlled motions to ensure consistent and accurate acceleration readings across all axes;
(ii) **Gyroscope calibration**: this requires determining any inherent bias of the gyroscope by measuring its output while stationary, then rotating the IMU at known rates to assess and adjust any discrepancies in angular velocity readings, ensuring consistency;
(iii) **Temperature calibration**: calibration across multiple temperature ranges compensates for any temperature-induced variations in sensor response, enhancing reliability across variable environmental conditions;
(iv) **Dynamic range and resolution**: confirm that the IMU can accurately measure the expected range of accelerations and angular velocities. This involves validating readings against known values in various scenarios to ensure resolution meets application requirements, particularly for subtle movements or orientation changes;
(v) **Calibration procedures and tools**: utilize specialized calibration software and equipment to facilitate the calibration process effectively.

Calibration for data processing

(i) **Sensor fusion calibration**:
- Alignment and synchronization**:** ensure that the IMU's accelerometer and gyroscope are correctly aligned and synchronized in time to improve sensor fusion algorithm accuracy (*e.g.*, Kalman filters, complementary filters);
- Tuning sensor fusion parameters: adjust parameters in sensor fusion algorithms, such as the process noise and measurement noise, to improve the output accuracy based on calibration results;

(ii) **Post-calibration validation**: After calibration adjustments, validate against reference standards to ensure data quality meets required accuracy levels;
(iii) **Periodic recalibration:** depending on the application and operating environment, periodic recalibration may be necessary to account for any drift or changes in the sensor characteristics over time.

4.4.1.5 Preliminary tests

Submergence testing

The ten instrumented blocks resulting from the latest prototype were subjected to a leakage test. These units were arranged in a single row and positioned at a height of 64.5 cm on a slope of 1V:1.5H. Subsequently, the blocks underwent tests using solitary waves with a maximum duration of six minutes, although their intended operation span is 6 to 8 hours.

Despite the reduced number of tests, faulty operation was detected in four out of the ten blocks. Two of them acquired incorrect data due to an inappropriate configuration, while the other two ceased to function entirely. Upon analysis, it was found that the interior of these two blocks contained water in the batteries, and there were areas of the IMU that were short-circuited. It is plausible that water entered through the base area, as the blocks heated up significantly during induction charging, causing the resin on the sides of the base to lift slightly, thus creating entry points for water.

Ultimately, 8 out of 10 blocks passed the submersion test. However, as a precautionary measure, the type of resin used in the base of the blocks was changed and the transition areas were reinforced to prevent future water entry issues in the system.

Axis convention and signal validation and quality

Afterwards, the final circuit underwent a series of evaluations for its IMU sensitivity, precision, consistency, hysteresis, and other typical instrumentation characteristics.

To perform prototype validation, the device was configured to operate with a sampling frequency of 100 Hz and to store the 6-axis data (accelerometer and gyroscope) into the microSD memory card. It is important to highlight that the data exported to the CSV file undergoes a transformation of axes, to be referred to the axis system commonly used, as presented in Fig.85.

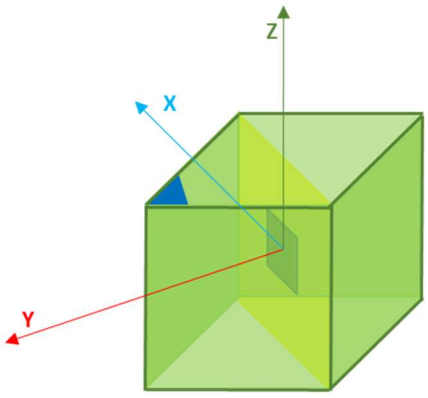

Fig.85 – Axis system axis commonly used.

To confirm the prototype axis orientation, the following experiment was performed:

(i) The prototype was positioned in the rest position, as presented in Fig.85, for circa 20 s,
(ii) The prototype was then rotated 90º on the *x*-axis for another 20 s,
(iii) Lastly, the prototype was rotated 90º on the *z*-axis for another 20 s.

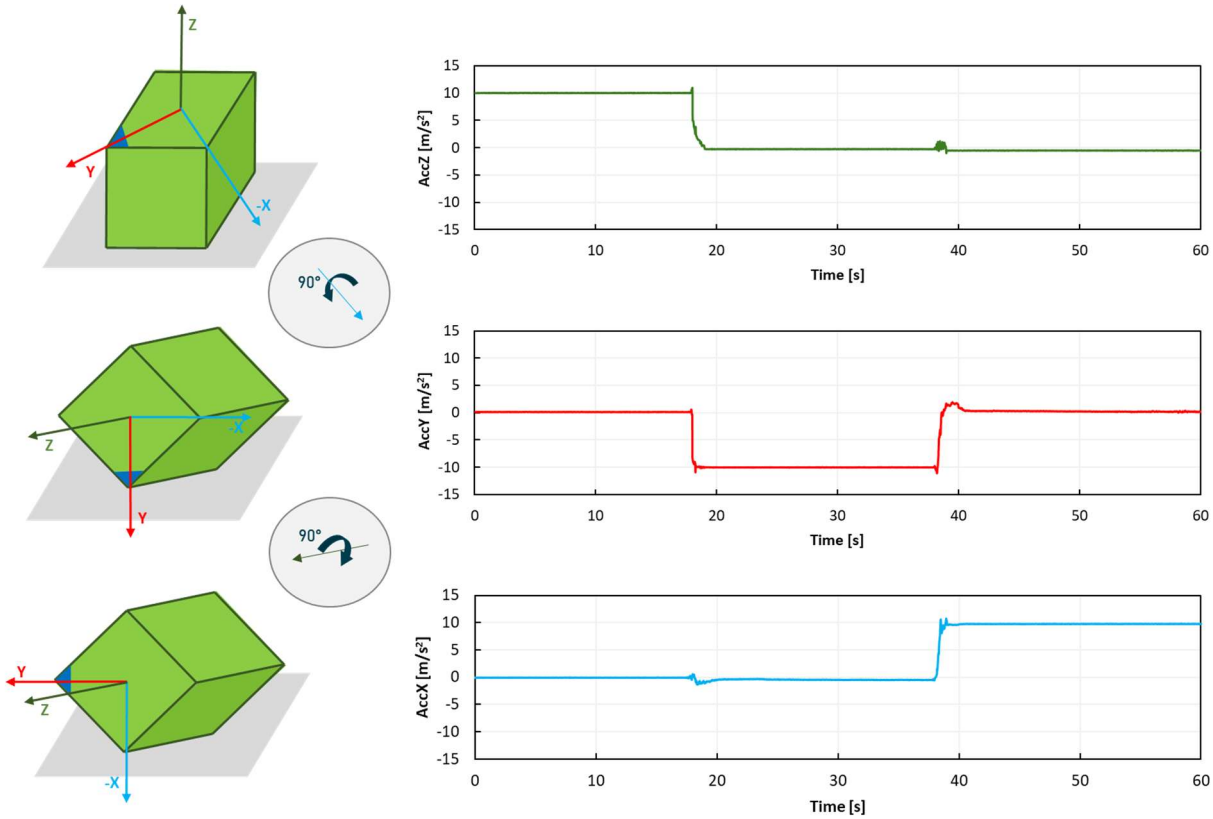

Fig.86 – Axis confirmation based on accelerometer data.

Fig.86 illustrates that during the initial 20 s, when the prototype was positioned vertically, a gravitational acceleration of positive 9.8 m/s² was registered along the z-axis. While resting stationary on a table, the block exhibits an "upward" acceleration of 9.8 m/s². Following a 90-degree rotation about the *x-axis* (between 20 and 40 s), the gravitational acceleration shifted to the y-axis, showing the expected negative value. Finally, with an additional 90-degree rotation about the *z*-axis (between 40 and 60 s), the gravitational acceleration began registering along the *x*-axis. This procedure can be periodically used for IMU calibration, such as in preparation for simulation.

Another simple test involved placing the block on a flat surface, with the z-axis vertical, and moving it in various directions to verify if the block recorded the linear accelerations (m/s^2) properly. Fig.87 shows three tests performed and the corresponding time series of accelerations along the *x*, *y* and *z*-axis.

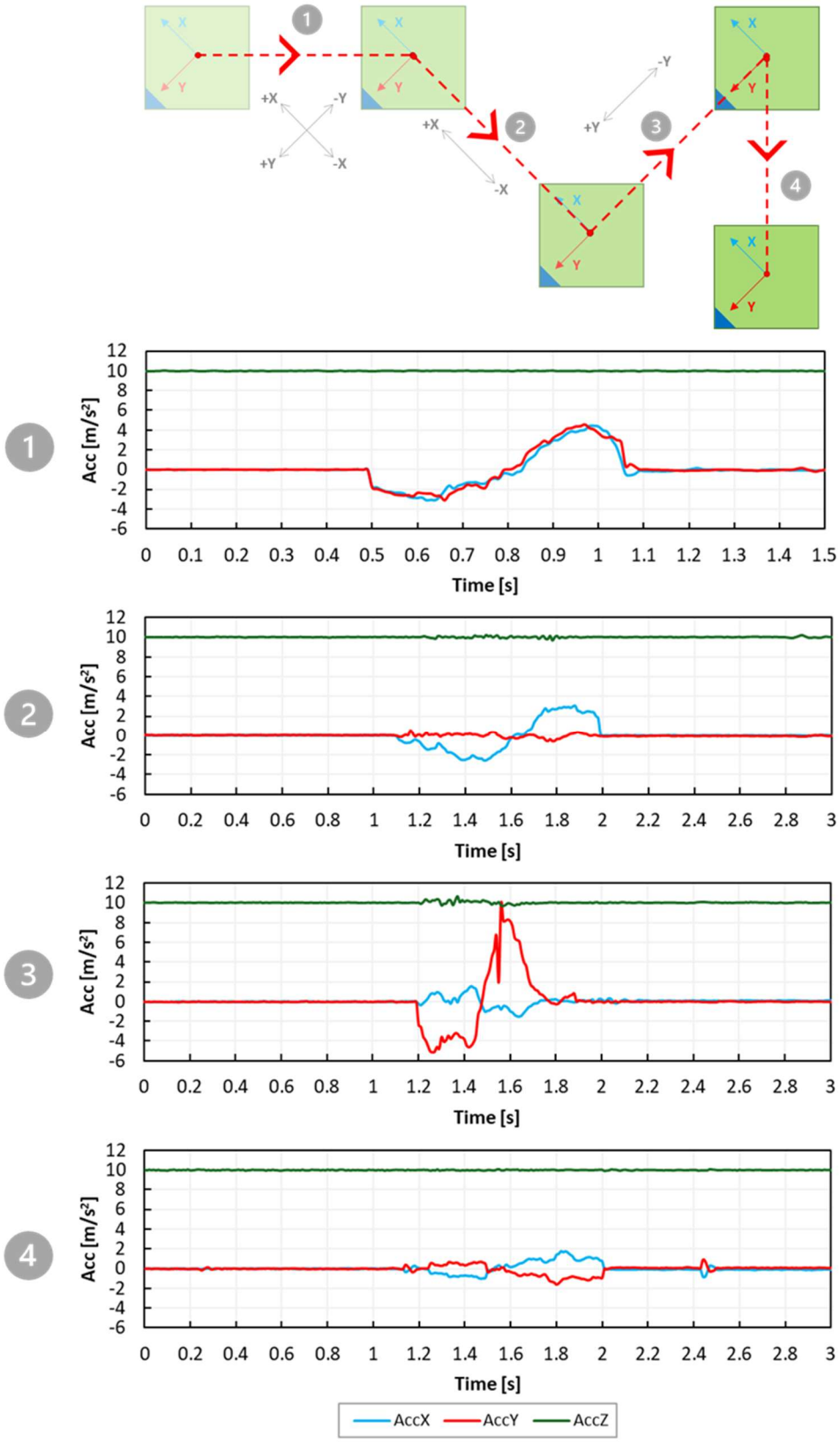

Fig.87 – Acceleration data of an instrumented block, considering three different movements of the block: *xy*-axis, *x*-axis and *y*-axis.

Upon analysing Fig.87, several key insights emerge regarding the movement and acceleration of the block within the *xy* plane:

- Since the block's movement is limited to the *xy* plane, the acceleration peaks are observed along these axes. As anticipated, gravitational acceleration is detected solely along the z-axis, with minimal movement observed in this direction;
- The first and fourth movements of the block follow a path determined by a resultant vector composed of two acceleration vectors along the *x* and *y* axes. In the first movement, as the block is pushed from left to right, both acceleration components are negative, as they point in the opposite direction to the positive axes. This combined motion means the block initially moves in a negative direction along both axes, with corresponding negative acceleration values. As it decelerates, the acceleration on both axes shifts from negative to positive, indicating the slowing of the block until it comes to rest. This transition is visible in the acceleration graphic, showing an initial negative peak followed by a positive peak as the block decelerates. In the fourth movement, the block is shifted downwards, generating a negative acceleration peak along the *x*-axis and a positive peak along the *y*-axis. The graph reflects this pattern as follows: the *x*-axis component shows an initial negative peak followed by a positive one, while the *y*-axis component shows a positive peak followed by a negative one, capturing the directional transition during this phase;
- In contrast, during the second and third movements, the block's displacement occurs exclusively along the *x*-axis and *y*-axis, respectively. These directional constraints are evident in the acceleration data, where activity is confined to one axis per movement, corresponding to the specific direction of each displacement. Since these movements progress from the negative to the positive direction on both axes, the acceleration graphs display an initial negative peak, followed by a positive one;
- While the individual *x*, *y*, or *z* components may display positive or negative values, the resultant linear acceleration magnitude is always positive. This distinction is essential for interpreting experimental data: the acceleration values alone do not directly indicate changes in speed, as positive acceleration does not always imply an increase in speed, nor does negative acceleration necessarily signify deceleration. Instead, these changes must be understood through the directional context and vector properties.

In essence, interpreting acceleration graphs from experiments requires careful attention to directionality, axis orientation, and vector magnitudes to accurately evaluate changes in velocity and movement direction.

The last test involved rotating the same block, placed on the flat surface, around the z-axis, clockwise and counterclockwise, to verify if the block recorded the angular velocity (rad/s). Fig.88 shows 3 tests performed and the corresponding time series of angular velocity around the z-axis.

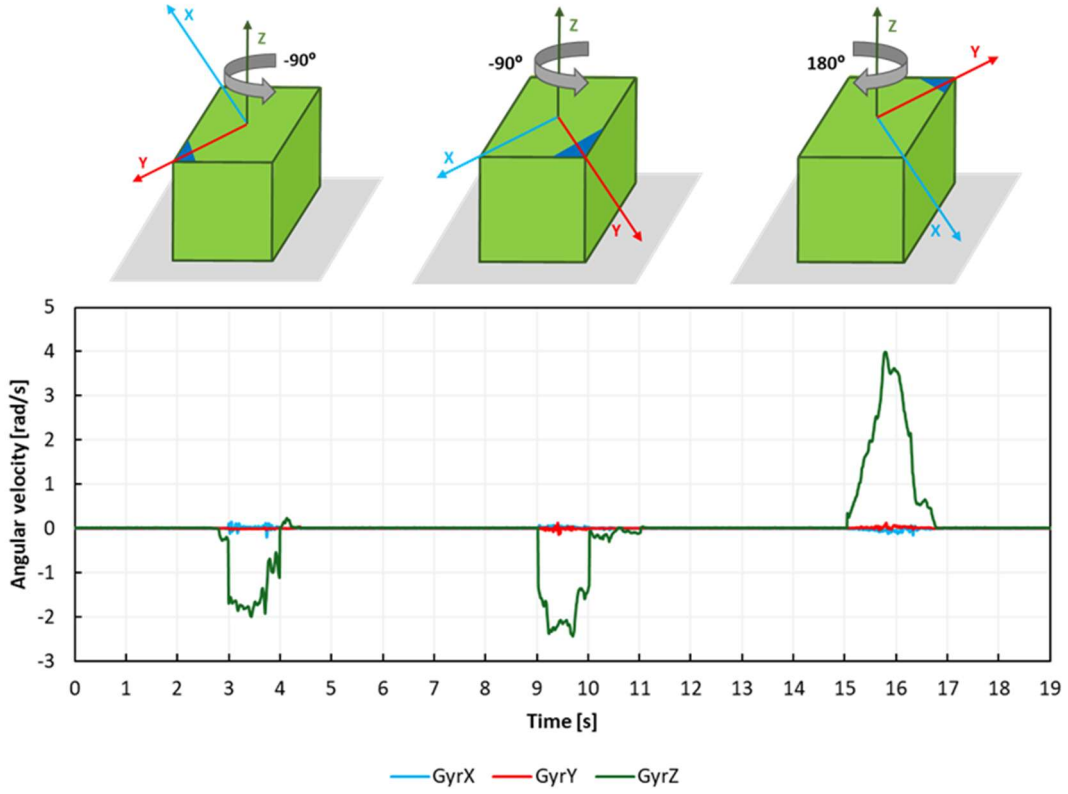

Fig.88 – Angular velocity data of an instrumented block, considering three different rotations of the block around the *z*-axis.

As anticipated, the angular velocity is observed exclusively along the z-axis, as the rotation occurs solely around this direction. Additionally, when the block rotates counterclockwise, the angular velocity registers as negative, as seen in the first and second movements. Conversely, when rotating clockwise, the angular velocity registers as positive, as illustrated in the third peak of the graph.

The operation of the magnetometer was not tested since it is not relevant for the experimental work carried out.

4.4.2 LABORATORY EXPERIMENTS

Based on the results of the previous testing stage, Phase 2, the subsequent experimental investigation refers to tests of the propagation and breaking process of a solitary wave running up a smooth slope armoured with one row of Antifer blocks, making use of instrumented blocks as presented in subsection 4.4.1. These experimental tests correspond to phase 3.2 and were performed in the same multidirectional wave basin presented in subsection 4.3.1. The outcomes of this phase include the recording of the water surface elevation, the average displacement of the blocks, the displacement of each instrumented block, and the forces on the SmartAntifer blocks. These experiments will showcase the benefits of utilizing instrumented blocks in experimental works of this nature, while also providing high-quality data for validating the numerical model.

4.4.2.1 Model configuration

Experimental set-up

The physical model corresponds to a simple slope, armoured with one row of seven instrumented Antifer blocks, reproduced on a geometric scale of 1:40. Building on the Phase 2 model, the reconstruction aimed to address several issues identified in the initial version. This updated model not only allows for the adjustment of the slope angle, facilitated by a movable supporting structure, but it has also been reinforced to mitigate bending due to its extended length. Fig.89 illustrates some of the details of the enhanced structure.

Fig.89 – Side view (top) and top views (bottom) of the model, smooth (bottom left) and rough (bottom middle and right) configurations.

The acrylic slope, with an established angle of 25.5º, was covered with two layers of paint to ensure the roughness. A printed 10 cm principal grid and a 2.5 cm secondary grid were used for a more effective qualitative and quantitative assessment of the block's movement. The model was positioned in a channel 0.80 m wide, 8 m long and 1.20 m high. The distance from the slope toe to the wavemaker paddle (when in its forward position) was equal to, approximately, 6 m. It was necessary to move the structure 3.5 cm forward to ensure that the extension of the slope was 6 m from the paddle when it was in its most forward position, as represented in Fig.91. The bathymetry in front of the structure was not reproduced. Thus, the water depth was kept constant and fixed at approximately 53 cm (21.2 m in the prototype). Five resistive-type hydrodynamic level probes (WG1, WG2, WG3, WG4, WG5) were installed in the channel at distances of 1.20m, 2.40m, 3.60m, 4.80m, and 5.40m from the model, respectively. The Antifer blocks were installed in the active zone of the slope. Fig.90 and Fig.91 present the final experimental setup.

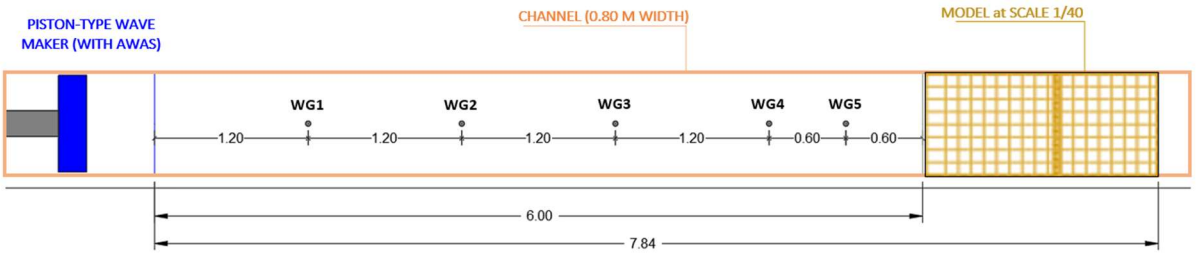

Fig.90 – Experimental setup top view in FEUP flume.

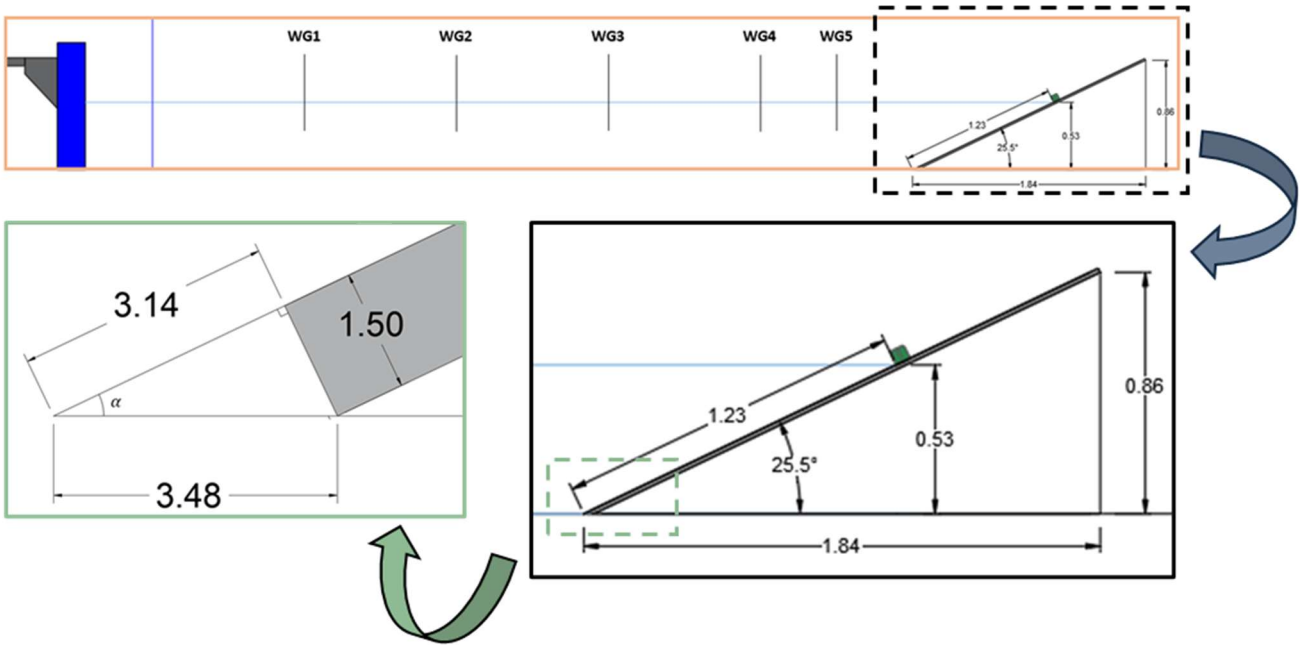

Fig.91 – Experimental setup profile in FEUP flume for series01.

Antifer blocks characteristics

The blocks used in this phase were the instrumented Antifers, SmartAntifers, introduced in the previous subsection 4.4.1. They presented the same geometric parameters introduced in Table 15, which follow the proportions shown in Fig.43. The corresponding geometric proportions and mass properties are outlined in Fig.92. Although made of aluminium, these blocks were designed to replicate the typical wet mass and behaviour of the standard blocks used in laboratory environments.

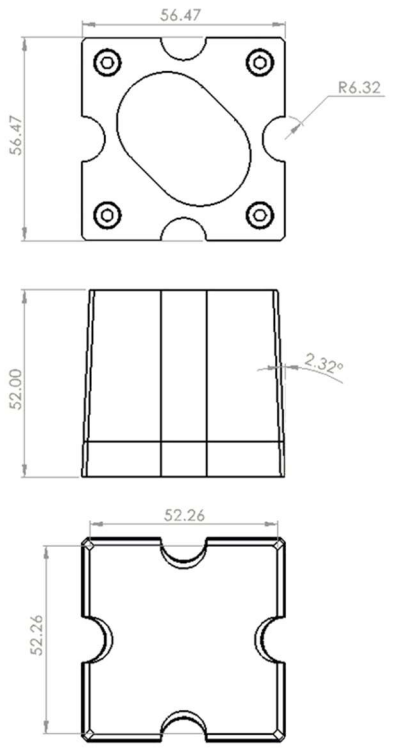

Mass properties of Bloco Antifer BBQ V3.0
Configuration: Default
Coordinate system: -- default --

Mass = 310.55 grams

Volume = 119946.45 cubic millimeters

Surface area = 55183.90 square millimeters

Center of mass: (millimeters)
X = -0.01
Y = 25.30
Z = 0.01

Principal axes of inertia and principal moments of inertia: (grams * square millimeters)
Taken at the center of mass.
Ix = (0.71, -0.01, -0.70) Px = 151115.15
Iy = (-0.70, 0.00, -0.71) Py = 156308.71
Iz = (0.01, 1.00, -0.01) Pz = 161017.24

Moments of inertia: (grams * square millimeters)
Taken at the center of mass and aligned with the output coordinate system.

Lxx = 153691.38	Lxy = -54.23	Lxz = -2596.37
Lyx = -54.23	Lyy = 161016.57	Lyz = 60.42
Lzx = -2596.37	Lzy = 60.42	Lzz = 153733.14

Moments of inertia: (grams * square millimeters)
Taken at the output coordinate system.

Ixx = 352488.57	Ixy = -161.35	Ixz = -2596.40
Iyx = -161.35	Iyy = 161016.64	Iyz = 117.38
Izx = -2596.40	Izy = 117.38	Izz = 352530.37

One or more components have overridden mass properties:
BBQ Electronica
LED<2><Default>

Fig.92 – Geometric proportions and mass properties of instrumented Antifer blocks (SmartAntifers).

4.4.2.2 Instrumentation

Equipment description and setup

As in the previous laboratory experiments, the principal equipment and measurements carried out during the tests were:

- Resistive wave probes to measure the water's free surface elevation and, consequently;
- Determine the incident wave height and estimate the reflection coefficient and run-up;
- Photographic and video cameras to assess the structural damage and for test recording, respectively.

Regarding the wave probes, although two probe sizes are available, 60 cm and 30 cm, only the 60 cm probes were used. The wave probes available were numbered from WG1 to WG5 and only module ID2, which has six channels available, was used. Table 23 indicates the relation between the probe identity and its number. This designation was used to identify the comma-separated values (.csv) files containing the information from each probe in the data sets, as previously mentioned in section 4.3.1.2.

Five wave probes were installed in the flume: the first four probes (WG1 to WG4) are evenly spaced 1.20 m apart, with WG1 positioned 1.20 m from the piston paddle when it is in its forward position. The WG5 probe is positioned closer to the model, at 60 cm from both the model and the WG4 probe, as presented in Fig.90. In this instance, given that the wave generated is a solitary wave, the wave probes were not spaced according to the wavelength and wave period. Instead, a more regular configuration along the flume was chosen to effectively capture the wave's progression.

Table 23 – Probes channels and designations.

Board 1 (ID1)			Board 2 (ID2)		
Probe	Channel	Designation	Probe	Channel	Designation
-	1	-	WG1	1	ID2_Ch1_Channel 1
-	2	-	WG2	2	ID2_Ch2_Channel 2
-	3	-	WG3	3	ID2_Ch3_Channel 3
-	4	-	WG4	4	ID2_Ch4_Channel 4
-	5	-	WG5	5	ID2_Ch5_Channel 5
-	6	-	-	6	-
-	7	-	-	7	-
-	8	-	-	8	-

Regarding the structural damage measurement, a 24.1 megapixel Canon EOS 2000D photographic camera was used to photograph the structure from above and track the Antifer blocks' movements. Prior to each test, a photograph of the model was captured to serve as reference, and following the completion of each test, another photograph was taken. It was possible to assess the movement of the blocks by comparing the resulting photographs. A GoPro camera was also used to record the different tests. Both cameras were assembled above and approximately normal to the slope.

In addition to the photographic setup, the instrumentation includes the SmartAntifer blocks, which by means of an accelerometer and a gyroscope estimate movement the blocks movement characteristics. The accelerometer data allow for the calculation of acceleration vectors, which provide insight into the forces acting on the blocks, while the gyroscope data capture the rotational dynamics that influence the blocks' orientation. By transforming and integrating these data, it is possible to derive detailed motion characteristics, including velocity and displacement, that are essential for understanding the behaviour of the blocks under wave-induced forces. This combined analysis (sensor fusion) provides a powerful tool for investigating the complex interactions between the blocks and the slope and forms the basis for evaluating their stability and motion in the context of the experimental tests.

Equipment calibration

The resistive wave probes need to be calibrated every day before being used to guarantee minimum error in the deviations. The process is the same as presented in subsection 4.3.1.2. It consists of manually changing the probe's immersion depth (Fig.48, top view) and associating the voltage between the two rods to the measured immersion depth for at least three known values; then, a linear relation is established. In this case, the immersion difference selected was of ±14 cm.

Prior to the calculations of movement characteristics, sensor data have to be calibrated. By addressing the calibration considerations presented on section 4.4.1.4, the accuracy and reliability of the IMUs' measurements can be significantly enhanced, contributing to the overall quality of the data collected during the experiments.

4.4.2.3 Test Procedure

The experimental tests were divided into four series:

- **Series C** – Physical model without blocks corresponding to a smooth slope (slope made of acrylic with two layers of paint) to test the wave conditions;
- **Series S#** – Arrangement of 1-row of 7 instrumented Antifer blocks (SmartAntifer) and a smooth slope (slope made of acrylic with two layers of paint), considering a slope of 25.5º (Fig.91):
  - Series S1 – SmartAntifer blocks spaced 4.36 cm apart from each other and placed above the water level (53 cm);
  - Series S2 – SmartAntifer blocks spaced 4.36 cm apart from each other and placed below the water level (48.7 cm);
  - Series S3 – SmartAntifer blocks in contact with each other and placed below the water level (48.7 cm).

So, three distinct scenarios were considered for the positioning of blocks within the active zone of the slope. The arrangements of blocks for series 1, 2, and 3 are illustrated in Fig.93. For the purposes of numerical reproduction using the DualSPHysics software, and due to the recording of accelerations of the instrumented blocks, it was decided to consider the blocks spaced apart in the scenarios of series 1 and 2. This ensures the evaluation of the independent movement of each block without the influence of collisions between them. Note that the red line marks the position on the slope corresponding to 0.53 m height and served as a guideline. Additionally, for an approximate qualitative and quantitative analysis of the movement of the blocks, a primary grid of 10 cm by 10 cm and a secondary grid of 2.5 cm by 2.5 cm were drawn.

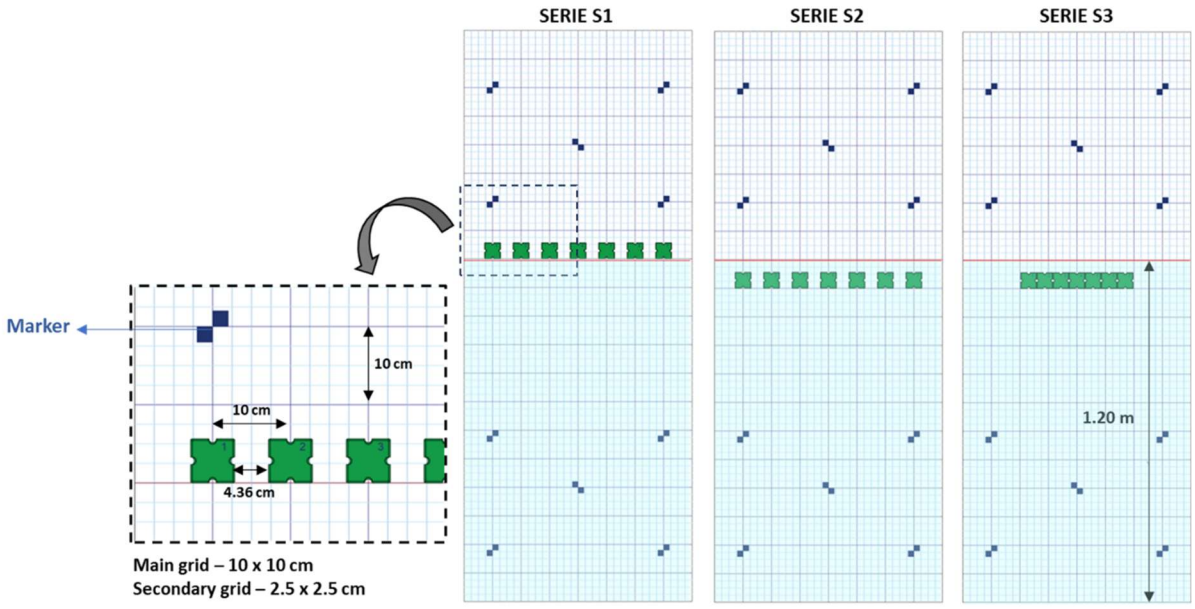

Fig.93 – Perpendicular view of SmartAntifer blocks arrangement for test series S1, S2 and S3.

Testing conditions

The structure was subjected to a normal wave action of solitary waves with heights of 3.2 cm, 5.9 cm and 8.9 cm at the offshore uniform depth (WG1 at Fig.90), considering a water depth of 53 cm.

As in previous tests, the waves were generated by the multi-element piston-type wavemaker designed by HR Wallingford (UK) and controlled by the HR WaveMaker software. The installed generation system allows for the creation of various types of waves, ranging from regular monochromatic waves, normal to the wave generator as in earlier laboratory tests, to solitary waves. The latter are generated using the externally generated seas module of the generation system, which allows a time series of paddle motions to be imported into HR WaveMaker and converted into a playback file. The piston motion time series to be imported to the HR WaveMaker should follow the example presented in Fig.94.

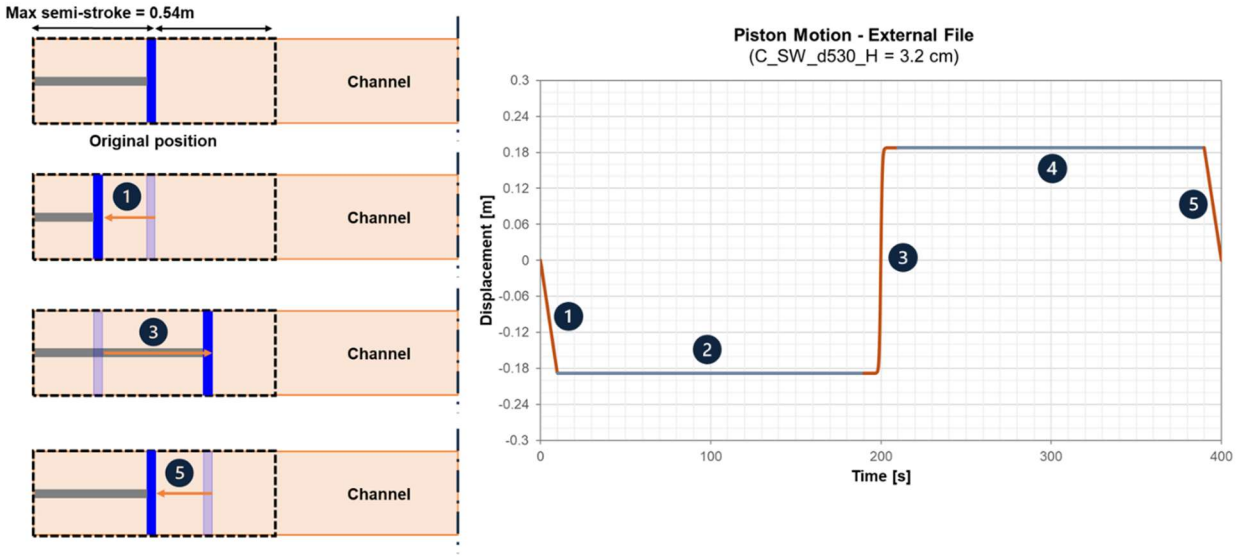

Fig.94 – Example of piston motion time series for Serie C (*H* = 3.2 cm): 1) The piston moves backwards (10 s); 2) Stays in that position for a few minutes for water stabilization; 3) Piston moves forward (20 s) – Solitary wave; 4) Stays in that position for a few minutes; 5) Return to the original position.

Note that the maximum wave heights are limited by the performance characteristics of the generation system, such as the maximum excursion (1.08 m), maximum speed (0.87 m/s), maximum force (1.5 kN), and nominal motor power (1.38 kW). Table 24 present the performance characteristics of the generation system for the tested solitary waves.

Table 24 – Performance characteristics of the generation system for tested solitary waves.

$H_{TARGETED}$ [cm]	Max. actuator velocity [m/s]	Max. actuator force [kN/m]	Max. actuator power [kW/m]	Max. piston semi-stroke [m]	Total Stroke [m]	H_{WG1} [cm]
5	0.23	0.26	0.06	0.19	0.37	3.2
7.5	0.35	0.39	0.13	0.23	0.46	5.9
10	0.47	0.52	0.24	0.27	0.53	8.9

The tests were named based on the following nomenclature: **S**#_**SW**_**d**530_**H**###_**R**##.

First, the test series is identified. Therefore, S# refers to series S1, S2 or S3. Then, the Wave Type and the water depth are identified, with "SW" meaning solitary waves and d530 referring to the water depth of 53 cm. Subsequently, the characteristics of the waves, namely the wave height, is specified through H###, where it could assume three different combinations: H050 (H_{WG1} = 3.2 cm), H075 (H_{WG1} = 5.9 cm) and H100 (H_{WG1} = 8.9 cm). Finally, the test iteration is specified. Each test (R##) is repeated at least 3 times. So, they are numbered sequentially as 00, 01, 02, 03, etc.

Fig.95 represents the time series of the free surface elevation for all three series of tests, S1, S2 and S3, considering the three wave heights, 3.2 cm, 5.9 cm and 8.9 cm. The wave probe acquisition frequency used was 100 Hz.

Based on the results obtained, it is observed that for all three series of tests, the greater the wave height, the shorter the period and the more pronounced the second peak, which corresponds to the wave reflection in the model. Regardless of the series, when considering the same wave height, the development of solitary waves is similar across the various scenarios, with slight differences appearing only in the reflected wave.

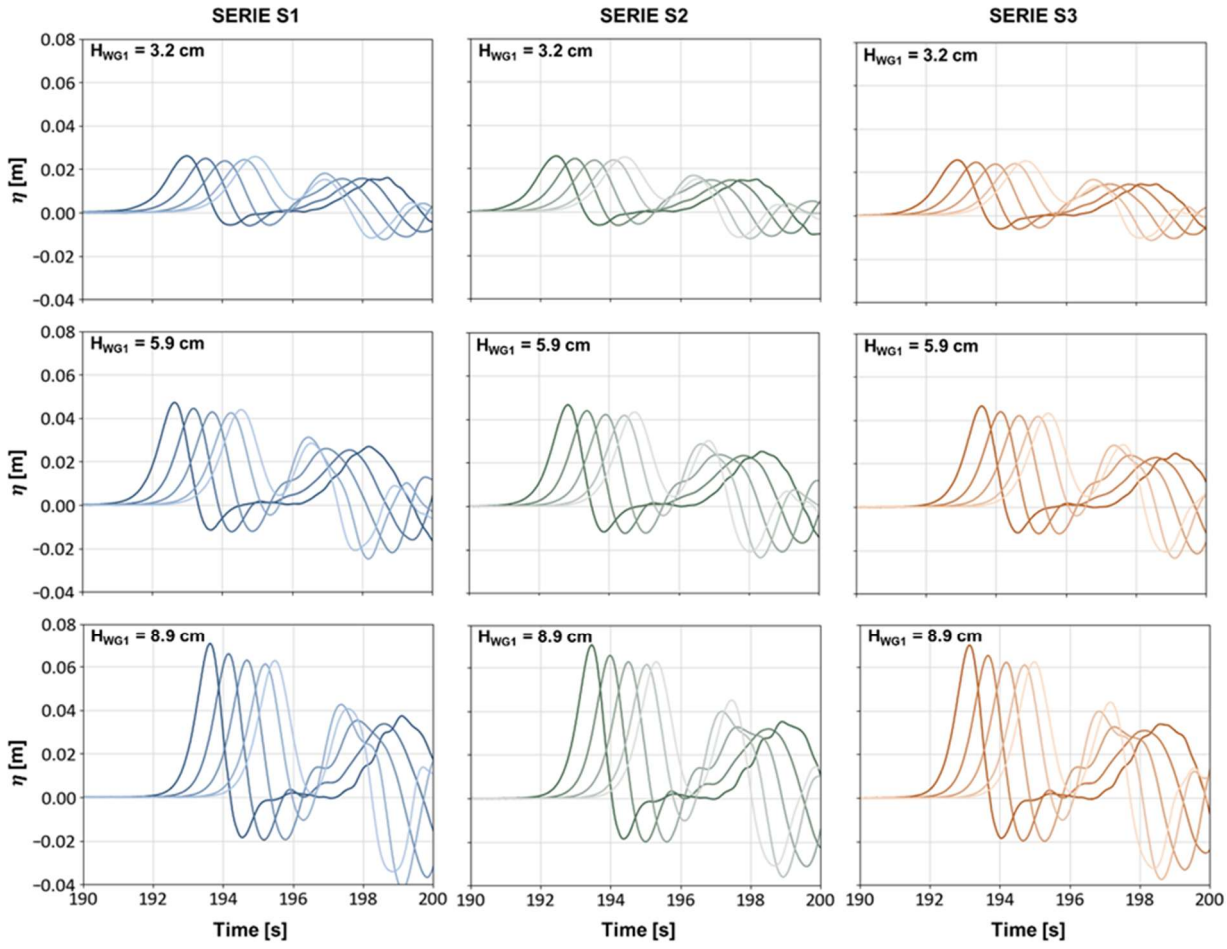

Fig.95 – Time series of the free-surface elevation for series S1, S2, and S3, for the three wave heights, *H* = 3.2 cm, 5.9 cm and 8.9 cm, considering the repetition R00 for all the tests.

Image processing

A Canon EOS 2000D photographic camera with a fixed focal length of 50 mm was used to photograph the structure from above and track the Antifer blocks' movements. The camera remained consistently positioned orthogonally to the slope and recorded the initial and final positions of the blocks for each test. In the end of each test, the Antifer blocks were re-installed at its original position, as presented from Fig.96 to Fig.98.

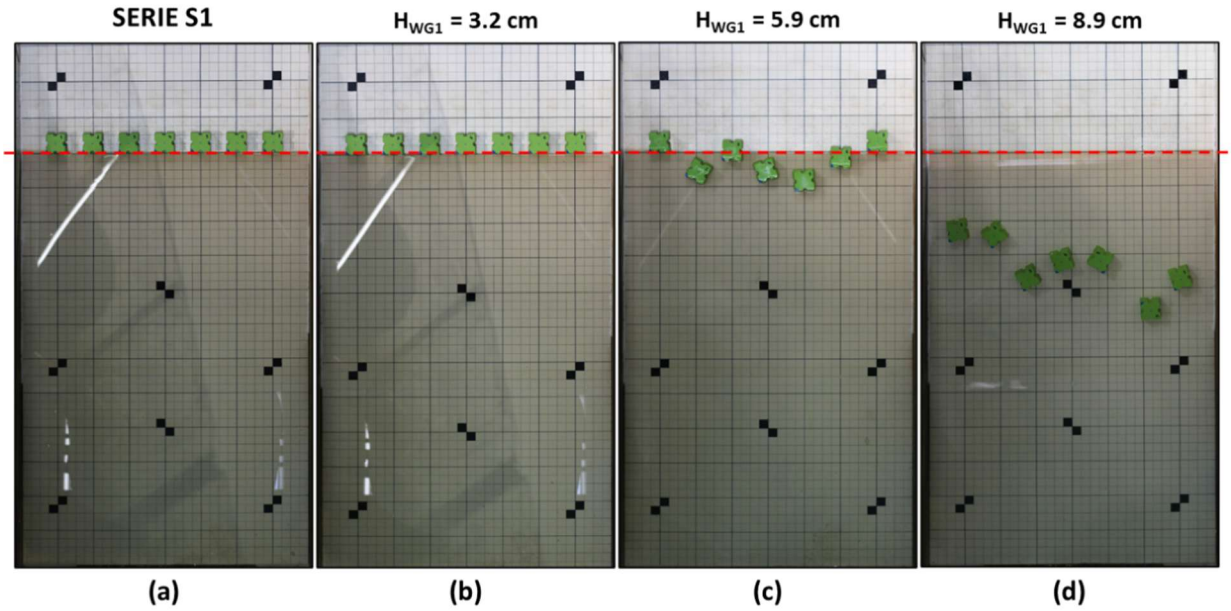

Fig.96 – Photographs for the initial (a) and final position of the blocks for tests S1_SW_d530_H050_R00 (b), S1_SW_d530_H075_R00 (c) and S1_SW_d530_H100_R00 (d).

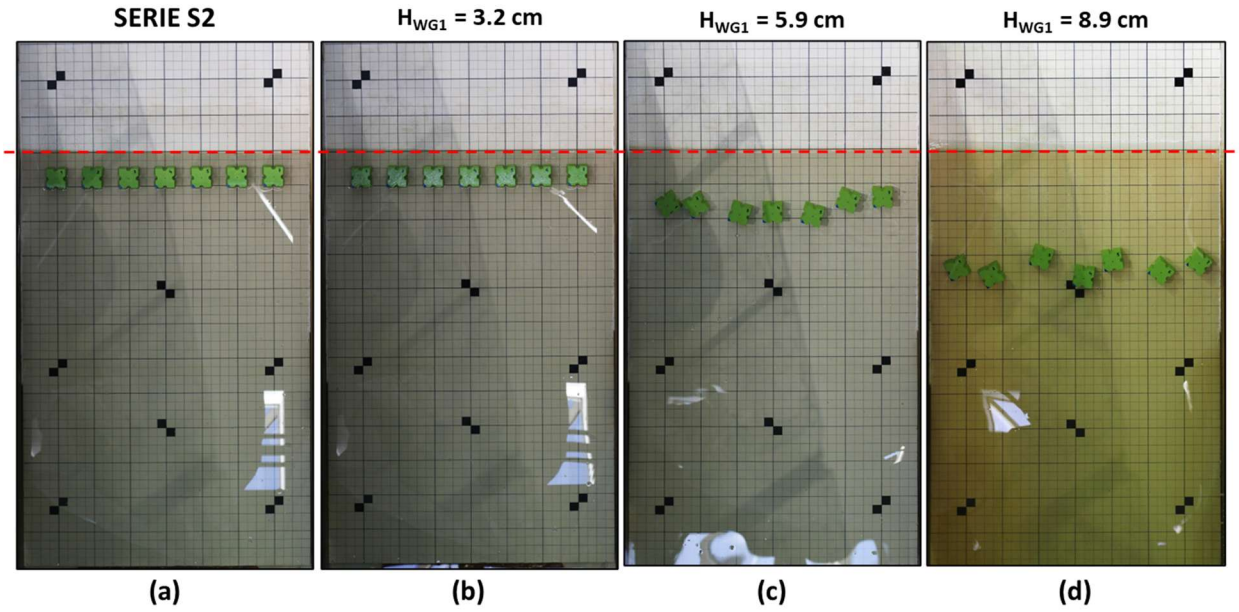

Fig.97 – Photographs for the initial (a) and final position of the blocks for tests S2_SW_d530_H050_R00 (b), S2_SW_d530_H075_R02 (c) and S2_SW_d530_H100_R03 (d).

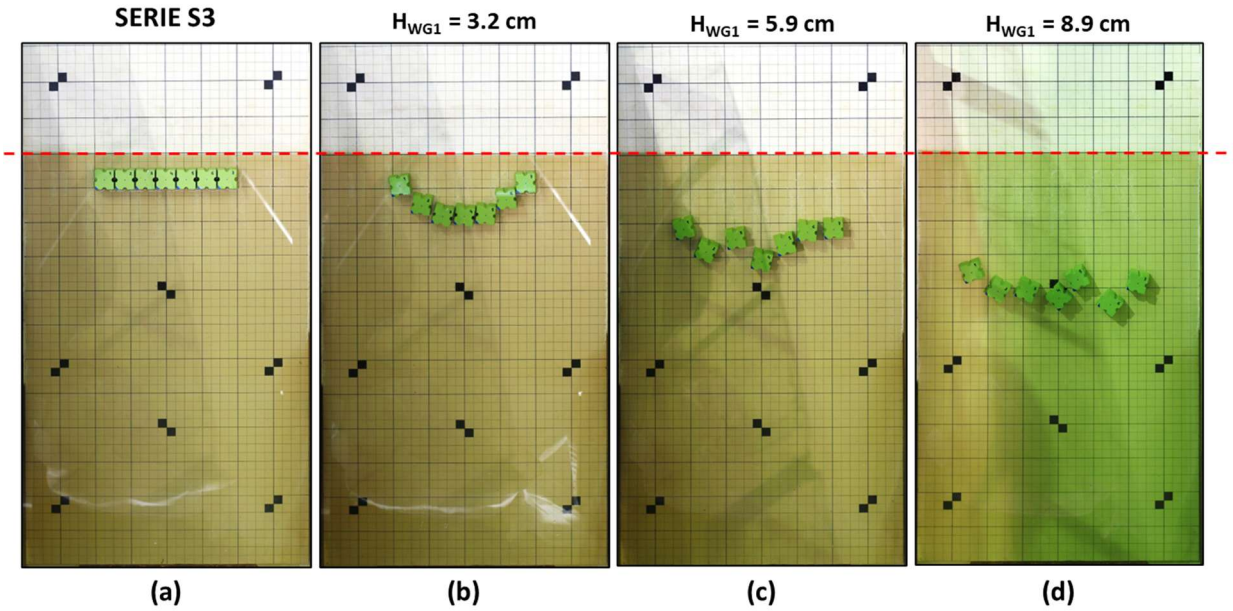

Fig.98 – Photographs for the initial (a) and final position of the blocks for tests S3_SW_d530_H050_R00 (b), S3_SW_d530_H075_R01 (c) and S3_SW_d530_H100_R01 (d).

The distortion of the resulting photos was corrected using Lightroom software. Then, the software ImageJ was utilised for quantitative analysis of the Antifer block movement. In these tests, the steps followed using ImageJ, which were slightly different from the previous experimental campaign, are described below:

1) Open the photo correspondent to the initial condition in ImageJ;
2) Open the photo correspondent to the final condition in Image J;
3) Overlay the final photo on the initial one, adopting a 50% opacity and adjusting the images based on the grids and the markers, using the tools Image>Overlay>Add Image (see Fig.99);
4) Save the overlaid image so that it can be worked on;
5) Use the tool *Straight* to draw a line correspondent to the distance between two known points;
6) Define the correspondence between the image pixels and the known measure (h), using the tool Analyze>SetScale (see Fig.99);
7) Draw a straight line between the centre of the blocks in their initial position and their final position;
8) Use the toll Analyze>Measure to determine the angle and length of the line (see Fig.99);
9) Repeat steps 7 and 8 for the remaining blocks;
10) Export the resultant table to a spreadsheet file.

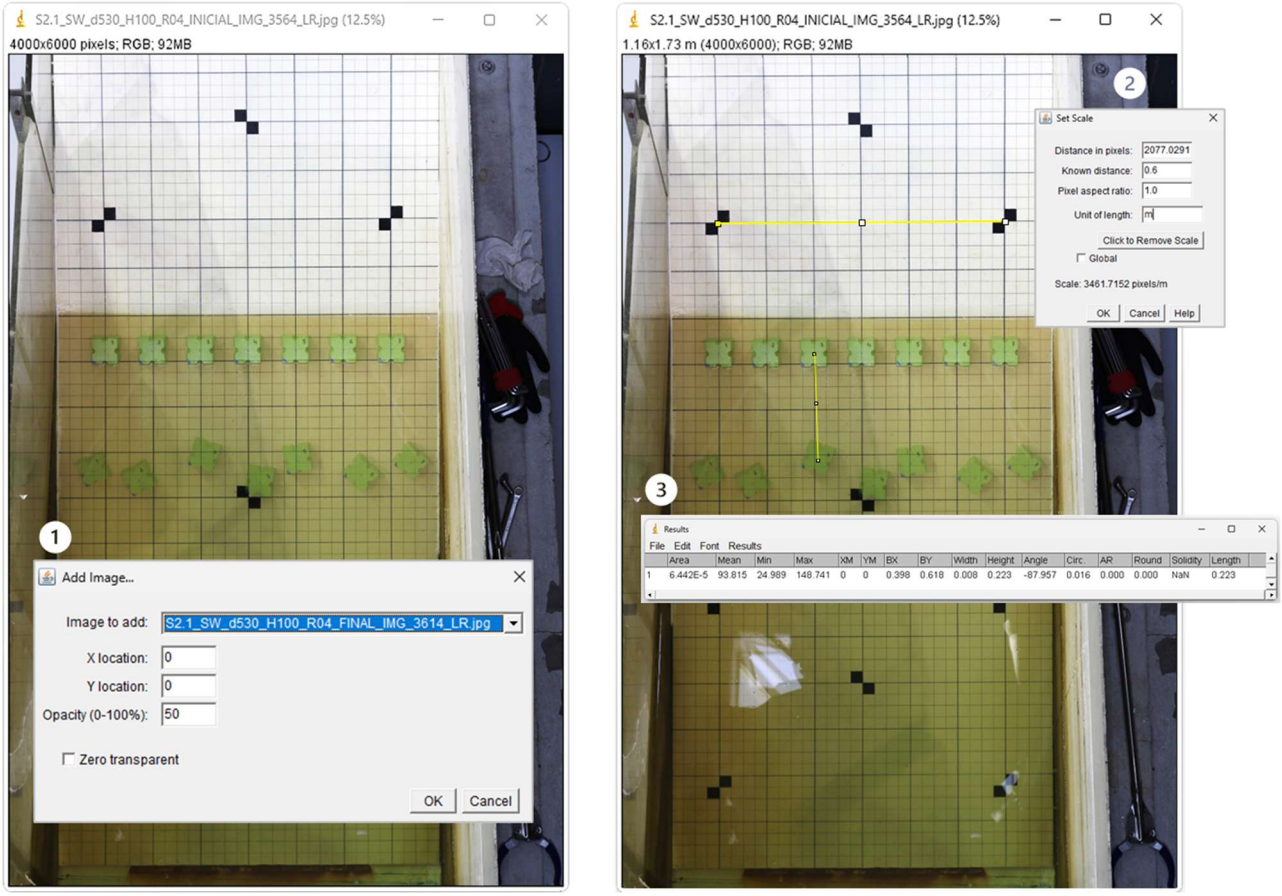

Fig.99 – ImageJ tools: 1. Overlay>Add Image; 2. Analyze>Set Scale; and 3. Analyze>Measure.

SmartAntifer *signal selection and processing*

The SmartAntifer data acquisition was conducted using the IMU accelerometers and gyroscopes at a sampling rate of 100 Hz. This frequency is consistent with previous studies, as referenced in Table 7 of section 2.2.3, and is deemed sufficient for capturing the dynamics of the blocks' motion.

Authors like Jamil *et al.* (2020) and Kok *et al.* (2017) presented quantitative approaches to derive by simple physical relations detailed motions characteristics, specifically displacement, from the IMU raw data. The flowchart provided in Fig.100 illustrates the sequence of steps involved in transforming raw IMU data into displacement measurements.

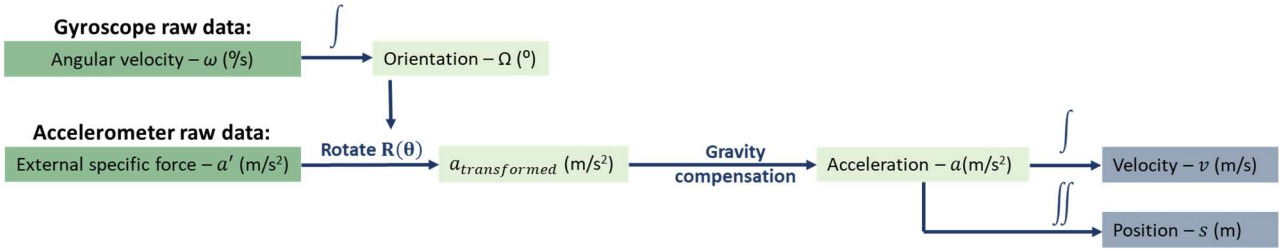

Fig.100 – SmartAntifer signal processing: from raw data to displacement measurements.

This section details the systematic approach presented above, with an emphasis on the planar motion of blocks confined to an inclined surface.

The first step in the process involves the acquisition of the angular velocity data from the gyroscope along the three axes. This data is subsequently integrated to determine the orientation of the Antifer over time. The integrated angular velocity, expressed as Ω_x, Ω_y and Ω_z, is fundamental for capturing the block's rotational behaviour, which directly influences its motion in the three-dimensional space. On this study, the block's motion is constrained primarily within the plane, with its orientation limited to rotations around the z-axis, while rotations around the x- and y-axes are negligible under normal conditions. Consequently, the dynamic analysis can be restricted to two translational degrees of freedom (x, y) and one rotational degree of freedom (Ω_z, the orientation angle about the z-axis).

The computed orientation is crucial for transforming accelerometer readings from the block's local coordinate system (x',y',z') to a global reference frame (x, y, z) aligned with the inclined plane, as presented in Fig.101.

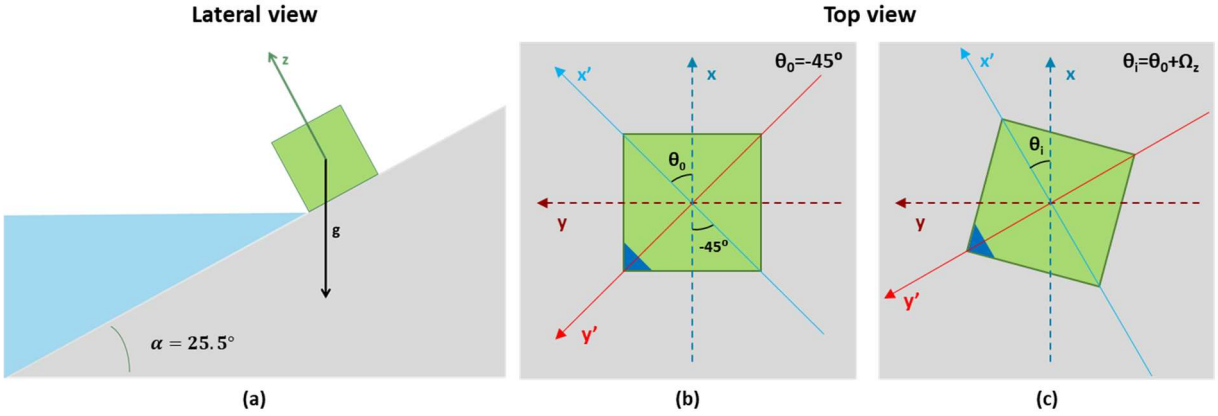

Fig.101 – Technical conventions: (a) lateral view of the z and z[f]-axis; (b) top view of the local and global reference frame at t = 0s; (c) top view of the local and global reference frame during motion.

At the starting position, t = 0s, the block's inner coordinate system is aligned with the fixed reference system through a static transformation. This ensures that the local z'-axis aligns with the global z-axis (perpendicular to the plane) and that the local x'-axis aligns with the x-axis at 45º to the slope direction (see Fig.101 (b)).

As the block moves and rotates (see Fig.101 (c)), given that the orientation changes are constrained around the z-axis, this simplifies the dynamic rotation matrix to account for planar motion:

$$R(\theta) = \begin{bmatrix} cos(\theta) & sin(\theta) & 0 \\ -sin(\theta) & cos(\theta) & 0 \\ 0 & 0 & 1 \end{bmatrix} \quad (104)$$

where, for an instant of time i, $\theta_i = \theta_{i-1} + \Omega_{z_{i-1}}$.

The transformed acceleration is given by:

$$a_{transformed} = R(\theta) \cdot a_{local} = \begin{bmatrix} cos(\theta) & sin(\theta) & 0 \\ -sin(\theta) & cos(\theta) & 0 \\ 0 & 0 & 1 \end{bmatrix} \cdot \begin{bmatrix} a'_x \\ a'_y \\ a'_z \end{bmatrix} \quad (105)$$

where a_{local} is the acceleration measured in the block's local coordinate system, and $R(\theta)$ is the rotation matrix.

After transforming the accelerometer data, gravity compensation is performed, which corresponds to the process of removing the effect of gravitational acceleration from the data measured by and accelerometer to isolate the true acceleration of the block relative to the global reference frame. An accelerometer inherently detects specific forces, encompassing both dynamic accelerations from external influences (such as hydrodynamic forces) and static acceleration resulting from gravity. This step ensures that only the relevant forces contributing to the block's motion are considered. The corrected acceleration is given by:

$$a_{corrected} = a_{transformed} - g_{plane} = \begin{bmatrix} a_{transformed,x} \\ a_{transformed,y} \\ a_{transformed,z} \end{bmatrix} - g \cdot \begin{bmatrix} \sin(\alpha) \\ 0 \\ \cos(\alpha) \end{bmatrix} \quad (106)$$

where g_{plane} accounts for the inclined plane's orientation, with α being the plane's angle relative to the horizontal.

The corrected accelerations, now expressed in the global frame and after gravity compensation, are integrated over time to compute the velocity of the block. A second integration is then performed to determine the displacement relative to the starting position. It is important to note that this two-step integration process is sensitive to initial conditions, making the calibration and correction of sensor drift essential for accurate results. Given the block's constraints within the plane, this two-step integration focuses exclusively on the *x*- and *y*-components, while the *z*-component, representing motion perpendicular to the plane, is excluded. The equations for velocity and displacement are:

$$\begin{aligned} a_x &= a_{corrected,x}\,, \quad a_y = a_{corrected,y} \\ v_x &= \int a_x(t)dt + v_{x,0}\,, \quad v_y = \int a_y(t)dt + v_{y,0} \\ s_x &= \int v_x(t)dt + s_{x,0}\,, \quad s_y = \int v_y(t)dt + s_{y,0} \end{aligned} \quad (107)$$

These equations describe the block's motion within the *xy* plane, with s_x and s_y representing the displacement components along the plane. The total planar displacement, d_t, is then obtained using the Pythagorean theorem to combine the contributions from both directions:

$$d_t = \sqrt{s_x^2 + s_y^2} \quad (108)$$

This scalar value represents the net distance travelled by the block within the plane of interest, effectively capturing the cumulative effect of motion in both x and y axes.

Beyond displacement measurements, instrumented blocks enable detailed force analysis, providing insights into block behaviour under changing hydrodynamic conditions. Since the block's mass and size are predetermined, this information can be combined with the recorded data to compute forces. By accurately quantifying gravitational components and frictional forces, they contribute to optimizing designs and improving stability evaluations in coastal engineering.

The stability of a block on the slope is determined by the balance between the gravitational force (F_W) pulling it downward and the frictional force (f) resisting its motion. The weight of the block acts vertically downward and can be decomposed into two components:

- Normal force ($W_\perp$): This component is perpendicular to the slope and determines the contact pressure between the block and the surface. It is critical in calculating the frictional force.

$$W_\perp = F_W \cdot \cos(\alpha) = m \cdot g \cdot \cos(\alpha) \tag{109}$$

- Downhill Force ($W_{//}$): This component acts parallel to the slope and drives the block's motion. Its magnitude depends on the slope angle α and the weight of the block.

$$W_\parallel = F_W \cdot \sin(\alpha) = m \cdot g \cdot \sin(\alpha) \tag{110}$$

The frictional force (f), which depends on the normal force and the coefficient of friction (μ) between the block and the slope, acts in the opposite direction to the downhill force:

$$f = \mu \cdot W_\perp = \mu \cdot m \cdot g \cdot \cos(\alpha) \tag{111}$$

For stability, the frictional force must equal or exceed the downhill force ($f \geq W_\parallel$). In static conditions, when the block remains stationary, the downhill force recorded by the sensors corresponds to the maximum frictional force resisting motion. This enables direct calculation of the coefficient of friction:

$$\mu = \frac{W_\parallel}{W_\perp} = \tan(\alpha) = \frac{a_{transformed,x}}{|a| \cdot \sin\left(\cos^{-1}\left(\frac{a_{transformed,z}}{|a|}\right)\right)} \tag{112}$$

Furthermore, under dynamic conditions (e.g., when hydrodynamic forces act on the block), the instrumented system can measure additional external forces. By analysing deviations in acceleration and orientation from static conditions, external forces such as wave impacts can be isolated. For instance, using Newton's second law of motion, the block's mass is multiplied by the recorded accelerations to compute the net forces acting on the block:

$$F_{net} = m \cdot a_{corrected} \tag{113}$$

4.4.3 VALIDATION OF THE DUALSPHYSICS MODEL

Task 3.3 corresponds to the numerical validation of the numerical model considering the experimental data previously obtained. The latest version of the coupling between the open-source codes DualSPHysics (v5.2) and the multiphysics library Project Chrono (v4.0.0) were used to model the propagation and interaction of the solitary waves with a smooth slope armoured with one row of Antifer blocks. The numerical setup is explained first, where special attention is paid to the boundary conditions used to discretise the complex geometry of the Antifers. The configuration of the DualSPHysics simulation was based on the real dimensions of the laboratory wave tank but with some adaptations and the numerical conditions were the same as the experimental test conditions. The research included discussion about the use of the Modified Dynamic Boundary Conditions (English *et al.*, 2022) and of the new density diffusion terms (Fourtakas *et al.*, 2019), as well as the definition of the geometries of the Antifer blocks in the collision detection algorithm of Project Chrono (Martínez-Estévez *et al.*, 2023). Then, a detailed validation is presented with comparisons of the: i) experimental and numerical surface elevation at wave gauge WG5, ii) numerical response between Antifer and Acrylic-slope testing different friction coefficients, iii) experimental and numerical displacement of the Antifers during the motion induced by the interaction with the different solitary waves, and iv) numerical force exerted by the fluid onto the blocks. Finally, this section also includes a convergence and performance analysis that helps to decide the best numerical resolution in terms of accuracy and computational runtime.

4.4.3.1 Definition of the case geometry and initial conditions

As mentioned in 4.3.2.1, there is a need to reduce the size of the simulation domain compared to the actual dimensions of the experimental work for computational purposes. In this case, a numerical tank 3.83 m long, 0.80 m wide, and 1.2 m high was considered, whereas the numerical domain was 8 m long, 1 m wide, and 1.2 m high. Fig.102 shows the three-dimensional representation of the numerical domain, considering the blocks initial setup of Serie 1. The initial water depth was 53 cm. The model setups from the experimental work (S1, S2 and S3) were considered: arrangement of 1-row of 7 Antifer blocks and a smooth slope, considering an angle of 25.5º.

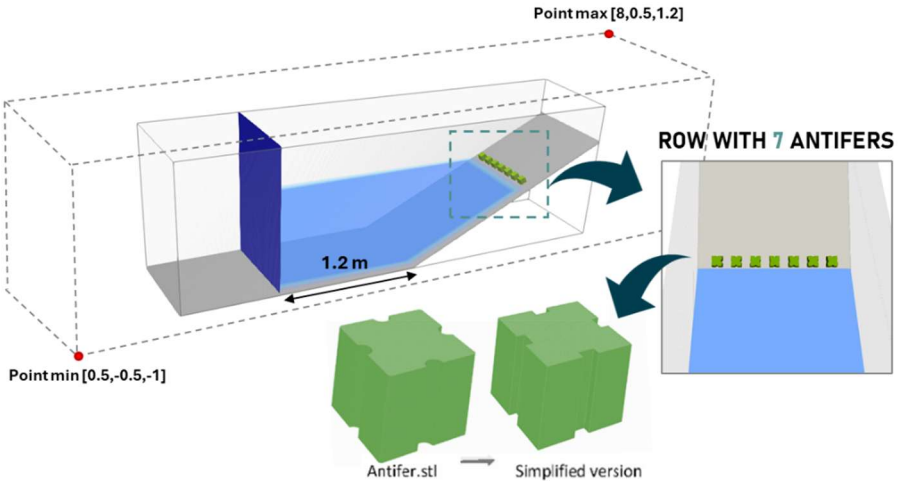

Fig.102 – Three-dimensional representation of the numerical domain (left) and top view (middle), considering the setup of Series 1.

4.4.3.2 Boundary conditions and other numerical parameters

The following conditions were activated during the numerical implementation:

- Inlet open boundaries using the buffer region strategy for wave generation (see subsection 3.3.3.3);
- Density Diffusion Term (DDT) (Fourtakas *et al.*, 2019);
- Consideration of STL files of the Antifer blocks to use Project Chrono and mDBC. These files were the same used in the experimental work of Phase 2 (see subsection 4.3.1.1);
- modified Dynamic Boundary Condition (mDBC) (English *et al.*, 2022) applied to the smooth slope, bottom, piston paddle and STL files of Antifers (see subsection 4.3.1.1);
- Project Chrono for the detection of collisions between blocks. First, the collision algorithm of Project Chrono (based on DEM) was activated defining a minimum distance to detect collisions between geometries (STL for example). In this case, Antifer blocks were initially positioned nearly in contact with the slope, maintaining a gap slightly larger than the defined minimum collision detection distance. Second, it was necessary to define Antifer parameters and coefficients for the numerical simulation, namely the friction coefficients between the Antifer blocks and between the blocks and the slope.

  One simple technique was applied to obtain the friction coefficient by placing some blocks at rest on the slope in a horizontal position and gradually increasing the angle until the blocks started to slide. The tangent of the threshold angle was then used as a measure of the coefficient of friction. From this test, an average friction coefficient of 0.88 (tan(41.4º)) was obtained. Upon conducting a critical analysis and comparing these results with the values previously used in Phase 2 of the tests, it was concluded that this friction coefficient was not the most appropriate. This discrepancy likely resulted from a measurement error, such as not maintaining the necessary conditions between the slope and the blocks.

  To obtain a more accurate estimation of the friction coefficient, results from instrumented blocks were utilised as an initial approximation.

  Knowing that the slope has an angle of 25.5º and considering the static position of the block, the component of the gravitational force along the slope was recorded by the instrumented block to be approximately 1.34 N. This indicates that the frictional force should at least match this value to prevent the block from moving. Through force analysis, the coefficient of friction can be determined, offering a reliable estimate based on precise measurements from instrumented blocks under controlled conditions. Based on the data provided, the friction coefficient was determined to be approximately 0.48. This calculated value serves as an initial reference point. If the angle of 25.5º is confirmed as the critical angle, this value aligns well with the coefficient of friction.

  It is important to highlight that in the numerical modelling, it is both plausible and often necessary to consider a range of friction coefficients between the blocks and the slope. This is because, in laboratory works, despite attempts to replicate the same conditions across multiple test repetitions, small variations are inevitable due to:

  (i) Material properties: the blocks are made of aluminium and have a hand-painted coating, which may differ slightly from block to block;
  (ii) Surface conditions: the slope surface, made of acrylic, also has a paint coating. This surface may have varying properties along its length or width, resulting in slightly different friction coefficients for blocks placed in different areas;
  (iii) Environmental factors: the tests were not all conducted on the same day, leading to variations in water temperature and viscosity due to external factors such as the presence of sand;

(iv) Wave interactions: The interaction between the waves and the blocks can also affect the friction. Different amounts of water or debris trapped under the blocks could change the friction coefficient; and
(v) Deliberate experimental design: for series S1, the blocks' starting position was above the still water level, while for series S2 and S3 the blocks were semi-submerged. The initial contact with water affects the friction coefficient.

Thus, using a range for the friction coefficient instead of a fixed value is not only acceptable but also more realistic and insightful, allowing for more accurate modelling and robust analysis.

Antifer properties and coefficients for the numerical simulation are detailed in Table 25. These values differ from those presented in Table 22 because the materials are different. For instance, the friction coefficient of 0.30 was selected as it is commonly cited in reference charts for aluminum materials (greased or lubricated) in the literature, providing a reliable baseline for the subsequent analysis.

Table 25 – Phase 3: Antifer parameters and coefficients for the numerical simulation of blocks collisions using DualSPHysics coupling with Project Chrono.

Parameter / Coefficient	Notation [Units]	Value
Moment of inertia (*)	$I_x\ [kg \cdot m^2]$	0.00015112
	$I_y\ [kg \cdot m^2]$	0.00015631
	$I_z\ [kg \cdot m^2]$	0.00016102
Friction coefficient	$\mu_{Antifer\ (Aluminium)\ VS\ Antifer\ (Aluminium)}[-]$	0.30
	$\mu_{Antifer\ (Aluminium)\ VS\ Slope\ (\text{Acrylic})}[-]$	0.48 – 0.50
Young modulus	$E_{c_{Aluminium}}\ [GPa]$; $E_{c_{Acrylic}}\ [GPa]$	69 ; 21
Poisson ratio	$\upsilon_{Aluminium}\ [-]$; $\upsilon_{Acrylic}\ [-]$	0.33 ; 0.35
Restitution coefficient	$C_{R_{Aluminium}}\ [-]$; $C_{R_{Acrylic}}\ [-]$	0.70 ; 0.80

(*) Results from CAD software.

4.4.3.3 Validation of wave conditions

In DualSPHysics, solitary waves can be generated in three different ways: (i) automatic generation according to implemented theories; (ii) imposing movement of an external file to the piston; (iii) inlet/outlet open boundary conditions.

When addressing three-dimensional domains, it is essential to reduce the simulation domain to ensure the feasibility of numerical tests within a reasonable timeframe, focusing on the area closest to the model (row of Antifer blocks). This domain reduction impacts the validation of wave conditions. For instance, both methods (i) and (ii) would necessitate positioning the piston as close as possible to the model, as depicted in option 1 from Fig.103.

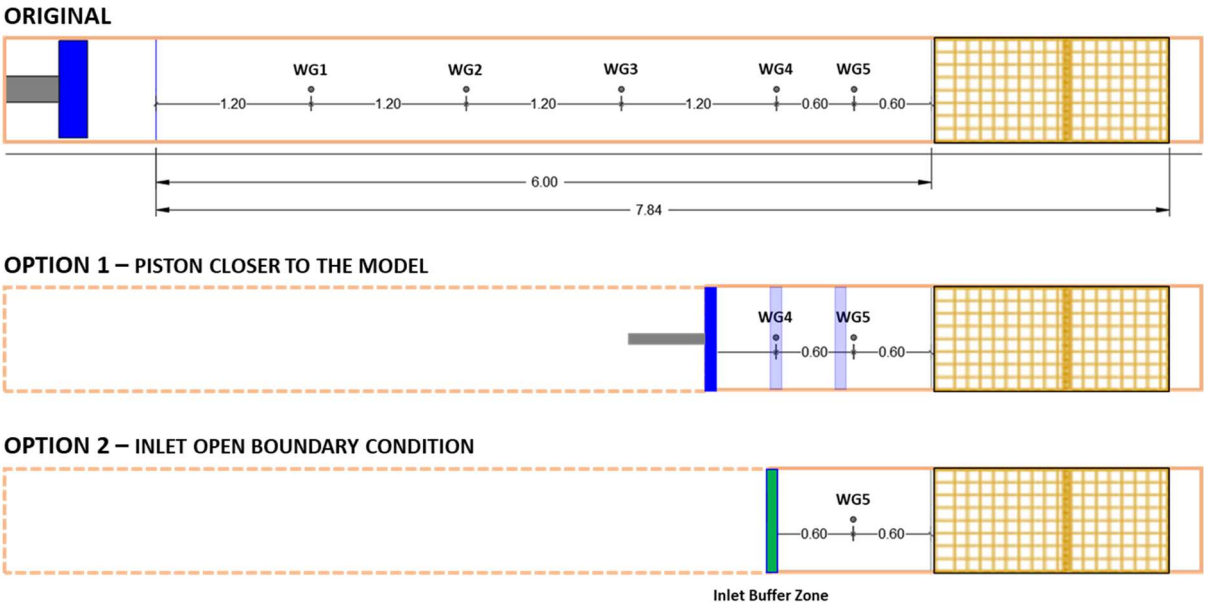

Fig.103 – Representation of the two techniques (option 1 and 2) in DualSPHysics to generate sea waves.

The positioning of the piston at a location of interest close to the model requires the adjustment of the wave conditions (wave height) in the case of automatic generation theories, or to the generation of an external file containing the piston's motion, since the same file used in laboratory tests cannot be employed. The primary drawback of selecting option 1 is that the piston continues to operate as a solid boundary condition. This effectively makes it function as a 'wall', leading to increased reflections and re-reflections due to the reduced dimensions of the tank.

Considering this aspect, option 2 from Fig.103, which involves the inlet open boundary condition described in subsection 3.3.3.3, was chosen for ensuring that the numerical model generates a solitary wave identical to the experimental wave within the defined time interval of interest. This interval extends from the wave's initial interaction with the model, causing blocks movement, until the blocks achieve a stable position. This choice is crucial as the initial run-up and run-down phases predominantly influence the blocks dynamics. Once stabilised, the blocks are no longer affected by wave reflections and re-reflections.

The validation of wave conditions involved a slope without blocks and a two-dimensional domain. Subsequently, the water surface elevation and velocity were imposed on the particles in the inlet buffer zone. These parameters were derived from the experimental results of series C. The water surface elevation measured at WG4 was used to calculate the velocity, U, based on the water surface elevation, η, using linear shallow water theory:

$$U(t) = \eta(t) \cdot \sqrt{\frac{g}{d + \eta(t)}} \tag{114}$$

After running the simulation of the 2D numerical model, measurements at WG5 were then compared with experimental data to verify the accuracy of wave generation and propagation. The results are presented in Fig.104.

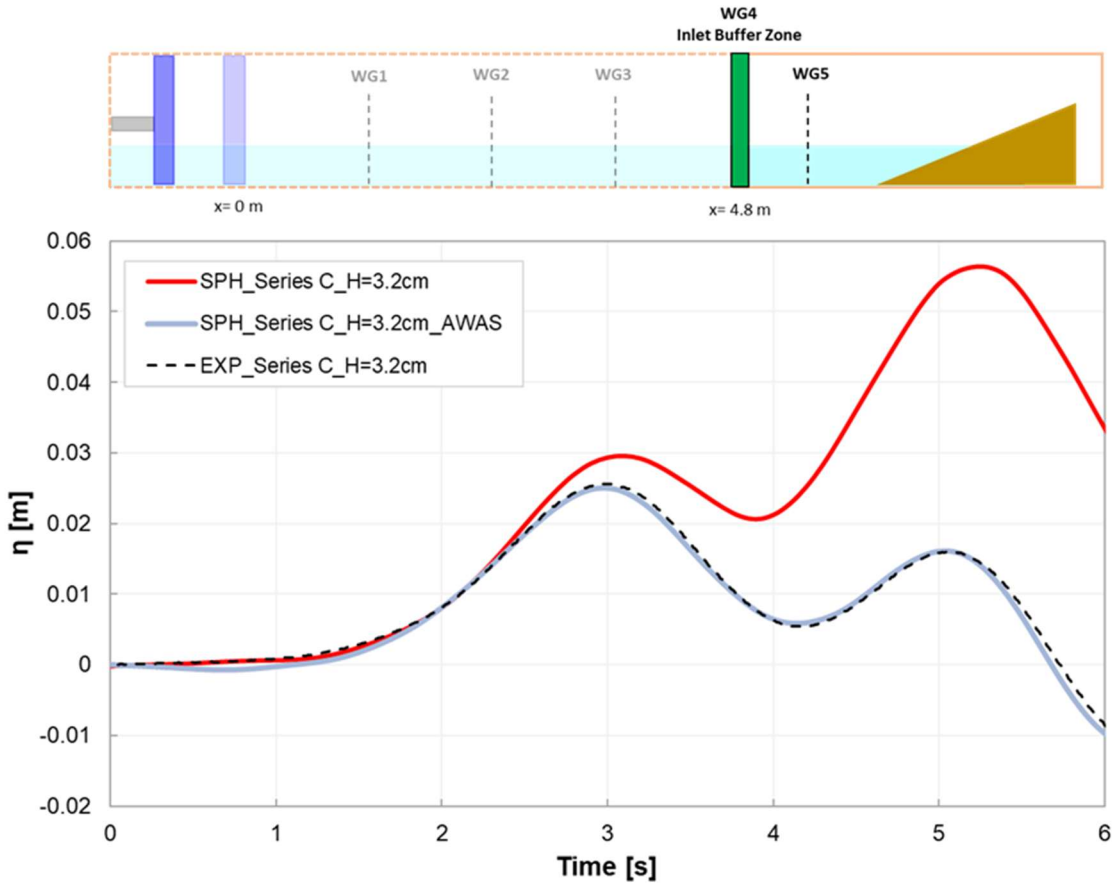

Fig.104 – Comparison of the free-surface elevation (η) of numerical and experimental tests at WG5, considering the series C and a wave height of 3.2 cm, without AWAS (blue line) and with AWAS (red line).

In the SPH simulation results, a clear reflection of the solitary wave by the slope is observed (Fig.104, red line). To mitigate these reflection effects, an alternative approach involves relocating the inlet buffer zone to WG1. This allows for the measurement of: (i) the water surface elevation and velocity profile at WG4 to create the input data files for the inlet; (ii) the water surface elevation at WG4 plus an additional 5 dp to generate the necessary files for AWAS correction. By utilising that numerical information, the inlet buffer zone can be relocated to WG4. The water surface elevation results at WG5 can then be compared with the experimental results to validate the simulation results (Fig.104, blue line). The results showed good agreement for all wave heights. These results confirm the validity of the analysis method for the propagation of the solitary wave, considering first a 2D analysis of the full domain and then a 3D analysis with a reduced domain by the SPH method using inlet/outlet conditions.

Once the use of inlet/outlet conditions for wave generation was validated, the 3D numerical simulations for series S1 to S3 were conducted. Comparing the numerical results for the free surface elevation of the three series with the experimental results, it was concluded that there is good agreement in wave

heights, with a difference inferior to *dp* (the numerical resolution). These results are illustrated in Fig.105, Fig.106 and Fig.107.

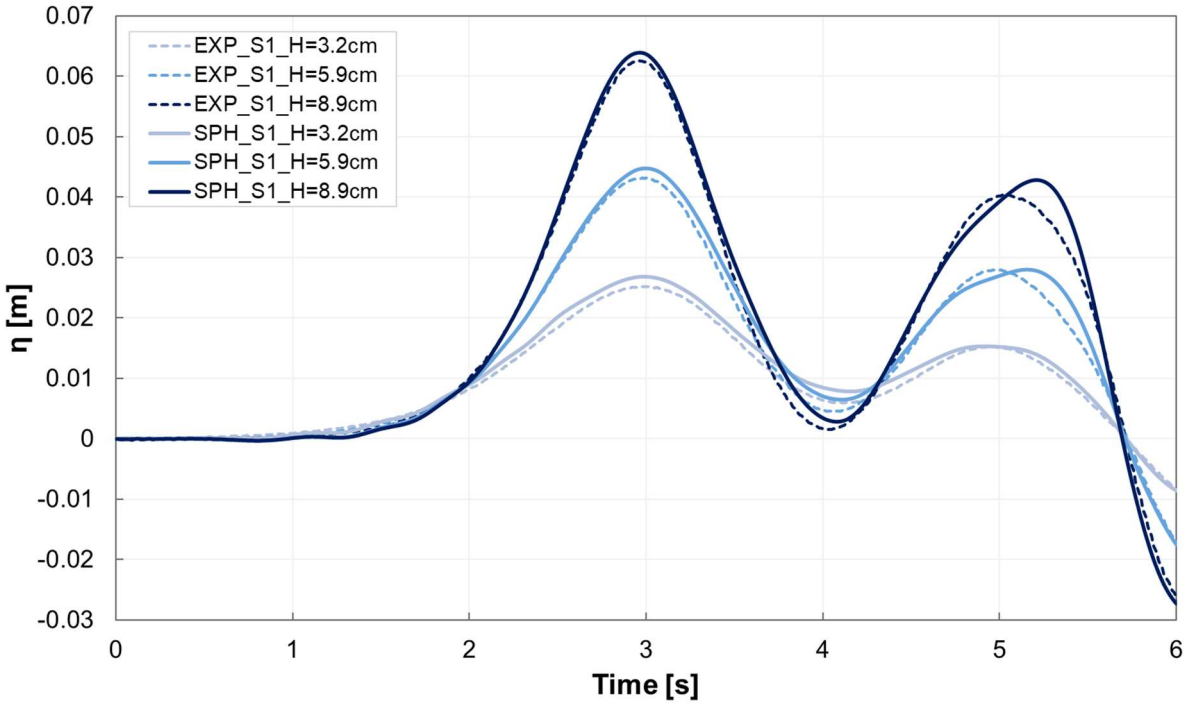

Fig.105 – Comparison of numerical and experimental free-surface elevation (η) at WG5 of series S1.

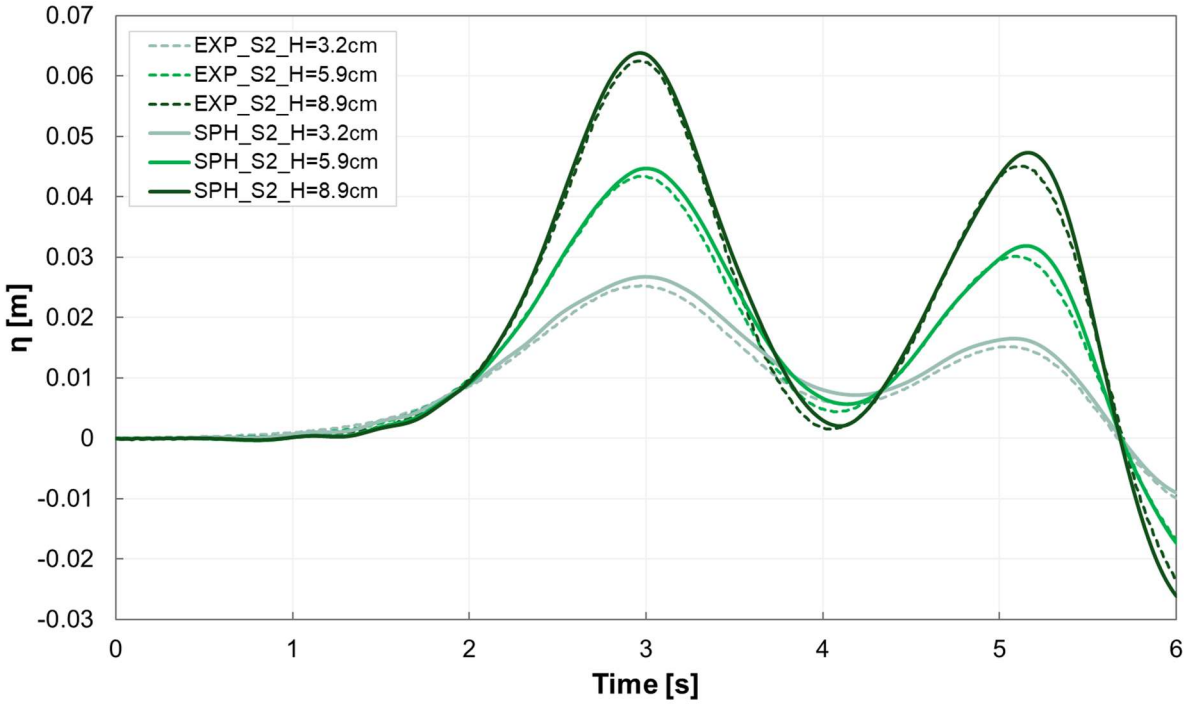

Fig.106 – Comparison of numerical and experimental free-surface elevation (η) at WG5 of series S2.

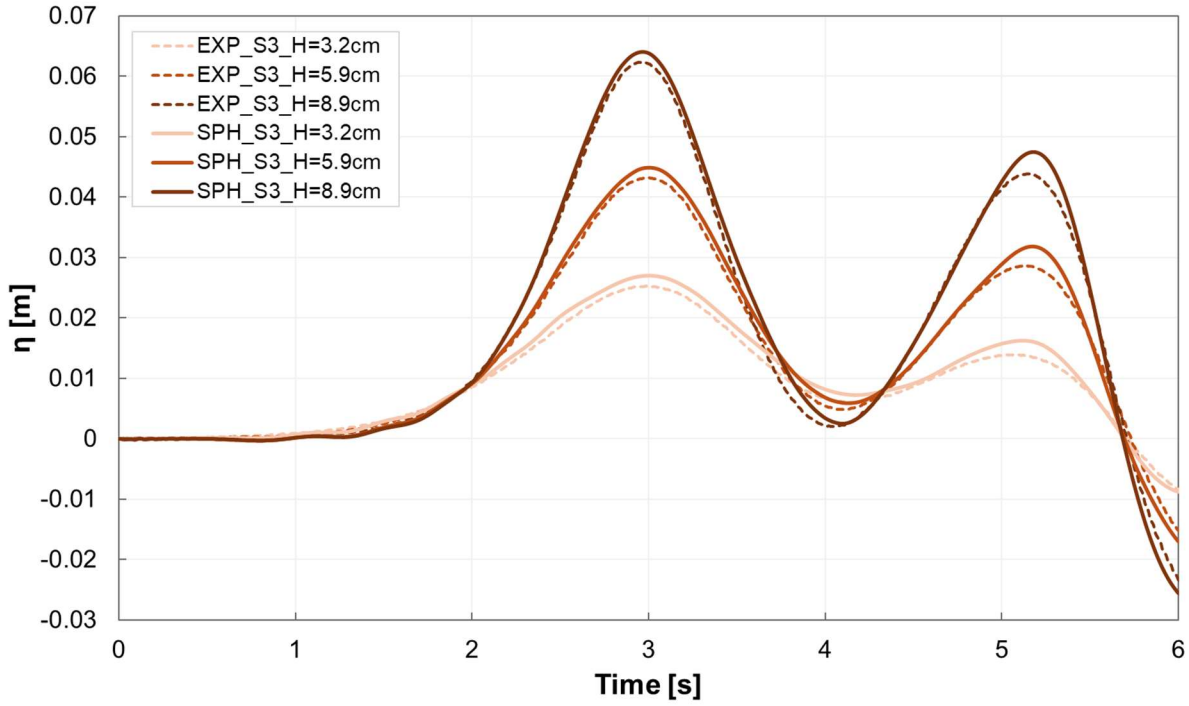

Fig.107 – Comparison of numerical and experimental free-surface elevation (η) at WG5 of series S3.

4.4.3.4 Numerical discretisation parameters

An initial distance between particles, dp, need to be established to discretise the numerical domain into particles. As mentioned in previous sections and following the recommendations in Altomare *et al.* (2017) and Roselli *et al.* (2018), a minimum of 5 particles need to be used to define the wave height (H) for accurate wave propagation ($H/dp > 5$). According to the minimum wave height measured at WG1 (Fig.90), $dp = 0.005\,m$ was initially considered, which means that H/dp is 6, 12 and 18 for the three different solitary wave heights (3.2, 5.9 and 8.9 cm, respectively) at WG1. Moreover, using this resolution, 11 particles were created in the characteristic size of a Antifer (5.6 cm). In subsection 4.4.4.4, a convergence and performance study are conducted, where different numerical resolutions and runtimes are analysed.

Note that the DualSPHysics software includes pre-processing tools that allow to introduce complex geometries by means of a wide range of input files including CAD, STL, PLY files, etc., making the setup of simulations straightforward. In this case, the actual geometry of the Antifers can be considered using STL files. The distance of interaction (kernel radius) is here defined as $2h = 0.026\,m$ (being $h = 1.5 \cdot \sqrt{3} \cdot dp$, in 3D). A total number of 7,908,137 particles are created with 8,344 particles discretising the 7 Antifers and 6,012,867 particles discretising the fluid. The simulation of 6 s of physical time took around 7 h (for the three solitary wave conditions) using NVIDIA L40S GPU with Intel i7-8700K CPU and 64 GB RAM. Around 40 minutes of that total execution time was spent by Project Chrono solving the interactions between Antifers and the slope. Whereas the DualSPHysics is executed on the GPU card, the collision detection of the Project Chrono library is executed on single-core CPU (Martínez-Estévez *et al.*, 2023).

4.4.4 RESULTS AND DISCUSSION

The experimental data, in CSV format, obtained using the instrumented blocks, were processed using a Matlab routine and validated qualitatively and quantitatively using the ImageJ software (4.4.4.1). After processing the experimental results, the numerical dataset was processed using Matlab routines and the ParaView visualization tool. In this section, comparative graphs of the results are presented (4.4.4.2), followed by a hydrodynamic field study (4.4.4.3) and a comprehensive analysis of the performance and convergence of the results (4.4.4.4), considering the influence of initially defined parameters and the quality of inputs (4.4.4.5). The critical analysis will yield the identification and prioritisation of areas for improvement in the numerical model DualSPHysics. Additionally, a set of recommendations will be listed for future software users, highlighting the best settings to achieve the best results.

4.4.4.1 Validation of SmartAntifers

This study examines the hydraulic stability of instrumented units influenced by hydrodynamic forces, frictional forces, and their own weight. This subsection delves into the signal selection, data processing, and motion analysis of instrumented blocks within a specific series (S2) utilizing the SmartAntifer system. The focus is on blocks 4 and 5 from this series (H_{WG1} = 5.9 cm, R02) to illustrate distinct movement behaviours under inclined plane conditions. The two blocks were chosen to showcase contrasting scenarios: block 4 maintains its orientation throughout motion, with its displacement vector aligned with the slope direction, whereas block 5 shows a deviation from this alignment, accompanied by a change in orientation. The scenario is illustrated in Fig.108.

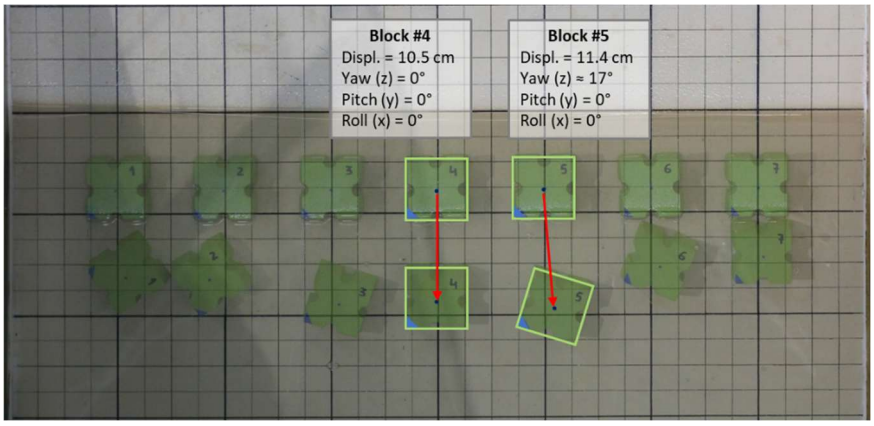

Fig.108 – Overlap of the initial and final photograph of the blocks for test S2_SW_d530_H075_R02.

First, a qualitative analysis of the calibrated raw data for blocks 4 and 5 was conducted using Fig.109 and Fig.110. In Fig.109(a) and Fig.110(a), the acceleration along each block's axis (see Fig.85) is shown in units of g ($1g \approx 9.81$ m/s^2), which can be used to track the translational dynamics of the blocks. Then, Fig.109(b) and Fig.110(b) represent the resultant acceleration magnitude, $|a'|$, which is calculated using the following formula:

$$|a'| = \sqrt{{a'_x}^2 + {a'_y}^2 + {a'_z}^2} \tag{115}$$

where a'_x, a'_y and a'_z represent the accelerations along the respective x', y' and z' axes. Finaly, Fig.109(c) and Fig.110(c) illustrate the gyroscope readings, showing angular velocity (ω) in degrees per second (°/s) around each block axis, which provide valuable insights into the rotational dynamics of the blocks. Throughout all plots, stationary periods are indicated by light grey vertical bars, while motion periods are highlighted with vertical bars in light yellow (indicating common motion phases for both blocks) and red.

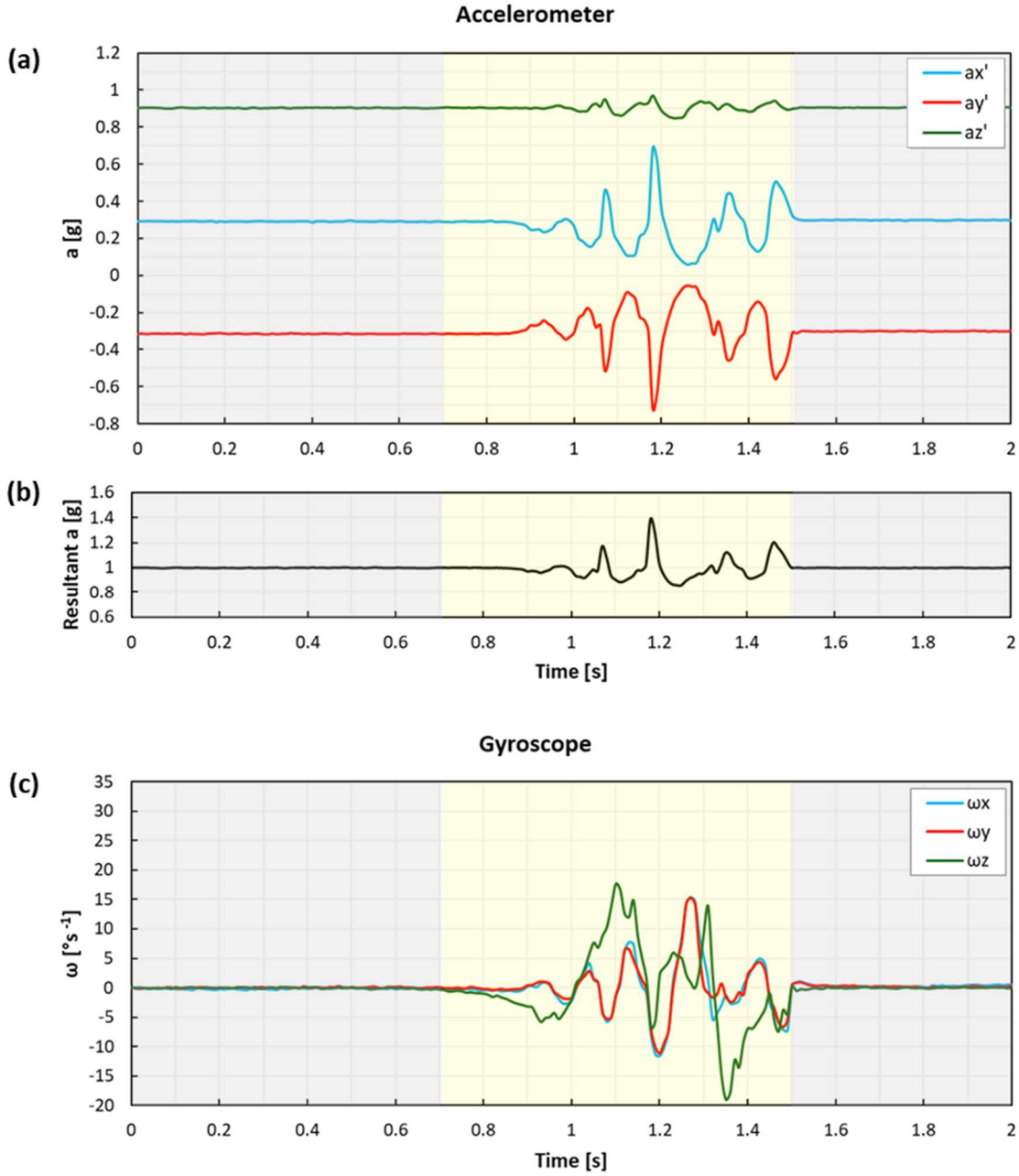

Fig.109 – Calibrated IMU data of block 4: (a) acceleration data on the three axes (a'_x, a'_y, a'_z), (b) resultant acceleration magnitude, and (c) gyroscope data around the three axes (ω_x, ω_y, ω_z).

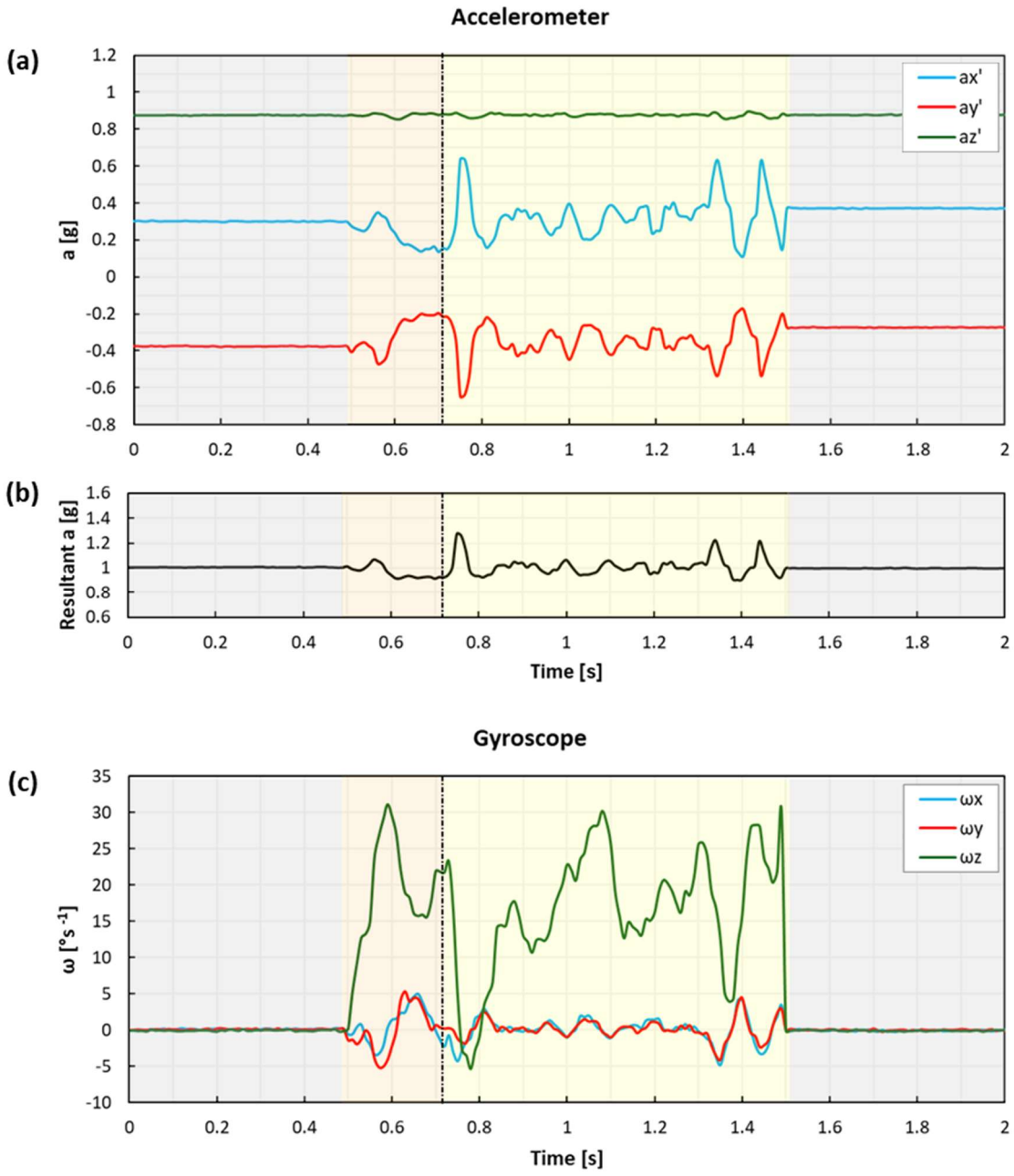

Fig.110 – Calibrated IMU data of block 5: (a) acceleration data on the three axes (a'_x, a'_y, a'_z), (b) resultant acceleration magnitude, and (c) gyroscope data around the three axes (ω_x, ω_y, ω_z).

Several key insights can be drawn from both figures. First, analysing the stationary conditions, before the onset of actual motion, both blocks record resultant acceleration magnitudes close to 1g. This pattern is characteristic of non-motion conditions where only gravitational acceleration is being detected. This conclusion is further corroborated by the gyroscope data in Fig.109(c) and Fig.110(c), which show zero angular velocity, confirming the absence of rotational motion. Since the blocks are positioned on an inclined plane, the accelerations recorded along all local axes represent components of the gravity vector, reflecting the block's orientation relative to the vertical gravity vector. For instance, measures in

block 4 indicate mean values of a'_x = 0.29g, a'_y = -0.31g and a'_z = 0.90g, while for block 5 records a'_x = 0.30g, a'_y = -0.38g and a'_z = 0.88g. These values are useful to determine the initial orientation of the Antifer blocks, θ_0, which can be computed using the following equation:

$$\theta_0 = \cos^{-1}\left(\frac{a'_x}{|a'| \cdot \sin(\alpha)}\right) \tag{116}$$

The slope presents an established angle, α, equal to 25.5º and theoretical considerations establish that the resultant acceleration magnitude $|a'|$ should equal 9.81 m/s². However, considering equation (115) and the previous mean values of a'_x, a'_y and a'_z, $|a'|$ assume a value of 9.95 m/s² for block 4, and 10.35 m/s² for block 5. Consequently, since α can be represented by:

$$\alpha = \cos^{-1}\left(\frac{a'_z}{|a'|}\right) \tag{117}$$

where α is equal to 25.3º for block 4 and 28.5º for block 5. That means that z' axis is not perpendicular to the slope of 25.5º. While these discrepancies are small for block 4, allowing to focus its analysis to only 3 freedom degrees, significant differences in the block 5 lead to the necessity of 6 degrees of freedom analysis. However, for simplification reasons, as the differences correspond to an error smaller than 15%, one is going to keep assuming that *x*'*y*' form the plane parallel to the slope, to still being able to apply equation (116). Making this assumption, the values of θ_0 for blocks 4 and 5, are, correspondingly, 47.3º and 51.3º. This means that the *x*' and *y*' axes are not perfectly aligned with the block's diagonals, i.e., the electronic components were not properly positioned inside it (Fig.111).

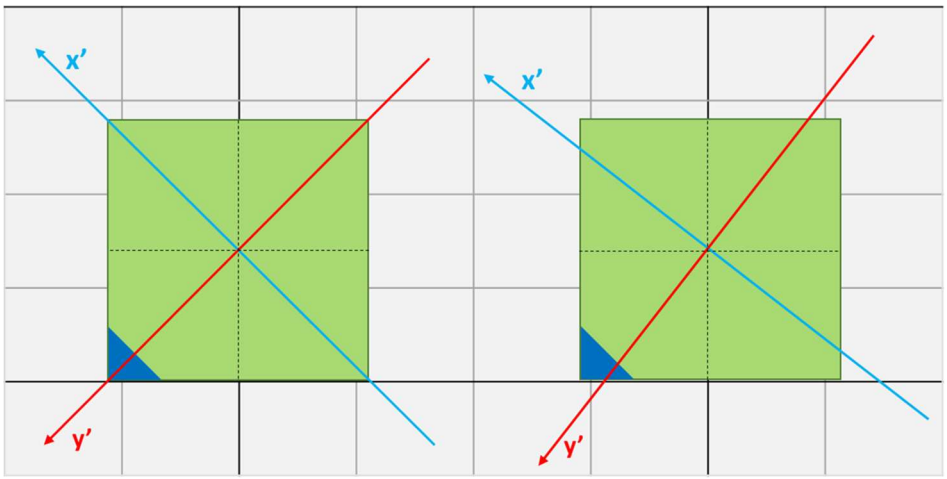

Fig.111 – Theoretical (left) vs real (right) positioning of block 5 IMU x' and y' axes.

These variations between blocks arise due to two primary factors: (i) minor manufacturing tolerances, which introduce quasi-constant offsets in the sensors' readings due to non-uniformity in internal mass distributions; and (ii) misalignments in the sensor placement within the blocks, compounded by the

manual positioning of the blocks on the slope, introducing additional inaccuracies. This situation underscores the importance of careful calibration and data interpretation.

Once the motion begins, the accelerometer data of block 4 indicate stable, almost symmetrical values for a'_x and a'_y, indicating minimal change in orientation during motion. The resultant vector in the *x*'*y*'-plane aligns with the slope direction, confirming translational motion without reorientation. Plus, little to no angular velocity around the *z*'-axis, confirm that its motion is primarily translational without significant reorientation. The motion phase lasts approximately 0.81 s.

In contrast, for block 5, the accelerometer data show noticeable changes in a'_x and a'_y, indicating rotation around the *z*'-axis and a reorientation during motion phase, resulting in a different final orientation compared to the initial state. Peaks in angular velocity in the gyroscope data confirm substantial rotational movement around *z*'-axis. This suggests that external forces, such as wave action, have caused the block to rotate as it moves down the slope. This motion phase lasts approximately 1.02 s, suggesting variations in their initial conditions or external forces influencing their dynamics, when compared with block 4.

For both blocks, the vertical component of acceleration (a'_z) remains stable, suggesting consistent gravitational influence during motion.

After the analysis of the motion mode, the next step corresponded to the quantification of the displacement along the inclined plane considering the procedure presented on 4.4.2.3. After finding the initial orientation, by means of the received angle Ω_z, the sensor readings a'_x, a'_y and a'_z were rearranged – application of rotation matrix (equations (104) and (105)) and gravity compensation (equation (106)) – to a_x, a_y and a_z. By integrating a_x and a_y (equation (107)) it was possible to obtain the blocks movement characteristics relative to its starting position: velocity, v_x and v_y , and displacement, s_x and s_y, plotted in Fig.112. Only the accelerations during the periods of motion were considered for integration. For stationary periods (before and after the motion periods) the acceleration values for both blocks were assumed to be 0 m/s².

Observing Fig.112, both blocks exhibit distinctive motion patterns that reveal the effects of interactions with the plane and their surrounding conditions. While there are similarities in the overall trends, key differences in their behaviour highlight the variability in the dynamics of motion under comparable experimental conditions.

For block 4 (Fig.112 a), the acceleration in the *x*-direction (a_x) begins oscillating around 0.8 s and continues until 1.5 seconds, reaching a peak of approximately 5.63 m/s² at 1.2 s. Meanwhile, the acceleration in the *y*-direction (a_y) remains constant and close to zero throughout the entire interval, indicating no significant force acting in that direction. The motion of the block along the *x*-axis is influenced by a combination of gravity, friction, and the wave's hydrodynamic drag forces. While gravity steady force pulling the block down the slope and friction resisting this motion create predictable deceleration, the wave's time-varying drag force introduces a chaotic nature, alternately accelerating and decelerating the block during its run-up and run-down phases. This interplay results in oscillatory and irregular patterns in a_x, contrasting with the smoother, more consistent behaviour along the *y*-axis. This behaviour is reflected in the velocity (v_x), which decreases from 0 m/s to −0.43 m/s between 0.7 s and 1.5 s, with some oscillations, which are indicative of minor surface irregularities or changes in the block's interaction with the surrounding boundaries. In contrast, the velocity in the *y*-direction (v_y) stays constant at zero, showing no motion in that axis. The position in the *x*-direction (s_x) gradually decreases, dropping from 0 m at 0.7 s to approximately −0.121 m by the end of the interval. The *y*-position (s_y) remains unchanged throughout, affirming the lack of motion or acceleration along the *y*-axis.

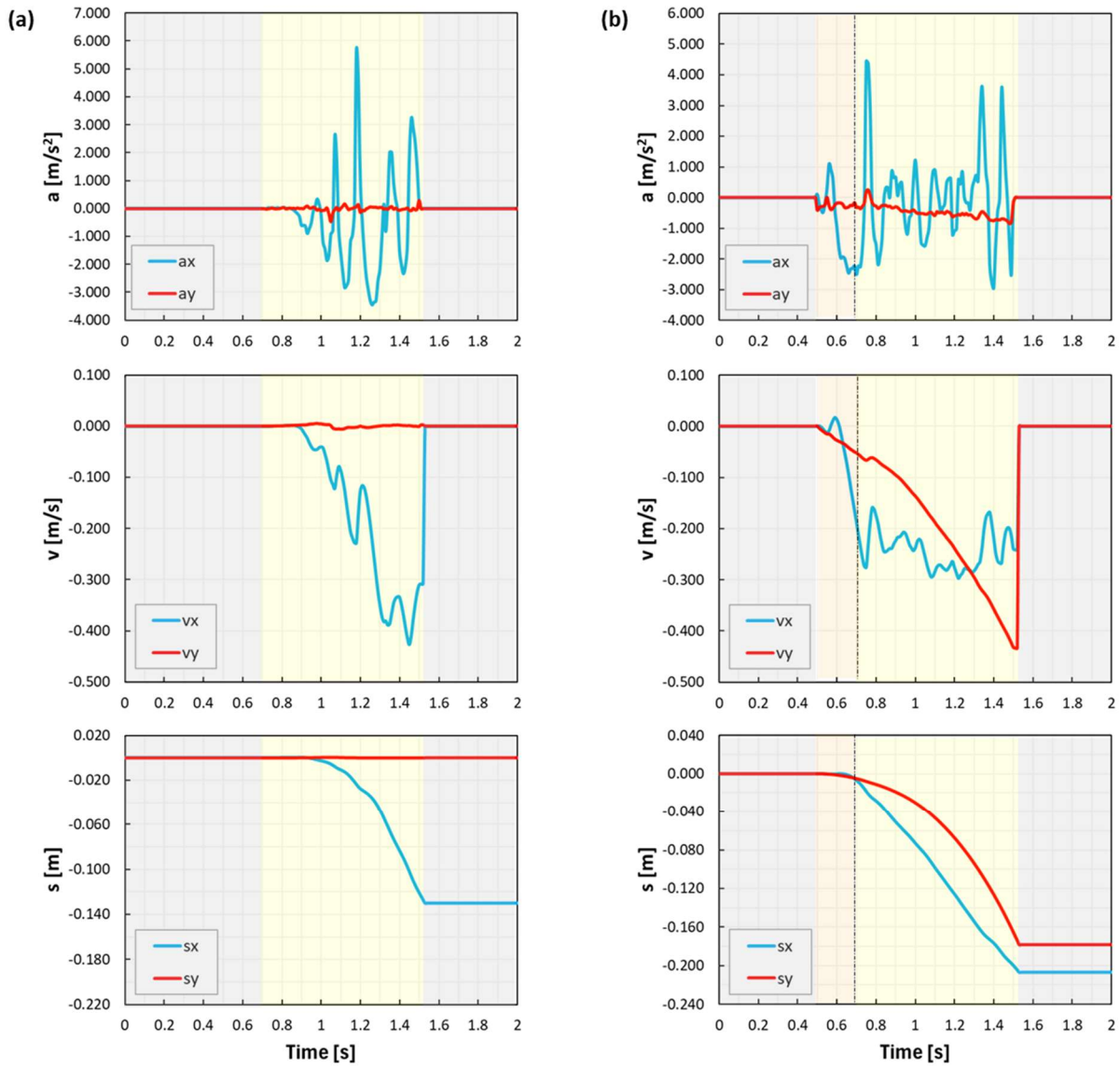

Fig.112 – Time series of the derived movement characteristics for acceleration (a [m/s^2]), velocity (v [m/s]) and displacement (s [m]) of block 4 (a) and block 5 (b).

In contrast, block 5 (Fig.112 b) exhibits a more complex kinematic behaviour, involving significant activity in both x and y components. The acceleration profile reveals a pronounced oscillatory pattern for a_x, which begins fluctuating around 0.5 s. These oscillations reach a peak value of approximately 4.45 m/s² near 0.8 s, reflecting the influence of time-varying forces such as wave drag and friction acting along the slope. In contrast, a_y exhibits a much steadier behaviour, with only minor fluctuations throughout the motion phase. Its variations remain within the range of approximately −1 m/s^2 to 0 m/s^2, indicating limited lateral force influence during the block's motion along the slope.

The velocity patterns further reflect the influence of these forces. The x-velocity (v_x) starts at 0 m/s and decreases steadily to approximately −0.275 m/s by 0.75 s, after which it oscillates, mirroring the irregularities in a_x. The motion ceases abruptly at 1.5 s, as v_x returns to zero. In contrast, the y-velocity (v_y) shows a smoother but more significant decline, dropping from 0 m/s at 0.5 s to −0.44 m/s at 1.5 s.

This difference arises from the cumulative nature of acceleration: while a_y does not oscillate significantly, its steady, prolonged influence leads to a more pronounced buildup of v_y.

The displacement plots (s_x and s_y) provide further insights into the block's motion. The *x*-displacement (s_x) shows a steady negative trend, decreasing from 0 m to approximately −0.207 m by the time the motion ceases at 1.5 s. The oscillatory behaviour observed in a_x and v_x does not significantly disrupt the overall steady progression of s_x, as these oscillations tend to cancel out over time. In contrast, the *y*-displacement (s_y) reveals a markedly different pattern, reflecting a more pronounced and dynamic motion in the *y*-direction. Starting from 0 m, s_y undergoes a significant decline, reaching approximately −0.165 m by the end of the motion phase.

Overall, Fig.112 a) reflects a system dominated by x-direction dynamics, with minimal or no influence in the y-direction. On the other hand, Fig.112 b) introduces significant motion along the y-axis, indicating a dynamic alteration, likely caused by an external force. Table 26, summarizing the peak values of acceleration, velocity, displacement, total displacement (applying equation (108) and rotation for both blocks, will provide additional context for these findings.

Table 26 – Summary of the peak values of acceleration, velocity, displacement and rotation for different timesteps.

	Time	a_x	a_y	v_x	v_y	s_x	s_y	Ω_z	θ	d
	[s]	[m/s²]		[m/s]		[m]		°		[m]
Block 4	0	0	0	0	0	0	0	0.0	-47.3	0.124
	0.50	0	0	0	0	0	0	0.0	-47.3	
	0.75	0	0	0	0	0	0	0.0	-47.4	
	0.80	0	0	0	0	0	0	-0.1	-47.4	
	1.18	5.625	0.068	-0.228	-0.002	-0.024	0	0.7	-46.6	
	1.5	0	0	-0.310	-0.001	-0.121	0	-0.2	-47.6	
	2	0	0	0	0	-0.124	0	-0.2	-47.6	
Block 5	0	0	0	0	0	0	0	0.0	-51.4	0.259
	0.50	0	0	0	0	0	0	0.0	-51.3	
	0.75	4.451	0.198	-0.276	-0.063	-0.019	-0.007	4.7	-46.6	
	0.80	-1.269	-0.258	-0.163	-0.059	-0.027	-0.009	4.7	-46.7	
	1.18	-1.210	-0.630	-0.265	-0.229	-0.124	-0.062	11.2	-40.2	
	1.50	0	0	-0.240	-0.428	-0.201	-0.161	17.1	-34.2	
	2	0	0	0	0	-0.203	-0.165	17.1	-34.2	

Considering all factors, the displacement results for block 4 align well with expectations when compared to the value obtained using the ImageJ software. As shown in Fig.108, the displacement occurs exclusively along the *x*-axis, with no observed rotations. This is consistent with the calculated displacement values, where s_x, equal to 0.124 m, was like the expected outcome of 0.105 m, s_y remained effectively zero, and the block's rotational measurement, Ω_z, indicated no rotation.

In contrast, the displacement results for block 5 deviate significantly from expectations. Although the block moved in the anticipated direction, the displacement magnitude exceeded more than double the expected value of 0.114 m obtained using ImageJ tool. Specifically, the displacement along the *x*-axis was approximately 70 % greater than anticipated, reaching 0.203 m instead of the expected 0.119 m, while along the *y*-axis, the displacement was dramatically higher – approximately 14 times the expected value – measuring 0.165 m instead of 0.0125 m.

This discrepancy points to potential issues in the interpretation or processing of IMU data, particularly in the y-direction. Factors contributing to these anomalies include:

(i) misjudgements in determining the non-stationary period's duration;
(ii) integration errors, arising from the inherent limitations of IMU data, such as integration drift; or
(iii) inaccuracies in defining the block's orientation.

The manual identification of the start and end of motion is particularly critical, as these were set based on observed declines in rotational readings (from the gyroscope) and low acceleration values indicative of gravitational influence. While the manual setting of these periods can always be debated, any misstep here could lead to erroneous displacement values. However, given the gradual decline of motion and the consistency of low acceleration magnitudes during the transition to stationary states, such misjudgements are expected to have only a minimal effect.

Integration drift, an inherent limitation of IMU data, may also play a significant role. The process of twice-integrating acceleration values to derive displacement amplifies minor inaccuracies, particularly when dealing with extended time intervals or larger displacements. This is compounded by finite sampling rates and sensor resolution, which introduce additional sources of error.

Notably, the rotational behaviour of block 5, like that of block 4, closely matched predictions, indicating no significant issues in capturing angular dynamics. This consistency suggests that the observed discrepancies are confined to the linear motion dynamics, particularly in the *y*-direction, rather than arising from rotational motion or systemic calibration errors.

4.4.4.2 Validation of numerical Antifers displacement

The analysis started with a comparison of the total displacements of the Antifer units from the S1 and S2 series. At the level of the Project Chrono, only the friction between the blocks and the slope was considered, as no collisions between blocks were observed in those series. Initially, a qualitative and preliminary quantitative analysis was conducted using Fig.113 and Fig.114, which provide an initial visual comparison, displaying images from one of the repetitions of each experiment on the left and corresponding simulation snapshots on the right, for series S1 and S2, respectively. The first frames (a) depict the initial state before the wave's arrival, while the subsequent images illustrate the final state after the solitary wave has interacted with the Antifers. This allows the observation of block displacement for each wave condition, for each series S1 and S2: H_{WG1} = 3.2 cm (b), H_{WG1} = 5.9 cm (c), and H_{WG1} = 8.9 cm (d). As anticipated, the results exhibit some variation; however, a detailed analysis of each wave reveals that the displacements in both the experimental and numerical data are closely aligned. The average displacements, when referenced against the grid matrix, are comparable across both sets of data. Additionally, the range of values obtained for each wave height is well-defined, further validating the consistency between the experimental and numerical observations.

Subsequently, a more detailed quantitative analysis is presented in Fig.115. This figure compares the average experimental individual displacement of the seven Antifer units for wave heights of 3.2 cm, 5.9 cm, and 8.9 cm, based on a minimum of three tests per wave height to ensure repeatability of the measurements. The standard deviation values for each block of the experimental results are also computed to quantify variability. These results are compared with the total displacement of the blocks from the numerical simulations, which consider three different friction coefficients (μ) rather than a single fixed value. This approach is not only acceptable, but it also provides a more realistic and insightful analysis, facilitating more accurate modelling and robust conclusions, as discussed in section 4.4.3.2..

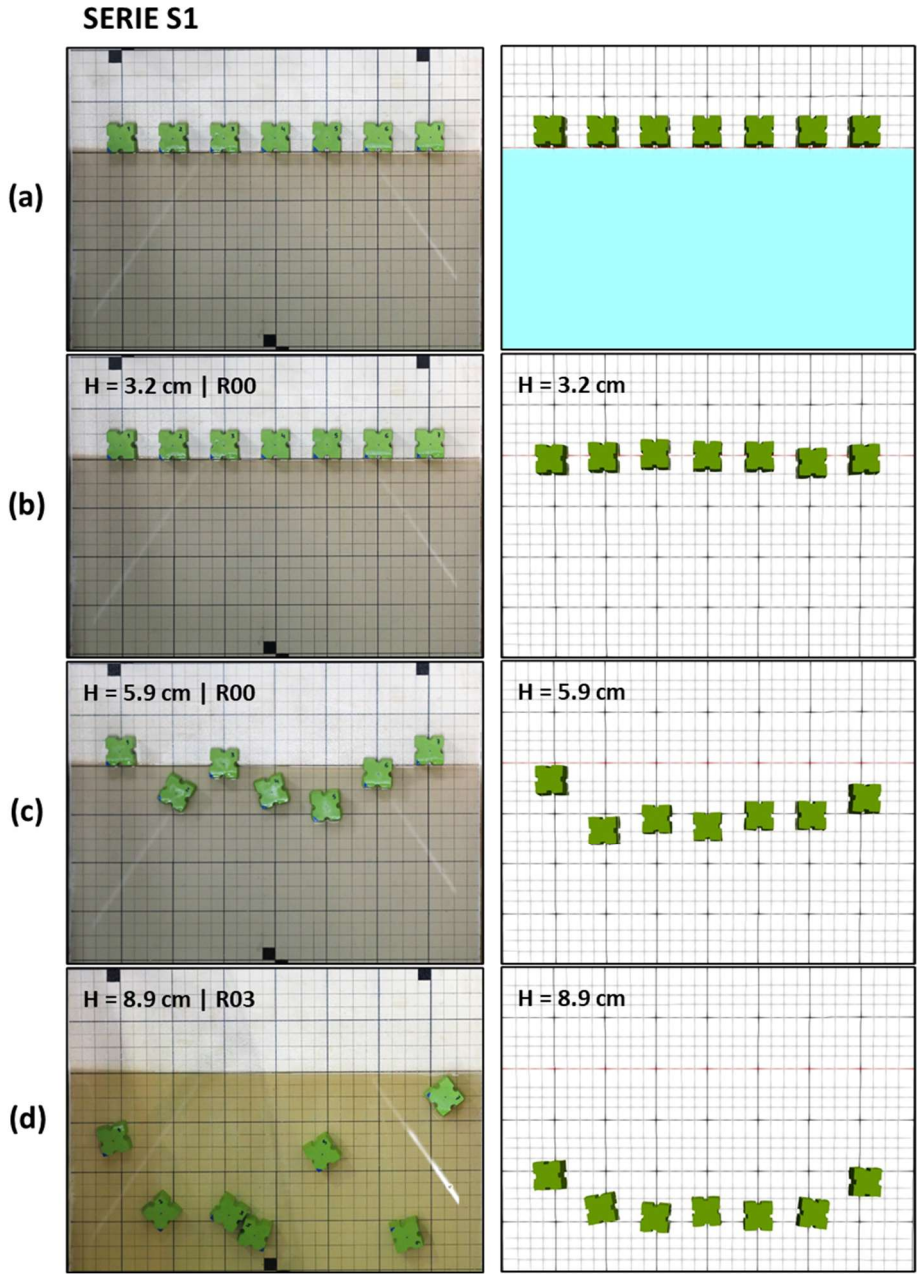

Fig.113 – Top view of the initial (a) and final situation of the Antifers after the interaction with the three different waves (b, c and d), during experiments (left), considering only one of the repetitions, and with the numerical simulation (right), μ = 0.50, for series S1.

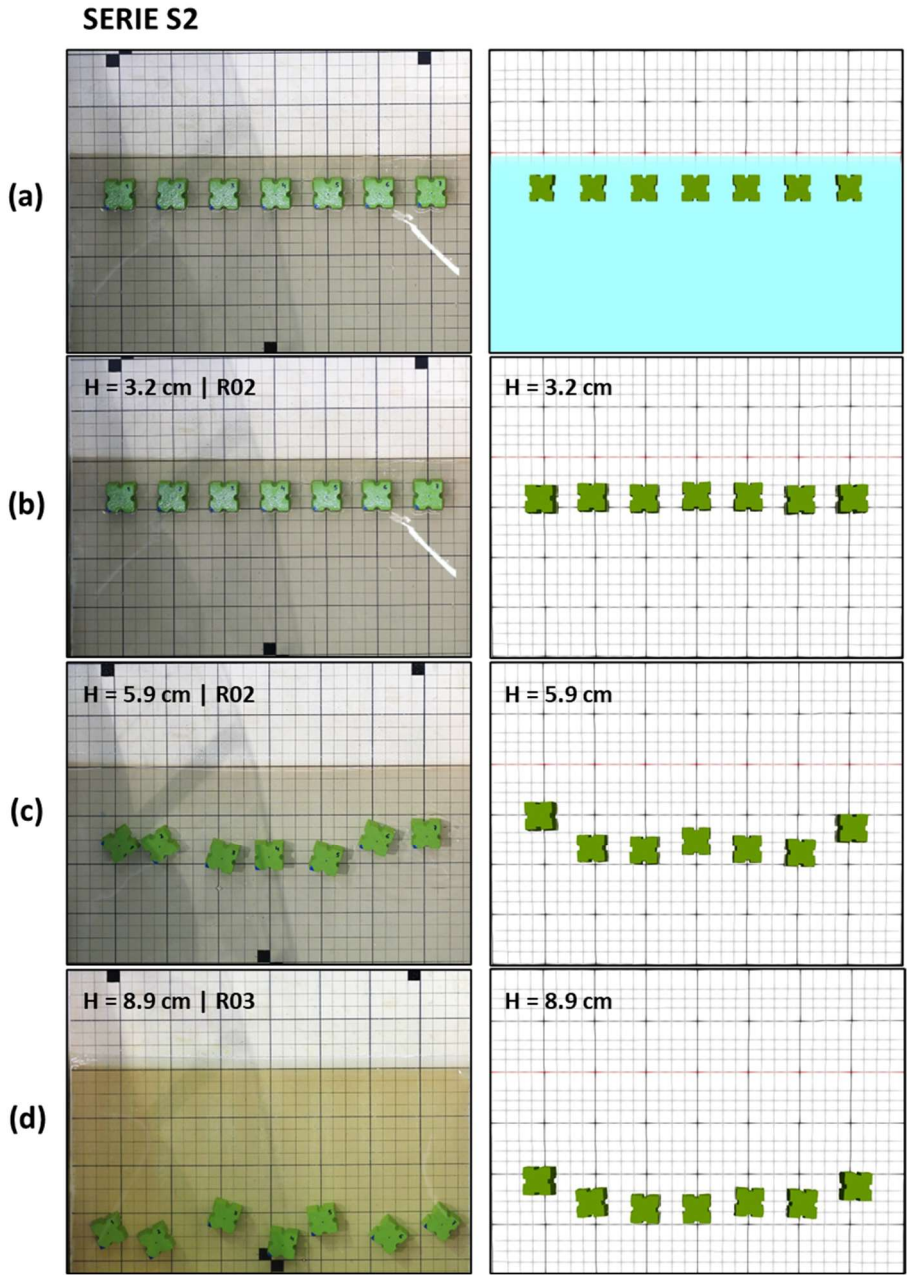

Fig.114 – Top view of the initial (a) and final situation of the Antifers after the interaction with the three different waves (b, c and d), during experiments (left), considering only one of the repetitions, and with the numerical simulation (right), μ = 0.50, for series S2.

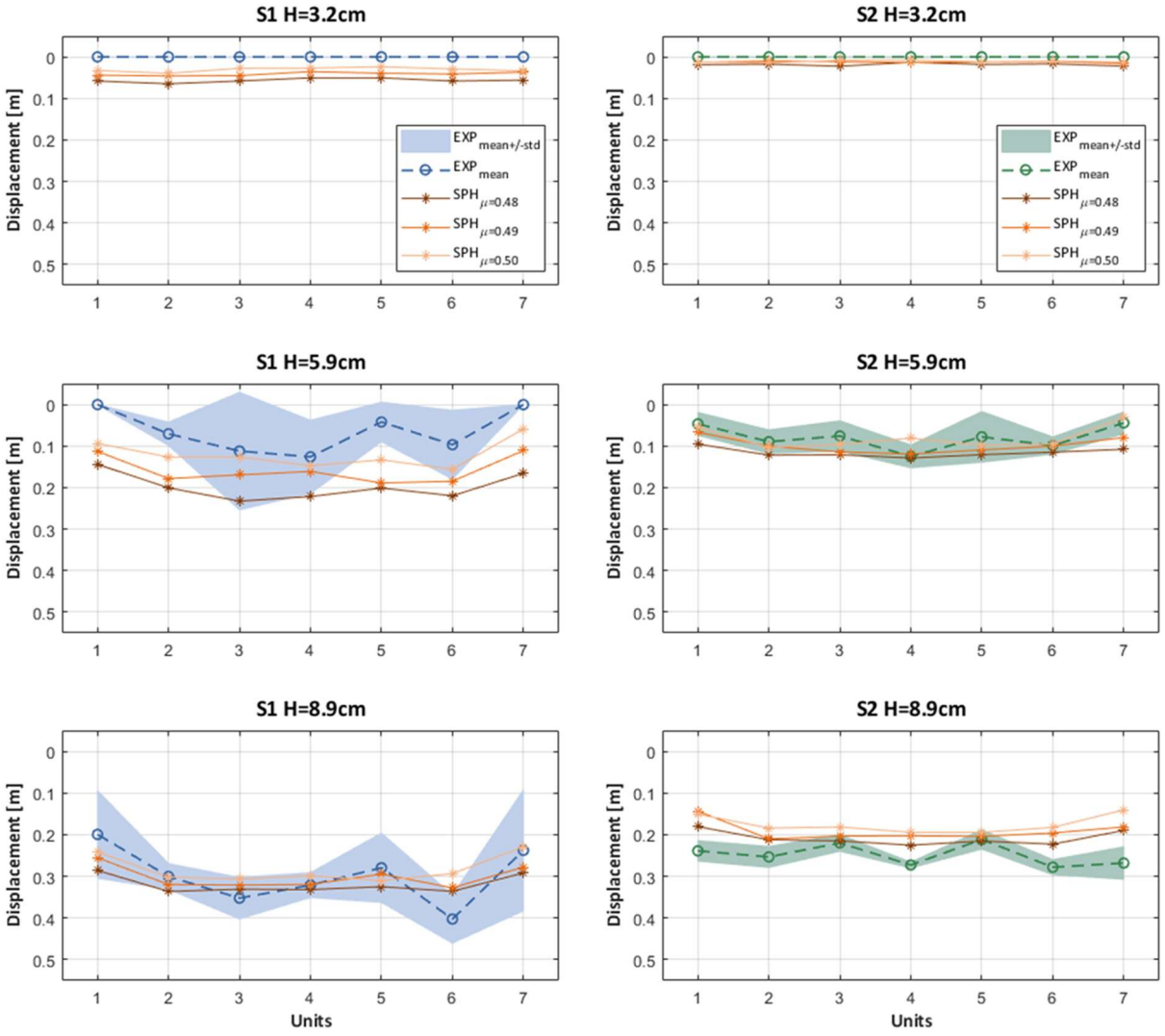

Fig.115 – Experimental and numerical displacements of the 7 Antifers for the different wave conditions of Series 1 and 2 (H = 3.2, 5.9 and 8.9 cm), considering three coefficients of friction (μ = 0.48, 0.49, 0.50).

First, analysing the results for the smallest wave height, H_{WG1} = 3.2 cm, the blocks did not move during the experiments in both series. However, in the numerical simulations, the blocks experienced small displacements ranging from 2.4 to 6.5 cm.

Evaluating the intermediate wave condition with a wave height of H_{WG1} = 5.9 cm, in series S1, the blocks had displacements which varied from no movement up to 31 cm, with an average displacement of 6.4 cm. In series S2, the displacements ranged from stationary to 18 cm, with an average total displacement of 8 cm. When compared with the numerical results, the μ = 0.50 produced the best results for both series. Series S1 showed an average displacement of 12 cm, and series S2 had an average displacement of 8 cm, indicating that the block movements were of the same order of magnitude.

Finally, evaluating the largest wave condition, with a wave height of H_{WG1} = 8.9 cm, the experimental results for series S1 varied between 8.1 cm and 47.3 cm, with an average total displacement of 29.6 cm. For series S2, the displacements ranged between 18.8 cm and 32.5 cm, with an average displacement of 24.8 cm. In comparison, the numerical displacements ranged from 23 to 33.6 cm in series S1 and from

14.1 to 22.5 cm in series S2. These results confirm that, for the selected range of coefficients of friction (μ), the block movements in the numerical simulations were of the same order of magnitude as those observed in the laboratory experiments.

Table 27 includes all the data and the errors between experimental and numerical results. First, the average of the displacements of the Antifers during experiments is computed for each repetition (EXP_R00, EXP_R01, EXP_R02, etc) and the average of the repetitions was computed again to obtain one experimental value of displacement for each solitary wave (EXP_mean), that are compared with the numerical values for the different friction coefficients. Overall, it can be noted that a coefficient of friction μ = 0.50 is the most suitable for more than 50% of the cases, yielding smaller errors. Additionally, series S2 produces smaller errors compared to series S1. It is important to emphasise that achieving high levels of repeatability in experimental work is challenging, highlighting the difficult to ensure accuracy between numerical and experimental results.

Table 27 – Experimental and numerical displacement of Antifers for series S1 and S2.

	SERIES S1			**SERIES S2**		
	H = 3.2 cm	H = 5.9 cm	H = 8.9 cm	H = 3.2 cm	H = 5.9 cm	H = 8.9 cm
EXP_R00	0.000	0.048	0.345	0.000	0.051	0.255
EXP_R01	0.000	0.092	0.3055 (*)	0.000	0.093	0.242
EXP_R02	0.000	0.030	0.341	0.000	0.091	0.249
EXP_R03		0.086	0.246		0.085	0.252
EXP_R04			0.243		0.064	0.242
EXP_R05					0.080	
EXP_R06					0.095	
EXP_mean	0.000	0.064 ± 0.030	0.296 ± 0.050	0.000	0.080 ± 0.017	0.248 ± 0.006
SPH_μ=0.48	0.057	0.198	0.320	0.018	0.116	0.209
Error		209.4%	7.9%		45.3%	15.9%
SPH_μ=0.49	0.041	0.158	0.302	0.013	0.099	0.192
Error		147.0%	2.0%		23.7%	22.8%
SPH_μ=0.50	0.030	0.120	0.283	0.011	0.080	0.176
Error		88.0%	4.4%		0.5%	29.3%

From a practical perspective, it is important to quantify the rate of damage in addition to measuring units' displacement. The damage level is defined as the number of blocks that moved more than the characteristic size of 5.2 cm relative to the total number of blocks. The results, presented in Table 28, include the damage level for each individual experiment repetition, the average damage level across different repetitions, and the numerical values.

In both series, considering the smallest wave height, H_{WG1} = 3.2 cm, no damage was recorded in either the experiments or the numerical simulations, except for the SPH_μ = 0.48 case, where 5 of the blocks displaced more than 5.2 cm. For the largest wave height, H_{WG1} = 8.9 cm, 100% damage was observed in both the experiments and the numerical simulations, as all blocks displaced more than 5.2 cm. For

the intermediate wave height, HWG1 = 5.9 cm, the experimentally recorded damage was lower than the numerically recorded damage.

Table 28 – Experimental and numerical damage of Antifers for series S1 and 2.

	SERIES S1			**SERIES S2**		
	H = 3.2 cm	H = 5.9 cm	H = 8.9 cm	H = 3.2 cm	H = 5.9 cm	H = 8.9 cm
EXP_R00	0% (0)	43% (3)	100% (7)	0% (0)	43% (3)	100% (7)
EXP_R01	0% (0)	43% (3)	100% (7)	0% (0)	86% (6)	100% (7)
EXP_R02	0% (0)	29% (2)	100% (7)	0% (0)	100% (7)	100% (7)
EXP_R03		57% (4)	100% (7)		100% (7)	100% (7)
EXP_R04			100% (7)		43% (3)	100% (7)
EXP_R05					43% (3)	
EXP_R06					86% (6)	
EXP_mean	0% (0)	43% (3)	100% (7)	0% (0)	71% (5)	100% (7)
SPH_μ=0.48	71% (5)	100% (7)	100% (7)	0% (0)	100% (7)	100% (7)
SPH_μ=0.49	0% (0)	100% (7)	100% (7)	0% (0)	100% (7)	100% (7)
SPH_μ=0.50	0% (0)	100% (7)	100% (7)	0% (0)	86% (6)	100% (7)

In conclusion, although there is some variability in the results obtained for each block, the range of values for each wave height is clearly defined. Overall, the numerical values align in a satisfactory way with the experimental data. It can be concluded that the DualSPHysics model, coupled with the Project Chrono library, can reproduce the hydrodynamic response of Antifer blocks with some accuracy, at least for configurations of series S1 and S2.

Finally, analysing series S3, it was necessary to consider not only the friction between the slope and the blocks but also the friction between the blocks themselves, which makes this case very challenging for both physical and numerical modelling. Building on the previous series, three distinct friction values were adopted for the interaction between the slope and the blocks, while a coefficient of friction μ = 0.30 was used for the interactions between the blocks. Comparing the experimental results with the numerical simulations, when exposed to the three different wave heights, Fig.116 provides a qualitative analysis of the block movements, whereas Fig.117 and Table 29 present a quantitative analysis.

Qualitatively evaluating the obtained results, it is noteworthy that the movement patterns observed in the experiments differ from those in the numerical simulations. Specifically, when comparing the numerical results with the experimental ones, the influence of the blocks on each other varies between the two cases for all three waves. In the experimental work, the blocks at the edges tend to move less than the central blocks, largely due to the influence of the side walls and the hydrodynamic effects in the lateral spaces during the run-up. On the contrary, in the numerical results, the central blocks move less than the blocks at the edges. A parabolic shape is observed for H_{WG1} = 3.2 cm, while for H_{WG1} = 5.9 cm the blocks form almost a perfect line. Only for H_{WG1} = 8.9 cm is observed an inverse parabolic shape in SPH.

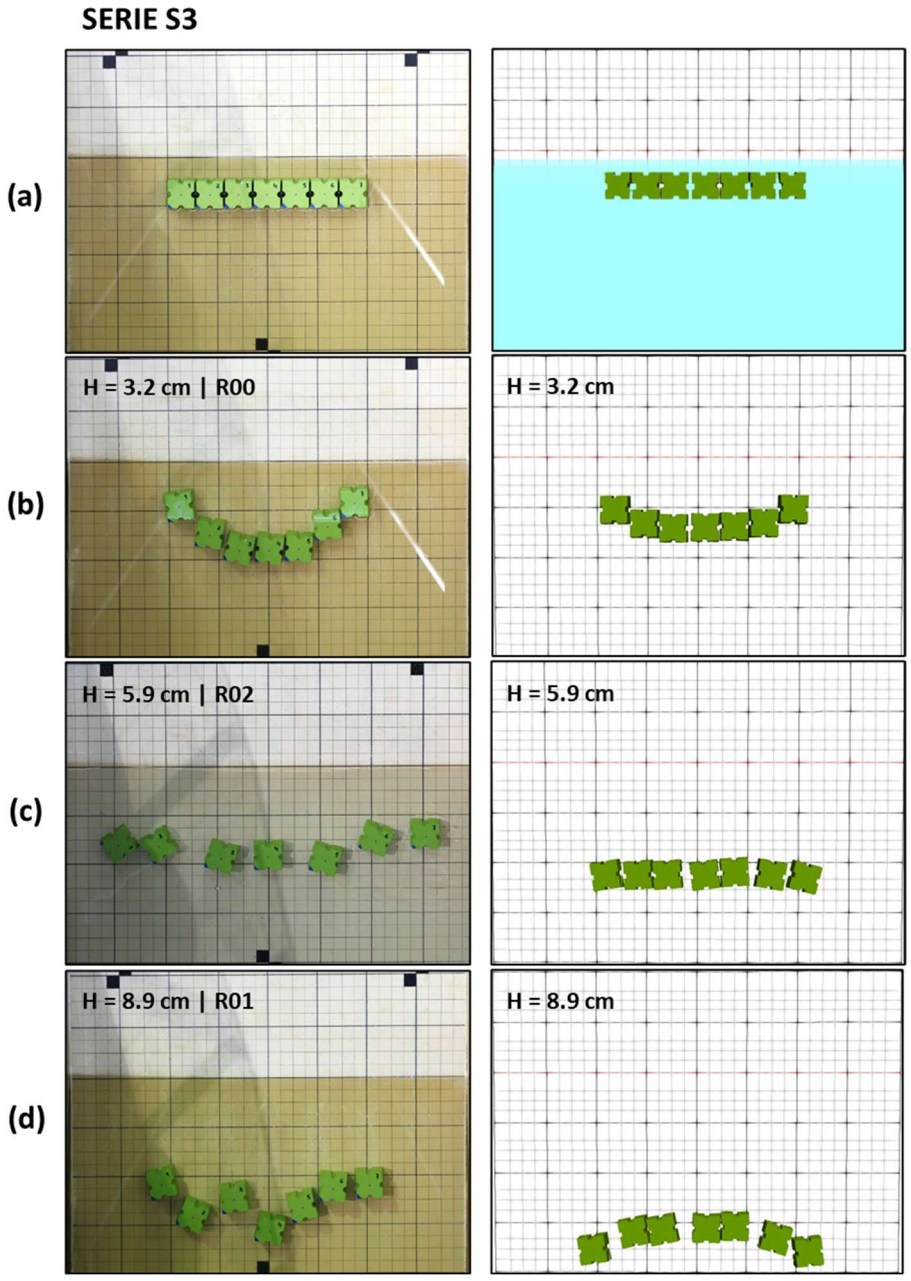

Fig.116 – Top view of the initial (a) and final situation of the Antifers after the interaction with the three different waves (b, c and d), during experiments (left), considering only one of the repetitions, and with the numerical simulation (right), for series S3.

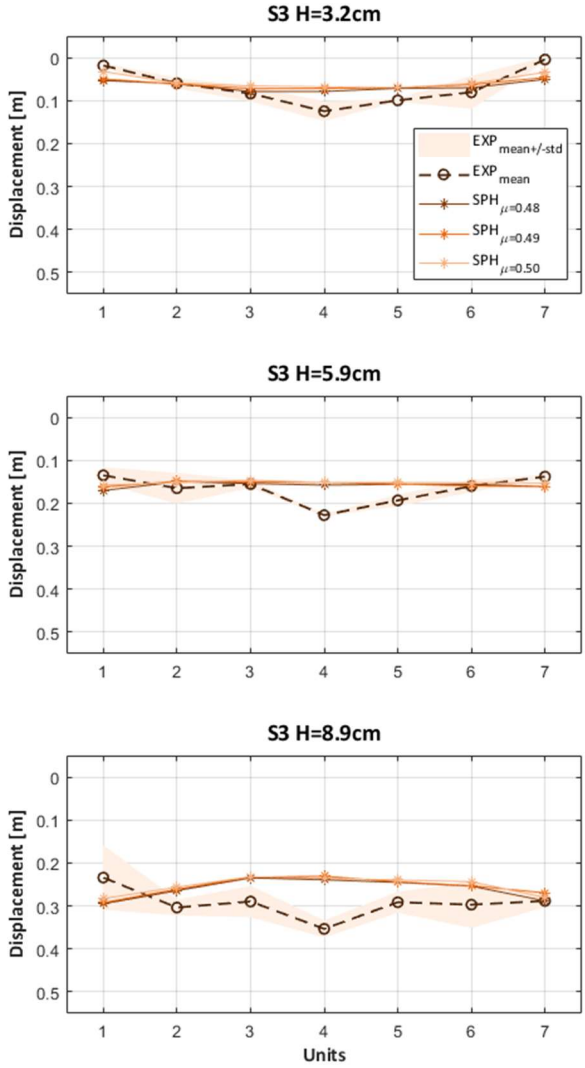

Fig.117 – Experimental and numerical displacements of the 7 Antifers for the different wave conditions of series S3 (H = 3.2, 5.9 and 8.9 cm), considering three coefficients of friction (μ = 0.48, 0.49, 0.50).

Table 29 – Experimental and numerical displacement of Antifers for series S3.

	SERIES S3		
	H = 3.2 cm	H = 5.9 cm	H = 8.9 cm
EXP_R00	0.064	0.167	0.273
EXP_R01	0.064	0.171	0.313
EXP_R02	0.074	0.165	0.296
EXP_mean	0.067 ± 0.006	0.168 ± 0.003	0.294 ± 0.020
SPH_μ=0.48	0.066	0.161	0.288
Error	1.6%	4.0%	2.0%
SPH_μ=0.49	0.062	0.156	0.255
Error	7.8%	7.2%	13.3%
SPH_μ=0.50	0.056	0.152	0.253
Error	17.3%	9.3%	14.0%

Quantitatively evaluating Fig.117 alongside Table 29, it is evident that for all three waves, the experimental and numerical results show less discrepancy when μ = 0.48 is considered between the blocks and the slope, resulting in errors of less than 4%. Focusing on this friction coefficient and analysing each wave individually, the experimental blocks moved an average of 6.7 cm and the numerical blocks 6.6 cm for the smallest wave (H_{WG1} = 3.2 cm). For the intermediate wave (H_{WG1} = 5.9 cm), the blocks displaced an average of 16.8 cm in the experiments and 16.1 cm in the numerical simulations. Finally, for the largest wave (H_{WG1} = 8.9 cm), the experimental Antifer units moved an average of 29.4 cm, while the numerical units moved 28.8 cm. From this analysis, the following can be inferred:

- For each wave height, the final displacements fall within a well-defined range when comparing numerical and experimental results;
- On average, the numerical blocks moved less than the experimental blocks for all three waves;
- The intermediate wave presented a higher discrepancy between numerical and experimental results, leading to a higher percentage error.

This series requires a more in-depth analysis, as, unlike series S1 and S2, more variables influence the results, specifically the friction and restitution coefficients in the simulations for the collisions between the blocks; the turbulence modelling; and the initial interdistance between the blocks. Therefore, it is necessary to test additional hypotheses by varying these parameters. For this reason, the analysis in the following sections will focus exclusively on series S1 and S2.

4.4.4.3 Hydrodynamic force analysis

The numerical model computes the pressure and velocity fields and the forces exerted on Antifer blocks by solitary waves. As mentioned before, when an Antifer block is impacted by a wave, several forces act on it, namely: (i) hydrodynamic forces, which includes the drag force (parallel to the flow direction, opposing block movement) and the lift force (perpendicular to the flow direction); (ii) hydrostatic force, due to water pressure on the block, acting perpendicular to its surface; (iii) gravitational force, due to the block's weight and divided into normal force ($N = W_{\perp}$) and downhill force ($W_{\parallel}$), driving the block downward; and (iv) frictional force (f), opposing the sliding motion, dependent on the normal force and the friction coefficient between the block and the slope.

When analysing the stability and movement of a block on a slope subjected to wave action, the balance of these forces is critical. The block remains stationary if the frictional force is equal to or greater than the downhill force. Movement occurs when the hydrodynamic force exceeds the resisting frictional force.

Fig.118 and Fig.119 illustrate the time series of the hydrodynamic force along the slope direction experienced by the blocks for series S1 and S2, using a coefficient of 0.50. The average force time series for the seven Antifer blocks are represented in red. Initially, the hydrostatic force, due to water pressure, differs slightly between S1 and S2 because of varying submersion levels. As the solitary wave reaches and passes over the blocks, a peak in the force signal is observed, particularly for larger waves. This peak corresponds to the moment when the wave's impact is at its maximum. The blocks move when this hydrodynamic force exceeds the frictional force, marked by a dashed line in the figures.

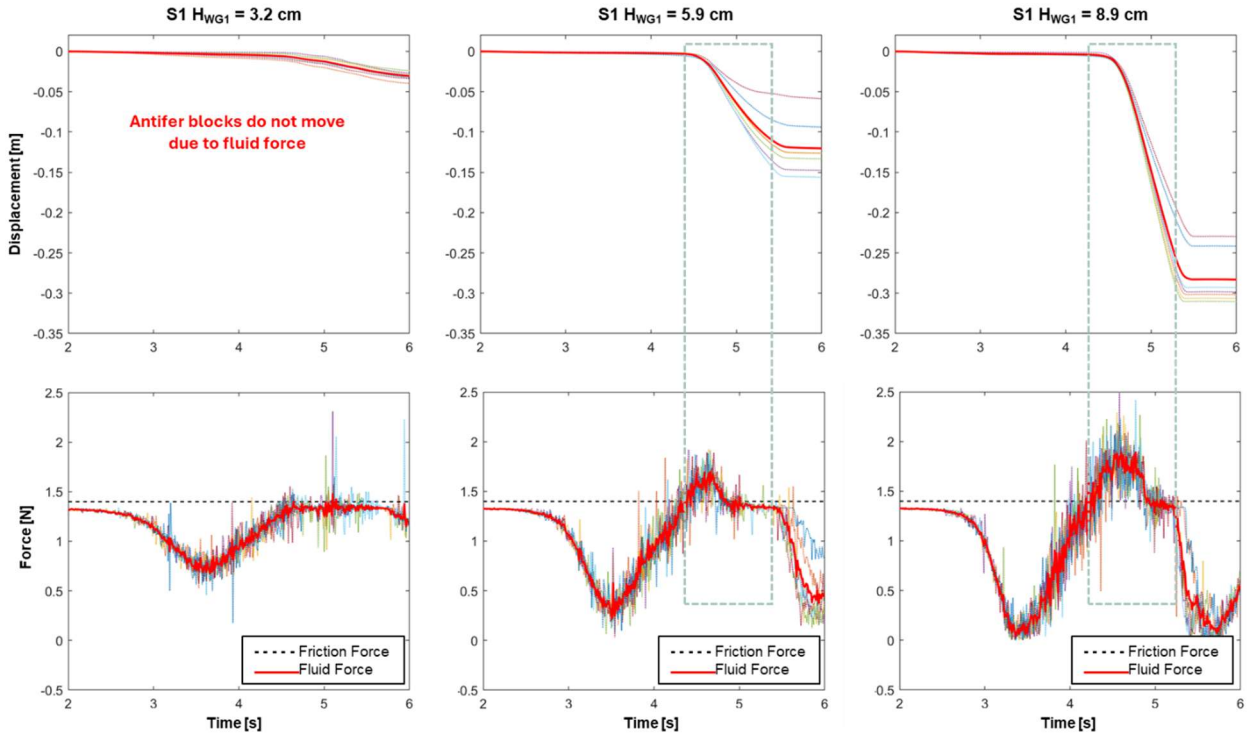

Fig.118 – Time series of the displacement and force exerted by the fluid onto the 7 Antifer blocks for the different wave conditions of series S1, considering a friction coefficient equal to 0.50.

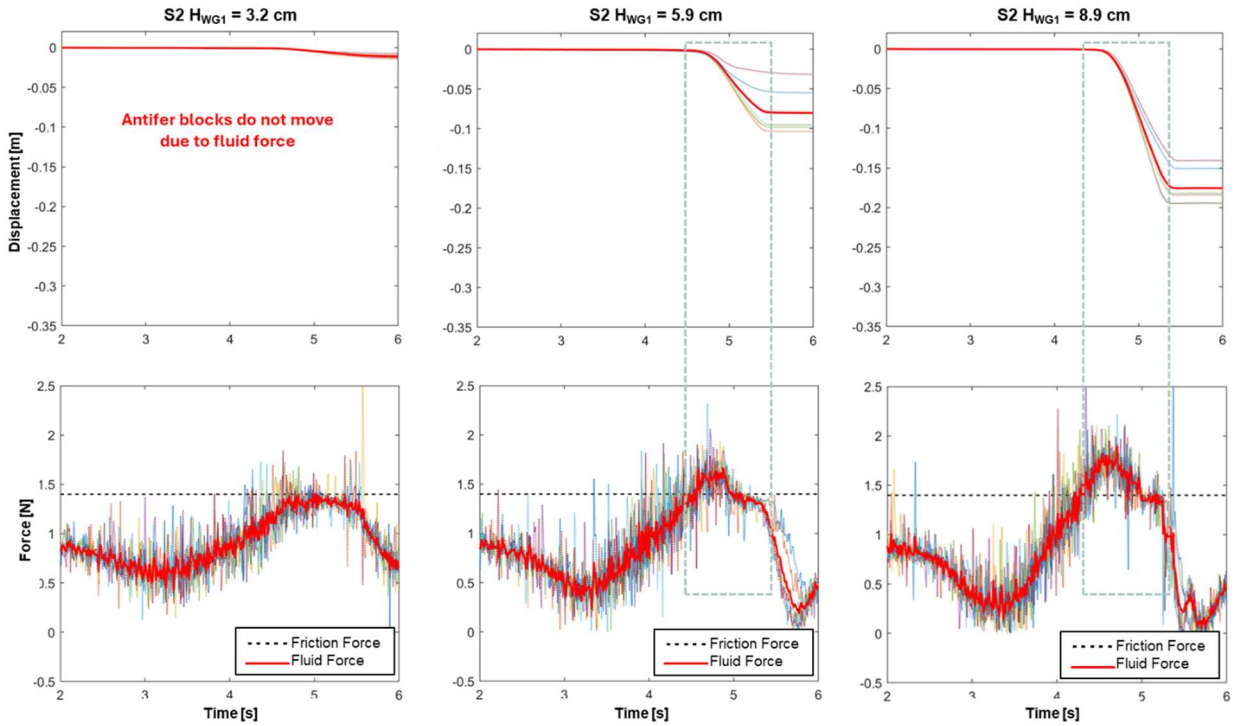

Fig.119 – Time series of the displacement and force exerted by the fluid onto the 7 Antifer blocks for the different wave conditions of series S2, considering a friction coefficient equal to 0.50.

Considering the series S1, where the blocks are initially not subjected to water pressure, the frictional force can be calculated using equation (111). Assuming a friction coefficient of 0.50, an angle (α) of 25.5º, a mass (m) of 0.316 kg, and gravitational acceleration (g) of 9.81 m/s², the resulting frictional force is 1.4 N.

After the initial impact and subsequent displacement of the blocks, there is a reduction in the hydrodynamic force acting on them. By examining these forces and their interactions, one can understand the conditions under which the blocks remain stable or start to move. This balance is crucial for evaluating the effectiveness and stability of the Antifer units under wave action.

4.4.4.4 Convergence and performance analysis

This section includes the convergence analysis that was performed to select the most suitable numerical resolution to obtain the results presented in the previous sections. All previous simulations use the initial interparticle distance of dp = 0.005 m, as indicated in section 4.4.3.4.. A complete convergence study includes the results of using different initial interparticle distances.

The convergence study will focus exclusively on series S2, considering the two largest wave heights. Based on the errors presented in Table 27, μ = 0.50 was selected for studies involving a wave height of 5.9 cm, and μ = 0.48 was chosen for studies involving a wave height of 8.9 cm.

Fig.120 and Fig.121 show the average displacement of the Antifer blocks, taking into account the various repetitions of the experimental work and the results of the numerical simulations for three different resolutions (dp = 0.0025, 0.005 and 0.01 m) used to discretise the Antifer blocks with 22, 11 and 5 particles per size, respectively (Table 30).

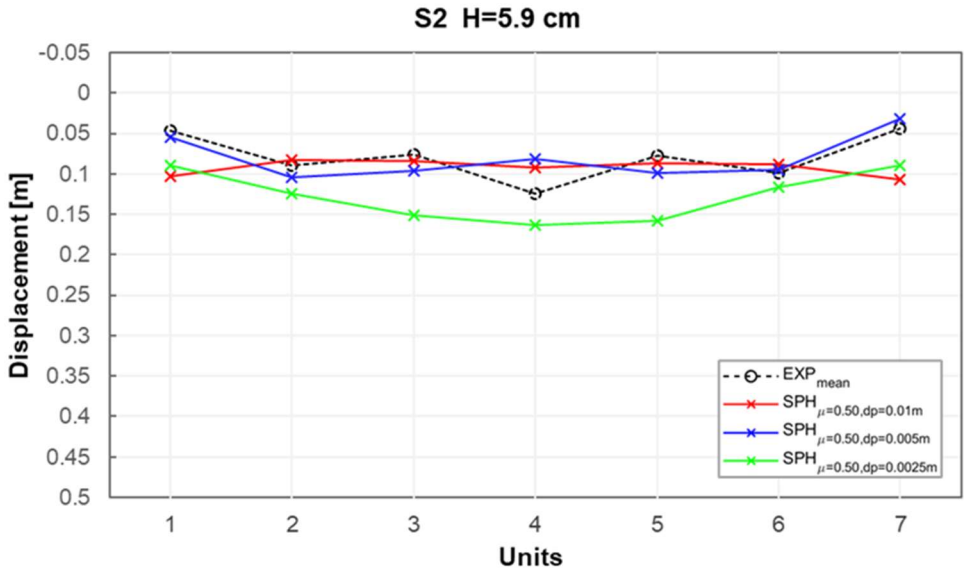

Fig.120 – Experimental and numerical displacements of the 7 Antifers for H_{WG1} = 5.9 of series S2, considering μ = 0.50 and three different resolutions (dp = 2.5, 5 and 10 mm).

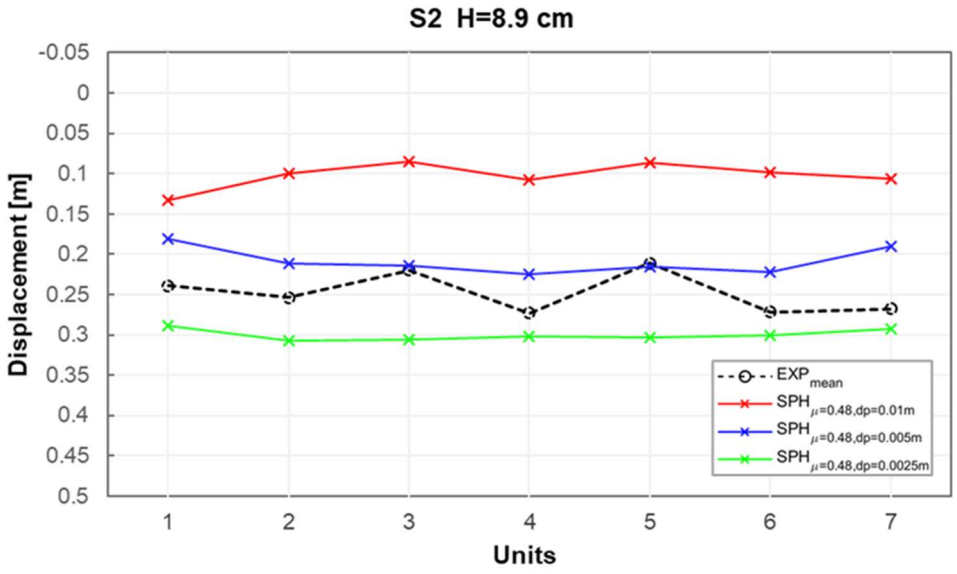

Fig.121 – Experimental and numerical displacements of the 7 Antifers for H_{WG1} = 8.9 cm of series S2, considering μ = 0.48 and three different resolutions (dp = 2.5, 5 and 10 mm).

For both scenarios, convergence is achieved using a dp of 0.005 m, with no significant improvements observed when employing a smaller interparticle distance but preventing the increase in the computational time.

Another crucial aspect in evaluating the capability of a numerical tool is its computational performance, as it is desirable for simulations to be executed within a reasonable computational time. Table 30 presents the runtimes of all previous convergence tests, which were conducted using an NVIDIA L40S GPU paired with an Intel i7-8700K CPU.

Table 30 – Initial particle spacing, number of particles and computational times and error comparing with experimental results using three different resolutions.

Configuration		dp	$\frac{H}{dp}$	Number of particles			Particles /Antifer size	Runtime		Error
				Total	Fluid	Floating		SPH + Chrono [h]	Chrono [min]	SPH vs EXP [%]
S2	H=5.9 cm	0.0025	24	54.162.894	47.827.640	64.953	22	128.57	91.9	59.3
		0.005	12	7.902.565	6.007.435	8.197	11	6.64	37.2	0.5
		0.01	6	1.237.249	758.037	980	5	0.76	20.6	15.4
	H=8.9 cm	0.0025	36	54.162.894	47.827.640	64.953	22	128.57	91.9	20.9
		0.005	18	7.902.565	6.007.435	8.197	11	6.64	37.2	-15.9
		0.01	9	1.237.249	758.037	980	5	0.76	20.6	-58.7

To determine the optimal numerical resolution, it is essential to achieve a good balance between accuracy and runtime. Based on the results presented in Table 30, simulations using a higher resolution, dp = 0.0025 m, take approximately 5 days to complete, whereas simulations with dp = 0.005 m are executed in just 6 hours. Moreover, for both wave heights, the most precise results are obtained with dp = 0.005 m. Therefore, dp = 0.005 m can be considered as a good compromise between accuracy and reasonable simulation runtimes.

As previously mentioned, DualSPHysics runs on a GPU card, while collision detection in the Project Chrono library operates on a single-core CPU. As shown in Table 30, increasing the resolution results in longer total simulation times due to the higher number of interactions and SPH particles that need to be processed with smaller time steps. However, the time spent on solving solid interactions does not increase significantly, as the number of colliding objects (and faces of the objects) that need to be handled by Chrono remains the same, independent of the SPH resolution. Therefore, special attention should be given when increasing the number of blocks to be simulated, as these factors significantly influence the runtime of the multiphysics library (Martínez-Estévez *et al.*, 2023).

4.4.4.5 Effect of changes on the friction coefficient

The numerical tool was rigorously validated through specific experiments, where the movements of the Antifer blocks were meticulously recorded. The actual geometry and properties (mass and friction coefficient) of the blocks and the slope were accurately incorporated into the simulations. The experimental campaign involved Antifer blocks made of aluminium and a slope made of acrylic, both coated with two layers of paint to impart some roughness.

For series S1 and S2, the friction coefficient between the blocks and the slope ranged between 0.48 and 0.50. This section explores variations in the friction coefficient to represent slopes of different materials or the effects of material deterioration over time or under cyclic loading, which inevitably alter surface properties and consequently the shear friction (Mitsui *et al.*, 2023; Taklas *et al.*, 2022). Specifically, the following values of the friction coefficient (μ) between the slope and the blocks were modelled: 0.1, 0.2, 0.3, 0.4, 0.5, 0.6, 0.7, 0.8, and 0.9.

The average displacement was calculated from the simulation results considering different coefficients of friction (μ), consistently using a dp of 0.005 m. All displacement values are plotted in Fig.122 for a comprehensive analysis.

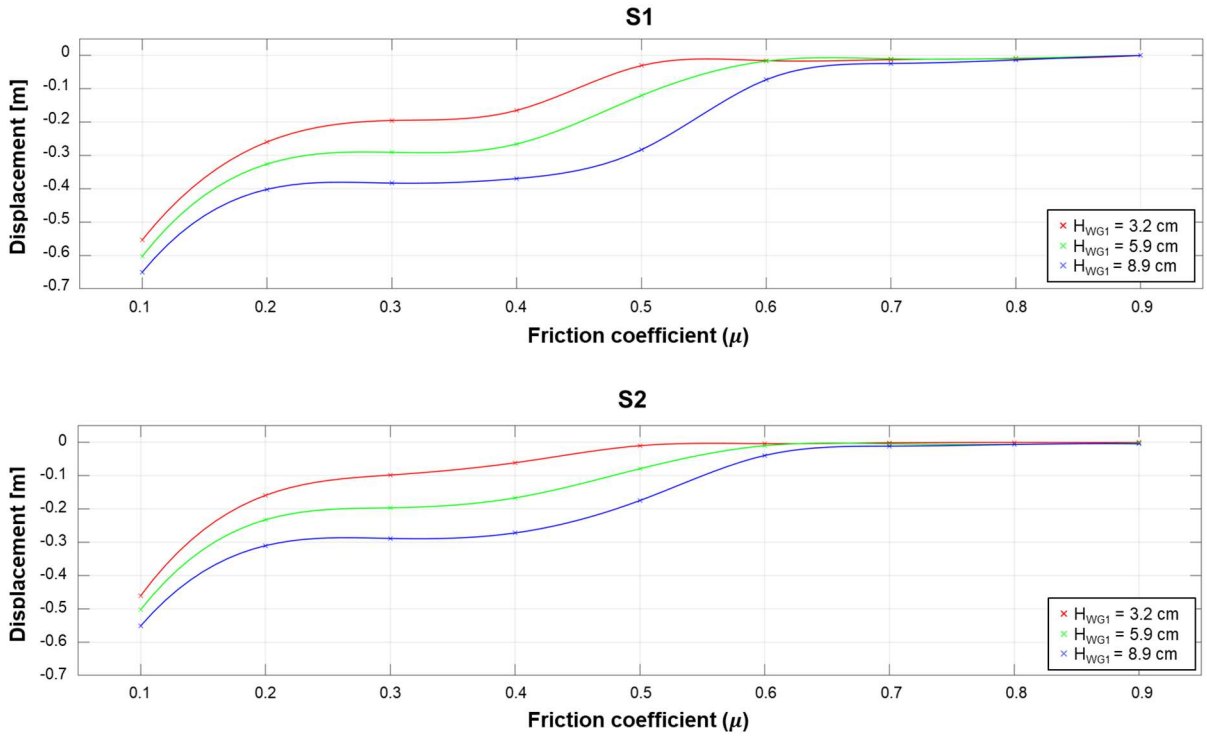

Fig.122 – Displacements for different friction coefficients between Antifers and slope, for series S1 (top) and S2 (bottom).

As expected, higher wave heights result in greater displacements for both series, S1 and S2. The simulations show that the minimum friction coefficient (0.1) leads to the highest displacements. Conversely, displacement decreases as the friction coefficient increases. Notably, for friction coefficients greater than 0.6, the Antifer blocks do not move at all for the first two solitary wave heights. Additionally, with H_{WG1} = 8.9 cm, displacements are less than 10 cm for friction coefficients exceeding 0.6. In conclusion, the results prove that the displacement of the units increases with wave height and decreases with the increments of the friction coefficient (*e.g.*, higher rugosity of the materials).

4.5 CONCLUSIONS

This chapter focused on studying the hydraulic and structural behaviour of rubble-mound breakwaters, employing a systematic approach that combined physical and numerical modelling techniques. The primary objective was to assess the critical performance aspects of breakwaters, including wave loadings, overtopping, and structural stability, using a combination of high-resolution experimental tests and advanced numerical simulations. A particular focus was placed on validating the DualSPHysics solver, coupled with Project Chrono, against high-quality experimental data to ensure accurate representation of complex fluid-structure interactions and block dynamics. The chapter also introduced innovative tools, such as the SmartAntifer block, to enhance experimental precision, thereby deeper insights into breakwater armour units' performance under different wave conditions. Organised into iterative phases, the study progressively refined methodologies, introduced innovations, and addressed challenges at each step while providing valuable recommendations to guide subsequent efforts.

The validation of the DualSPHysics solver, coupled with Project Chrono, confirmed its effectiveness in simulating complex fluid-structure interactions. The model showed promise in reproducing experimental results, with final block displacements falling within a well-defined range under various wave scenarios. First, a particle resolution was defined as an optimal compromise between computational accuracy and runtime efficiency. Additionally, coupling techniques and hardware optimisations effectively reduced simulation domain sizes, addressing computational challenges associated with large-scale 3D models. The numerical model's ability to simulate these interactions is essential for understanding the impact of hydraulic forces on breakwater stability and optimizing design approaches for coastal infrastructure.

The experimental tests conducted in a multidirectional wave basin offered valuable data on wave propagation, wave breaking, and block stability under regular and solitary wave conditions. These tests provided a clearer understanding of the impact of slope configuration, block arrangement, and wave height on block displacement, contributing to the improvement of numerical simulations. The experimental setup was simplified, particularly through the use of solitary waves, as they minimized complex wave interactions, such as reflections and re-reflections, enabling more direct comparisons between experimental and numerical results.

The integration of the SmartAntifer blocks further enhanced the experimental phase. These instrumented blocks, equipped with Inertial Measurement Units (IMUs), enabled precise measurements of block movements, rotations, and accelerations during the tests. The SmartAntifer blocks' standardised design, with consistent geometry, weight, and surface roughness, ensured improved experimental repeatability. This standardization eliminated inconsistencies typically associated with variations in block properties, providing more reliable experimental data to calibrate and validate the numerical models.

An iterative methodology was crucial to refining both experimental and numerical techniques. Each iteration led to improvements in accuracy, efficiency, and the reliability of results. Key findings include:

- **(i)** Data-driven validation: systematic and precise data collection and carefully controlled experimental setups were pivotal for validating numerical models and achieving meaningful comparisons;
- **(ii)** Technological integration: advances in numerical tools (*e.g.*, coupling techniques, mDBC) and experimental methods (*e.g.*, SmartAntifer blocks with IMUs) significantly improved the fidelity and scope of the research;
- **(iii)** Balance of accuracy and efficiency: numerical modelling efforts highlighted the trade-off between simulation accuracy and computational efficiency, necessitating careful parameter selection and hardware optimization.

These findings deepen the understanding of block stability and dynamics under complex hydrodynamic conditions. The integration of physical and numerical modelling provides valuable insights into wave loads, block interactions, and structural stability, improving the reliability of breakwater design and coastal infrastructure resilience.

This research lays the foundation for future studies, offering methodologies that can be further refined to enhance breakwater design accuracy. The integration of hybrid numerical approaches and continued standardization of experimental setups will be key to developing efficient, sustainable coastal protection systems that can withstand the challenges posed by climate change.

5
DISCUSSION AND CONCLUSIONS

5.1 INTRODUCTION

This chapter offers an in-depth discussion of the key findings, methodologies, and challenges encountered during the study of rubble-mound breakwaters. By integrating numerical and experimental approaches, the research initially aimed for a holistic perspective on breakwater performance, including overtopping, run-up, and overall structural stability. However, as the study progressed, the focus shifted to the hydraulic instability and damage of the breakwater trunk armour layer – a critical factor in structural failure. This evolution reflected the need to address specific gaps in the literature and respond to key questions about damage progression measurement and mitigation.

The following research questions were addressed:

- How are rubble-mound breakwaters made of artificial units designed to prevent destabilization?
- What physical phenomena contribute to hydraulic instability?
- Is damage often related to the hydraulic instability of the armour layer?
- How can damage progression in the armour layer be effectively measured?
- What are the current trends and areas of interest in assessing damage of rubble-mound breakwaters of artificial units?
- What kinds of loads do the artificial blocks in the armour layer experience, and can these loads be measured experimentally?
- What other methods are available for modelling the interactions between waves and structures, as well as inter-unit interactions?
- Is the SPH formulation, particularly the DualSPHysics solver, the most suitable method for simulations involving wave-breakwater interactions?
- How can one contribute to the development and validation of the model?
- What valuable insights can be obtained by using instrumented units for experimental testing that are not typically captured by standard experimental techniques?
- How can instrumented units generate novel datasets for calibrating DualSPHysics solver? Are the numerical results accurate and dependable?
- What kind of insights can be gained from fully replicated real breakwater interactions using these calibrated numerical models?
- Is this method computationally efficient and easily integrated as a tool for coastal engineers?

These questions were shaped by the gaps identified in the literature review and the practical challenges posed by the evolution of coastal environments and engineering needs.

Chapter 2 highlighted that rubble-mound breakwaters are exposed to increasingly severe environmental stresses due to climate change, sea-level rise, and evolving storm patterns. Damage in rubble-mound breakwaters is often linked to the hydraulic instability of the armour layer, where wave forces cause movements such as rocking, displacements, and settlements. These processes can lead to progressive reshaping of the armour layer, core exposure, and eventual structural failure. Despite the availability of empirical techniques and probabilistic approaches for assessing damage (*e.g.*, Van der Meer (1988b), Campos *et al.* (2020a)), a lack of standardised experimental methodologies and limitations in quantifying stochastic wave loading, critical factors like block-unit collisions and hydrodynamic pressures remain significant challenges. Accurately quantifying damage in rubble-mound breakwaters remains a significant challenge, with existing methods, such as visual assessments and volumetric reconstructions, presenting trade-offs between practicality, precision, and reproducibility. Advanced numerical tools such as Smoothed Particle Hydrodynamics (SPH) – and specifically DualSPHysics – have emerged as powerful alternatives for addressing these gaps. As reviewed extensively in Chapter 3, its meshless Lagrangian framework is particularly well-suited for modelling free-surface flows, large deformations, and intricate boundary conditions that characterize the hydrodynamics of rubble-mound breakwaters. Recent advancements and integration with Project Chrono for rigid body dynamics, have extended its capabilities to simulate the movement and interaction of individual armour units under wave action. This makes it an ideal solver for analysing hydrodynamic forces, unit displacement, and inter-unit collisions, which are critical for understanding the damage progression in breakwater structures. The need for robust validation of its results against high-quality experimental data remains paramount, and this study contributes to bridging that gap by integrating the numerical simulations with experimental findings using innovative tools such as the SmartAntifer blocks.

This chapter begins by interpreting the outcomes of the iterative methodological advancements across the research phases and discussing their implications for answering the research questions. It then examines the methodological challenges encountered, the contributions to knowledge and practice, and the broader implications for the field of coastal engineering. The discussion concludes with recommendations for future research and practical applications.

5.2 SYNTHESIS OF FINDINGS AND CRITICAL ANALYSIS OF METHODOLOGICAL CHALLENGES

Phase 1: Advancing numerical modelling with DualSPHysics

In Phase 1, DualSPHysics was employed to simulate the wave-structure interactions of rubble-mound breakwaters, leveraging experimental data from FEUP experiments under H2020-HydraLab+ and SE@PORTS projects.

The primary goal was to test the model's ability to simulate wave-by-wave overtopping, run-up and damage progression across a range of geometries and wave conditions. The DualSPHysics model was selected due to its demonstrated ability to accurately model complex hydrodynamic phenomena such as wave breaking (Farahani and Dalrymple, 2014), wave overtopping (Shao *et al.*, 2006), wave run-up (Shadloo *et al.*, 2016), and wave impact (Altomare *et al.*, 2014). Additionally, the prior experience with the software and the familiarity with its capabilities and limitations further motivated the choice of DualSPHysics for this work. This phase of the research work was important for: i) reviewing the software's capabilities, ii) establishing the parameters to consider for achieving the best results and computational performance, and iii) identifying areas of interest for further development and validation.

First results highlighted the model's capacity to simulate complex hydrodynamic phenomena such as wave breaking, overtopping, and wave impact. However, challenges emerged related to computational cost, particularly in large-scale 3D simulations. The precision limitations observed during these early stages underscored the importance of balancing particle resolution (*dp*), hardware capabilities (*e.g.*, GPU memory) and simulation duration to achieve computational efficiency.

Key insights from this phase included:

- the adoption of coupling techniques reduces simulation domain sizes and number of particles, enabling more feasible computations;
- the use of Project Chrono for improved collision resolution is instrumental in achieving qualitative analysis about wave-structure interactions but requires more systematic experimental data for robust validation.

This phase contributed to answering the question of how numerical models can be used to assess wave-induced damage in breakwaters, particularly regarding the feasibility of modelling complex breakwater geometries at different scales. Recommendations emerging from phase 1 emphasized the need to ensure the reliability, repeatability and reproducibility of the experimental tests to foster favourable numerical outcomes. It included simplifying simulation domains (use of wave conditions of smaller order) and refinements in input parameters, including precise data collection (*e.g.*, wave probe placement, water surface elevations, and friction coefficients).

Phase 2: Experimental validation with Antifer blocks

Phase 2 involved laboratory-scale experiments on smooth and rough slopes armoured with Antifer blocks, designed for comparison purposes when testing the stability of Antifer blocks using numerical model tools. The choice of Antifer blocks was motivated by their previous application in the SE@PORTS project, where they were extensively tested. Since these blocks were already available in the laboratory, they provided a practical and well-documented choice for this study.

One recurring challenge in breakwater research is balancing experimental simplicity with the need to replicate realistic field conditions. While studies, such as Mitsui *et al.* (2023), also tested the movement of armour units using DualSPHysics, they typically employed simplified setups, such as block configurations in horizontal planes and solitary wave conditions. These configurations limit the ability to replicate the dynamic and cumulative effects seen in real-world conditions. In contrast, this research introduced a more realistic and complex experimental setup by placing Antifer blocks on a slope and subjecting them to repetitive wave action through regular wave conditions. This allowed for a more accurate simulation of the sustained hydrodynamic forces that would be encountered in the field, enabling a better assessment of wave-structure interactions over time, while solitary wave setups are generally suited for one-off impacts and not sustained interactions.

The main objective of this phase was to test DualSPHysics' capability to simulate fluid-structure and inter-block interactions. Key elements of the numerical modelling included:

- Mimicking experimental wave conditions in the numerical tank;
- Determining the minimum resolution required for accuracy;
- Implementing modified Dynamic Boundary Conditions (mDBC) (English *et al.*, 2022) and updated density diffusion terms (Fourtakas *et al.*, 2019);
- Defining Antifer block geometries for Project Chrono's collision detection algorithm (Canelas *et al.*, 2018; Mitsui *et al.*, 2023).

The most challenging aspects were accurately replicating the wave conditions due to reflections in the laboratory wave tank and defining Antifer block geometries for collision detection. The high wave reflections made it difficult to perfectly simulate the incident wave characteristics in the numerical tank, emphasizing the importance of precise modelling of the experimental setup.

Despite these challenges, the results showed good agreement between the experimental and numerical data, with block displacements exhibiting a comparable order of magnitude in movement. This confirmed DualSPHysics' potential for simulating block movements under dynamic wave conditions, though some discrepancies remained.

The key achievements of this phase included:

- Laboratory experiments provided insights into wave propagation and breaking processes over smooth and rough slopes, with one or more rows of Antifer blocks used to mimic realistic conditions. Phase 1 recommendations were followed, such as strategic wave gauge placement and systematic data recording, which ensured repeatability. The results highlighted the impact of slope configuration, block arrangement, and wave height on block stability, providing valuable data for numerical model validation;
- Numerical simulations benefitted from the introduction of mDBC and density diffusion terms, which improved wave surface representation, while Project Chrono enhanced block interaction modelling;
- Agreement between experimental and numerical data was observed, although discrepancies in wave reflections and variations in wave heights persisted. The displacements recorded in the numerical simulation were much more regular than in the experimental campaign. These differences underscored the challenges of perfectly matching physical and numerical setups.

This phase addressed the question of how experimental methods can be integrated with numerical simulations to enhance the understanding of block displacement and breakwater stability, particularly regarding wave-induced forces on individual armour units. To refine future studies, recommendations included:

(i) integrating instrumented Antifer blocks with IMUs for precise displacement tracking;
(ii) replacing regular waves with solitary waves to minimize reflection effects and simplify the analysis, and
(iii) carefully controlling wave generation, experimental setups, and instrumentation placement to ensure reproducibility.

Phase 3: SmartAntifer integration and numerical model validation

Although the results of phase 2 demonstrated DualSPHysics' ability to reproduce the movement of individual blocks and their interaction, further simplification of the scenario and a more appropriate selection of parameters were necessary to ensure repeatability, reproducibility, and accuracy of numerical results when compared to experimental data. Building on the insights from phases 1 and 2, phase 3 focused on the validation of a 3D numerical model using data from an experimental campaign, which setup was constituted by a smooth slope with a unique raw of Antifers, initially not in touch, and exposed to solitary waves only.

To further enhance the quality and increase the quantity of the data usually gathered during standard experimental campaigns, the centrepiece of this phase was the development of the SmartAntifer, an IoT-enabled Antifer block equipped with Inertial Measurement Units (IMUs) designed to track movements

and forces during experimental tests. The development of the SmartAntifer instrumented block adhered to the recommendations outlined in subsection 2.2.3.1. Compared to instrumented blocks used in previous studies, the SmartAntifer offers several key advantages. First, the blocks are fully wireless, following the concept previously introduced by block designs presented by other authors such *Gronz et al.* (2016), Hofland *et al.* (2018), and Santos *et al.* (2019), unlike the wired designs employed by authors like Arefin (2017), which constrain the block's degrees of freedom. This wireless design ensures greater freedom of movement, allowing for more accurate simulation of real-world conditions. Additionally, the SmartAntifer features an extended battery life and an innovative charging system, eliminating the need to open the block for data retrieval or recharging. This not only enhances durability but also simplifies operational workflows. Furthermore, compared to other studies with a similar goal - measure, record, process, and transmit data related to the 3D displacements of an armour unit in a laboratory context (*e.g.*, Gronz *et al.* (2016); Santos *et al.* (2019)) – the SmartAntifer boasts a significantly higher data acquisition frequency, ensuring more detailed and reliable movement tracking.

These advancements make the SmartAntifer a cutting-edge tool for analysing block dynamics under different wave conditions, offering standardized and precise measurement capabilities. The development and deployment of this device addressed several practical challenges, bridging gaps between numerical and experimental approaches. The data obtained aimed to be used to analyse forces acting on individual armour units, final displacement of breakwater armour units, and impact velocity of rocking Antifer blocks. However, during its implementation, practical challenges were encountered, including:

- Waterproofing issues, which led to water ingress in some blocks, compromising their electronic components, necessitating enhanced sealing techniques;
- Misalignments between sensor axes and block coordinate systems, which impacted data reliability, emphasizing the need for precise calibration during setup;
- Errors defining motion periods, and inaccuracies during manual identification of stationary states;
- Integration drift, caused by errors accumulated during double integration of accelerometer data, a known limitation of IMU-based systems, underscored the importance of advanced filtering and sensor fusion methods;
- Rounding or quantization errors that propagate and amplify during integration due to IMUs collection data at discrete intervals and with finite resolution.

Even when stationary, two identical IMUs may produce different acceleration magnitudes due to factors such as manufacturing tolerances, calibration differences, and environmental influences. Misalignments between sensor axes and block coordinate systems can further amplify these discrepancies, emphasizing the need for precise calibration and alignment. Additionally, inherent noise, temperature effects, and gravitational variations at different locations contribute to measurement variability. Techniques such as averaging readings, correcting for temperature-dependent drifts, and ensuring consistent placement during experiments are essential to minimize these inconsistencies.

These errors contribute for the discrepancies noticed in the linear motion dynamics of the blocks when compared to the results obtained through image processing. Strategies such as applying Kalman filters, leveraging external reference systems (*e.g.*, GPS or optical tracking), regular calibration processes, and automated methods to reduce errors, avoiding manual adjustments, were identified as critical for improving measurement accuracy.

Despite these challenges, the SmartAntifer blocks contributed indirectly by ensuring better experimental repeatability. Their uniform weight, geometry, and surface roughness met laboratory-specific requirements, ensuring compatibility with existing setups while maintaining physical properties akin to conventional Antifer blocks. This improved consistency reduced variability in experimental setups, indirectly enhancing numerical model simulations and facilitating more accurate comparisons between results. Numerical simulations, supported by advanced GPUs, were validated by experimental findings, comparing block displacements, water surface elevations, and fluid forces. These comparisons yielded the following outcomes:

- Reasonable agreement between DualSPHysics and experimental wave conditions was achieved, proving the validity of the 3D analysis with a reduced domain using inlet/outlet open boundary conditions (Domínguez et al., 2022);
- In physical modelling, variations in friction coefficients due to material properties, surface conditions, environmental factors, and experimental design were identified as critical parameters affecting block displacement and tests repeatability. Numerical simulations reflected these effects, providing a range of plausible outcomes consistent with experimental variability;
- Consequently, despite improvements in the alignment of numerical simulations and physical test results, discrepancies in block displacements persisted, moving the numerical blocks less than the experimental blocks for all the three waves considered;
- The numerical results underscored the importance of optimising numerical resolution (*e.g.*, dp = 0.005 m) to balance accuracy and runtime.

This phase contributed to answering the questions of how to enhance the accuracy of numerical simulations through experimental data and how instrumented blocks can provide novel insights into the dynamic behaviour of breakwater armour units.

5.3 CONTRIBUTIONS TO KNOWLEDGE AND PRACTICE

This research significantly advances the field of coastal engineering by:

(i) Bridging experimental and numerical approaches

This iterative process demonstrated that numerical and physical modelling are not standalone solutions but are interdependent. Numerical models rely on experimental validation to ensure their accuracy and realism, while physical tests benefit from numerical insights to refine their focus and interpret their outcomes. Together, these approaches provide a comprehensive toolkit for addressing the dynamic challenges of modern coastal engineering, including adapting to changing wave patterns, intensifying storm conditions, and achieving sustainability goals. This synergy not only enhances the accuracy of breakwater predictions but also aids in the optimization of coastal defence designs. The combined use of these methods ensures that engineers can accurately assess breakwaters resilience and make informed decisions about their performance under varying environmental conditions.

(ii) Enhancing numerical modelling with DualSPHysics

A major contribution of this study is the enhanced application of DualSPHysics for simulating wave-structure interactions. The model was successfully validated with detailed experimental data, providing new insights into armour unit dynamics and hydrodynamic forces. Key methodological advancements include:

- The refinement of boundary conditions and particle resolution, optimizing the balance between computational efficiency and model accuracy;
- The ability to simulate complex, non-linear wave-structure interactions that are challenging to measure physically, establishing DualSPHysics as a reliable tool for breakwater design.

These contributions make DualSPHysics a more robust and versatile tool for understanding breakwater behaviour, providing a scalable and cost-effective complement to physical testing.

(iii) Innovation in experimental instrumentation: SmartAntifer blocks

The development and deployment of SmartAntifer blocks equipped with IMUs represent a groundbreaking advancement in experimental instrumentation. These blocks enable precise measurement of 3D displacements, rotations, and accelerations. Unlike previous designs, the SmartAntifer's wireless capability, extended battery life, and high data acquisition frequency make it an ideal tool for capturing detailed block movements and improving model calibration. This innovation not only enhances the accuracy of experimental results but also contributes to better experimental repeatability by maintaining consistent physical properties (*e.g.*, geometry, weight, surface roughness) across all blocks. The SmartAntifer blocks allow for long-term assessments of breakwaters resilience under various wave conditions, offering a valuable dataset for future numerical model validation.

(iv) Linking to broader themes

This study aligns with broader themes in coastal engineering and contributes to global sustainability goals by addressing the need for climate-resilient breakwaters. By advancing both experimental techniques and numerical modelling, this research supports the design of breakwaters capable of withstanding increasingly severe environmental conditions.

Overall, this research provides practical tools to improve coastal engineering practices, offering more efficient and cost-effective methods for designing resilient infrastructure that can withstand intensifying wave conditions due to climate change.

5.4 FUTURE DEVELOPMENTS AND RECOMMENDATIONS

Throughout this research, significant progress has been made in understanding wave-induced forces and breakwater performance using experimental and numerical approaches. However, several research areas remain open for further investigation to refine methodologies, validate numerical models, and enable their practical application in real-world scenarios. The following topics outline key areas of intervention and future directions to enhance breakwater design and analysis:

(i) Enhanced realism and high-quality experimental data

High-quality physical experiments are essential for validating numerical models and understanding breakwater performance under more realistic conditions. Future studies must prioritize conducting physical experiments that replicate more realistic conditions, particularly focusing on instrumented units like the SmartAntifer blocks. Physical experiments should reproduce sections of rubble-mound breakwaters under controlled conditions, with instrumented SmartAntifer blocks strategically placed in critical zones, such as the toe berm and within the armour layer. These tests will provide detailed measurements of block displacement, rotation, and hydrodynamic forces, enabling direct comparisons with numerical simulations. This targeted approach will also help identify areas of intense unit-to-unit interactions, offering insights into damage progression and structural vulnerabilities.

To ensure greater consistency and comparability across studies, standardized experimental protocols should be developed. This includes consistent wave generation techniques, damage assessment methods, and measurement procedures. Standardization will allow for more effective collaboration across research teams and enhance the applicability of findings to real-world engineering challenges.

(ii) SmartAntifer technology refinement and broader applications

Advancements in SmartAntifer technology are essential to improve data acquisition capabilities. Future work should focus on enhancing the wireless transmission system for real-time monitoring, establishing effective calibration methods, and refining signal processing techniques to ensure precise measurements of displacement and rotation. These improvements will make SmartAntifer units more reliable for both laboratory and field applications.

Expanding the use of SmartAntifer units' technology, whether through its implementation in other types of armour units or its application to other coastal structures such as seawalls, groynes, and artificial reefs, will provide valuable insights into their performance under diverse environmental conditions. Moreover, integrating SmartAntifer units into field-scale experiments will facilitate the transition from laboratory-based studies to real-world coastal protection scenarios, enabling long-term monitoring of infrastructure under dynamic wave conditions.

(iii) Refinement and expansion of numerical models:

Refining numerical models to improve accuracy, efficiency, and realism is another key area for future research. The DualSPHysics framework should be further developed to improve both its accuracy and computational efficiency. Current limitations in fully replicating three-dimensional simulations of breakwaters damage progression laboratory campaigns should be addressed by focusing on modelling critical sections of the breakwater, where the effects of armour units' interactions are most pronounced.

Additionally, numerical models should be used iteratively to identify areas with intense unit-to-unit interactions, guiding the placement of instrumented blocks in future experimental tests. This targeted approach will improve our ability to predict damage patterns and structural vulnerabilities, while also providing a direct link between experimental results and numerical simulations.

The modelling of block interactions can be further refined by investigating the effects of different friction coefficients, accounting for material properties, slope porosity and environmental conditions. To address computational inefficiencies, hybrid methods that combine GPU and CPU resources should be explored. These methods will enable more detailed and practical large-scale simulations, which are critical for coastal engineers.

Finally, refining numerical models based on experimental findings will improve the accuracy of loading assessments in the armour layer and toe berm. This enhancement will make the DualSPHysics framework a more reliable tool for design optimization and sensitivity analyses, strengthening its position in breakwater design research.

(iv) Addressing climate change and realistic scenarios

Future research must also address the challenges posed by climate change, particularly the impact of rising sea levels and increased storm intensity. To assess structural responses and identify vulnerabilities under these evolving conditions, numerical and experimental models must simulate climate-driven scenarios, including more extreme wave conditions, storm surges, and complex wave patterns. These simulations will provide critical insights into the future performance of breakwater structures and inform design strategies to improve their durability. Moreover, additional physical

studies are needed to assess overtopping and wave run-up, which will further inform the development of more robust coastal defence strategies.

(v) Development of new design formulas

The strategic placement of instrumented SmartAntifer blocks on the toe berm and other critical zones will provide essential data for developing new damage formulas, particularly for under-researched areas. The response of toe berm, a key component in breakwater stability, remains poorly understood, and targeted research here will improve existing empirical models for breakwater design. Future work should also focus on revising design frameworks based on experimental and numerical findings. This includes evaluating existing empirical formulas and proposing improvements to reflect new insights into the behaviour of breakwaters.

By addressing these future developments, research will align experimental and numerical methodologies more closely, fostering the creation of accurate and efficient tools for sustainable coastal engineering. Additionally, to the detailed future developments outlined above, the following key recommendations summarize the main priorities from this research:

- Start with simplified systems in both physical and numerical modelling and progressively increasing complexity;
- Prioritize the integration of instrumented units to enhance data accuracy and numerical model validation;
- Standardize experimental protocols to ensure reproducibility and comparability across studies;
- Optimize numerical simulations for accuracy and efficiency, balancing resolution and computational cost;
- Focus research on critical structural components, such as the toe berm, to develop improved damage and stability formulas;
- Incorporate climate change scenarios, flow through porous media and turbulence into breakwater design and analysis methodologies;
- Foster interdisciplinary collaboration between experimentalists, model developers, and engineers to align research outcomes with real-world applications.

5.5 FINAL REMARKS

This thesis represents a significant step forward in the study of rubble-mound breakwaters by integrating advanced experimental and numerical approaches to tackle the challenges of hydraulic instability and damage progression. Through the application of innovative tools such as the SmartAntifer blocks and the DualSPHysics framework, this work has provided new insights into the complex interactions between wave forces, breakwater stability, and armour unit dynamics.

The research has underscored the importance of combining physical and numerical modelling to achieve a more comprehensive understanding of coastal structures. By bridging these methodologies, the study not only validated the potential of numerical simulations to replicate real-world conditions but also highlighted the role of experimental data in refining these models for enhanced accuracy and reliability. These contributions mark a critical advancement in the iterative development of breakwater design methodologies.

Beyond its technical achievements, this thesis aligns with broader objectives in coastal engineering, including the need for sustainable and climate-resilient infrastructure. As coastal regions face increasingly severe environmental pressures, the findings of this research provide actionable insights for designing structures that are more adaptive to evolving wave patterns and storm intensities.

Despite the challenges encountered – ranging from computational constraints to experimental complexities – this work has laid a solid foundation for future developments in the field. It has not only demonstrated the potential of cutting-edge technologies to address long-standing engineering problems but also emphasized the need for continued interdisciplinary collaboration to push the boundaries of innovation.

In conclusion, this thesis contributes to advancing the knowledge, tools, and methodologies necessary for addressing contemporary coastal engineering challenges. It paves the way for future research and development, supporting the creation of resilient, efficient, and sustainable coastal protection systems that safeguard communities and ecosystems for generations to come.

REFERENCES

ABANADES, J.; GÓMEZ, R.; CASTILLO, C.; MOLINA, R. (2011) - *Revisión Histórica de Las Variables y Modelos de Evolución de Daño En Diques En Talud y Su Adecuación Al Estudio Del Fenómeno*. In XI Jornadas Españolas de Costas y Puertos. Las Palmas, Spain: 2011.

ADAMI, S.; HU, X.; ADAMS, N. (2012) - *A generalized wall boundary condition for smoothed particle hydrodynamics.* Journal of Computational Physics. 231:21. 7057-7075.

AKARSH, P.; CHAUDHARY, B. (2022) - *Review of Literature on Design of Rubble Mound Breakwaters*.

ALTOMARE, C.; CRESPO, A.; DOMÍNGUEZ, J.; GÓMEZ-GESTEIRA, M.; SUZUKI, T.; VERWAEST, T. (2015a) - *Applicability of Smoothed Particle Hydrodynamics for estimation of sea wave impact on coastal structures.* Coastal Engineering. 96: 1-12.

ALTOMARE, C.; CRESPO, A. J. C.; ROGERS, B. D.; DOMINGUEZ, J. M.; GIRONELLA, X.; GÓMEZ-GESTEIRA, M. (2014) - *Numerical modelling of armour block sea breakwater with smoothed particle hydrodynamics.* Computers & Structures. 130: 34-45.

ALTOMARE, C.; DOMÍNGUEZ, J.; CRESPO, A.; GONZÁLEZ-CAO, J.; SUZUKI, T.; GÓMEZ-GESTEIRA, M.; TROCH, P. (2017) - *Long-crested wave generation and absorption for SPH-based DualSPHysics model.* Coastal Engineering. 127: 37-54.

ALTOMARE, C.; DOMÍNGUEZ, J.; CRESPO, A.; SUZUKI, T.; CACERES, I.; GÓMEZ-GESTEIRA, M. (2015b) - *Hybridization of the wave propagation model SWASH and the meshfree particle method SPH for real coastal applications.* Coastal Engineering Journal. 57:4. 1550024-1-1550024-34.

ALTOMARE, C.; GIRONELLA, X.; CRESPO, A. (2021) - *Simulation of random wave overtopping by a WCSPH model.* Applied Ocean Research. 116: 102888.

ALTOMARE, C.; TAFUNI, A.; DOMÍNGUEZ, J.; CRESPO, A.; GIRONELLA, X.; SOSPEDRA, J. (2020) - *SPH simulations of real sea waves impacting a large-scale structure.* Journal of Marine Science and Engineering. 8:10. 826.

ALTOMARE, C.; TAGLIAFIERRO, B.; DOMINGUEZ, J.; SUZUKI, T.; VICCIONE, G. (2018) - *Improved relaxation zone method in SPH-based model for coastal engineering applications.* Applied Ocean Research. 81: 15-33.

ANTUONO, M.; COLAGROSSI, A.; MARRONE, S.; MOLTENI, D. (2010) - *Free-surface flows solved by means of SPH schemes with numerical diffusive terms.* Computer Physics Communications. 181:3. 532-549.

AREFIN, S. (2017) - *Measurement on Rocking of cubes in a Double Layer on a Breakwater: Rocking revisited II*. Delft, The Netherlands: Delft University of Technology.

BARTHEL, V.; MANSARD, E.; SAND, S.; VIS, F. (1983) - *Group bounded long waves in physical models.* Ocean Engineering. 10:4. 261-294.

BATCHELOR, G. (1974) - *An introduction to fluid dynamics*. Cambridge university press.

BIESEL, F.; SUQUET, F. (1951) - *Etude théorique d'un type d'appareil à houle.* La Houille Blanche. 6:2. 152-165.

BRODERICK, L.; AHRENS, J. (1982) - *Riprap stability scale effects.*

BSI (1991) - Part 7: Guide to the design and construction of breakwater. BS 6349-7:1991. In Maritime Structures. London: British Standards Institution

BURCHARTH, H. F; LIU, Z. (1992) - *Design of Dolos armour units*. Venice, Italy, 1992.

BURCHARTH, H. F.; LIU, Z. (1995) - *The Application of Load-cell Technique in the Study of Armour Unit Responses to Impact Loads Tests*. Sorrento, Italy, November 1995, 1995.

CALDERA, G. (2019) - *Rocking of single layer armour units: Rocking revisited III*. Delft, The Netherlands: Delft University of Technology.

CALHEIROS-CABRAL, T.; CLEMENTE, D.; ROSA-SANTOS, P.; TAVEIRA-PINTO, F.; RAMOS, V.; MORAIS, T.; CESTARO, H. (2020) - *Evaluation of the annual electricity production of a hybrid breakwater-integrated wave energy converter.* Energy. 213: 118845.

CAMPBELL, P. (1989) - *Some new algorithms for boundary value problems in smooth particle hydrodynamics*

CAMPOS, A. (2014) - *A methodology for the analysis of damage progression in rubble mound breakwaters*. ETSI de Caminos, Canales y Puertos de Ciudad Real, Universidad de Castilla-La Mancha.

CAMPOS, A.; CASTILLO, C.; MOLINA-SANCHEZ, R. (2020a) - *Damage in Rubble Mound Breakwaters. Part I: Historical Review of Damage Models.* Journal of Marine Science and Engineering. Vol. 8:5. 317.

CAMPOS, A.; MOLINA-SANCHEZ, R.; CASTILLO, C. (2020b) - *Damage in Rubble Mound Breakwaters. Part II: Review of the Definition, Parameterization, and Measurement of Damage.* 8:5. 306.

CANELAS, R.; BRITO, M.; FEAL, O.; DOMÍNGUEZ, J.; CRESPO, A. (2018) - *Extending DualSPHysics with a differential variational inequality: modeling fluid-mechanism interaction.* Applied Ocean Research. 76: 88-97.

CANELAS, R.; DOMÍNGUEZ, J.; CRESPO, A.; GÓMEZ-GESTEIRA, M.; FERREIRA, R. (2015) - *A Smooth Particle Hydrodynamics discretization for the modelling of free surface flows and rigid body dynamics.* International Journal for Numerical Methods in Fluids. 78:9. 581-593.

CASTILLO, C.; CASTILLO, E.; FERNÁNDEZ-CANTELI, A.; MOLINA, R.; GÓMEZ, R. (2012) - *Stochastic model for damage accumulation in rubble-mound breakwaters based on compatibility conditions and the central limit theorem.* Journal of Waterway, Port, Coastal, Ocean Engineering. 138:6. 451-463.

CEM (2006) - *Coastal Engineering Manual: Overview And Coastal Hydrodynamics*. Washington DC, USA: U.S. Army Corps of Engineers.

CHA, S.; WHITWORTH, A. (2003) - *Implementations and tests of Godunov-type particle hydrodynamics.* Monthly Notices of the Royal Astronomical Society. 340:1. 73-90.

CHEGINI, V.; AGHTOUMAN, P. (2006) - *An investigation on the stability of rubble mound breakwaters with armour layers of antifer cubes.* Journal Of Marine Engineering. Vol. 2:1. 86-93.

CIRIA; CUR; CETMEF (2007) - *The Rock Manual. The use of rock in hydraulic engineering (second edition) (C683)*. CIRIA, CUR, CETMEF.

CLAMOND, D.; GERMAIN, J. (1999) - *Interaction between a Stokes wave packet and a solitary wave.* European Journal of Mechanics-B/Fluids. 18:1. 67-91.

CLEARY, P.; PRAKASH, M.; HA, J.; STOKES, N.; SCOTT, C. (2007) - *Smooth particle hydrodynamics: status and future potential.* Progress in Computational Fluid Dynamics, an International Journal. 7:2-4. 70-90.

CLEMENTE, D.; CALHEIROS-CABRAL, Tomás; ROSA-SANTOS, P.; TAVEIRA-PINTO, F. (2021) - *Hydraulic and Structural Assessment of a Rubble-Mound Breakwater with a Hybrid Wave Energy Converter.* Journal of Marine Science and Engineering 9:9. 922.

COLAGROSSI, A.; ANTUONO, M.; SOUTO-IGLESIAS, A.; LE TOUZÉ, D. (2011) - *Theoretical analysis and numerical verification of the consistency of viscous smoothed-particle-hydrodynamics formulations in simulating free-surface flows.* Physical Review E. 84:2. 026705.

COLAGROSSI, A.; LANDRINI, M. (2003) - *Numerical simulation of interfacial flows by smoothed particle hydrodynamics.* Journal of computational physics. 191:2. 448-475.

CRESPO, A.; ALTOMARE, C.; DOMÍNGUEZ, J.; GONZÁLEZ-CAO, J.; GÓMEZ-GESTEIRA, M. (2017) - *Towards simulating floating offshore oscillating water column converters with smoothed particle hydrodynamics.* Coastal Engineering. 126: 11-26.

CRESPO, A.; DOMÍNGUEZ, J.; ROGERS, B.; GÓMEZ-GESTEIRA, M.; LONGSHAW, S.; CANELAS, R.; VACONDIO, R.; BARREIRO, A.; GARCÍA-FEAL, O. (2015) - *DualSPHysics: Open-source parallel CFD solver based on Smoothed Particle Hydrodynamics (SPH).* Computer Physics Communications. 187: 204-216.

CRESPO, A.; GÓMEZ-GESTEIRA, M.; DALRYMPLE, R. (2007) - *Boundary conditions generated by dynamic particles in SPH methods.* Computers, materials and continua. 5:3. 173-184.

CUMMINS, S.; RUDMAN, M. (1999) - *An SPH projection method.* Journal of computational physics. 152:2. 584-607.

CUR (1989) - *Golfbrekers. Sterkte Betonnen Afdekelementen. Integratie van Fasen 1-3. Verslag werkgroep 1.* Civiel Centrum Uitvoering Research en Regelgeving. In Dutch.

--- (1990) - *Golfbrekers. Sterkte Betonnen Afdekelementen. Samenvatting onderzoek. Verslag werkgroep 1.* Civiel Centrum Uitvoering Research en Regelgeving. In Dutch.

DALRYMPLE, R.; ROGERS, B. (2006) - *Numerical modeling of water waves with the SPH method.* Coastal engineering. 53:2-3. 141-147.

DAVIES, M. H.; MANSARD, E. ; CORNETT, A. (1994) - *Damage analysis for rubble-mound breakwaters*. Kobe, Japan, 1994.

DE ALMEIDA, E.; VAN GENT, M. R. A.; HOFLAND, B. (2019) - *Damage characterization of rock slopes.* Journal of Marine Science Engineering. 7:1. 10.

DE JONG, T. J. (1996) - *Stability of Tetrapods at Front Crest and Rear of a Low-Crested Breakwater.* Delft Hydraulics Publication.453.

DE SMET, L. (2016) - *Excel-based design tool for the assessment of rubble-mound and caisson breakwaters*. Gent University of Gent. Master Thesis.

DEHNEN, W.; ALY, H. (2012) - *Improving convergence in smoothed particle hydrodynamics simulations without pairing instability.* Monthly Notices of the Royal Astronomical Society. 425:2. 1068-1082.

DHANAK, M.; XIROS, N. (2016) - *Springer handbook of ocean engineering*. Springer.

DIDIER, E.; NEVES, M. G. (2010) - *Modelação da Interacção entre uma Onda e uma Estrutura de Protecção Costeira usando um Modelo Numérico SPH-Smoothed Particles Hydrodynamics.* Revista de Gestão Costeira Integrada-Journal of Integrated Coastal Zone Management. 10:4. 435-455.

DILTS, G. (1999) - *Moving-least-squares-particle hydrodynamics—I. Consistency and stability.* International Journal for Numerical Methods in Engineering. 44:8. 1115-1155.

DISCO, MJ (2012) - *A generic quantitative damage description for rubble mound structures: Investigation of damage to roundheads by using a 3D high-resolution measurement technique in a physical model*. Delft: TU Delft 73 p. Master Thesis.

General Xbloc specification, Xbloc technical guidelines.(Consultado em 29th october). Disponível em WWW: <URL: www.xbloc.com>.

DOMÍNGUEZ, J. (2014) - *DualSPHysics: Towards High Performance Computing using SPH technique*. Universidad de Vigo. PhD Thesis.

DOMÍNGUEZ , J. (2017) - *HPC for SPH methods: Multicore, GPU and multiGPU*. Parma, Italy, 2017.

DOMÍNGUEZ, J.; ALTOMARE, C.; GONZALEZ-CAO, J.; LOMONACO, P. (2019) - *Towards a more complete tool for coastal engineering: solitary wave generation, propagation and breaking in an SPH-based model.* Coastal Engineering Journal. 61:1. 15-40.

DOMÍNGUEZ, J.; CRESPO, A.; GÓMEZ-GESTEIRA, M. (2013) - *Optimization strategies for CPU and GPU implementations of a smoothed particle hydrodynamics method.* Computer Physics Communications. 184:3. 617-627.

DOMÍNGUEZ, J.; FOURTAKAS, G.; ALTOMARE, C.; CANELAS, R.; TAFUNI, A.; GARCÍA-FEAL, O.; MARTÍNEZ-ESTÉVEZ, I.; MOKOS, A.; VACONDIO, R.; CRESPO, A.; ROGERS, B.; STANSBY, P.; GÓMEZ-GESTEIRA, M. (2022) - *DualSPHysics: from fluid dynamics to multiphysics problems.* Computational Particle Mechanics. 9:5. 867-895.

DOST, J.; GRONZ, O.; CASPER, M.; KREIN, A. (2020) - *The potential of Smartstone probes in landslide experiments: how to read motion data.* Natural Hazards Earth System Sciences. 20:12. 3501-3519.

EDEN, D. (2019) - *Forces and Pressures on Core-Loc Armour Units in Rubble Mound Breakwaters Measured via Instrumented "Smart-Units"*. Canada: University of Ottawa. Master Thesis.

ENGLISH, A.; DOMÍNGUEZ, J.; VACONDIO, R.; CRESPO, A.; STANSBY, P.; LIND, S.; CHIAPPONI, L.; GÓMEZ-GESTEIRA, M. (2021) - *Modified dynamic boundary conditions (mDBC) for general-purpose smoothed particle hydrodynamics (SPH): application to tank sloshing, dam break and fish pass problems.* Computational Particle Mechanics. 1-15.

ENGLISH, A.; DOMÍNGUEZ, J.M.; VACONDIO, R.; CRESPO, A.; STANSBY, P.; LIND, S.; CHIAPPONI, L.; GÓMEZ-GESTEIRA, M. (2022) - *Modified dynamic boundary conditions (mDBC) for general-purpose smoothed particle hydrodynamics (SPH): application to tank sloshing, dam break and fish pass problems.* Computational Particle Mechanics. 9:5. 1-15.

EVERTS, P.S. (2016) - *Probabilistic design of a rubble mound breakwater*. Delft: TU Delft. Master Thesis.

FARAHANI, R.; DALRYMPLE, R. (2014) - *Three-dimensional reversed horseshoe vortex structures under broken solitary waves.* Coastal Engineering. 91: 261-279.

FERRAND, M.; LAURENCE, D.; ROGERS, B.; VIOLEAU, D.; KASSIOTIS, C. (2013) - *Unified semi-analytical wall boundary conditions for inviscid, laminar or turbulent flows in the meshless SPH method.* International Journal for Numerical Methods in Fluids. 71:4. 446-472.

FERRARI, A.; DUMBSER, M.; TORO, E.; ARMANINI, A. (2009) - *A new 3D parallel SPH scheme for free surface flows.* Computers & Fluids. 38:6. 1203-1217.

FORTES, Conceição Juana; CAPITÃO, Rui; LEMOS, Rute; MENDONÇA, Ana; PINHEIRO, Liliana; NEVES, Diogo; POSEIRO, Pedro; PEDRO, Francisco; HENRIQUES, Maria (2017) - *Desenvolvimentos, desafios e oportunidades para a modelação física em engenharia costeira e portuária*. In 9ªs Jornadas Portuguesas de Engenharia Costeira e Portuária. LNEC, Lisbon, Portugal: 2017.

FOURTAKAS, G.; DOMINGUEZ, J.; VACONDIO, R.; ROGERS, B. (2019) - *Local uniform stencil (LUST) boundary condition for arbitrary 3-D boundaries in parallel smoothed particle hydrodynamics (SPH) models.* Computers & Fluids. 190: 346-361.

FREITAS, P. (2013) - *Hydraulic stability of antifer block armour layers. Physical model study*. Lisbon, Portugal: Técnico Lisboa. Master Thesis.

FRIGAARD, P.; HGEDAL, M.; CHRISTENSEN, M. (1993) - *Wave generation theory*. Hydraulics and Coastal Engineering Laboratory, Dept. of Civil Engineering, Aalborg University, Aalborg (Denmark).

GINGOLD, R.; MONAGHAN, J. (1977) - *Smoothed particle hydrodynamics: theory and application to non-spherical stars.* Monthly notices of the royal astronomical society. 181:3. 375-389.

GOMES, F. V.; TAVEIRA-PINTO, F. ; VALENTE, P. A.; ROSA-SANTOS, P. J.; LOPES, H. (2013) - *Projeto de Criação de um Novo Terminal Para Contentores no Porto de Leixões*. Instituto de Hidráulica e Recursos Hídricos, Porto, Portugal.

GOMEZ-GESTEIRA, M.; ROGERS, B.; CRESPO, A.; DALRYMPLE, R.; NARAYANASWAMY, M.; DOMINGUEZ, J. (2012) - *SPHysics–development of a free-surface fluid solver–Part 1: Theory and formulations.* Computers & Geosciences. 48: 289-299.

GOMEZ-GESTEIRA, M.; ROGERS, B. D.; VIOLEAU, D.; GRASSA, J.; CRESPO, A. (2010a) - *Foreword: SPH for free-surface flows.* Journal of Hydraulic Research. 48:sup1. 3-5.

GOMEZ-GESTEIRA, M.; ROGERS, B.; DALRYMPLE, R.; CRESPO, A. (2010b) - *State-of-the-art of classical SPH for free-surface flows.* Journal of Hydraulic Research. 48:sup1. 6-27.

GÓMEZ-MARTÍN, M.; MEDINA, J. (2005) - Wave-to-wave exponential estimation of armor damage progression. In Coastal Engineering 2004: (In 4 Volumes). World Scientific.p. 3592-3604.

--- (2007) - Damage progression on cube armored breakwaters. In Coastal Engineering 2006: (In 5 Volumes). World Scientific.p. 5229-5240.

GONZÁLEZ-CAO, J.; ALTOMARE, C.; CRESPO, A.; DOMÍNGUEZ, J.; GÓMEZ-GESTEIRA, M.; KISACIK, D. (2019) - *On the accuracy of DualSPHysics to assess violent collisions with coastal structures.* Computers & Fluids. 179: 604-612.

GORING, D. (1978) - *Tsunamis--the propagation of long waves onto a shelf.*

GOTOH, H. (2001) - *Sub-particle-scale turbulence model for the MPS method-Lagrangian flow model for hydraulic engineering.* Computational Fluid Dynamics Jour. 9:4. 339-347.

GOTOH, H.; KHAYYER, A. (2018) - *On the state-of-the-art of particle methods for coastal and ocean engineering.* Coastal Engineering Journal. 60:1. 79-103.

GOTOH, H.; SHAO, S.; MEMITA, T. (2004) - *SPH-LES model for numerical investigation of wave interaction with partially immersed breakwater.* Coastal Engineering Journal. 46:1. 39-63.

GRONZ, O.; HILLER, P.; WIRTZ, S.; BECKER, K.; ISERLOH, T.; SEEGER, M.; BRINGS, C.; ABERLE, J.; CASPER, M.; RIES, J. (2016) - *Smartstones: A small 9-axis sensor implanted in stones to track their movements.* Catena. 142: 245-251.

GUI, P.; TANG, L.; MUKHOPADHYAY, S. (2015) - *MEMS based IMU for tilting measurement: Comparison of complementary and kalman filter based data fusion*. 2015. IEEE.

HAGEMEIER, T.; THÉVENIN, D.; RICHTER, T. (2021) - *Settling of spherical particles in the transitional regime.* International Journal of Multiphase Flow. 138: 103589.

HANSEN, N.; SAND, S.; LUNDGREN, H.; SORENSEN, T.; GRAVESEN, H. (1980) - Correct reproduction of group-induced long waves. In Coastal Engineering 1980. p. 784-800.

HOFLAND, B.; AREFIN, S.; VAN DER LEM, C.; VAN GENT, M. R. A. (2018) - *Smart rocking armour units*. Santander, Cantabria, Spain, 2018.

HOFLAND, B.; DISCO, M.; VAN GENT, M. R. A. (2014) - *Damage characterization of rubble mound roundheads*. Varna, Bulgaria, 2014.

HOFLAND, B.; HOUTZAGER, D.; CALDERA, G.; ANTONINI, A.; VAN GENT, M. R. A.; BAKKER, P.; VAN DER LEM, C. (2023) - *Rocking of single-layer armour units measured by embedded sensors.* Journal of Coastal Hydraulic Structures. 3: 28.

HOFLAND, B.; ROSA-SANTOS, P.; TAVEIRA-PINTO, F.; DE ALMEIDA, E.; MENDONÇA, A.; LEMOS, R.; FORTES, J. (2017) - *Measuring damage in physical model tests of rubble mounds*. Liverpool, UK, 2017. ICE - Institution of Civil Engineering.

HOFLAND, Bas; DIAMANTIDOU, Eleni; VAN STEEG, Paul; MEYS, Paul (2015) - *Wave runup and wave overtopping measurements using a laser scanner.* Coastal engineering. 106: 20-29.

HOFLAND, Bas; GENT, Marcel van; RAAIJMAKERS, Tim; LIEFHEBBER, Freek (2013) - Damage evaluation using the damage depth. In Coastal Structures 2011. World Scientific.p. 812-823.

HOLTZHAUSEN, A. H.; GUERRERO, F. M. (2017) - *Dolos Hydraulic-Stability Formula Update and Optimum Packing Density.* Journal of Waterway, Port, Coastal, and Ocean Engineering. Vol. 143:3. 04016021.

HOUTZAGER, D.; HOFLAND, B.; CALDERA, G.; VAN DER LEM, C.; VAN GENT, M.R.A.; BAKKER, P.; ANTONINI, A. (2024) - Embedded Rocking Measurement of Single Layer Armour Units. Development and First Results. In Coasts, Marine Structures and Breakwaters 2023: Resilience and adaptability in a changing climate. Emerald Publishing Limited.p. 385-397.

HUGHES, S. (1993) - *Physical models and laboratory techniques in coastal engineering*. Singapore: World Scientific.

INFANTE, M.; MARSICO, A.; PENNETTA, L. (2012) - *Some results of coastal defences monitoring by ground laser scanning technology.* Environmental Earth Sciences. 67:8. 2449-2458.

INUTSUKA, S. (2002) - *Reformulation of smoothed particle hydrodynamics with Riemann solver.* Journal of Computational Physics. 179:1. 238-267.

JAMIL, F.; IQBAL, N.; AHMAD, S.; KIM, D. (2020) - *Toward accurate position estimation using learning to prediction algorithm in indoor navigation.* Sensors. 20:16. 4410.

KAKU, S.; KOBAYASHI, N.; RYU, C. (1991) - *Design Formulas for Hydraulic Stability of Rock Slopes under Irregular Wave Attack*. Restin, VA, USA, 1991.

KOK, M.; HOL, J.; SCHÖN, T. (2017) - *Using inertial sensors for position and orientation estimation.*

KULASEGARAM, S.; BONET, J.; LEWIS, R.; PROFIT, M. (2004) - *A variational formulation based contact algorithm for rigid boundaries in two-dimensional SPH applications.* Computational Mechanics. 33:4. 316-325.

LE, T. N. (2016) - *Rocking Revisited 1: Rocking of a Singe Cube on a Breakwater Slope*.

LE TOUZÉ; SHADLOO, M. ; OGER, G. (2016) - *Smoothed particle hydrodynamics method for fluid flows, towards industrial applications: motivations, current state, and challenges.* Comput Fluids. 136: 11-34.

LEE, E.; MOULINEC, C.; XU, R.; VIOLEAU, D.; LAURENCE, D.; STANSBY, P. (2008) - *Comparisons of weakly compressible and truly incompressible algorithms for the SPH mesh free particle method.* Journal of computational Physics. 227:18. 8417-8436.

LEIMKUHLER, B.; MATTHEWS, C. (2016) - *Molecular Dynamics. With Deterministic and Stochastic Numerical Methods*. JSTOR.

LEIMKUHLER, B.; REICH, S.; SKEEL, R. (1996) - Integration methods for molecular dynamics. In Mathematical Approaches to biomolecular structure and dynamics. Springer.p. 161-185.

LEMOS, R.; HENRIQUES, M.; MURALHA, A.; JÓNATAS, R.; FORTES, C.; CAPITÃO, R. (2017) - *Survey of a two-dimensional scale model of a rubble-mound breakwater using different stereo-photogrammetric techniques*. In 7th International Conference on Engineering Surveying. Lisbon, Portugal: 2017.

LEMOS, R.; SANTOS, J.A. (2013) - *Photogrammetric profile survey in scale model tests of rubble-mound breakwaters*. In 6th SCACR – International Short Course/Conference on Applied Coastal Research. Lisbon, Portugal: 2013.

LEMOS, R.; SILVA, L. (2013) - *LNEC experience in maritime hydraulic studies. Scale model tests and recent damage assessment techniques.* PIANC.

LEROY, A.; VIOLEAU, D.; FERRAND, M.; KASSIOTIS, C. (2014) - *Unified semi-analytical wall boundary conditions applied to 2-D incompressible SPH.* Journal of Computational Physics. 261: 106-129.

LI, S.; LIU, W. (2007) - *Meshfree particle methods*. Springer Science & Business Media.

LIND, S.; ROGERS, B.; STANSBY, P. (2020) - *Review of smoothed particle hydrodynamics: towards converged Lagrangian flow modelling.* Proceedings of the Royal Society A. 476:2241.

LIND, S.; XU, R.; STANSBY, P.; ROGERS, B. (2012) - *Incompressible smoothed particle hydrodynamics for free-surface flows: A generalised diffusion-based algorithm for stability and validations for impulsive flows and propagating waves.* Journal of Computational Physics. 231:4. 1499-1523.

LIU, G.; LIU, M. (2003) - *Smoothed particle hydrodynamics: a meshfree particle method*. World scientific.

LIU, M.; LIU, G. (2006) - *Restoring particle consistency in smoothed particle hydrodynamics.* Applied numerical mathematics. 56:1. 19-36.

LIU, Z.; FRIGAARD, P. (1999) - *Generation and analysis of random waves.*

LO, E.; SHAO, S. (2002) - *Simulation of near-shore solitary wave mechanics by an incompressible SPH method.* Applied Ocean Research. 24:5. 275-286.

LOSADA, M. A.; DESIRE, J.; ALEJO, L. (1986) - *Stability of blocks as breakwater armor units.* 112:11. 2392-2401.

LOWE, R.; BUCKLEY, M.; ALTOMARE, C.; RIJNSDORP, D.; YAO, Y.; SUZUKI, T.; BRICKER, J. (2019) - *Numerical simulations of surf zone wave dynamics using Smoothed Particle Hydrodynamics.* Ocean Modelling. 144: 101481.

LUO, M.; KHAYYER, A.; LIN, P. (2021) - *Particle methods in ocean and coastal engineering.* Applied Ocean Research. 114: 102734.

MADSEN, O. (1971) - *On the generation of long waves.* Journal of Geophysical Research. 76:36. 8672-8683.

MANIATIS, G. (2021) - *On the use of IMU (inertial measurement unit) sensors in geomorphology.* Earth Surface Processes Landforms. 46:11. 2136-2140.

MANSARD, E.; FUNKE, E. (1980) - The measurement of incident and reflected spectra using a least squares method. In Coastal Engineering 1980. p. 154-172.

MARRONE, S.; ANTUONO, M.; COLAGROSSI, A.; COLICCHIO, G.; LE TOUZÉ, D.; GRAZIANI, G. (2011) - *δ-SPH model for simulating violent impact flows.* Computer Methods in Applied Mechanics and Engineering. 200:13-16. 1526-1542.

MARTÍNEZ-ESTÉVEZ, I.; DOMÍNGUEZ, J.; TAGLIAFIERRO, B.; CANELAS, R.; GARCÍA-FEAL, O.; CRESPO, A.; GÓMEZ-GESTEIRA, M. (2023) - *Coupling of an SPH-based solver with a multiphysics library.* Computer Physics Communications. 283: 108581.

MAYRHOFER, A.; ROGERS, B.; VIOLEAU, D.; FERRAND, M. (2013) - *Investigation of wall bounded flows using SPH and the unified semi-analytical wall boundary conditions.* Computer Physics Communications. 184:11. 2515-2527.

MEDINA, J. (1996) - *Wave climate simulation and breakwater stability*. Orlando, FL, USA, 1996.

MELBY, J. A. (1999) - *Damage Progression on Rubble-mound Breakwaters*. US Army Engineer Waterways Experiment Station.

MELBY, J. A.; KOBAYASHI, N. (1998a) - *Damage progression on breakwaters*. Copenhagen, Denmark, , 1998a.

--- (1998b) - *Progression and Variability of Damage on Rubble Mound Breakwaters* Journal of Waterway, Port, Coastal, and Ocean Engineering. Vol. 124:6. 286 - 294.

--- (1999) - *Damage progression and variability on breakwater trunks*. Santander, Spain, 1999.

MELBY, J. A.; TURK, G. F. (1997) - *CORE-LOC Concrete Armor Units: Technical Guidelines* Vicksburg, MS

MELBY, J.; HUGHES, S. (2003) - *Armor Stability Based on Wave Momentum Flux*. Portland, OR, USA, 2003.

MELBY, J.; KOBAYASHI, N. (2011) - *Stone armor damage initiation and progression based on the maximum wave momentum flux.* Journal of Coastal Research. 27:1. 110-119.

MITSUI, J.; ALTOMARE, C.; CRESPO, A.; DOMÍNGUEZ ALONSO, J.; SUZUKI, T.; KUBOTA, S.; GÓMEZ-GESTEIRA, M. (2021) - *SPH simulation of hydrodynamic behaviour of Tetrapods against solitary wave*. 2021. New Jersey Institute of Technology.

MITSUI, J.; ALTOMARE, C.; CRESPO, A.; DOMÍNGUEZ, J.; MARTÍNEZ-ESTÉVEZ, I.; SUZUKI, T.; KUBOTA, S.; GOMÉZ-GESTEIRA, M. (2023) - *DualSPHysics modelling to analyse the response of Tetrapods against solitary waves.* Coastal Engineering. 183: 104315.

MOLTENI, D.; COLAGROSSI, A. (2009) - *A simple procedure to improve the pressure evaluation in hydrodynamic context using the SPH.* Computer Physics Communications. 180:6. 861-872.

MONAGHAN, J. (1992) - *Smoothed particle hydrodynamics.* Annual review of astronomy and astrophysics. 30:1. 543-574.

--- (1994) - *Simulating free surface flows with SPH.* Journal of computational physics. 110:2. 399-406.

--- (2005) - *Smoothed particle hydrodynamics.* Reports on progress in physics. 68:8. 1703.

MONAGHAN, J.; KAJTAR, J. (2009) - *SPH particle boundary forces for arbitrary boundaries.* Computer physics communications. 180:10. 1811-1820.

MONAGHAN, J.; KOS, A. (1999) - *Solitary waves on a Cretan beach.* Journal of waterway, port, coastal, and ocean engineering. 125:3. 145-155.

MONAGHAN, J.; KOS, A.; ISSA, N. (2003) - *Fluid motion generated by impact.* Journal of waterway, port, coastal, and ocean engineering. 129:6. 250-259.

MONAGHAN, J.; LATTANZIO, J. (1985) - *A refined particle method for astrophysical problems.* Astronomy and astrophysics. 149: 135-143.

MOREIRA, A. (2021) - *Numerical modelling of spillways and energy dissipators using the smoothed particle hydrodynamics method.*

MOULIN, Frederic (2018) - *Hydralab +: Protocols for representing variability and unsteadiness in flume facilities*.

NĂSTĂSESCU, V.; GAVRILĂ, L. (2012) - *CONTROLLED FLOW SIMULATION USING SPH METHOD.* Scientific Research & Education in the Air Force-AFASES. 1:

NEIVA, J.; PAIVA, S.; LOPES, S. (2021) - *Monitoring the hydraulic stability of Antifer blocks: an IoT-based approach*. 2021. IEEE.

OUMERACI, H.; KORTENHAUS, A.; ALLSOP, W.; DE GROOT, M.; CROUCH, R.; VRIJLING, H.; VOORTMAN, H. (2001) - *Probabilistic design tools for vertical breakwaters*. Netherlands: A. A. Balkema Publishers.

OZBULUT, M.; YILDIZ, M.; GOREN, O. (2014) - *A numerical investigation into the correction algorithms for SPH method in modeling violent free surface flows.* International Journal of Mechanical Sciences. 79: 56-65.

PARSHIKOV, A.; MEDIN, S.; LOUKASHENKO, I.; MILEKHIN, V. (2000) - *Improvements in SPH method by means of interparticle contact algorithm and analysis of perforation tests at moderate projectile velocities.* International Journal of Impact Engineering. 24:8. 779-796.

PILARCZYK, K. (2003) - *Hydraulic and coastal structures in international perspective*: ASCE.

PRASHANTH, J. (2013) - *Parametric Studies on Stability of Reshaped Berm Breakwater with Concrete Cubes as Armor Unit*. National Institute of Technology Karnataka, Surathkal. PhD Thesis.

PRINGGANA, G.; CUNNINGHAM, L.; ROGERS, B. (2016) - *Modelling of tsunami-induced bore and structure interaction.* Proceedings of the Institution of Civil Engineers-Engineering and Computational Mechanics. 169:3. 109-125.

PUENTE, Iván; LINDENBERGH, R; GONZÁLEZ-JORGE, Higinio; ARIAS, P (2014a) - *Terrestrial laser scanning for geometry extraction and change monitoring of rubble mound breakwaters*. 2014a.

PUENTE, Iván; SANDE, José; GONZÁLEZ-JORGE, Higinio; PEÑA-GONZÁLEZ, Enrique; MACIÑEIRA, Enrique; MARTÍNEZ-SÁNCHEZ, Joaquín; ARIAS, Pedro (2014b) - *Novel image analysis approach to the terrestrial LiDAR monitoring of damage in rubble mound breakwaters.* Ocean Engineering. 91: 273-280.

PUERTOS DEL ESTADO (2001) - *ROM 0.0-01.*

PURI, K.; RAMACHANDRAN, P. (2014) - *A comparison of SPH schemes for the compressible Euler equations.* Journal of Computational Physics. 256: 308-333.

REIS, Maria Teresa; SILVA, Luís Gabriel; NEVES, Mara Graça; LEMOS, Rute; CAPITÃO, Rui; FORTES, Conceição Juana (2015) - *Physical modelling as a fundamental tool for the design of harbours and maritime structures.* PIANC.

REN, B.; HE, M.; DONG, P.; WEN, H. (2015) - *Nonlinear simulations of wave-induced motions of a freely floating body using WCSPH method.* Applied Ocean Research. 50: 1-12.

ROGERS, B. D.; MOKOS, A.; FOURTAKAS, G.; CRESPO, A. J. C.; DOMINGUEZ, J. M.; ALTOMARE, C.; CANELAS, R. (2015) - *Developing SPH simulations for coastal applications accelerated on GPUs using DualSPHysics.* Hydrolink. 3:3. 81-84.

ROPERO-GIRALDA, P.; CRESPO, A.; TAGLIAFIERRO, B.; ALTOMARE, C.; DOMÍNGUEZ, J.; GÓMEZ-GESTEIRA, M.; VICCIONE, G. (2020) - *Efficiency and survivability analysis of a point-absorber wave energy converter using DualSPHysics.* Renewable Energy. 162: 1763-1776.

ROSELLI, R.; VERNENGO, G.; ALTOMARE, C.; BRIZZOLARA, S.; BONFIGLIO, L.; GUERCIO, R. (2018) - *Ensuring numerical stability of wave propagation by tuning model parameters using genetic algorithms and response surface methods.* Environmental Modelling & Software. 103: 62-73.

RUSSHAKIM, N.A.S.; ARIFF, M.F.M.; MAJID, Z.; IDRIS, K.M.; DARWIN, N.; ABBAS, M.A.; ZAINUDDIN, K.; YUSOFF, A.R. (2019) - *The Suitability of Terrestrial Laser Scanning for Building Survey and Mapping Applications.* International Archives of the Photogrammetry, Remote Sensing and Spatial Information Sciences. 42:2/W9.

SANTOS, J.; LEMOS, R. ; WEIMPER, J.; GRONZ, O.; HOFLAND, B.; SANDE, J.; PEÑA, E.; REIS, M.; FORTES, C.; FIGUERO, A.; BORNSCHEIN, A.; KERPEN, N.; PEDRO, F.; COIMBRA, M. ; KÖRNER, M.; VAN DEN BOS, J.; DOST, B. ; CARVALHO, R. ; ALVARELLOS, A.; POHL, R. (2019) - *Data Storage Report. Rodbreak - Wave Run-up, Overtopping and Damage in Rubble-mound Breakwaters Under Oblique Extreme Wave Conditions Due to Climate Change Scenarios*

SARFARAZ, M.; PAK, A. (2018) - *Numerical investigation of the stability of armour units in low-crested breakwaters using combined SPH–Polyhedral DEM method.* Journal of Fluids and Structures. 81: 14-35.

SATO, K.; KAWASAKI, K.; WATANABE, K.; KOSHIMURA, S. (2021) - *Validation of the applicability of the particle-based open-source software DualSPHysics to violent flow fields.* Coastal Engineering Journal. 63:4. 545-572.

SCHÄFFER, H.; KLOPMAN, G. (2000) - *Review of multidirectional active wave absorption methods.* Journal of waterway, port, coastal, and ocean engineering. 126:2. 88-97.

SERRE, F. (1953) - *Contribution à l'étude des écoulements permanents et variables dans les canaux.* La Houille Blanche.6. 830-872.

SHADLOO, M.; OGER, G.; LE TOUZÉ, D. (2016) - *Smoothed particle hydrodynamics method for fluid flows, towards industrial applications: Motivations, current state, and challenges.* Computers & Fluids. 136: 11-34.

SHAO, S. (2005) - *SPH simulation of solitary wave interaction with a curtain-type breakwater.* Journal of Hydraulic research. 43:4. 366-375.

SHAO, S.; JI, C.; GRAHAM, D.; REEVE, D.; JAMES, P.; CHADWICK, A. (2006) - *Simulation of wave overtopping by an incompressible SPH model.* Coastal engineering. 53:9. 723-735.

SHAO, S.; LO, E. (2003) - *Incompressible SPH method for simulating Newtonian and non-Newtonian flows with a free surface.* Journal of Advances in Water Resources. 26:7. 787-800.

SHEN, Yueqian; LINDENBERGH, Roderik; HOFLAND, Bas; KRAMER, Roy (2017) - *Change analysis of laser scans of laboratory rock slopes subject to wave attack testing*. Wuhan, China, 2017.

SKILLEN, A.; LIND, S.; STANSBY, P.; ROGERS, B. (2013) - *Incompressible smoothed particle hydrodynamics (SPH) with reduced temporal noise and generalised Fickian smoothing applied to body–water slam and efficient wave–body interaction.* Computer Methods in Applied Mechanics and Engineering. 265: 163-173.

SMITH, W.; KOBAYASHI, N.; KAKU, S. (1992) - *Profile changes of rock slopes by irregular waves*. Venice, Italy, 1992.

SOGREAH (2000) - *General specification for Áccropode armour*. Grenoble, France Sogreag, Port and Coastal Engineering Departmant.

SOUTO-IGLESIAS, A. (2021) - *Modeling viscous forces in SPH*. 2021.

STREICHER, M.; HOFLAND, B.; LINDENBERGH, RC. (2013) - *Laser ranging for monitoring water waves in the new Deltares Delta Flume*. 2013. ISPRS.

SUBRAMANIAM, S.; SCHERES, B.; SCHILLING, M.; LIEBISCH, S.; KERPEN, N.; SCHLURMANN, T.; ALTOMARE, C.; SCHÜTTRUMPF, H. (2019) - *Influence of convex and concave curvatures in a coastal dike line on wave run-up.* Water. 11:7. 1333.

SUZUKI, T.; GARCÍA-FEAL, O.; DOMÍNGUEZ, J.; ALTOMARE, C. (2022) - *Simulation of 3D overtopping flow–object–structure interaction with a calibration-based wave generation method with DualSPHysics and SWASH.* Computational Particle Mechanics. 1-13.

TAFUNI, A.; DOMÍNGUEZ, J.; VACONDIO, R.; CRESPO, A. (2018) - *A versatile algorithm for the treatment of open boundary conditions in Smoothed particle hydrodynamics GPU models.* Computer Methods in Applied Mechanics and Engineering. 342: 604-624.

TAKLAS, Mohamad; LEBLOUBA, Moussa; BARAKAT, Samer; FAGEERI, Ahmed; MOHAMAD, Firass %J Scientific Reports (2022) - *Concrete-to-concrete shear friction behavior under cyclic loading: experimental investigation.* 12:1. 9451.

TASORA, A.; SERBAN, R.; MAZHAR, H.; PAZOUKI, A.; MELANZ, D.; FLEISCHMANN, J.; TAYLOR, M.; SUGIYAMA, H.; NEGRUT, D. (2016) - *Chrono: An open source multi-physics dynamics engine*. Soláň, Czech Republic, 2016. Springer.

TENNEKES, H.; LUMLEY, J.; LUMLEY, J. (1972) - *A first course in turbulence*. MIT press.

TULSI, Kishan Ramesh (2016) - *Three dimensional method for monitoring damage to dolos breakwaters*. Stellenbosch University.

VACONDIO, R. (2020) - *Online Course on Smoothed Particle Hydrodynamics (SPH) numerical methods*. Parma, Italy.

--- (2021) - *New density diffusion term*. 2021.

VACONDIO, R.; ALTOMARE, C.; DE LEFFE, M.; HU, X.; LE TOUZÉ, D.; LIND, S.; MARONGIU, J.; MARRONE, S.; ROGERS, B.; SOUTO-IGLESIAS, A. (2021) - *Grand challenges for Smoothed Particle Hydrodynamics numerical schemes.* Computational Particle Mechanics. 8:3. 575-588.

VACONDIO, R.; ROGERS, B.; STANSBY, P.; MIGNOSA, P. (2016) - *Variable resolution for SPH in three dimensions: Towards optimal splitting and coalescing for dynamic adaptivity.* Computer Methods in Applied Mechanics and Engineering. 300: 442-460.

VACONDIO, R.; ROGERS, B.; STANSBY, P.; MIGNOSA, P.; FELDMAN, J. (2013) - *Variable resolution for SPH: a dynamic particle coalescing and splitting scheme.* Computer Methods in Applied Mechanics and Engineering. 256: 132-148.

VAN DER MEER, J. W. (1988a) - *Deterministic and probabilistic design of breakwater armor layers.* Journal of waterway, port, coastal, and ocean engineering. Vol. 114:1. 66-80.

--- (1988b) - *Rock slopes and gravel beaches under wave attack*. Delft: Delft University of Technology. PhD Thesis.

--- (1988c) - *Stability of cubes, tetrapod and accropode. Design of Breakwaters*. London: Thomas Telford.

--- (1998) - Application and stability criteria for rock and artificial units. In PILARCZYK, K. Dikes and revetments: Design, maintenance and safety assessment. Rotterdam, Netherlands: A.A. Balkema.p. 191-215.

VAN DER MEER, J. W.; HEYDRA, G. (1991) - *Rocking armour units: Number, location and impact velocity.* Coastal Engineering. 15:1-2. 21-39.

VAN GENT, M. R. A.; D'ANGREMOND, K.; TRIEMSTRA, R. (2001) - *Rubble mound breakwaters; single armour layers and high density units*. London, UK, 2001. T. Telford.

VAN GENT, M. R. A.; DE ALMEIDA, E.; HOFLAND, B. (2019) - *Statistical analysis of the stability of rock slopes.* Journal of Marine Science Engineering. 7:3. 60.

VAN GENT, M. R. A.; LUIS, L. (2013) - *Application of Cubes in a single layer*. Lisbon, Portugal, 2013.

VAN GENT, M. R. A.; PLATE, S. E.; BERENDSEN, E.; SPAAN, G. B. H.; VAN DER MEER, J. W.; D'ANGREMOND, K. (1999) - *Single-layer rubble mound breakwaters*. Santander, Spain, 1999. A.A. Balkema.

VERBRUGGHE, T.; STRATIGAKI, V.; ALTOMARE, C.; DOMÍNGUEZ, J.; TROCH, P.; KORTENHAUS, A. (2019) - *Implementation of open boundaries within a two-way coupled SPH model to simulate nonlinear wave–structure interactions.* Energies. 12:4. 697.

VERLET, L. (1967) - *Computer" experiments" on classical fluids. I. Thermodynamical properties of Lennard-Jones molecules.* Physical review. 159:1. 98.

VIDAL, C.; LOSADA, M.; MEDINA, R. (1991) - *Stability of mound breakwater's head and trunk.* 117:6. 570-587.

VIDAL, C.; MARTIN, F.; NEGRO, V.; GIRONELLA, X.; MADRIGAL, B.; GARCÍA-PALACIOS, J. (2004) - Measurement of armor damage on rubble mound structures: comparison between different methodologies. In Coastal Structures 2003. p. 189-200.

VIEIRA, F.; TAVEIRA-PINTO, F.; ROSA-SANTOS, P. (2021) - *Damage evolution in single-layer cube armoured breakwaters with a regular placement pattern.* Coastal Engineering. 169: 103943.

VIOLEAU, D. (2012) - *Fluid mechanics and the SPH method: theory and applications*. Oxford University Press.

VIOLEAU, D.; LEROY, A. (2014) - *On the maximum time step in weakly compressible SPH.* Journal of Computational Physics. 256: 388-415.

VIOLEAU, D.; ROGERS, B. (2016) - *Smoothed particle hydrodynamics (SPH) for free-surface flows: past, present and future.* Journal of Hydraulic Research. 54:1. 1-26.

WALLINGFORD, HR (2013) - *HR DAQ-Data acquisition and analysis software programme: user manual.* HR Walingford Ltd.

WEN, H.; REN, B.; WANG, G. (2018) - *3D SPH porous flow model for wave interaction with permeable structures.* Applied ocean research. 75: 223-233.

WENDLAND, H. (1995) - *Piecewise polynomial, positive definite and compactly supported radial functions of minimal degree.* Advances in computational Mathematics. 4:1. 389-396.

WORSTER, G.; MOFFATT, K.; BATCHELOR, G. (2000) - *Perspectives in Fluid Dynamics: A Collective Introduction to Current Research*. Cambridge University Press Cambridge, UK.

XU, R.; STANSBY, P.; LAURENCE, D. (2009) - *Accuracy and stability in incompressible SPH (ISPH) based on the projection method and a new approach.* Journal of computational Physics. 228:18. 6703-6725.

ZEIDLER, B.; TARNOWSKA, M.; PRUSAK, Z.; BASINKSI, T. (1992) - *Effectiveness of coastal defence measures: Design background for coastal defence and management: near field and far-field factors in overall (geometrical) and structural design*: RIJKSWATERSTAAT, DWW.

ZHANG, F.; CRESPO, A.; ALTOMARE, C.; DOMÍNGUEZ, J.; MARZEDDU, A.; SHANG, S.; GÓMEZ-GESTEIRA, M. (2018) - *DualSPHysics: a numerical tool to simulate real breakwaters.* Journal of Hydrodynamics. 30:1. 95-105.